Recherche de la double désintégration beta sans émission de neutrino. Le détecteur BiPo

Xavier Sarazin

ORSAY *LAL 12-130*

n^0 d'ordre :

Université de Paris-Sud 11
UFR scientifique d'Orsay

Mémoire d'habilitation
à diriger les recherches

par

Xavier Sarazin

Recherche de la double désintégration beta sans émission de neutrino

Le détecteur BiPo

Soutenue le 3 mai 2012, devant le jury composé de :

Jules Gascon	(Rapporteur)
François Mauger	
Stefan Schönert	(Rapporteur)
Achille Stocchi	(Président)
Mossadek Talby	(Rapporteur)

Avant-propos

Il y a 75 ans, Ettore Majorana montrait que le neutrino, seule particule élémentaire de matière de charge électrique nulle, pouvait théoriquement être identique à son antiparticule. Si tel est le cas, alors un phénomène naturel nouveau devrait apparaître pour quelques rares isotopes : leur double désintégration beta sans émission de neutrino ($\beta\beta0\nu$). La signature expérimentale de ce processus est simple : l'observation de deux électrons émis par le noyaux dont la somme de leur énergie correspond à l'énergie de transition. Mais ce processus, s'il existe, est infiniment rare. La principale difficulté dans cette recherche est donc instrumentale : réussir à développer un détecteur ultra basse radioactivité, sans aucun bruit de fond.

J'ai toujours été impressionné de voir la grande variété des techniques expérimentales utilisées pour y parvenir. J'ai donc choisi comme première partie de mon HDR, d'écrire une revue *expérimentale* relativement détaillée des différents projets, mon souhait étant de montrer pour chaque expérience, ses avantages et limitations en mettant l'accent sur les techniques utilisées pour supprimer les bruits de fond. Ayant été très impliqué dans l'expérience NEMO-3, et travaillant maintenant dans le nouveau projet SuperNEMO, j'ai davantage détaillé ces deux expériences. J'ai également détaillé les projets de bolomètres scintillants. C'est en effet une technique que j'avais particulièrement étudiée ces dernières années (entre autre dans le cadre du réseau européen double beta) car elle me semble être prometteuse. Le dernier chapitre de cette première partie est un résumé permettant au lecteur qui le souhaite une revue plus rapide des différents projets actuels.

Depuis 5 ans, je suis responsable du développement d'un détecteur basse radioactivité, appelé BiPo, dont l'objectif est de mesurer la radiopureté en ^{238}U et ^{232}Th des futures feuilles sources émettrices double beta qui seront installées dans le détecteur SuperNEMO. J'ai donc choisi comme deuxième partie de mon HDR, de présenter ce détecteur et de résumer les différents résultats obtenus.

Table des matières

Première partie

Review of the double beta experiments for the search of the Majorana neutrino

Chapitre 1

The majorana neutrino and the neutrinoless double beta decay

The neutrino is one of the most puzzling elementary particle with very unique properties. It has no electrical charge [1], it is thus only sensitive to weak interaction and its mass is very light. The absence of electrical charge could be considered as a minor characteristic. But it is not. Ettore Majorana showed that a neutral elementary particle which does not contain any discrete quantum number (as the neutrino), can be described by a so-called Majorana field, in which the distinction between matter and antimatter vanishes [2]. In other words, a neutrino might be identical to its own anti-particle.

If the neutrino is a Majorana neutrino, an important consequence is that Lepton Number Violation (LNV) must occur [3][4]. LNV is a required condition for Grand Unified Theories (GUT), in which quarks and leptons are components of the same multiplet, and hence both lepton and baryon numbers are not expected to be conserved quantities. Leptogenesis is an example of model, which uses the LNV from the decay of heavy Majorana neutrinos to produce the observed asymetry of matter and antimatter in the Universe. Another motivation for the Majorana neutrino is the see-saw mechanism [5][3], which splits the Majorana mass term of neutrinos in light and heavy Majorana neutrinos and thus could explain the very small mass of the observed neutrinos, with the condition that the mass of the heavy one is at the GUT energy scale of about 10^{15} GeV.

The most sensitive method to answer the nature of the neutrino is the search of the neutrinoless double beta decay ($\beta\beta0\nu$).

1.1 The neutrinoless double beta decay

The standard double beta decay with emission of two electrons and two neutrinos ($\beta\beta2\nu$) is a second order process of β-decay, which is produced by isotopes whose β-decay is forbiden (due to a higher energy level of the daughter nuclei or due to angular momentum conservation).

$$(A, Z) \rightarrow (A, Z-2) + 2e^- + 2\nu_e$$

1. The limit on $\bar{\nu}_e$ magnetic moment gives $q/e < 3.7\ 10^{-12}$ and astrophysical considerations give $q/e < 2\ 10^{-14}$ [1]

The Feynman diagram is shown in Figure 1.1-a. This standard process is very rare but it has been already observed for 7 isotopes with a hal-life varying from about 7 10^{18} years for ^{100}Mo and ^{150}Nd, to about 10^{21} years for ^{76}Ge and ^{136}Xe, and about 2 10^{24} years for ^{128}Te. Table 1.1 lists the double beta isotopes used in the search of the $\beta\beta0\nu$-decay and their measured $\beta\beta2\nu$ half-life.

If we now consider that the neutrino is a Majorana particle, identical to its own antiparticle, then it becomes possible that the neutrino emitted at the first vertex of the W boson decay is absorbed by the second W vertex and thus only two electrons are emitted by the nucleus (the exchange neutrino is virtual). It corresponds to the neutrinoless double beta decay ($\beta\beta0\nu$) where two neutrons decay into two protons emitting only two electrons :

$$(A, Z) \rightarrow (A, Z-2) + 2e^-$$

This process violates the lepton number by two units ($\Delta L = 2$), and is thus forbidden by the Standard Model.

Experimentaly, the two decay modes, $\beta\beta2\nu$ and $\beta\beta0\nu$ are distinguished by the fact that the sum of the two electron energies in $\beta\beta0\nu$-decay is constant and equal to the transition energy $Q_{\beta\beta}$ while it varies continuously in $\beta\beta2\nu$-decay up to the same energy as its limit (with a maximum around 1/3 $Q_{\beta\beta}$).

The $\beta\beta0\nu$-decay was first proposed by Furry in 1939 [6]. We note that Furry expected a larger $\beta\beta0\nu$-decay rate since only two particles are emitted in the $\beta\beta0\nu$-decay, corresponding to a larger phase space factor. However, because of the absence of right-handed current in the weak interaction (not yet known at the time of Furry's calculation), the helicity of the neutrino emitted at the first vertex must be flipped in order to be absorbed by the second vertex. It is possible since the neutrino is a massive particle, and therefore there is a tiny admixtures of opposite helicity in neutrino of order of m_ν/E where m_ν is the neutrino mass and E its energy. The $\beta\beta0\nu$-decay rate is then strongly suppressed and is proportional to m_ν/E.

The mechanism which as been described is only one possible process (considered as the standard process) but other mechanisms are possible and any source of lepton number violation can induce $\beta\beta0\nu$ decay and contribute to its amplitude. For instance if there is a right-handed component in the weak interaction (V+A current), the right-handed neutrino emitted at the first vertex is directly absorbed via V+A current by the second W boson without requirement of flip helicity (see Figure 1.1). In this case the expected angular distribution between the two emitted electrons is different from the distribution in the case of the standard mechanism. As it will be discussed later, only tracko-calo experiments like NEMO-3 and SuperNEMO can measure the angular distribution and therefore can distinguish the two processes in case of a positive signal. Another possible mechanism is the exchange of a supersymetric particle χ, instead of a Majorana neutrino, with short-range or long-range R-parity violating SUSY contributions. See the complete review of possible mechanisms in [8]. Finally another alternative mechanism is the emission of a Majoron, a goldstone (massless) boson related to the $L - B$ symetry breaking (see Figure 1.1). In this case, the $\beta\beta$ energy sum spectrum of the two electrons is expected to be distorded. The deformation depends on the spectral index (or number of emitted Majoron) as illustrated in Figure 1.2.

Even if many mechanisms are possible to produce $\beta\beta0\nu$-decay, any observation of $\beta\beta0\nu$-decay would prove that the neutrino is a Majorana particle. Indeed all realizations of the

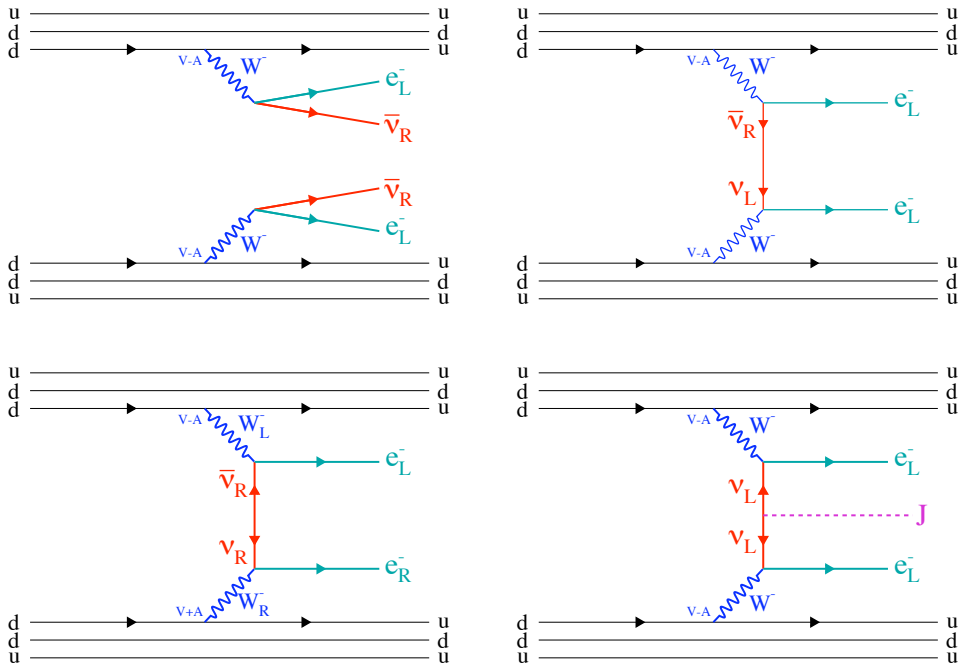

FIGURE 1.1: Feynman diagram of the double beta processes. Upper left : standard $\beta\beta$-decay with emission of two neutrinos ; Upper right : neutrinoless $\beta\beta0\nu$-decay in the case of the exchange of a virtual Majorana neutrino ; Lower left : $\beta\beta0\nu$-decay in the case of right handed weak coupling, Lower right : $\beta\beta0\nu$-decay in the case of a Majoron emission.

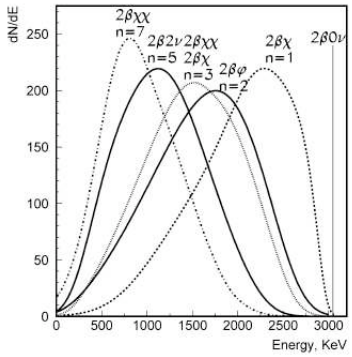

FIGURE 1.2: Energy spectra of different modes of $\beta\beta$-decay of ^{100}Mo with the emission of Majoron.

$\beta\beta0\nu$-decay are connected to a Majorana neutrino mass via the black-box diagramm illustrated in Figure 1.3, or the Schechter-Valle theorem [7][4]. The result is a $\bar{\nu}_e \rightarrow \nu_e$ transition, which is nothing but a Majorana mass term. However this is a tiny mass generated, at the 4-loop level and of the order of 10^{-23} eV [9], too small to explain the lower limit on the neutrino masses from the oscillation experiments. The neutrino mass obviously is generated via another mechanism.

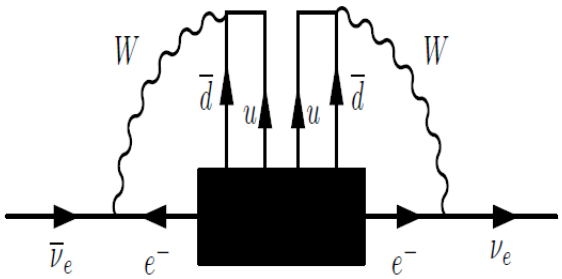

FIGURE 1.3: Black-box diagram equivalent to the $\beta\beta0\nu$ diagram.

We should also note that there are similar processes called neutrinoless double beta$^+$ decay ($0\nu\beta^+\beta^+$), or β^+-decay electron capture ($0\nu\beta^+EC$), or double electron capture ($0\nu EC\ EC$) of bound state electrons e_b^-, which can also be searched for :

$$(A,Z) \rightarrow (A,Z-2) + 2e^+ \quad (0\nu\beta^+\beta^+)$$

$$e_b^- + (A,Z) \rightarrow (A,Z-2) + e^+ \quad (0\nu\beta^+EC)$$

$$2e_b^- + (A,Z) \rightarrow (A,Z-2)^* \quad (0\nu EC\ EC)$$

Observation of one of those processes would also imply the non-conservation of the lepton number. However the creation of one or two positrons reduces the phase space factor. Therefore the ($0\nu\beta^+\beta^+$) or ($0\nu\beta^+EC$) decay rates are strongly reduced. It is also the case for ($0\nu EC\ EC$) although the ^{152}Gd-^{152}Sm transition has recently been identified as a possible interesting candidate [10]. We will focus in this review on the $\beta\beta0\nu$-decay.

1.2 Constraints from neutrino oscillations

If we assume that the dominant lepton number violation mechanism at low energies is the light Majorana neutrino exchange, the half-life of $\beta\beta0\nu$-decay can be written as :

$$\left(T_{1/2}^{0\nu}\right)^{-1} = G_{0\nu}(Q_{\beta\beta},Z)\,|M_{0\nu}|^2\,\frac{\langle m_{ee}\rangle^2}{m_e^2}$$

where $G_{0\nu}(Q_{\beta\beta},Z)$ is the phase space factor. It contains the kinematic information about the final state particles, and is exactly calculable to the precision of the input parameters (see Table 1.2). $|M_{0\nu}|$ is the nuclear matrix element, m_e is the mass of the electron, and $\langle m_{ee}\rangle$ is the effective Majorana mass of the electron neutrino. It is defined as :

$$\langle m_{ee}\rangle = \left|\sum_i U_{ei}^2 m_i\right|$$

where m_i are the neutrino mass eigenstates and U_{ei} are the elements of the neutrino mixing Pontecorvo-Maki-Nakagawa-Sakata (PMNS) matrix U.

The PMNS matrix U has been introduced to explain the observed neutrinos oscillations. Its formalism is that in the charged current term of electroweak interactions, the neutrino flavour states ν_e, ν_μ and ν_τ are superpositions of neutrino mass states ν_1, ν_2 and ν_3 :

$$\nu_\alpha = U^*_{\alpha i}\nu_i$$

where $\alpha = e, \mu, \tau$ and $i = 1, 2, 3$. The PMNS mixing matrix U is unitary and can be written in its standar parametrization (see [8] or [3] for instance) as

$$U = \begin{pmatrix} c_{12}c_{13} & s_{12}c_{13} & s_{13}e^{-i\delta} \\ -s_{12}c_{23} - c_{12}s_{23}s_{13}e^{i\delta} & c_{12}c_{23} - s_{12}s_{23}s_{13}e^{i\delta} & s_{23}c_{13} \\ s_{12}s_{23} - c_{12}c_{23}s_{13}e^{i\delta} & -c_{12}s_{23} - s_{12}c_{23}s_{13}e^{i\delta} & c_{23}c_{13} \end{pmatrix} P$$

where $c_{ij} = \cos\theta_{ij}$, $s_{ij} = \sin\theta_{ij}$ and δ is the possible *Dirac phase* which could produce a CP violation in neutrino oscillations. A diagonal phase matrix P has been introduced, containing the two *Majorana phases* α and β (physical if neutrinos are Majorana) :

$$P = diag(1, e^{i\alpha}, e^{i(\beta+\delta)})$$

The effective Majorana mass of the electron neutrino can be written in term of the neutrino oscillation parameters :

$$\langle m_{ee}\rangle = \left|\sum_i U^2_{ei} m_i\right| = \left|m_1 c^2_{12}c^2_{13} + (m_2 s^2_{12}c^2_{13})e^{2i\alpha} + (m_3 s^2_{13})e^{2i\beta}\right|$$

Results of the neutrino oscillation measurements provide constraints on the variation of the effective Majorana mass $\langle m_{ee}\rangle$ as a function of the neutrino mass scale. However, the constraints depend on the neutrino mass pattern, which is unfortunatly not known. Indeed, neutrino oscillations are only sensitive to the absolute value of the difference of the square of the neutrino mass $\left|\Delta m^2\right|$. Since we cannot measure the sign of Δm^2_{atm} in the atmospheric neutrino oscillation, there are two possible patterns of the eigenstate neutrino masses, as illustrated in Figure 1.4 :

- In the normal hierarchy (NH) case, the gap between the two lightest mass eigenstates corresponds to the small mass difference, measured by solar experiments.
- In the inverted hierarchy (IH) case, the gap between the two lightest states corresponds to the large mass difference, measured by atmospheric experiments.
- Finally, the particular case in which the neutrino mass differences are very small compared with their absolute scale dorresponds to quasi-degenerate (QD) pattern.

Figure 1.5 shows the predicted value of $\langle m_{ee}\rangle$ as a function of the smallest mass of neutrinos m_{min} [11], with the three possible neutrino mass patterns :

- In the case of normal hierarchy, $\langle m_{ee}\rangle$ can be as low as 1 meV. In the "catastrophe scenario", $\langle m_{ee}\rangle$ can vanish due to cancelation of the coefficients by appropriate Majorana phases.
- In the case of inverted hierarchy, the expected range is $10\text{meV} < \langle m_{ee}\rangle < 50\text{meV}$ [12]. The lower limit depends upon the exact value of $\sin^2\theta_{12}$ and on the Majorana phase pattern. In case of low $\sin^2\theta_{12}$ (0.27) or in case of violation of CP-symetry, the lower limit can be 20 meV.

– In the case of quasi-degenerated neutrino mass pattern, larger values for $\langle m_{ee} \rangle$ can be obtained, , approximately above 50 meV.

I remind that these constraints are valid only for the standard $\beta\beta0\nu$ mechanism with the exchange of a virtual light Majorana neutrino. As previously said, other mechanisms can also contribute and thus can increase (positive interferences) or decrease (negative interferences) the $\beta\beta0\nu$-decay rate.

In conclusion, let's try first to detect a $\beta\beta0\nu$-decay, whatever the expectations !

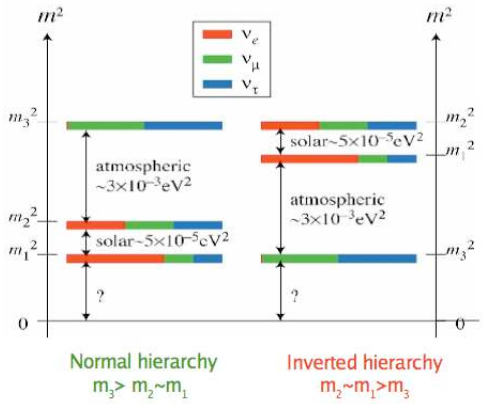

FIGURE 1.4: Patterns in the case of normal or inverted hierarchy of the eigenstate neutrino masses. Colors show the mixing of the flavour neutrino eigenstates inside the mass neutrino eigenstates.

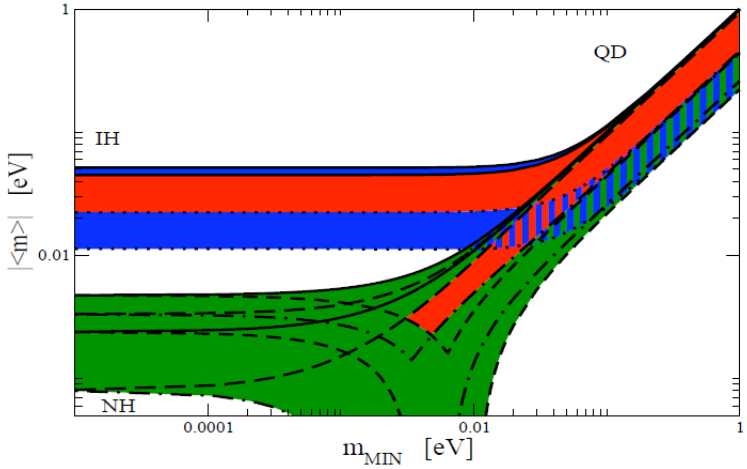

FIGURE 1.5: The predicted value of $\langle m_{ee} \rangle$ as a function of m_{min}, obtained using the 2σ allowed ranges of Δm^2_{atm}, $\Delta m^2_{\odot}$, $\sin^2\theta^2_{\odot}$ and $\sin^2\theta^2_{13}$. The regions shown in red correspond to violation of CP-symmetry while the rest of the regions correspond to the four different sets of CP-conserving values of the two Majorana phases with the green region for normal hierarchy and blue region for inverted hierarchy.

1.3 The nuclear matrix elements

Theoretical uncertainties for the nuclear matrix element (NME) calculations are the main limitation in making interpretation of $\beta\beta0\nu$-decay or in comparing the sensitivity (or hopefuly signal amplitude!) between different experiments measuring different isotopes. We can list 5 methods to calculate the NME : the Quasi-particle Random Phase Approximation (QRPA, including its many variants and evolution steps) [13][14], the Nuclear Shell Model (NSM) [15], the Interacting Boson Model (IBM) [16], the Generating Coordinate Method (GCM) [17], and the Projected Hartree-Fock-Bogoliubov model (PHFB) [18]. Basicaly, QRPA uses a large number of active nucleons in a large space but with a specific type of correlation suited for collective motion, whereas NSM uses a small number of nucleons within a limited space.

I would like to underline that the NME calculations for the standard $\beta\beta2\nu$-decay and the $\beta\beta0\nu$-decay are very different. The $\beta\beta2\nu$ process involves only Gamow-Teller transitions through intermediate 1^+ states only because of low momentum transfer. In contrast, for $\beta\beta0\nu$-decay, the exchange Majorana neutrino has a relatively high momentum of about $q \approx 100$ MeV (corresponding to the average distance $r \approx 1/q \approx 1$ fm between the two decaying neutrons). Therefore the $\beta\beta0\nu$ process involves all the J^+ intermediate states and it is evaluated at two pointlike Fermi vertices containing a Fermi and a Gamow-Teller part.

Important studies of various nuclear effects and impact on the NME calculation have been performed in the last years both in QRPA and in NSM. It has been sumarized in [19]. I mention few examples :

- The main contribution to NME comes from short internucleon distances ($r < 2-3$ fm) [20], and the nucleons tend to overlap. Short-range correlations (SRC) now take the hard core repulsion into account. There are different methods to treat SRC : Jastrow-like function, Unitary Correlation Operator Method (UCOM) and Coupled Cluster Method (CCM). The Jastrow method leads to a reduction of the NME of $\approx$ 20% while UCOM and CCM, which are favored models, reduce NME by $\approx 5\%$ [20][13].
- The difference in the nucleon configuration of the initial and final nuclei is an important input to NME. Reactions such as (d,p), (α,^{3}He) and (d,^{3}He) were used to study the occupation of valence neutron or proton orbits in ^{76}Ge and ^{76}Se [21][22]. These data were then used to constrain calculations of NME by both the shell model [23] and QRPA [13][24] methods. For the Shell Model, the value of the NME is enhanced by about 15% compared to previous calculations, whereas in the QRPA the NMEs are reduced by 20% [23]. This diminishes the discrepancies between both approaches. This points out the importance of spectroscopic information in order to test the validity of the NME calculations.
- It is very difficult to calculate the relative strengths of the virtual J^+ states of the intermediate nuclei involved in the $\beta\beta0\nu$ decay. Muon capture on the final nucleus also excites all these states [25], and therefore provides additional experimental data for the theoretical calculations.
- Accurate measurement of the $\beta\beta2\nu$ half-lives along with electron capture of the intermediate nuclei can help determine the g_{pp} parameter used in QRPA (particle-particle interaction strength).
- Finally, being able to calculate the $\beta\beta2\nu$ half-life can be also considered a necessary, but not a sufficient condition for demonstrating a correct $\beta\beta0\nu$ NME calculation.

A complete compilation of the most recent NME calculations (with the 5 different techniques) have been recently proposed in [12]. It has been scaled to a radius $r = 1.2$ fm and to a free nucleon axial-vector coupling constant $g_A = 1.25$ (QRPA NME are reduced by about 15% if one use a quenched constant $g_A = 1$ [13]). In the following I will use this compilation which is summarized in table 1.2.

We see that the NME's can vary by a factor 2 to 3. In most cases the results of the Shell Model calculations are the smallest ones, while the largest ones may come from the IBM, QRPA or GCM. It results to a factor of uncertainty of about 4 to 10 on the required sensitivity to $T^{0\nu}_{1/2}$ or on the required mass of isotope, when we compare different experiments using different isotopes.

Finally, all these calculations discussed here have been performed for the standard mechanism with the exchange of a virtual light Majorana neutrino. Rare and old calculations have been done in the case of V+A mechanism or in the case of exchange of SUSY particles with R-parity violation.

1.4 Current limits on the effective mass and required sensitivities for the future

We list in table 1.1 the current limits on the $\beta\beta0\nu$ half-life $T^{0\nu}_{1/2}$, obtained with various experiments. Except KAMLAND-Zen, all the other experiments are finished. 4 experiments have reached the "10^{24} club", it means they have set a limit on $T^{0\nu}_{1/2}$ higher than 10^{24} years : Heidelberg-Moscow/IGEX with about 10 kg of ^{76}Ge, NEMO-3 with about 7 kg of ^{100}Mo, CUORICINO with about 10 kg of ^{130}Te and recently Kamland-Zen with about 300 kg of ^{136}Xe. The corresponding lower and upper limits on the effective Majorana mass are in the same range, about 0.2 and 0.7 eV, respectively. We note that, although the limit obtained on $T^{0\nu}_{1/2}$ with ^{76}Ge is a factor 10 higher than for ^{100}Mo or ^{130}Te, the limit on the effective neutrino mass is in the same range. It is mostly due to a lower phase space factor for ^{76}Ge.

The observation of a $\beta\beta0\nu$ signal in Ge, claimed by a part of the Heidelberg-Moscow collaboration, will be discussed in Chapter 3 (germanium experiments). The reader can also refer to V.I. Tretyak's paper [26], which summarizes all the "discoveries" of $\beta\beta$ decays (including $\beta\beta0\nu$) which were disproved in the subsequent investigations.

Figure 1.6 shows the required sensitivity on $T^{0\nu}_{1/2}$ in order to start exploring the inverted hierarchy region, corresponding to an upper limit of $\langle m_{ee}\rangle = 50$ meV. For a given isotope, there is an uncertainty of ≈ 5 to 10 due to the NME's, as discussed above. But roughly speaking, we see that a sensitivity of $\approx 10^{26}$ years for ^{100}Mo and up to $\approx 10^{27}$ years for ^{76}Ge is needed.

1.5 Experimental aspects

In case of no signal, the half-life sensitivity for a $\beta\beta0\nu$ experiment is given by :

$$T^{0\nu}_{1/2} > \ln 2 \frac{\mathcal{N} M \varepsilon}{A} \frac{T_{obs}}{N_{excl}}$$

where M is the mass of enriched isotope, A its atomic mass, $\mathcal{N}$ the Avogadro, ε the $\beta\beta0\nu$ efficiency of the detector, T_{obs} is the duration of the measurement and N_{excl} is the number

Isotope	$T^{2\nu}_{1/2}$ (yr)	Experiment	$T^{0\nu}_{1/2}$ (yr) (90% C.L.)	Experiment	$\langle m_{ee}\rangle$ (eV) Min.	Max.
^{48}Ca	$4.2^{+2.1}_{-1.0}$ 10^{19}	NEMO-3	5.8 10^{22}	CANDLES [111]	3.55	9.91
^{76}Ge	1.5 ± 0.1 10^{21}	HDM	**1.9 10^{25}**	HDM [46]	**0.21**	**0.53**
^{82}Se	9.0 ± 0.7 10^{19}	NEMO-3	3.2 10^{23}	NEMO-3 [40]	0.85	2.08
^{96}Zr	2.0 ± 0.3 10^{19}	NEMO-3	9.2 10^{21}	NEMO-3 [35]	3.97	14.39
^{100}Mo	7.1 ± 0.4 10^{18}	NEMO-3	**1.0 10^{24}**	NEMO-3 [40]	**0.31**	**0.79**
^{116}Cd	3.0 ± 0.2 10^{19}	NEMO-3	1.7 10^{23}	SOLOTVINO [81]	1.22	2.30
^{130}Te	0.7 ± 0.1 10^{21}	NEMO-3	**2.8 10^{24}**	CUORICINO [65]	**0.27**	**0.57**
^{136}Xe	2.38 ± 0.14 10^{21}	Kamland	**5.7 10^{24}**	Kamland-Zen [93]	**0.25**	**0.6**
^{150}Nd	7.8 ± 0.7 10^{18}	NEMO-3	1.8 10^{22}	NEMO-3 [37]	2.35	8.65

TABLE 1.1: $\beta\beta2\nu$ half-lives and $\beta\beta0\nu$ half-life limits measured in a variety of experiments. Last two rows show the minimal and maximal upper limits on the effective majorana neutrino mass $\langle m_{ee}\rangle$, using NME's from table 1.2.

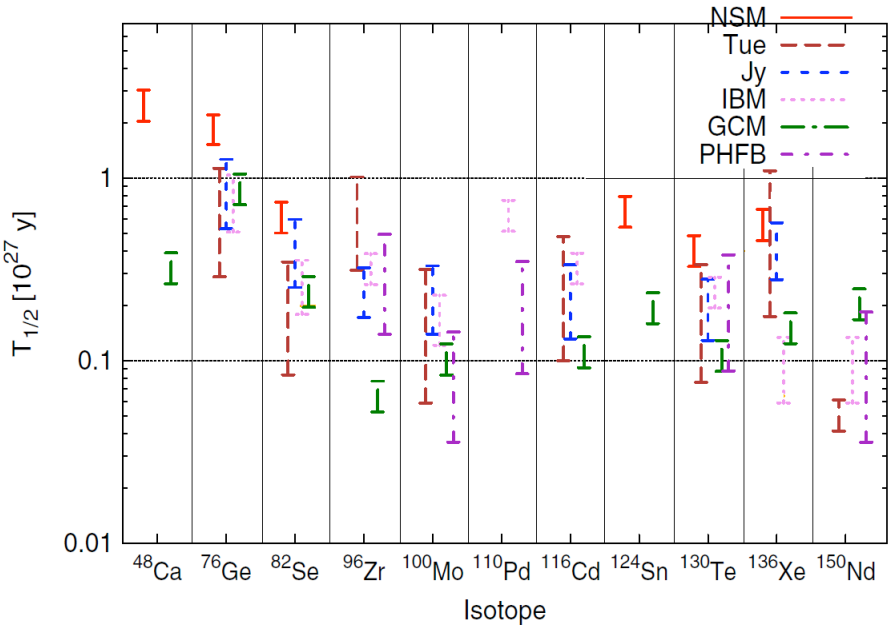

FIGURE 1.6: Required half-life sensitivities in order to start exploring the inverted hierarchy, corresponding to an effective Majorana neutrino mass of about 50 meV (from [12]).

of excluded $\beta\beta0\nu$ events.

From this relation, and due to the low rates of the $\beta\beta0\nu$ process, it is clear that the essential requirement of the double beta experiments is to achieve an extremely low radioactive background and large mass of isotopes.

It is also important to note that in the case of no background (a dream!), the half-life sensitivity increases as the duration of observation T_{obs}, while in the case of relatively larger

background, it increases only as $\sqrt{T_{obs}}$.

A large variety of experimental techniques have been developped for the search of $\beta\beta0\nu$ decay. There are basicaly two types of approaches : the calorimetric and the tracko-calo methods.

In the calorimetric technique, the source is embedded in the detector itself which provides a high detection efficiency. With a proper choice of detector, a very high energy resolution up to FWHM=0.1% at $Q_{\beta\beta}$ can be achieved as in Germanium or bolometer detectors. However it is difficult to reconstruct the event topology and to identify the background components (with the exception of Xenon TPC but at the price of a lower energy resolution). The capacity to prove that the observation is indeed a $\beta\beta0\nu$-decay, and not an unidentified background, is then limited. Recently large existing liquid scintillator detectors, initialy developped for neutrino oscillation measurements (Kamland, SNO), have been reused as $\beta\beta$ detectors by adding isotope inside the liquide scintillator. It allows to reach quickly a large amount of isotope ($\approx$ 100 kg) but with a limited energy resolution and thus a non negligible background.

The tracko-calo method separates the detector from the source and the detector combines a calorimeter and a tracking detector. It allows to reconstruct directly the track of each of the two emitted electrons from the source foil and also to identify and measure each background component. However the price is a lower $\beta\beta0\nu$ efficiency and a lower energy resolution. We mention that it is also the most sensitive technique for the search of the $\beta\beta0\nu$ with V+A right-handed weak current, since it provides the angular distribution between the two emitted electrons.

We emphasize that the search of $\beta\beta0\nu$-decay requires several experimental techniques and more than one isotope. This is because there could be unknown background and gamma transitions, and a line observed at the end point in one isotope does not necessarily imply that $\beta\beta0\nu$ decay was discovered. Nuclear matrix elements are also not very well known.

In the next chapters, I will review the different $\beta\beta$ experimental approachs. My purpose is to detail, for each technique, the different origins of background, how they can be identified, and how they can be reduced. Advantages and limitations will be discussed.

I will first present the tracko-calo NEMO-3 and SuperNEMO experiments. I work on these two experiments since 15 years. So it was natural to start with them with a relatively more exhaustive description. I will then present the germanium technique. This is today the most sensitive technique on the $\beta\beta0\nu$ half-life. I will then review the bolometer technique. I will describe in detail the recent progress in scintillating bolometers because I think that it is one of the most promising technique. Finally I will review the large liquid scintillator detectors and Xenon TPC.

The reader who has not the courage to read this entire review, is allowed to go directly to the summary given in Chapter 6.

Isotope	$G^{0\nu}$ (10^{-14} y^{-1})	$Q_{\beta\beta}$ (keV)	Nat. ab. (%)	Nuclear Matrix Elements NSM [15][23] (UCOM)	QRPA-Tu. [13] (CCM)	QRPA-Jy [14] (UCOM)	IBM [16] (Jastrow)	GCM [17] (UCOM)	PHFB [18] (Mixed)
^{48}Ca	6.35	4273.7	0.187	0.85	...	...	...	2.37	...
^{76}Ge	0.623	2039.1	7.8	3.26	4.44-7.24	4.19-5.36	4.64-5.47	4.6	...
^{82}Se	2.70	2995.5	9.2	2.64	3.85-6.46	2.94-3.72	3.80-4.41	4.22	...
^{96}Zr	5.63	3347.7	2.8	...	1.56-2.31	2.76-3.12	2.53	5.65	2.24-3.46
^{100}Mo	4.36	3035.0	9.6	...	3.17-6.07	3.10-3.93	3.73-4.22	5.08	4.71-7.77
^{110}Pd	1.40	2004.0	11.8	...	...	...	3.62	...	5.33-8.91
^{116}Cd	4.62	2809.1	7.6	...	2.51-4.52	3.00-3.94	2.78	4.72	...
^{124}Sn	2.55	2287.7	5.6	2.62	...	...	...	4.81	...
^{130}Te	4.09	2530.3	34.5	2.65	3.19-5.50	3.48-4.22	3.37-4.06	5.13	2.99-5.12
^{136}Xe	4.31	2461.9	8.9	2.19	1.71-3.53	2.38-2.80	3.35	4.2	...
^{150}Nd	19.2	3367.3	5.6	...	3.45	...	2.32-2.89	1.71	1.98-3.7

TABLE 1.2: A compilation of the most recent NME calculations, from [12] (NME have been normalized with $r = 1.2$ fm).

Chapitre 2

NEMO Tracko-Calo Experiments

At the end of the 80's, it was decided in France to start developping a serie of tracko-calo detectors, so-called NEMO detectors. The $\beta\beta$ sources are in the form of very thin and large foils and are separated from the detector. The combination of a tracking detector and a calorimeter provides both the measurement of the $\beta\beta$ energy spectrum and the direct reconstruction of the tracks of the two emitted electrons from the source foil. The efficiency to reject the background is therefore very high. However the energy resolution and the efficiency to detect a possible $\beta\beta0\nu$ signal are relatively low compared to pure calorimetric detectors. Moreover the size of the detector must be relatively large in order to contain a large mass of $\beta\beta$ source foils.

I will first present the result of the NEMO-3 experiment which took data in the Modane underground laboratory (LSM) from early 2003 up to january 2011 and measured several double beta isotopes for a total mass of ≈ 10 kg. The two main isotopes for the $\beta\beta0\nu$ search were ^{100}Mo (35 kg.y of exposure) and ^{82}Se (4.5 kg.y of exposure).

I will then present the SuperNEMO project which is based on an extension and an improvement of the experimental techniques used in NEMO-3.

2.1 NEMO-3 Experiment

2.1.1 Description of the detector

The NEMO-3 detector is cylindrical in design and divided into 20 equal sectors. Figure 2.1 shows a schematic view of the detector.

The source foils are in the form of very thin strips (40 to 60 mg/cm^2) and are fixed vertically. It corresponds to a large cylinder of 3.1m in diameter and 2.5m in height (≈ 20 m^2). Different sources of double beta emitters have been installed. The two main isotopes are ^{100}Mo (6914 g, 12 sectors) and ^{82}Se (932 g, 2.5 sectors) and are devoted for the $\beta\beta0\nu$ search. Other isotopes have been also added in relatively smaller mass for the $\beta\beta2\nu$ measurement : ^{116}Cd (405g, 1 sector), ^{130}Te (454 g, 2 sectors), ^{150}Nd (37 g), ^{96}Zr (9 g) and ^{48}Ca (7 g). Also 1.5 sectors equipped with natural tellerium (614 g of TeO_2) and 1 sector equipped with pure copper (621 g) are used for external background measurements.

On both sides of the sources, there is a gaseous tracking detector which consists of 6180 open drift cells operating in the Geiger mode allowing three-dimensional track reconstruction. To minimize the multiple scattering, the gas is a mixture of 95% helium, 4% ethyl

alcohol, 1% argon, and 0.1% water. The wire chamber is surrounded by a calorimeter which consists of 1940 plastic scintillator blocks coupled to very low radioactive photomultipliers (PMT's). The energy resolution (FWHM) of the calorimeter is about 15% at 1 MeV for the scintillators equipped with the 5" PMT's on the external wall and 17% for the 3" PMT's on the internal wall. The resolution of the summed energy of the two electrons in the $\beta\beta0\nu$ decay is mainly a convolution of the energy resolution of the calorimeter and the fluctuation in the electron energy loss in the foil source which gives a non-Gaussian tail. The FWHM of the expected two-electron energy spectrum of the $\beta\beta0\nu$ decay is 350 keV. Timing information of the PMT's signals is used to discriminate between external particles crossing the detector and internal particles emitted from the source foils, allowing background studies and rejection. The time resolution is around 250 ps (r.m.s.) for 1 MeV electrons.

A solenoid surrounding the detector produces a 25 gauss magnetic field in order to distinguish electrons from positrons with an efficiency of about 95% for 1 MeV electrons.

An external shield of 19 cm of low radioactivity iron, a water shield, and a wood shield cover the detector to reduce external γ's and neutrons.

We started taking data in February 2003. But we observed a Radon contamination inside the tracking detector, ten times too high. A quick analysis showed that it was due to a diffusion of external Radon present in the lab. Thus, end of 2004, a Radon-tight structure surrounding the detector has been installed and free-Radon air passing through charcoal at low temperature (-50C) has been flushed inside this buffer volume in order to reduce the observed Radon contamination inside the detector. Data taken between February 2003 until september 2004 correspond to Phase 1 with Radon background. Data taken from January 2005 until January 2011 correspond to Phase 2 with low Radon background.

Some pictures of the detector are given in Figures 2.2 and 2.3. A complete description of the NEMO-3 detector is given in the *Technical design and performance* article in reference [27]. More detailed informations can also be found in [28].

The trigger condition requires at least 1 PMT with an energy above 150 keV and three Geiger cells fired. With these conditions, the trigger rate was only about 5 Hz.

A two-electron ($2e^-$) event (see Figure 2.4) candidate for a $\beta\beta$ decay is defined as follows : two tracks come from the same vertex on the source foil, each track must be associated with a fired scintillator, its curvature must correspond to a negative charged particle emitted from the source, and the time of flight must correspond to the two electrons being emitted from the same source position. For each electron an energy threshold of 200 keV is applied.

2.1.2 Energy, timing and efficiency calibrations

Absolute energy calibrations were carried out every $\approx$ 40 days using ^{207}Bi sources which provides conversion electrons of 482 and 976 keV (K lines) with a branching ratio of 1.5 and 7.0%, respectively. A calibration run took about 24 hours to collect enough statistics. Figure 2.5 shows an example of energy spectrum obtained for one counter after a calibration run. A dedicated long run at the begining of the NEMO-3 was also performed using ^{90}Sr source. The measurement of the end-point of the β spectrum of ^{90}Y (daughter of ^{90}Sr) at 2.283 MeV gave one additional calibration point to control the linearity. We mention also that the integration of all the ^{207}Bi calibration runs over the 7 years data taking gave enough statistics to observe also the rare 1682 keV conversion electron (branching ratio of only 0.02%) in ^{207}Bi. It allowed to check a posteriori the energy linearity up to 1.7 MeV of

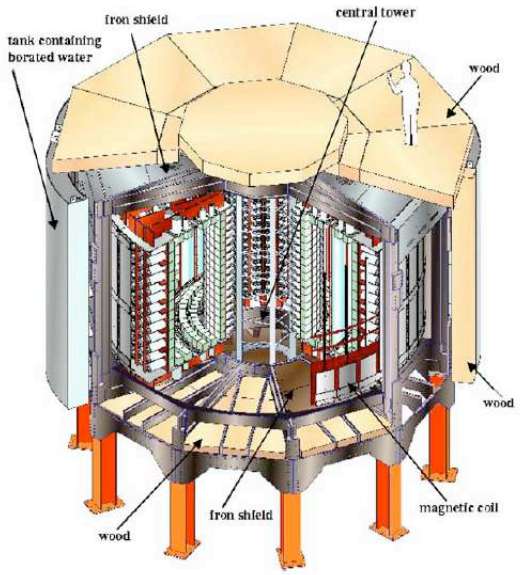

FIGURE 2.1: An exploded view of the NEMO-3 detector. Note the coil, iron g-ray shield, and the two different types of neutron shields, composed of water tanks and wood. The paraffin shield under the central tower is not shown on the picture.

each counter during all the period of NEMO-3 running.

The calibration lines obtained with the two ^{207}Bi peaks as well as the fit combining ^{207}Bi and ^{90}Sr results do not necessarily intersect the origin of the axes. The extrapolated energy offset at ADC equal to zero (electronic pedestal subtracted) is in average 33 keV (after impact correction, see below) with an uncertainty of about 3 keV. This effect was previously observed with data obtained with an electron spectrometer during the test and assembly of the scintillator blocks of NEMO-3. It is due to a non linearity of plastic scintillator at low energy, below about 100 keV (quenching of low energy electrons), already observed and reported in litterature in other experiments.

By adding ^{207}Bi calibration runs, one can also measure the response of each scintillator block to 1 MeV electron as a function of the impact position of the electron track on the entrance surface of the scintillator. This effect was previously observed with data obtained with the electron spectrometer in CENBG Bordeaux during the NEMO-3 calorimeter assembly. The impact corrections are relatively weak for the scintillator blocks equipped with 3" PMT's, typicaly $1-2\%$ (with 3×3 corrections points), but is stronger for those equipped with 5" PMT's, up to 10% (with 5×5 corrections points). This effect has a non-negligible consequence on the energy resolution and is thus corrected offline by applying the impact correction factors measured for each scintillator block. This non uniform response of the block is due to the mechanical design of the coupling of the PMT to the scintillator as shown in Figure 2.6. The optical guide is cylindrical in design with a diameter equal to the PMT one. However the scintillator block is rectangular in design with a size (side) almost twice larger. As it will be discussed in the next section (relating to SuperNEMO), the limited energy resolution of NEMO-3 is also strongly correlated to this design.

We mention also an independant test which has been performed in order to verify the

FIGURE 2.2: (Left) View of a sector inside the LSM clean room during the assembly of the source foil. Note the double beta foil strips (in white) and the copper calibration tube besides, the scintillator blocks wrapped with aluminized mylar, the PMT's in the back surrounding by black tubes and the copper rings on the top and bottom of the tracking Geiger cells (the wires are too thin to be seen here. (Right) view inside of the detector during the dismounting of the sources foils in April 2011.

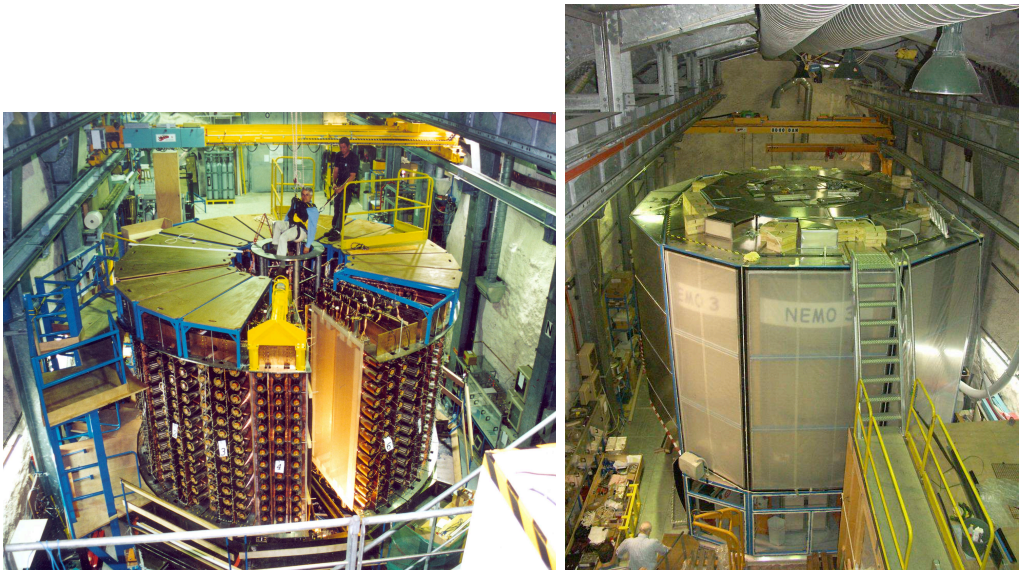

FIGURE 2.3: (Left) View of the NEMO-3 detector in the LSM before the installation of the last sector in August 2000. (Right) View of the complete detector in LSM with the Radon-tight structure surrounding the detector.

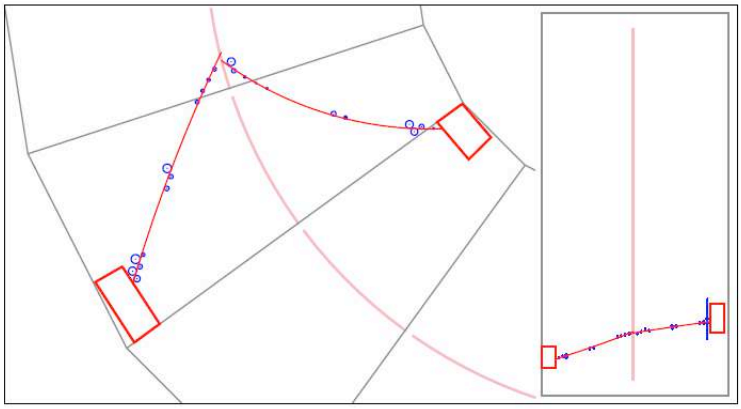

FIGURE 2.4: Transverse (left) and longitudinal (right) view of a reconstructed $\beta\beta0\nu$ candidate event selected from the data with a two-electron energy sum of 2812 keV.

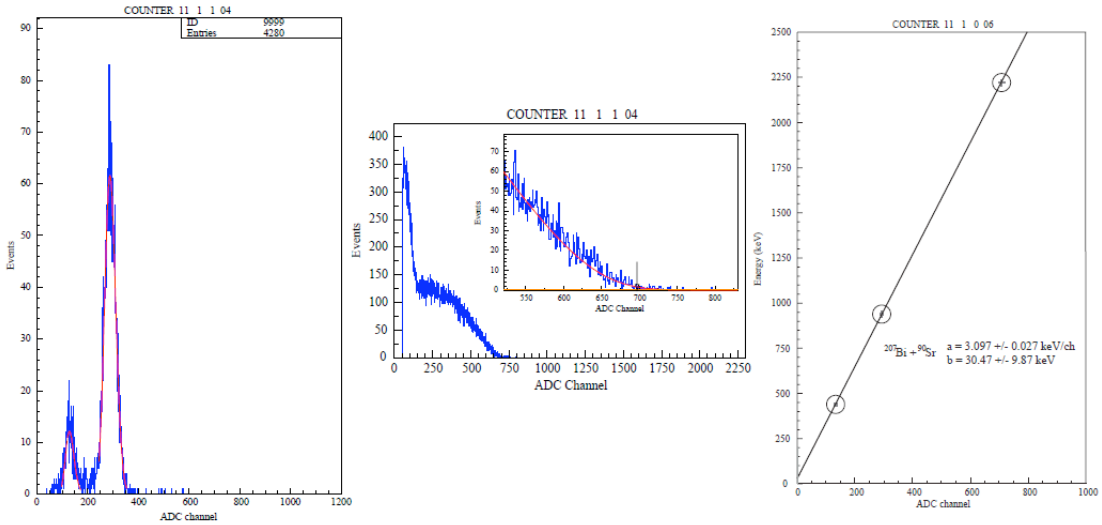

FIGURE 2.5: (Left) Spectral fit of the 482 and 976 keV γ-rays coming from ^{207}Bi decays for one counter ($\approx$ 3 keV/channel) ; (Center) Energy spectrum of the β-decay of ^{90}Sr (low energy) and ^{90}Y with the full spectrum and in zoom the fit to the high-energy tail (endpoint) of the spectrum, which is made with a function describing the shape of a single β spectrum of ^{90}Y, convolved with the energy resolution function of the scintillator bloc and taking into account the mean energy loss of the electrons ; (Right) the linear fit of the three calibration points with the energy offset at null charge of $\approx$ 30 keV.

energy calibration from 2 to 3.3 MeV [31]. The β-decay of the ^{214}Bi (Q_β = 3.274 MeV), which is present on the surface of the wires, has been measured via the ^{214}Bi-^{214}Po cascade by selecting an e^- and a delayed α emitted from the same vertex inside the tracking chamber (see next section). Figure 2.7 shows the reconstructed β energy spectrum of the ^{214}Bi, in very good agreement with the simulations above 0.5 MeV and up to 3.3 MeV (the small discrepency at lower energy is due to the energy losses of the electrons on the wires). This test gives a cross-check of the energy calibration between 2.2 and 3.3 MeV.

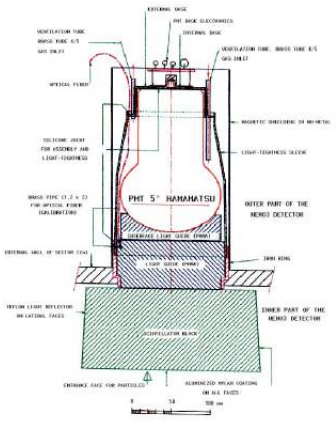

FIGURE 2.6: Layout of an external scintillator block coupled via to successive optical guides to a 5" PMT.

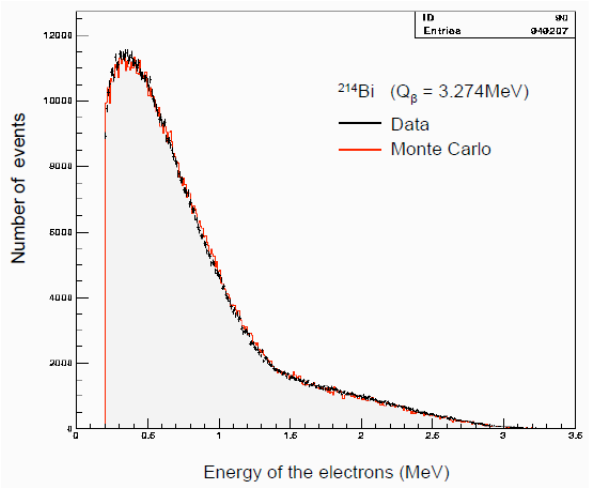

FIGURE 2.7: Energy spectrum of the ^{214}Bi β-decay from the wires measured with the (e^-, delay-α) [31]. The black histogram corresponds to the data and the red one to the Monte-Carlo simulations.

The energy measurement is meaningfull only if the energy calibration of each counter is stable in time and if any possible drift is well controlled. A laser calibration system was used to survey the asbolute energy. Two laser runs were performed every day. The gain peak stability is surveyed with an accuracy of about 3%. During a 40 days time interval between two consecutive absolute ^{207}Bi calibration runs : in average $\approx$ 95% of PMT's appeared stable within the 3% accuracy and no gain correction was applied ; and $\approx$ 5% of PMT's are detected unstable because of an apparent gain instability (unstable PMT or HV or unstable laser response for this channel after reference correction). These apparent unstable PMT's were rejected for the analysis (also suppressed for the Monte Carlo simulation for the same effective duration). However laser survey corrections can be applied to $\approx$ 70% of the available data, and the effective $\beta\beta0\nu$ efficiency becomes $\epsilon(\beta\beta0\nu) = 12.5\%$.

For timing calibration, first the relative offsets for each channel are determined with a ^{60}Co source, which emits two coincident γ-rays with energies of 1332 and 1173 keV. Spectra of arrival time differences are collected to establish time delays between the 1940 channels. Then the two-electrons events from ^{207}Bi (corresponding to the two conversion electrons of 0.5 and 1 MeV emitted simultaneously) are used for time alignment and time resolution measurement with electrons. Possible drift or unstability of the TDC between two consecutive ^{207}Bi calibration run are also studied with daily laser runs [33].

The efficiency of the detector to detect two electron events ($\beta\beta$-like events) has been directly measured with dedicated ^{207}Bi runs using four low active ($\sim$ 10 Bq) and calibrated ^{207}Bi sources at four opposite position inside the detector. The two conversion electrons emitted simultaneously by the ^{207}Bi sources were selected. Knowing the activity of the Bi source, the two-electrons detection efficiency was measured. It was in agreement with the Monte Carlo efficiency within a systematic error of 5%.

The two electron events emitted by ^{207}Bi sources were also used to measure the vertex resolution for the two-electron channel used to reconstruct $\beta\beta$ events. If we define the transverse dispersion $\delta R\phi$ and the the longitudinal dispersion δZ as the distance between the vertices associated with the two reconstructed tracks, the vertex resolution for $\beta\beta$ events is $\sigma(\delta R\phi) = 0.6$ cm and $\sigma(\delta Z) = 1.0$ cm. If one constrains the two tracks to have a common vertex, one gets $\sigma(\delta R\phi) = 0.1$ cm. These resolutions allow one to make a distinction between two strips in a source foil in a given sector, which is crucial for sectors composed of different sources. Finally, thanks to the very high statistics of collected events, the comparison of the experimental angular distribution between the two reconstructed conversion electrons and the expected one obtained with Monte Carlo, has shown a small discrepency. An effective correction obtained using these data was then applied to the measured $\beta\beta$ angular distribution, leading to a perfect agreement with the expected Monte Carlo $\beta\beta$ angular distribution, as shown in the next subsection.

Finally data with two low active and calibrated ^{90}Sr sources (^{90}Y, daughter of ^{90}Sr, is a pure β emitter), deposited on small thin natural molybdenum foils (60 mg/cm^2) and placed in the calibration tubes, have been used to test the energy losses of electrons and the bremsstralung γ production in Molybdenum foils. The reconstructed activities of the two sources with NEMO-3 using single electron channel (β event) are in perfect agreement with the activity previously measured in IRES (Strasbourg), but limited by the precision of the IRES measurements of only 10%. The reconstructed energy spectrum is shown in Figure 2.8 with a good agreement between data and Monte-Carlo simulations. A small systematic distorsion is observed but it is at the level of the Monte-Carlo uncertainty for the theoretical ^{90}Sr β spectrum.

2.1.3 The background components

The combined tracking-calorimetry technique used in NEMO-3 is a very powerfull technique to identify the origin of the different components of background and to measure the level. An article presenting the methods and results has been published in [30]. I give here a summary.

The background present in NEMO-3 can be distinguished in four different components (as illustrated in Figure 2.9)

1. **The external background** produced by the interaction of external γ's originating

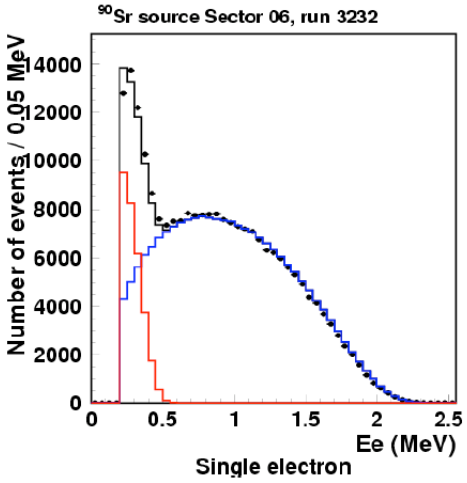

FIGURE 2.8: Energy spectrum with a low active and calibrated ^{90}Sr sources, deposited on small thin natural molybdenum foils : black dots corresponds to data, blue histogram to the Monte-Carlo ^{90}Y β-decay (daughter of ^{90}Sr), red histogram to the Monte-Carlo ^{90}Sr β-decay, black histogram to the total Monte-Carlo spectrum (background is negligeable).

from the natural radioactivity of the detector (outside of the source) or produced by external neutrons or cosmic rays from the LSM lab. If an external γ is undetected by the crossed scintillator (50% γ tagging efficiency at 1 MeV, 33% at 3 MeV), it can reach the $\beta\beta$ source foil without being tagged (gamma does not ionize the gas of the wire chamber). Thus the interaction of the γ can mimic $\beta\beta$ events by e^+e^- pair creation, double Compton scattering or Compton followed by Möller scattering (see Figure 2.10). The external background is an important component in the $\beta\beta2\nu$ energy region but becomes negligible at $\approx$3 MeV in the $\beta\beta0\nu$ energy region for ^{100}Mo and ^{82}Se (with very rare γ-rays from ^{214}Bi above 2.6 MeV).

2. **The internal background** coming from radioactive contaminants inside the $\beta\beta$ source foils. The main internal background contribution due to natural radioactive impurities comes from the β-decay of ^{214}Bi ($Q_\beta = 3.27$ MeV) and ^{208}Tl ($Q_\beta = 4.99$ MeV) from ^{238}U and ^{232}Th decay chains respectively (see Figures 2.11 and 2.12). They can mimic $\beta\beta$ events by a β-decay accompanied by an electron conversion process, by a Möller scattering of the β-decay electrons in the source foil, or by a β-decay emission to an excited state followed by a Compton scattered γ (see Figure 2.10). This process can be detected as a two electron events if the γ is not detected.
3. **The Radon and Thoron contaminations inside the tracking detector**. Radon (^{222}Rn, $T_{1/2} = 3.824$ days) and Thoron (^{220}Rn, $T_{1/2} = 55.6$ s) are α-decay isotopes, which have ^{214}Bi and ^{208}Tl as daughter isotopes respectively (see Figure 2.11). Coming mainly from the rocks and present in the air, the ^{222}Rn and ^{220}Rn (rare gases) are very diffusion prone, and can enter the detector and contaminate the interior of the tracking chamber. Subsequent α-decays of these gases give ^{218}Po^{++} and ^{216}Po^{++} ions respectively, which drifts mainly to the cathodic wires. If the deposition is close to the $\beta\beta$ source foils, this becomes like an internal background critical for the $\beta\beta0\nu$ search. The Thoron contamination is generaly much lower than Radon due to its short half-life

which limits its diffusion capacity.

4. **The tail of the $\beta\beta2\nu$ energy spectrum** due to the limited energy resolution is the ultimate background. I would like to emphasize that the $\beta\beta2\nu$ background corresponds to a very steep energy spectrum, just below the $\beta\beta0\nu$ energy region. Thus any unstability of the energy response of a calorimeter block, which has not been identified correctly, may lead to an overestimated energy of the $\beta\beta2\nu$ events. Such event will "fall like a rock" from the $\beta\beta2\nu$ "big wall" into the $\beta\beta0\nu$ energy region. I like to call these $\beta\beta2\nu$ background events the *Yosemite* events.

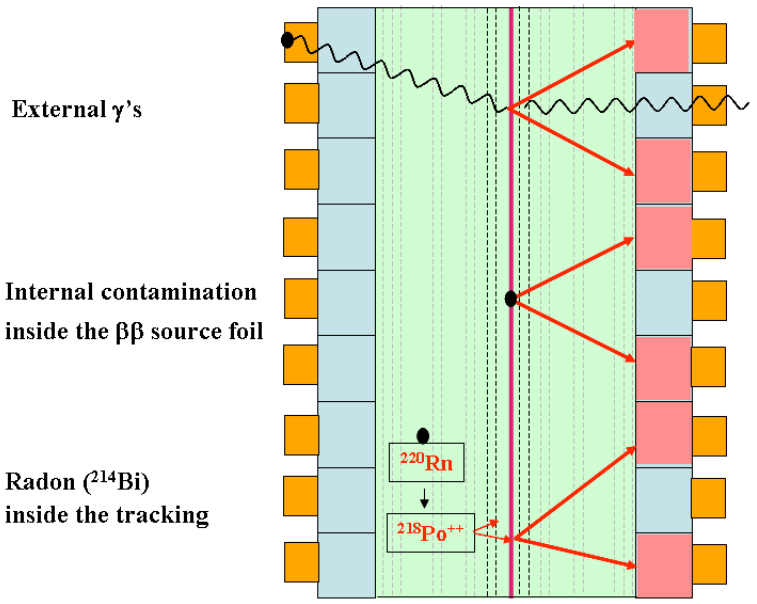

FIGURE 2.9: Schematic view of the three types of NEMO-3 background, which mimic $\beta\beta$ events : external γ's (up), radioactive contamination inside the $\beta\beta$ source foils (middle) and Radon contamination inside the wire chamber (down). See text for explanations.

2.1.4 Measurement of the different background components using the NEMO-3 data

Each component of background can be identified and measured separately using different dedicated topologies of events.

External background measurement

Two topologies of events are used to measure the external background (see Figure 2.13) :

1. External (e^-, γ) events defined as one track coming from the source foil and associated with a scintillator hit (electron) and one isolated scintillator (γ) with a time of flight between the two fired scintillators in agreement with an external γ hypothesis firing a first scintillator and producing a Compton electron in the source foil.

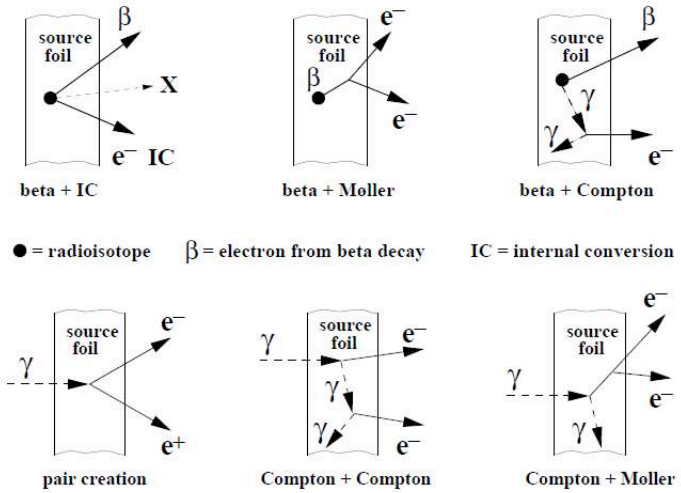

FIGURE 2.10: Mechanisms to produce a $\beta\beta$-like event produced by β decays of internal radioactive impurities inside the source foils (up) or by external γ's (down).

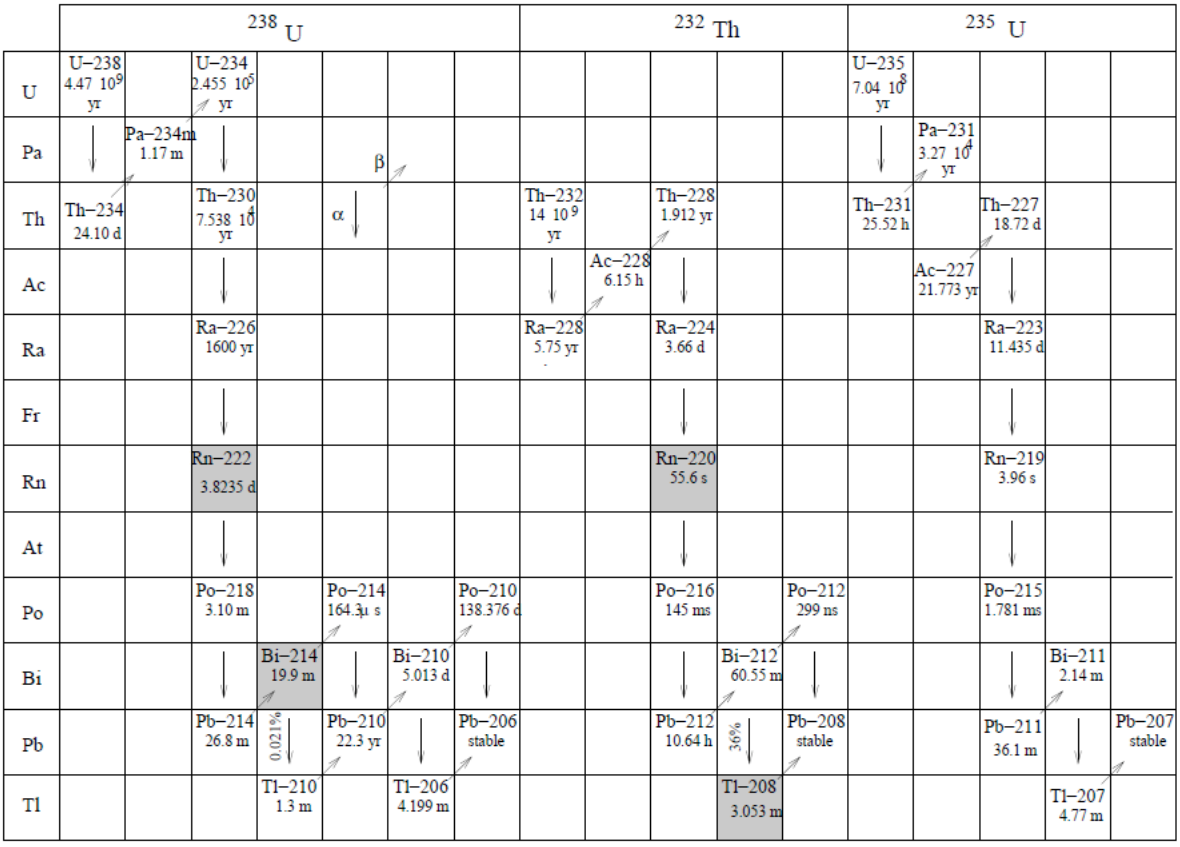

FIGURE 2.11: Natural radioactivity chains.

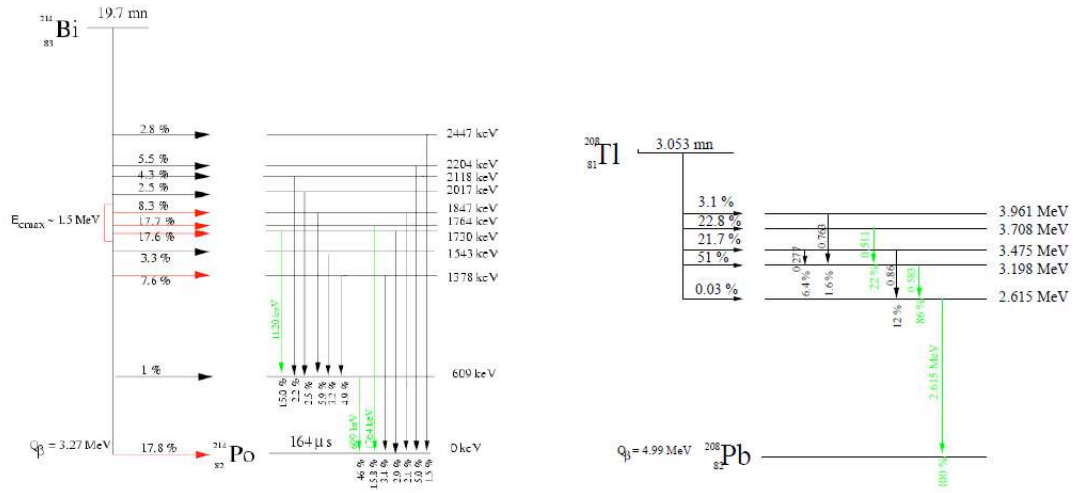

FIGURE 2.12: ^{214}Bi and ^{208}Tl decay diagrams.

2. Crossing-e^- defined as a track crossing the detector and associated on each ends to a fired scintillator with a time of flight in agreement with a crossing electron hypothesis.

A very accurate external background model has been developped in order to fit the observed data in both channels of analysis (external (e^-, γ) and crossing-e^- events). This model assumes contaminations in ^{238}U, ^{232}Ra and ^{40}K inside the PMT's, contamination in ^{60}Co (cosmogenic) inside the mechanical structure, and external γ's in LSM. Activities of each components in the Monte-Carlo are fitted to the observed data using a global fit of several parameters (energy sum, energy of the e^-, energy of the γ, angle between γ and e^-). Figure 2.14 shows the excellent agreement of the energy sum distribution of the (e^-, γ) events and the crossing-e^- events obtained for the whole detector during Phase 2 and the result of the fitted background model in Monte Carlo. Morever, the activities of each components obtained from the global fit are in agreement with the previous HPGe radioactivity measurements of the detector materials.

One may expect that the background may vary from one sector to another due to possible inhomogeneities of the detector materials. Thus the background model is actually calculated separately for each isotopes (located in different sectors).

Concerning the neutron background, it has been shown using dedicated runs with an AmBe neutron source outside of the shield that contribution of neutrons to the external background (via the neutron capture process resulting in emission of γ's) is negligible even in the $\beta\beta0\nu$ energy region [30] (the neutron background is measured using crossing electrons with a total energy above 4.5 MeV). This result has been verified by analysing the e^+/e^- events emitted from the source foils with the NEMO-3 physics data. Only 3 e^+/e^- events with an energy above 3 MeV have been observed after ≈ 3 years of data [32]. Their energy are contained between 3 and 3.8 MeV. Taking into account an unefficiency of $\approx 10\%$ to distinguish a positron to an electron with the track curvature, and assuming that these three events are produced by external neutrons, it would corresponds to an expected number of less than about 0.1 (e^-, e^-) events per year (90% C.L.) in the $[2.8 - 3.2]$ MeV $\beta\beta0\nu$ energy window.

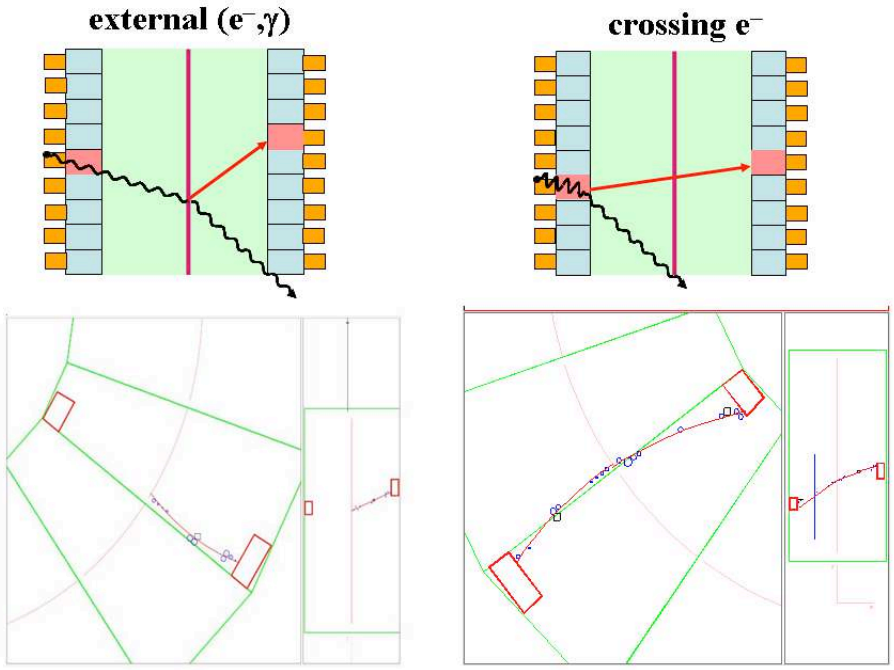

FIGURE 2.13: The two event topologies used to measure the external background : (left) external (e^-, γ) event ; (right) crossing-e^-.

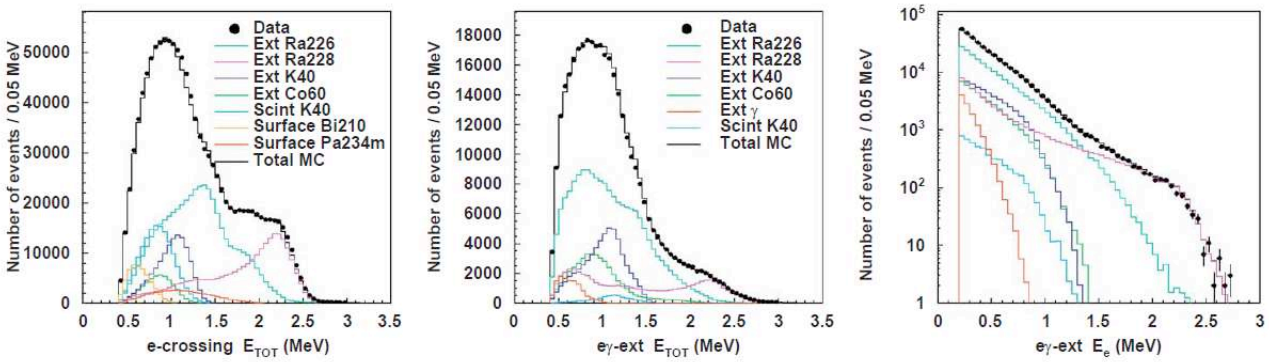

FIGURE 2.14: Result of the fit of the external background model to the observed data (black dots) of the Phase 2 data, for the whole detector : (left) energy sum of crossing electrons, (center) energy sum of the electron and γ for external (e^-, γ) events and (right) detected energy of the electron for external (e^-, γ) events.

Radon and Thoron measurements

The Radon contamination is measured by detecting inside its decay chain the electron from the β-decay of Bi followed by the delayed α from the α-decay of Po with a short half-life of 164 μs, the so-called BiPo events. In order to detected the delayed α, a dedicated electronic has been developped for the tracking detector which allows to readout any delayed Geiger hit inside the wire chamber with a delay up to 700 μs. A Bipo event is thus defined in

NEMO-3 as an electron (a track inside the wire chamber associated with a fired scintillator) with at least one delay Geiger hit in the wire chamber close to the emission vertex of the electron. Displays of BiPo events detected in NEMO-3 are given in Figure 2.15. The delay is required to be greater than 90 μs and 30 μs for events with only one delayed Geiger hit and events with more than one delayed hit respectively, in order to suppress possible refiring of neighboring Geiger cells from the electron tracks. Applying these criteria, the mean efficiency to select a BiPo event produced on a wire surface has been estimated by Monte-Carlo simulation to be 16.5%.

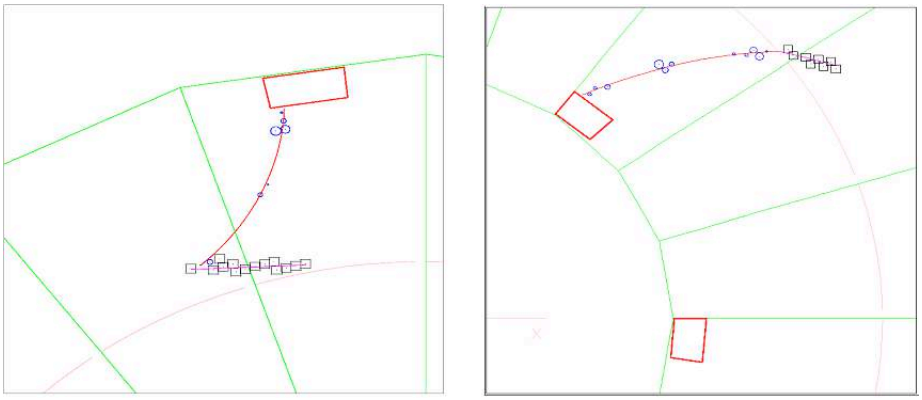

FIGURE 2.15: Example of BiPo events observed in NEMO-3 : (left) ^{214}Bi decayed on a wire inside the tracking volume ; (right) ^{214}Bi decayed on the surface of the foil.

The time distribution of the delayed tracks (see Figure 2.16 for single delayed hits) provides an efficient way to validate the quality of the event selection. The fitted half-life of the ^{214}Po is $T_{1/2} = 162.9 \pm 0.8$(stat. only) μs, and is in agreement with the table value of $T_{1/2} = 164.3 \pm 2.0$ μs [116]. The proportions of BiPo events due to refirings and random coincidences are found to be negligibly small, about 1%. This method allows to measure the Radon activity inside the wire chamber every day with a good accuracy. The average Radon and ^{214}Bi activity measured in Phase 1 (high Radon activity) was $\approx$ 30 mBq/m^3. The average Radon and ^{214}Bi activity measured in Phase 2 (after installing the Radon-tight structure surrounding the detector and after flushing Radon-free air inside) was $\approx$ 5 mBq/m^3 (a reduction factor $\approx$ 6). The volume of the wire chamber is $\approx$ 30 m^3, it corresponds to a total activity in Radon and ^{214}Bi of $\approx$ 150 mBq.

We also mention that the Radon contamination has been also measured separately using (e^-, γ) events with both particles emitted from the same vertex inside the tracking chamber. Despite of a less sensitive analysis, this second measurement has given results in agreement with the analysis using e^- delayed α.

The study of the spatial distribution of the e^-/α emission vertex in Phase 2 (low Radon activity) has shown that the ^{214}Bi activity is mainly on the wires which are on the edge of the large gas gaps. It confirms the drift of polonium ions to the wires. However higher activities have been observed either on the top or bottom of the wires for the internal or external part respectively of the tracking chamber. This asymetry has not yet been understood. The comparison of ^{214}Bi distribution of Phase 2 relatively with Phase 1 has shown that the residual ^{214}Bi activity is mainly near the scintillator walls and the end caps (top and

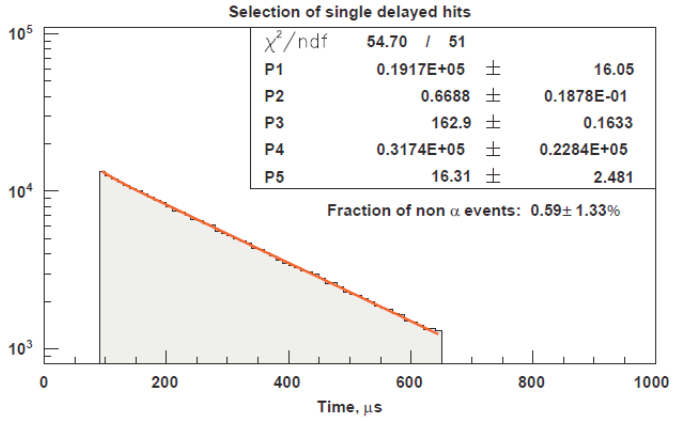

FIGURE 2.16: The time distributions of events selected with single delayed signals. Each distribution was fit to the function : $f(t) = P1e^{-ln2t/P3} + P2 + P4e^{-ln2/P5}$ where t is the event time, $P1$ and $P4$ are scaling constants, $P2$ is the amplitude of random coincidences, $P3$ the ^{214}Po half-life in μs and $P5$ the time constant of the refirings.

bottom) of the wire chamber and, but to a lesser degree, near the $\beta\beta$ source foils.

The study of possible origins of Radon contamination observed inside the tracking volume has been performed and is given in [29]. It results in four possible origins of Radon contamination :

1. Emanation of Radon from both the aluminized mylar and the teflon used to wrap the scintillator blocks inside the tracking chamber. Only upper limits for the activity in ^{214}Bi have been set with HPGe measurements : < 20 mBq/kg (equivalent to < 414 mBq taking into account the total mass) for teflon and < 35 mBq/kg (equivalent to < 126 mBq taking into account the total mass) for aluminized mylar.
2. The silicon seals (RTV 160) used to close the tracking chamber are porous to Radon. Any Radon contamination outside the tracking chamber might diffuse inside the detector. The HPGe measurements have shown that the RTV 160 itself is also contaminated in ^{214}Bi with an activity of 35 ± 10 mBq/kg corresponding to a total activity of 95 ± 27 mBq.
3. Outside of the tracking chamber, the dominant source of Radon is the PMT's glasses. The total activity in ^{214}Bi of all the 5" PMT's is about 240 Bq and $\approx 85\%$ of Radon is expected to emanate from the 1mm thick glass (the diffusion constant of Radon in the glass is $\approx 1.7\ 10^{-11}$ m^2/s giving a diffusion length of 2.9 mm). A small fraction ($\approx\ 10^{-3}$) of the emanated Radon through the RTV seals can give the observed contamination of Radon inside the tracking chamber.
4. The Radon measurement using the (e^-, γ) events indicates a possible contamination from the calibration tubes with some hot spots. Possible external Radon leaks through the seals of the calibration tube or contamination of ^{238}U inside the tubes could explain this Radon background.

Regarding Thoron background, the ^{208}Tl activity inside the tracking chamber has been measured using $e^-\gamma\gamma$ events (see next section). The ^{208}Tl activity measured in Phase 2

is $\approx$ 3 mBq ($\approx$ 0.1 mBq/m^3). Taking into account the 36% branching ratio of ^{208}Tl in the ^{232}Th chain, it corresponds to an activity in Thoron of $\approx$ 8 mBq ($\approx$ 0.3 mBq/m^3). Monte Carlo simulations show that this low level of Thoron is more than one order of magnitude lower than the background originating from Radon for the two-electrons events and is therefore negligeable in the $\beta\beta0\nu$ region.

Another source of background in the wire chamber is the contamination in ^{210}Pb ($T_{1/2}$ = 22.3 y) on the surface of the wires. ^{210}Pb belong to the ^{238}U decay chain and its contamination comes from the deposition of Radon during the wiring of the wire chamber. ^{210}Pb decays to ^{210}Bi, which is a β emitter with a Q_β = 1.16 MeV. It is of no concern for $\beta\beta0\nu$ decay search, but it must be considered in the precise measurement of the $\beta\beta2\nu$ decay spectra, especialy for for ^{130}Te. One electron events with an energy greater than 600keV and their vertices associated with Geiger cells are selected to measure the ^{210}Bi activity on the wire surfaces. A large variation of ^{210}Bi activity from one sector to another is observed. The origin of the non-uniformity in ^{210}Pb deposition on the wires is most probably due to the different histories of the wires and conditions during the wiring of the sectors.

Internal contaminations of the $\beta\beta$ source foils

The β-decay of ^{208}Tl is mainly accompanied by two or three γ's. Therefore its contamination inside the sources foils is measured by using internal $(e^-, \gamma\gamma)$ and $(e^-, \gamma\gamma\gamma)$ events defined as one track coming from the source foil and associated with a scintillator hit (electron) and two or three isolated scintillators (γ's) with a time of flight analysis in agreement with the hypothesis that all the particles involved have been emitted from the track vertex on the foil. The most important background for this analysis is due to Thoron and Radon inside the tracking chamber. The two event topologies $(e^-, \gamma\gamma)$ and $(e^-, \gamma\gamma\gamma)$ give consistent results. The ^{208}Tl activity in the $\beta\beta$ source foils and in the copper foils are presented in Figure 2.17.

The selenium foils had not been purified before their installation in the NEMO-3 detector, because of its relatively low quantity compared to molydbenum. It explains the relatively high activity of $\approx$ 0.4 mBq/kg measured in NEMO-3. It is remarkable that this measurement is in agreement with the HPGe measurements done before their installation inside the NEMO-3 detector. Another positive HPGe measurement for ^{208}Tl contamination was obtained for the Nd foils and is also in agreement with the measured value in NEMO-3. It demonstrates the reliability of the ^{208}Tl measurement.

The ^{208}Tl contaminations measured inside the Mo foils are the same for the two types of foils : 0.11$\pm$0.01 mBq/kg for the composite foils (thin and chemically purified ^{100}Mo powder mixted with PVA glue and water and deposited between mylar foils) and 0.12$\pm$0.01 mBq/kg for the metallic foils (pure ^{100}Mo monocrystal heated and rolled in the form of foils). Both are in agreement with the upper limits obtained with HPGe (best limit is $<$ 0.13 mBq/kg).

The copper foils appear to be highly radiopure although the S/B signal-to-background ratio for the ^{208}Tl measurement in NEMO-3 is quite low. The ^{208}Tl activity is estimated to be 0.03 ± 0.01 mBq/kg, in agreement with HPGe upper limit of < 0.033 mBq/kg.

The measurement of ^{214}Bi contamination inside the source foils is limited by the Radon background in the tracking volume near the foil. However the distribution of the length of the delayed α tracks gives some indications of the possible fraction of Bi contamination inside tthe foil, relatively to the Radon background near, or on the surface of the foil. Only

ββ material	N	S/B	ε (%)	A (mBq/kg)	A_{HPGe} (mBq/kg)
^{100}Mo(m)	666	2.4	1.7	0.11 ± 0.01	$<0.13; <0.1; <0.12^{*}$
^{100}Mo(c)	1628	1.7	1.8	0.12 ± 0.01	<0.17
^{82}Se(I)	446	2.0	2.0	0.34 ± 0.05	<0.670
^{82}Se(II)	507	3.4	1.9	0.44 ± 0.04	$0.4 \pm 0.13^{**}$
^{48}Ca	42	4.1	1.4	1.15 ± 0.22	$<2.$
^{96}Zr	158	7.9	1.8	2.77 ± 0.25	$<10.; <5.^{*}$
^{150}Nd	1002	39.4	1.8	9.32 ± 0.32	$10. \pm 1.7$
^{130}Te	448	1.1	2.0	0.23 ± 0.05	<0.5
^{nat}Te	495	1.9	1.8	0.27 ± 0.04	<0.08
^{116}Cd	196	0.7	1.7	0.17 ± 0.05	$<0.83; <0.5^{*}$
Cu	66	0.6	1.5	0.03 ± 0.01	<0.033

*Different foil samples have been measured.
**Samples of ^{82}Se(I) and ^{82}Se(II) having a combined mass of 800 g have been measured. The ^{82}Se(II) was not measured separately.

FIGURE 2.17: Number N of observed $(e^-, \gamma\gamma)$ and $(e^-, \gamma\gamma\gamma)$ events, signal-to-background ratio (S/B), signal efficiency (ϵ) and results of the measurements of ^{208}Tl activity of the source foils compared to the HPGe measurements.

limit has been defined for Mo foils and in agreement with the upper limits obtained with HPGe measurements < 0.34 mBq/kg for composite foils and < 0.39 mBq/kg for metallic foils.

We emphasize that NEMO-3 can also measure possible contamination of pure β emitters inside the foil by analysing the single e^- events coming from the foil. The energy spectra of single e^- events emitted from the ^{150}Nd source, the ^{130}Te source and the copper foil are presented in Figure 2.18. The excellent agreement between the data and the fitted Monte Carlo background shows the capacity to distinguish and measure the β emitters inside the source foils like ^{234m}Pa from the ^{238}U chain, ^{40}K, ^{210}Bi from the deposition of the Radon on the foil during the construction, or accidental contamination like ^{152}Eu inside the ^{150}Nd source foils. However these β contaminants represent a background only for the $\beta\beta2\nu$-decay measurement.

2.1.5 Test of the complete background model and background budget

The highly radiopure copper foils (1 sector) are used to compare the NEMO-3 data with the expected background calculated by Monte Carlo simulation using the complete background model described above. Two different event topologies have been tested : Single e^- events emitted from the foil and internal (e^-,γ) events from the foil. Excellent agreements have been obtained in both channels. Finally, since copper is not a $\beta\beta$ emitter, it provides a test for the validity of the background model with the two electrons events where $\beta\beta$-decay is searched for. Figure 2.19 shows the distributions of the energy sum of the two electrons, the single electron energies and angular correlation of two-electron events coming from the copper foils, observed in Phase 2. They are in excellent agreement with the expected

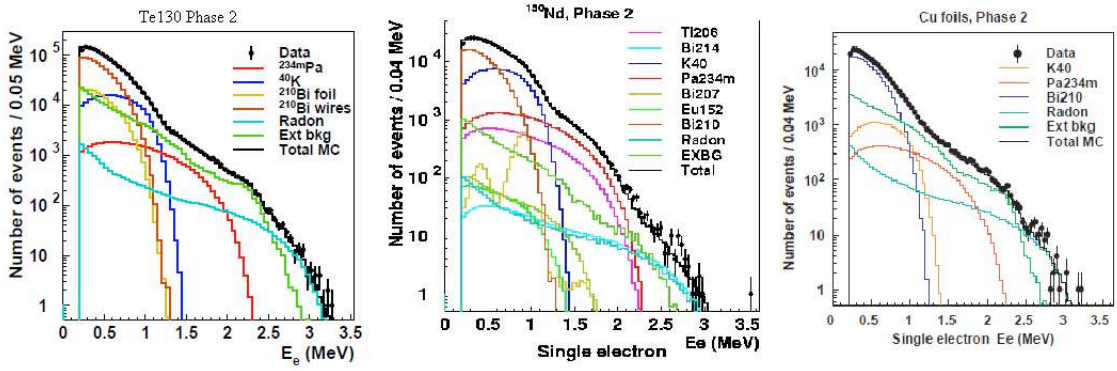

FIGURE 2.18: Energy spectrum of single electrons emitted from the ^{150}Nd source (left), the ^{130}Te source (center) and the copper foil (right).

background calculated by Monte Carlo simulation using the NEMO-3 background model.

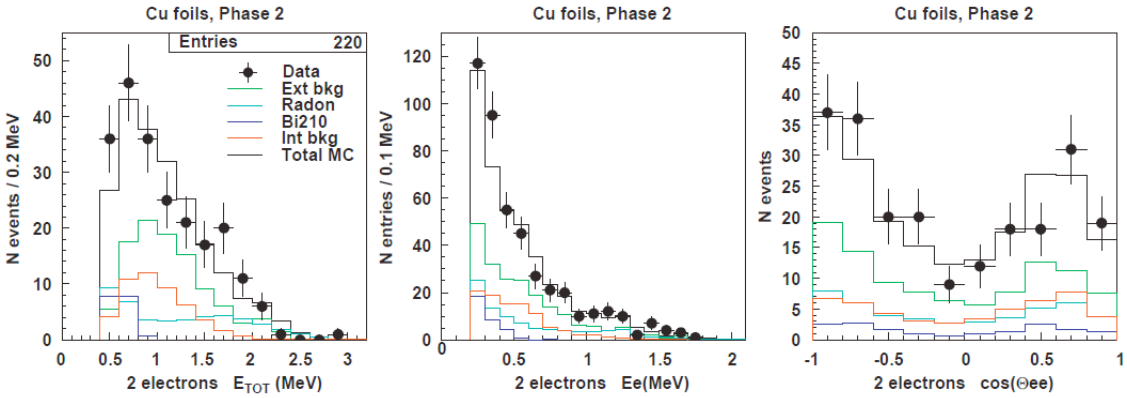

FIGURE 2.19: Background model prediction compared to the data for two electrons events from the copper foils.

I also mention another test performed using the two electrons channel with at least one associated γ-ray emitted in time from the source foil ($e^-e^-, N\gamma$). Above 2.5 MeV, this channel is dominated by ^{208}Tl contamination inside the foil, and to a lesser extent, Radon. However $\beta\beta2\nu$ is strongly supressed in this channel. Figure 2.20 shows the sum energy spectrum of the two electrons in the ($e^-e^-, N\gamma$) channel, from ^{100}Mo source foils, with 3.78 years of collected data in Phase 2. Data are in good agreement with the expected background dominated by ^{208}Tl contamination inside the foils. It validates the contribution of the ^{208}Tl contamination.

The estimated background in the $\beta\beta0\nu$ energy region is summarized in Table 2.1 for ^{100}Mo. The relative contribution of each background components is given in terms of number of counts/(kg.y) in the $[2.8 - 3.2]$ MeV energy window where the $\beta\beta0\nu$ signal is searched for (it takes into account the NEMO-3 energy resolution). With 7 kg of ^{100}Mo in NEMO-3, ≈ 3.5 counts per year are expected in the $[2.8 - 3.2]$ MeV energy window.

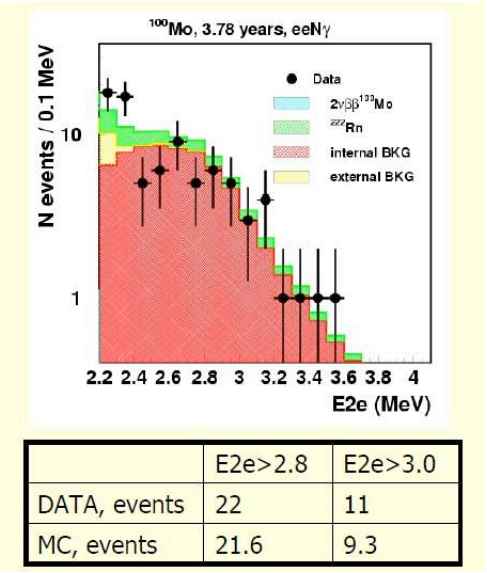

	E2e>2.8	E2e>3.0
DATA, events	22	11
MC, events	21.6	9.3

FIGURE 2.20: Sum energy spectrum of the two electrons using $(e^-e^-, N\gamma)$ channel from ^{100}Mo, with 3.78 years of collected data in Phase 2 and expected background from Monte-Carlo simulation.

		cts/(kg.yr) $[2.8-3.2]$ MeV	Fraction
Radon	≈ 5 mBq/m^3	0.16	30%
^{208}Tl in the foil	≈ 100 μBq/kg	0.11	20%
External bkg		$\leq 10^{-3}$	negligible
$\beta\beta2\nu$	$T_{1/2} = 7\ 10^{18}$ yr	0.23	50%
TOTAL		0.5	

TABLE 2.1: Background budget in NEMO-3 calculated using the background simulations for ^{100}Mo in terms of number of counts per kg and per year in the $[2.8-3.2]$ MeV energy window where the $\beta\beta0\nu$ signal is searched for.

2.1.6 $\beta\beta$ results

NEMO-3 has been running from February 2003 until January 2011. During the Phase 1 (high Radon background until September 2004), about 1 year of data has been collected. During the Phase 2 (low Radon background from december 2004), about 4 years of data have been collected. First results obtained only with Phase 1 and with Mo and Se have been published in [34]

$\beta\beta2\nu$ process

Figure 2.21 shows the distribution of the energy sum of the two electrons emitted from the ^{100}Mo foils, observed during Phase 2. The distributions of the minimum electron energy and the angular correlation between the two electrons are also presented. About 700000 $\beta\beta$ like events have been observed in 4 years with a very low background and a very

high signal-to-background ratio of $S/B = 77$. The detection efficiency of the $\beta\beta2\nu$-decay for Phase 2 is $\epsilon(\beta\beta2\nu) = 4.2\%$ for ^{100}Mo (without applying laser survey rejection) ; and the systematic error on the efficiency is estimated to be 5%. It corresponds to the $\beta\beta2\nu$-decay half-life for ^{100}Mo :

$$\mathrm{T}^{\beta\beta2\nu}_{1/2}(^{100}\mathrm{Mo}) = (7.16 \pm 0.01(\mathrm{stat.}) \pm 0.36(\mathrm{syst.}))\ 10^{18}\ \mathrm{y}$$

The measured half-life and the energy spectrum are similar (within the accuracy) if the laser survey procedure is applied.

The value of the $\beta\beta2\nu$ half-life $T^{\beta\beta2\nu}_{1/2}(^{100}Mo)$ has been used to study several possible extra systematics :

1. $T^{\beta\beta2\nu}_{1/2}(^{100}Mo)$ measured separately with composite or metallic Mo foils are in agreement within the 5% systematic error (the half-life measured with composite foils appears to be slightly larger than with metalic foils)
2. $T^{\beta\beta2\nu}_{1/2}(^{100}Mo)$ has been measured year by year separately and appears to be stable within the statistic and systematic errors.
3. $T^{\beta\beta2\nu}_{1/2}(^{100}Mo)$ has been measured using only the sector number 13 where the wire chamber was unstable (with some periodes of refiring geiger cells). The measured value is in agreement with the average value. It demonstrates the validity of the procedure to detect hot regions of the wire chamber and to supress them both in data and in simulations.

The distributions of the $\beta\beta2\nu$-decay measured with ^{82}Se foils in Phase 2, are presented in Figure 2.22. 15348 $\beta\beta$ like events have been observed in 4 years with a signal-to-background ratio of $S/B = 3.07$. The measured efficiency of the $\beta\beta2\nu$-decay is $\epsilon(\beta\beta2\nu) = 5.8\%$ for ^{82}Se. It corresponds to the $\beta\beta2\nu$-decay half-life :

$$\mathrm{T}^{\beta\beta2\nu}_{1/2}(^{82}\mathrm{Se}) = (9.6 \pm 0.1(\mathrm{stat.}) \pm 0.5(\mathrm{syst.}))\ 10^{19}\ \mathrm{y}$$

The $\beta\beta2\nu$-decay has been also measured in NEMO-3 with 5 other isotopes : ^{48}Ca, ^{96}Zr, ^{116}Cd, ^{130}Te and ^{150}Nd. The measured half-lives are summarized in Table 2.2.

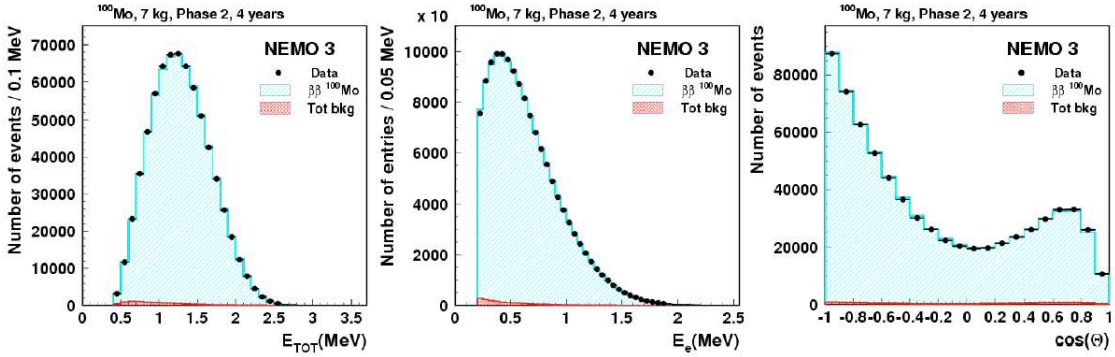

FIGURE 2.21: Sum energy spectrum (left), single energy spectrum (center) and angular distribution (right) of the two electrons events, for ^{100}Mo, obtained after 4 years of collected data in Phase 2.

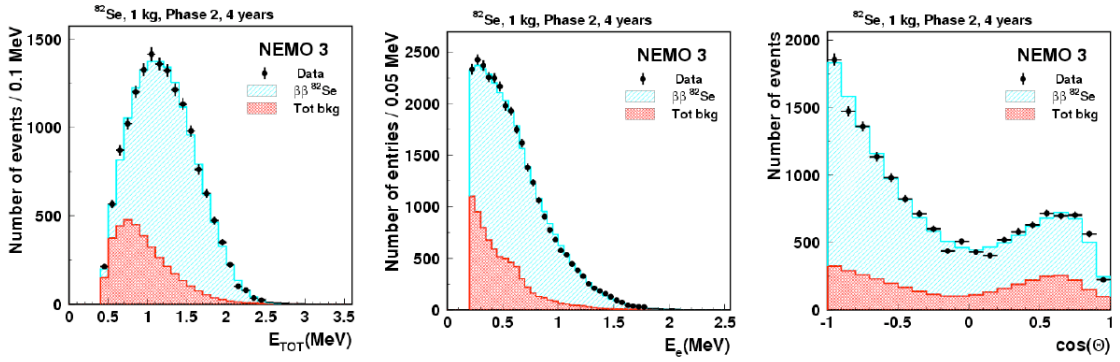

FIGURE 2.22: Sum energy spectrum (left), single energy spectrum (center) and angular distribution (right) of the two electrons events, for ^{82}Se, obtained after 4 years of data collection in Phase 2.

Isotope	$T_{1/2}(\beta\beta 2\nu)$
^{100}Mo	$(7.16 \pm 0.01(stat.) \pm 0.36(syst.))\ 10^{18}\ y$ [34]
^{82}Se	$(9.6 \pm 0.1(stat.) \pm 0.5(syst.))\ 10^{19}\ y$ [34]
^{48}Ca	$(4.4 \pm 0.5(stat.) \pm 0.4(syst.))\ 10^{19}\ y$
^{96}Zr	$(2.35 \pm 0.14(stat.) \pm 0.16(syst.))\ 10^{19}\ y$ [35]
^{116}Cd	$(2.88 \pm 0.04(stat.) \pm 0.16(syst.))\ 10^{19}\ y$
^{130}Te	$(7.0 \pm 0.9(stat.) \pm 0.9(syst.))\ 10^{20}\ y$ [36]
^{150}Nd	$(9.11 \pm 0.25(stat.) \pm 0.63(syst.))\ 10^{18}\ y$ [37]

TABLE 2.2: Summary of $\beta\beta 2\nu$-decay measured with NEMO-3 for 7 isotopes, using Phase 1 and Phase 2 until end 2009 (4.5 years of data). Published results are indicated with references. Otherwise it corresponds to preliminary results

$\beta\beta 0\nu$ process

The analysis for the search of the $\beta\beta 0\nu$ process has been presented at the summer conferences in 2011, using the data of Phase 1 and Phase 2 until end of 2009 (4.51 years of data). Analysis of the data 2010 has not yet been presented.

Figure 2.23 present the energy sum spectra above 2 MeV for the two electrons emitted from the ^{100}Mo foils or from the ^{82}Se foils using data of Phase 1 and Phase 2 until end of 2009 (4.51 years of data) and using the procedure for laser survey corrections.

The limits set by Modified Frequentist Method (CLs) on the $\beta\beta 0\nu$ process, using the full distribution and assuming that the $\beta\beta 0\nu$ process is governed by the exchange of a virtual Majorana neutrino, are for ^{100}Mo (≈ 31.2 kg.yr) and for ^{82}Se (≈ 4.2 kg.yr) [40] :

$$T_{1/2}^{\beta\beta 0\nu}(^{100}\mathrm{Mo},\ \langle m_\nu \rangle) > 1.0\ 10^{24}\ \mathrm{y}\ (90\%\ \mathrm{C.L.})$$

$$T_{1/2}^{\beta\beta 0\nu}(^{82}\mathrm{Se},\ \langle m_\nu \rangle) > 3.2\ 10^{23}\ \mathrm{y}\ (90\%\ \mathrm{C.L.})$$

If one includes the systematic uncertainty of 5% on the $\beta\beta 0\nu$ detection efficiency and a systematic background uncertainty of 10%, the limits become

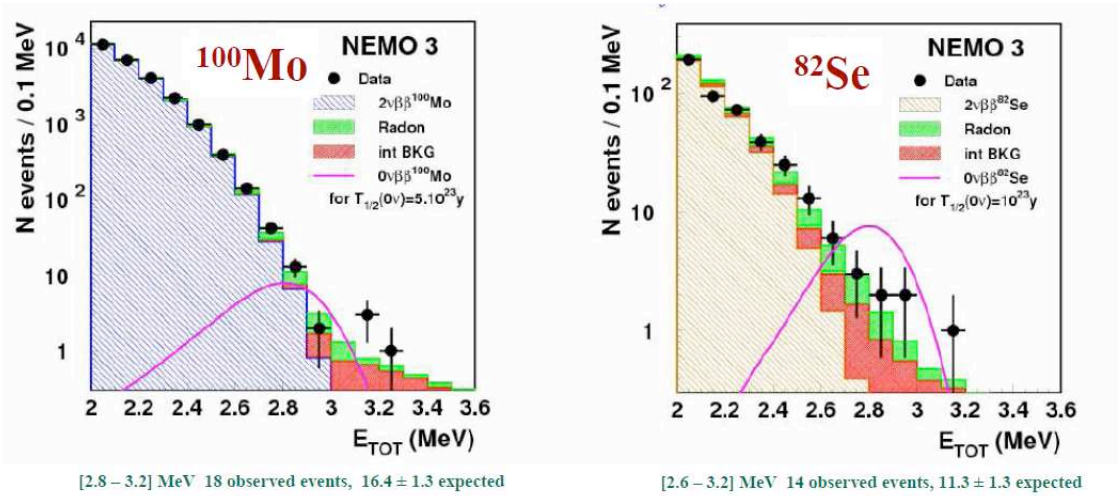

FIGURE 2.23: Sum energy spectrum of the two electrons obtained after 4.5 y of collected data, (left) for ^{100}Mo and (right) for ^{82}Se.

$$T_{1/2}^{\beta\beta0\nu}(^{100}\text{Mo},\ \langle m_\nu \rangle) > 0.75\ 10^{24}\ \text{y (90\% C.L.)}$$

$$T_{1/2}^{\beta\beta0\nu}(^{82}\text{Se},\ \langle m_\nu \rangle) > 3.2\ 10^{23}\ \text{y (90\% C.L.)}$$

However the background uncertainty is still under study. Its reduction would improve the limit on ^{100}Mo. The limit obtained with ^{82}Se is unchanged if the systematic uncertainties are taken into account because of its much smaller background : its higher $\beta\beta2\nu$ half-life reduces the $\beta\beta2\nu$ background and its smaller available mass inside the detector and therefore its smaller surface of source foil reduces the Radon background.

The $\beta\beta0\nu$ detection efficiency in the full energy range is $\epsilon(\beta\beta0\nu) = 18\%$. After applying the laser correction (for PMT gain survey), the effective $\beta\beta0\nu$ efficiency becomes $\epsilon(\beta\beta0\nu) = 12.5\%$ because laser corrections can be applied to $\approx 70\%$ of the available data. We emphasize that the laser procedure is crucial. Indeed, without any PMT's gain stability survey, few counts are observed every year in the $\beta\beta0\nu$ energy region due to some unstable PMT gains.

Same limits on $T_{1/2}(\beta\beta0\nu)$ are obtained if one compares the number of events observed in the $\beta\beta0\nu$ energy window with the number of expected background events. Numbers of observed and expected events are summarized in Table 2.3. The energy windows have been optimized with Monte Carlo simulation and are [2.8−3.2] MeV for ^{100}Mo and [2.6−3.2] MeV for ^{82}Se. The lower energy limit for ^{82}Se is due to a lower $\beta\beta2\nu$ background (higher half-life and lower available mass of source).

- For ^{100}Mo : between 2.8 and 3.2 MeV, during Phase 1, 6 events have been observed for 5.3±0.6 expected background events, and during Phase 2 (until end of 2009), 12 events have been observed for 11.1±0.9 expected background events.
- For ^{82}Se : between 2.6 and 3.2 MeV, during Phase 1, 4 events have been observed for 3.6 expected background events, and during Phase 2 (until end of 2009), 10 events have been observed for 7.3 expected background events.

Isotope Isotope	Energy window	Phase 1 (1 yr) # observed events	Phase 1 (1 yr) # expected background	Phase 2 (3.5 yrs) # observed events	Phase 2 (3.5 yrs) # expected background
^{100}Mo	[2.8-3.2] MeV	6	5.3±0.6	12	11.1±0.9
^{82}Se	[2.6-3.2] MeV	4	3.6	10	7.3

TABLE 2.3: Number of observed events and expected background.

$\beta\beta0\nu$ processes with V+A current or Majoron emission

In the case of $\beta\beta0\nu$-decay with right-handed V+A weak current, the angular distribution between the two emitted electrons is expected to be different, compared to the "standard" $\beta\beta0\nu$-decay process. Therefore NEMO-3 is the most sensitive $\beta\beta$ detector for the search of the V+A $\beta\beta0\nu$-process.

A maximum likelihood fit using not only the energy sum of the two electrons but also the angular distribution and the single electron energy has been applied [29]. No excess of events has been observed and limits on the half-life of the process have been derived for ^{100}Mo and ^{82}Se [40] :

$$T_{1/2}^{\beta\beta0\nu,\ V+A}(^{100}\text{Mo}) > 5.7\ 10^{23}\ \text{years (90\% C.L.)}$$

$$T_{1/2}^{\beta\beta0\nu,\ V+A}(^{82}\text{Se}) > 2.4\ 10^{23}\ \text{years (90\% C.L.)}$$

It corresponds to a limit on the $\langle\lambda\rangle$ parameter of the right-handed V+A current

$$\langle\lambda\rangle < 1.4\ 10^{-6}\ \text{(90\% C.L.)} \quad (^{100}\text{Mo})$$

$$\langle\lambda\rangle < 2.0\ 10^{-6}\ \text{(90\% C.L.)} \quad (^{82}\text{Se})$$

The $\beta\beta$ energy sum spectrum of the two electrons is expected to be distorded, in the case of the emission of a Majoron. Limits obtained only with Phase 1 data are sumarized in Table 2.4 [41].

Isotope	$n=1$	$n=2$	$n=3$	$n=7$
^{100}Mo	$> 2.7\ 10^{22}$ y	$> 1.7\ 10^{22}$ y	$> 1.0\ 10^{22}$ y	$> 7\ 10^{20}$ y
^{82}Se	$> 1.5\ 10^{22}$ y	$> 6.0\ 10^{21}$ y	$> 3.1\ 10^{21}$ y	$> 5\ 10^{20}$ y

TABLE 2.4: Limits obtained with Phase 1 data on $T_{1/2}(\beta\beta0\nu)$ in the case of $\beta\beta0\nu$-decay with a Majoron emission, as a function of the spectral index [41].

$\beta\beta$-decay to excited states

The tracko-calo technique allows to study the $\beta\beta$-decay for transitions involving excited states with a direct detection of the γ's emitted by the excited state, associated to the two electrons.

For the first time, the $\beta\beta2\nu$-decay of ^{100}Mo to the excited state 0_1^+ of ^{100}Ru (see Figure 2.24) has been directly measured by selecting events containing two electrons and two

γ's (539.5 and 590.8 keV) with a time of flight analysis in agreement with the hypothesis that all the particles involved have been emitted from the same vertex on the foil and with a γ energy distribution in agreement with expected Monte-Carlo simulations. The measurement of the half-life, using only Phase 1 data has been published in [38] and is :

$$T^{\beta\beta 2\nu}_{1/2}(^{100}\text{Mo} \rightarrow ^{100}\text{Ru}, 0^+_1) = 5.7^{+1.3}_{-0.9}(\text{stat.}) \pm 0.8(\text{syst.})\ 10^{20}\ \text{y}$$

It corresponds to about 40 signal events observed with a signal-to-background ratio of about 4. Radon was the dominant background. Update analysis using Phase 2 data give a result in agreement with the published one but with a much larger signal-to-background ratio of about 30 (result not yet presented).

The limit on the $\beta\beta 0\nu$-decay of ^{100}Mo to the excited state 0^+_1 of ^{100}Ru has been also determined with Phase 1 data (the improved limit using Phase 2 is not yet public) :

$$T^{\beta\beta 0\nu}_{1/2}(^{100}\text{Mo} \rightarrow ^{100}\text{Ru}, 0^+_1) > 8.9\ 10^{22}\ \text{y (90\% C.L.)}$$

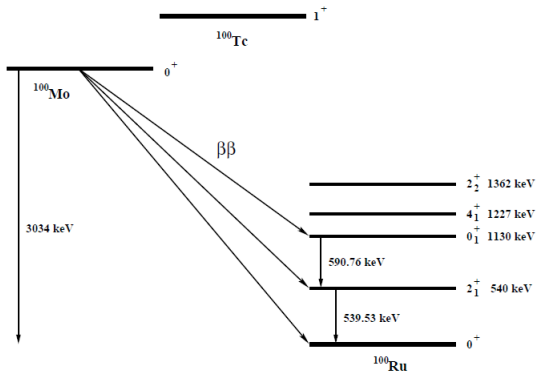

FIGURE 2.24: A double beta decay scheme of ^{100}Mo showing the decay to the ground and excited states of ^{100}Ru. The latter transitions are followed by de-excitation γ-rays.

2.2 SuperNEMO Experiment

The SuperNEMO experiment is based on an extension and an improvment of the experimental technique used in the NEMO-3 detector, by combining calorimetry and tracking. The goal is to accomodate about 100 kg of enriched $\beta\beta$ isotope in order to reach a sensitivity of 10^{26} years on the $\beta\beta 0\nu$ half-life [42].

The SuperNEMO design is a planar geometry. The current design envisages about twenty identical modules, each housing 5 kg of enriched $\beta\beta$ isotope. The design of a SuperNEMO detector module is shown in Figure 2.25. The source is a thin (40 mg/cm^2) foil inside the detector. It is surrounded by a gas tracking chamber followed by calorimeter walls. The tracking volume contains 2000 wire drift cells operated in Geiger mode which are arranged in nine layers parallel to the foil. The calorimeter is divided into 500 to 700 plastic scintillator blocks (depending of the final size) which cover most of the detector outer area and are coupled to low radioactive PMT's. A γ veto is added on the top and bottom

(calorimeter veto) and lateral sides (calorimeter X-walls, see Figure 2.25) of the tracking chamber, allowing a 4π γ coverage.

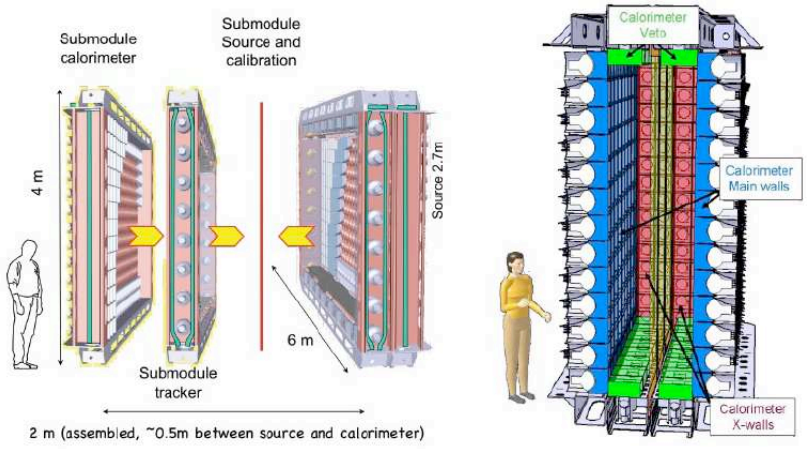

FIGURE 2.25: Mechanical view of a SuperNEMO module.

The choice of isotope for SuperNEMO is aimed at maximising the $\beta\beta0\nu$ signal over the background of $\beta\beta2\nu$-decay and other nuclear decays mimicking the process. Therefore the isotope must have a long two-neutrino half-life, a high endpoint energy and a large phase space factor. And of course, the possibility of isotopic enrichment on a large scale is also a factor for the selection of the isotope. Today, the isotope for SuperNEMO is ^{82}Se. The $\beta\beta2\nu$ half-life of Se is about 14 times higher than for Mo. Therefore, for a constant energy resolution, the contribution of the $\beta\beta2\nu$ background in the $\beta\beta0\nu$ energy region with 100 kg of ^{82}Se (case of SuperNEMO) is identical to the $\beta\beta2\nu$ background with 7 kg of ^{100}Mo (NEMO-3 case) ! In parallel, SuperNEMO plans to improve by a factor of two the energy resolution in order to reduce by a factor two the $\beta\beta2\nu$ background. The SuperNEMO collaboration is also investigating the possibility of enriching large amounts of ^{150}Nd via the method of atomic vapour laser isotope separation (AVLIS). AVLIS is based on isotope-selective optical pumping by very narrow bandwidth laser followed by efficient infrared photo-ionization. A 50% rate of enrichment seems to be feasible in a reasonable time scale. One could argue that the $\beta\beta2\nu$ half-life for Nd and Mo are almost equal. However, the large number of valence electrons in Nd produces a Coulomb screening which disfavours the emission of the two β's with maximum available energy $Q_{\beta\beta}$, and consequently reduces the number of $\beta\beta2\nu$ background events around $Q_{\beta\beta}$ in the $\beta\beta0\nu$ energy region. Thus $\beta\beta2\nu$ background is expected to be roughly the same with ^{150}Nd or ^{82}Se. Finally, new collaborators from South Korea are in charge of providing significant amount of ^{48}Ca (1 kg within 3 years). Enrichment is performed using the same AVLIS method as ^{150}Nd [43].

The expected sensitivity of SuperNEMO on $T_{1/2}(\beta\beta0\nu)$ at 90% C.L. is given in Table 2.5 for the three possible isotopes. With 100 kg of Nd (and 50% enrichment in ^{150}Nd), the SuperNEMO sensitivity becomes 3 10^{25} years (90% C.L.). It is still very competitive to other isotopes because of the large phase factor for ^{150}Nd. Morever, the $\beta\beta$ transition energy for Nd is $Q_{\beta\beta} = 3.367$ MeV, above the transition energy of ^{214}Bi $Q_{\beta} = 3.27$ MeV. Thus ^{214}Bi and Radon cannot contribute anymore to the background in the $\beta\beta0\nu$ energy region. It

makes the life much easier ! Life is even much easier if one uses ^{48}Ca. Its $\beta\beta$ transition energy is $Q_{\beta\beta} = 4.274$ MeV, near the transition energy of ^{208}Tl $Q_\beta = 4.99$ MeV. The requirement for the ^{208}Tl radiopurity of the $\beta\beta$ foils is thus much less stringent ($< 100\mu$Bq/kg) than for ^{82}Se and ^{150}Nd ($< 2\mu$Bq/kg, see below).

Isotope	Limit on $T_{1/2}(\beta\beta0\nu)$ (90% C.L.)
^{82}Se	$> 10^{26}$ y
^{150}Nd (50% enrichement)	$> 0.3\ 10^{26}$ y
^{48}Ca (50% enrichement)	$> 0.75\ 10^{26}$ y

TABLE 2.5: Sensitivity of SuperNEMO on $T_{1/2}(\beta\beta0\nu)$ at 90% C.L. for various isotopes. See text for background discussion.

To reach the sensitivity of 10^{26} years with 100 kg of ^{82}Se and 5 years of data, the required level of background in the $[2.8-3.2]$ MeV energy window [1] must be around 1 count per year with the following background budget : a $\beta\beta2\nu$ background less than ≈ 0.25 count/year, a background due to Radon contamination inside the tracking chamber less than ≈ 0.25 count and a background due to ^{208}Tl and ^{214}Bi contamination inside the $\beta\beta$ source foils less than ≈ 0.5 count.

Therefore, the three main improvements required for SuperNEMO (compared to NEMO-3) are

1. the energy resolution and the energy calibration and survey (in order to reduce the $\beta\beta2\nu$ background)
2. the radiopurity of the $\beta\beta$ source foils (in order to reduce the ^{208}Tl and ^{214}Bi background)
3. the Radon purity inside the tracking chamber.

These parameters have been studied extensively during the current design study phase with Monte-Carlo simulations. The SuperNEMO sensitivity calculated by Monte Carlo simulations as a function of these parameters, is summarized in Figure 2.26. Their requirements (to reach a sensitivity of 10^{26} years) are summarized in Table 2.6 and compared to NEMO-3 characteristics. The energy resolution must be improved by a factor 2. We will see that it has already been obtained with prototypes. The Radon and ^{208}Tl contaminations measured in NEMO-3 must be reduced by a factor ≈ 50 in SuperNEMO. I will present the achievements and current status of this three issues. All other details are given in [42].

2.2.1 Energy resolution

An energy resolution of FWHM= 7% at 1 MeV is required to reach a sensitivity of $T_{1/2}(\beta\beta0\nu) > 10^{26}$ years for an exposure of 500 kg.year with ^{82}Se, and assuming a radiopurity of the foils of 2 μBq/kg in ^{208}Tl and 10 μBq/kg in ^{214}Bi (see Figure 2.26).

An extensive R&D program has been performed in order to study how to reach an energy resolution of FWHM= 7% at 1 MeV. Only organic scintillators have been studied because it limits the backscattering of electrons and guarantee a very high radiopurity. The energy resolution has been improved thanks to three modifications :

1. It corresponds to the energy window which optimizes the sensitivity.

	NEMO-3	SuperNEMO
Isotope	^{100}Mo	^{82}Se (^{150}Nd, ^{48}Ca)
Mass	7 kg	100 kg
Energy resolution (FWHM @ 1 MeV)	15%	7%
Source radiopurity		
^{208}Tl	$\approx 100\mu$Bq/kg	$< 2\mu$Bq/kg
^{214}Bi	$< 300\mu$Bq/kg	$< 10\mu$Bq/kg
Radon	≈ 5 mBq/m^3	< 0.1 mBq/m^3

TABLE 2.6: Comparison of the NEMO-3 characteristics with the SuperNEMO requirements.

1. The surface of the PMT photocathode has been increase (in comparison to the entrance surface of the scintillator) by using larger 8" PMT's
2. The PMT has been coupled directly to the scintillator in order to avoid any extra light loss through the optical guide
3. The characteristics of the scintillator blocks have been improved by selecting the best available organic scintillating material and by testing the best geometry and wrapping of the scintillators to optimize the collection of the scintillating photons to the photocathode.

Other issues have been also considered. The granularity of the calorimeter has been optimized in order to minimize the γ pile-up in the scintillator blocks with respect to cost considerations. The final choice of the geometry layout is the result of a compromise between the geometry efficiency and the number of channels. The thickness of the scintillator block is constrained by the γ tagging efficiency, which must be greater than 50% at 1 MeV

A mechanical view of an optical module of the calorimeter is presented in Figure 2.27.

Photomultipliers

Today the 8" photomultipliers developed for the SuperNEMO project have quantum effciency (QE) around 35% at 420 nm. Such performances have been achieved after developments on smaller size of tubes. Tens of 3" and 5" Photonis PMT's have been tested at CENBG before extrapolating the high QE process for 8" tubes. First measurements on the energy resolution of such large tubes highlighted defects on the vacuum quality of the tubes and on the collection of photoelectrons. Such defects have been solved by Photonis and Hamamatsu on their new tubes registered as XP1886 for Photonis and R5912MOD for Hamamatsu. Studies and developments have been necessary to guaranty the linearity of the 8" PMts. The linearity of these tubes has been tested with calibrated electrons up to 2 MeV and satisfies the requirements. Tests with LED light are under progress to confirm these performances up to 8 MeV. The performances on the energy resolution depend also on the homogeneity of the PMt's cathode as scintillating photons illuminate the entire photocathode. Important improvements have been also realized by Hamamatsu to increase the quantum efficiency on the sides of the phototocathode. Finally, Hamamatsu PMT's have been selected, since Photonis decided to stop producing PMT's (a strange and unintelligible capitalism decision...).

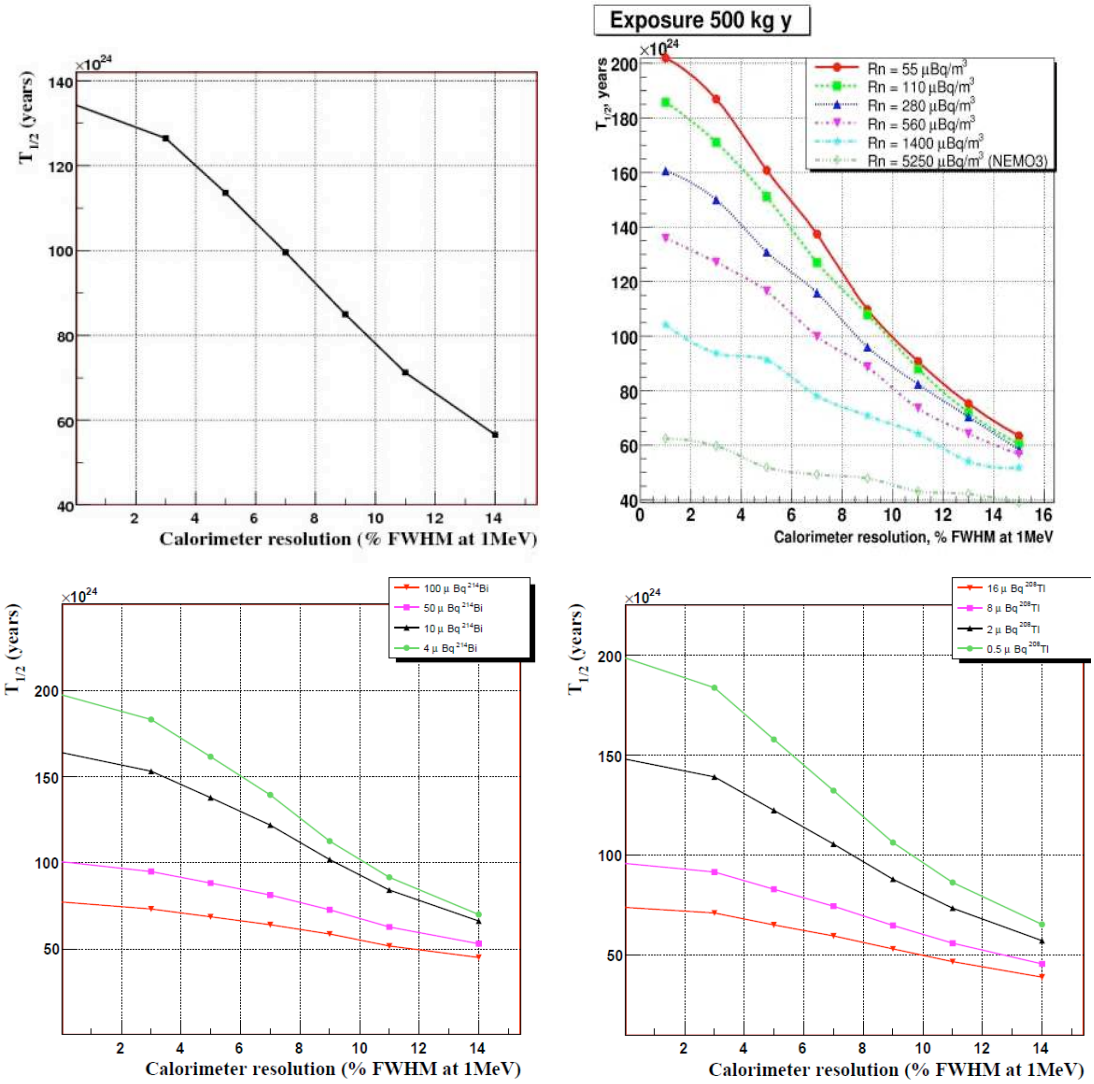

FIGURE 2.26: Sensitivity of SuperNEMO to $T_{1/2}(\beta\beta0\nu)$ at (90% C.L.) as a function of the energy resolution (FWHM at 1 MeV) assuming ^{82}Se foils, for an exposure of 500 kg.year. Upper left : with 10 μBq/kg of ^{214}Bi and 2 μBq/kg of ^{208}Tl and no Radon ; Upper right : assuming several Radon activity (but without any ^{214}Bi nor ^{208}Tl internal contamination) ; Lower left : for 4 μBq/kg (green), 10 μBq/kg (black), 50 μBq/kg (cyan) and 100 μBq/kg (red) of ^{214}Bi (assuming no ^{208}Tl contamination and no Radon) ; Lower right : for 0.5 μBq/kg (green), 2 μBq/kg (black), 8 μBq/kg (cyan) and 16 μBq/kg (red) of ^{208}Tl (assuming no ^{214}Bi contamination and no Radon).

Scintillator blocks

The design study of the scintillators is based on organic materials which limit the backscattering of electrons and guarantee a very high radiopurity. The goal of the study was to define the best material, the geometry and the wrapping of the scintillators to optimize the

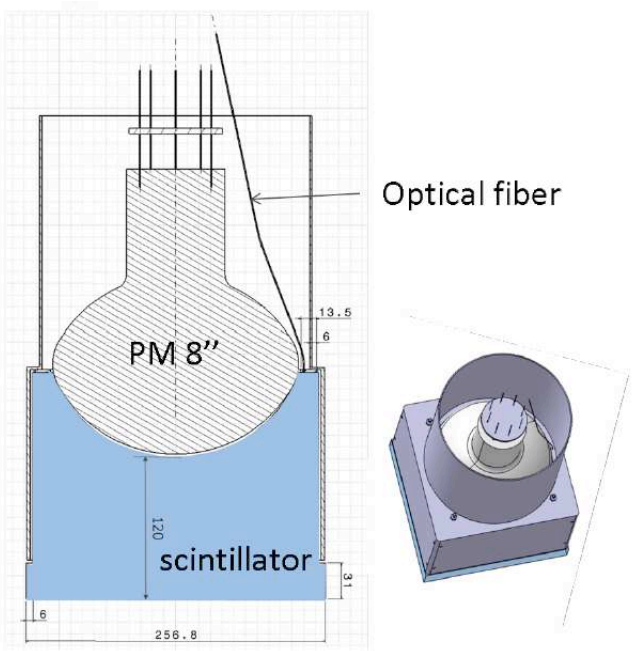

FIGURE 2.27: Mechanical view of an optical module of the calorimeter : a scintillator block coupled to a 8" PMT and surrounded by a magnetic shield.

collection of the scintillating photons to the photocathode. Several geometries have been designed and studied by GEANT4 simulations and measurements with the electron spectrometers and ^{207}Bi sources. These studies and the mechanical constraints led to the choice of a cubic block with two possible entrance surfaces of 257 mm^2 or 308 mm^2 and a minimal thickness of 120 mm to detect the γ-rays . The light collection is improved by a wrapping of Teflon on the sides of the blocks and 6 μm of aluminized Mylar on the entrance face. The main walls of the calorimeter consist in 374 or 520 optical modules depending on the scintillator size.

Two materials have been selected and tested : polystyrene-base scintillator produced in JINR Dubna and Poly-Vinyl-Toluene (PVT). The two different geometries of blocs have been characterized with the electron spectrometers for PS and PVT scintillators coupled to the Hamamatsu R5912MOD PMT (baseline PMT for SuperNEMO). Table 2.7 presents the energy resolution obtained at 1 MeV. PVT has a larger light yield and provides a higher energy resolution. However its production is much more expansive than standard polystyren scintillator. Larger scintillator block allow to reduce the number of channels. However, the energy resolution is also reduced and there is a larger risk of γ/β pile-up, which reduces the capability to reject γ-rays from background.

These results have been confirmed with several blocks and phototubes, and with different test benches. The energy spectrum measured with the 257 mm^2 PVT bloc is given in Figure 2.28. It has been verified that the energy resolution of the optical module is inversely proportional to the square root of the energy of the electron, as shown in Figure 2.28.

	Cubic block 257×257 mm^2	Cubic block 308×308 mm^2
Polystyrene	$8.7 \pm 0.1\%$	$9.8 \pm 0.1\%$
Poly-Vinyl-Toluene	$7.3 \pm 0.1\%$	$8.3 \pm 0.1\%$

TABLE 2.7: Energy resolution (FWHM) for 1 MeV electrons with scintillators of different sizes and materials.

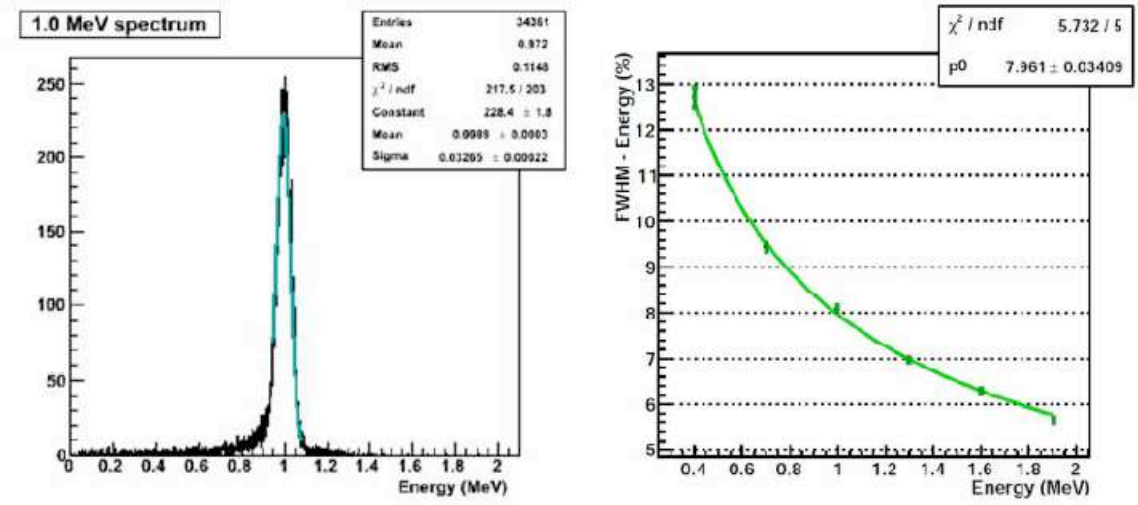

FIGURE 2.28: (Left) Charge of 1 MeV electron measured with a PVT cubic block (256mm^2 entrance surface) coupled to a R5912MOD PMT. The energy resolution has to be corrected by -0.5% due to the energy losses of the electrons in the trigger system. (Right) Energy resolution as a function of the energy of the electron and fit of the square root function.

2.2.2 Radiopurity of the source foils

Figure 2.26 shows the SuperNEMO sentitivity for various levels of internal contaminations in inside the source foils. Selenium foil radiopurities of 2 μBq/kg in ^{208}Tl and 10 μBq/kg in ^{214}Bi are required to reach a sensitivity of 10^{26} years after 500 kg.yr with ^{82}Se. Thus enriched selenium must be first purified, then foils must be produced and finally its radiopurity must be controlled. Nevertheless, the best detection limit that can be reached by γ spectrometry with ultra low background HPGe detectors is around 50 μBq/kg for ^{208}Tl, which is one order of magnitude less sensitive than the required value. In order to achieve the required sensitivity for SuperNEMO, the collaboration has decided to develop a BiPo detector (under the responsability of LAL Orsay), dedicated to the measurement of ultra-low levels of contamination in ^{208}Tl and ^{214}Bi in the foils of SuperNEMO. The development of the BiPo detectors is presented separately in the second part of this document. I present here the status of the selenium purification.

Purification

The selenium can be purified by two different processes : the chemical process and the distillation process.

The principle of the chemical purification is to remove long lived radioactive isotopes of the ^{238}U and ^{232}Th decay chains while filling Radium sites with Barium by spiking samples during the processing. The process takes advantage of an equilibrium break in the ^{238}U and ^{232}Th decay chains, which can selectively transform these chains to non-equilibrium states in which only short lifetime daughters exist. So, the objective is to remove ^{226}Ra in the ^{238}U chain, and ^{228}Ra and ^{228}Th in the ^{232}Th chain.

This technique had been used by INL (Idaho National Laboratory, USA) to purify enriched ^{100}Mo powder for NEMO-3 [39] and an extraction factor of 100 for ^{226}Ra was measured. The selenium purification process is similar to the one used for molybdenum and very high extraction factor can be also achieved. The critical point of this method is to use very pure chemical products (water and acid have to be distillate), especially barium chloride. NEMO-3 purification succeeded by using an old and ultra radiopure barium chloride reagent. About 0.5 kg of enriched ^{82}Se has been purified by INEL with this technique. Table 2.8 shows the chemical extraction factors deduced from the activities measured by γ-ray spectroscopy before and after purification. Only lower limits have been obtained due to the limited sensitivity of the HPGe measurement. However a factor at least 50 has been obtained for ^{226}Ra. We also mention that the sample was slightly contaminated in Ruthenium with a measured extraction ratio of 162.

Sample (mBq/kg)	Mass (g)	Time (h)	^{40}K	^{60}Co	^{226}Ra	^{228}Ra	^{228}Th	Ru
^{82}Se	196	447	668 ± 31	< 1	46 ± 2	13 ± 2	11 ± 2	485
Purified ^{82}Se	563	436	< 20	< 0.7	< 0.9	< 2.4	< 1.6	3
Reduction Factor			> 33		> 51	> 5.4	> 6.9	162

TABLE 2.8: Table of the chemical extraction factors obtained for an enriched ^{82}Se sample purified in INEL. The purification factors are deduced from the activities (in mBq/kg) measured by γ-ray spectroscopy before and after purification. Only lower limits are obtained for K, U and Th chains.

Another radiochemical process is currently under R&D in LSM in collaboration with JINR Dubna. It proposes to use resin to retain specific radio impurities. This technique is very efficient because in aqueous media, selenium is dissolved as anions and impurities such as Thorium, Radium and Uranium are cations. The use of cationic resin (for instance Dowex1X50) would retain only impurities and would keep selenium free. The advantage of this method is that chemical products are purified as well as selenium. The addition of a reverse cleaning of the resin allows to use continuously the same resin with a constant purification efficiency. There is a possibility to automatize the method in order to purify large amounts of enriched isotopes and this is under investigation. Such a method could be used also for neodynium purification.

Selenium can also be purified by distillation. Melting and boiling points depend on the structures of the raw selenium compounds. For instance, the RaSe structure has to be taken

into account in the case of radium contamination. Distillation of 2 kg of natural selenium has been performed by the Institute of Chemistry of High Purity Substances (IChHPS) in Russia. However, the final products are under the form of metallic selenium ingots and must be first transformed in the form of powder before measuring it. New distillation process leading to selenium powder with small grain has to be developped.

Foil production

The SuperNEMO source foils will be produced using the method developped for NEMO-3. First selenium powder with diameters smaller than $\approx 50\mu$m is required. Then the powder is mixed with an organic binder (PolyVinyl Alcohol, named PVA) and ultra pure water. The binder contribute to $\approx 10\%$ in weight to the final product. This paste is uniformly ($\pm 10\%$) deposited between two holey Mylar strips, called baking film. The thickness of the Mylar is 10 μm (corresponding to about 1.4 mg/cm^2). For the SuperNEMO demonstrator, the thickness of the source foils is 55 mg/cm^2 (comparable to NEMO-3) in order to accomodate 7 kg of source foil. For the final SuperNEMO detector, the thickness will be 40 mg/cm^2. In this process the losses of enriched product are less than 1% and it is relatively easy to recover the enriched material. Another advantage of this method is the possibility to use any metallic powder (Nd, Ca,...).

One of the issue is to obtain very radiopure holey Mylar foils. Mylar must undergo special treatment in which a large number of microscopic holes are produced in order to ensure a good bond with the PVA glue and also to allow the water evaporation during the drying of the glue. For NEMO-3, the holes have been produced by irradiating the Mylar at JINR with an ion beam and then by etching the Mylar in a Sodium hydroxide solution. Although all the chemical products used in this process have been selected for their radiopurity they are probably a source of residual contamination of the NEMO-3 source foils.

For SuperNEMO, a new approach based on laser drilling is currently developped by CPPM Marseille in collaboration with LP3 (Lasers, Plasmas et Procédés Photoniques, Université de la Méditerrané), in order to reduce the risk of radio contamination. They have demonstrated that a picosecond UV laser can produce holes of 100μm diameters in a mylar foil of 20 μm thick. First samples of holey Mylar (few hundreds cm^2) have been produced using this method. The production of a natural selenium foil with this Mylar sample is under test. The main advantage of this laser technique is that there is no risk of radio contamination.

The use of polyesther mesh is also studied by the collaboration.

The other requirements to produce an ultra radiopure selenium foils are :

- Select a radiopure mylar at the level of $\approx 15\mu$Bq/kg [2] in ^{208}Tl and $\approx 75\mu$Bq/kg in ^{214}Bi, since Mylar is $\approx 7\%$ in weight of the complete source foil.
- Select PVA at the level of $\approx 10\mu$Bq/kg in ^{208}Tl and $\approx 50\mu$Bq/kg in ^{214}Bi, since the PVA concentration is $\approx 10\%$ in weight of the complete source foil ;
- If the grain sizes of the purified selenium (at the end of the purification process) are too large (diameter be less than $\approx 50\mu$m), selenium must be grained using a radiopure technique.

2. We assume here that both the Mylar and PVA contributions to the source foil contamination are each at the level of 1 μBq/kg in ^{208}Tl and 10 μBq/kg in ^{214}Bi.

Radiopurity measurement

A first radiopurity measurement of purified selenium samples can be performed by γ spectrometry with ultra low background HPGe (High Purity Germanium) detectors. Nevertheless, the best detection limit that can be reached with this technique for ^{208}Tl is around 50 μBq/kg, which is one order of magnitude less sensitive that the required value. In order to achieve the required sensitivity for SuperNEMO, we are developping the BiPo-3 detector dedicated to the measurement of ultra-low levels of contamination in ^{208}Tl and ^{214}Bi in the foils of SuperNEMO. This detector will be able to qualify the radiopurity of the foils in their final form, before installation into the SuperNEMO detector. It can also validate the radiopurity of the selected Mylar and PVA. The BiPo-3 detector will be installed in Canfranc Underground Laboratory (Spain) in summer 2012. A complete description of the BiPo detector is presented in the second part of this document.

2.2.3 Strategies against Radon contamination inside the gas of the tracking chamber

Figure 2.26 presents the sensitivity of the full SuperNEMO detector with ^{82}Se sources as a function of the Radon activity, assuming a null activity of ^{214}Bi of the source foils. Typically, a Radon contamination of 280 μBq/m^3 is equivalent to a contamination of 10 μBq/kg in ^{214}Bi inside the source foils. For the full SuperNEMO detector, the sensitivity gain on $T_{1/2}(\beta\beta0\nu)$ obtained by reducing the Radon activity below 0.1 mBq/m^3 is not significant (from 1.1 10^{26} years to 1.4 10^{26} years for a calorimeter resolution of 7% FWHM at 1 MeV).

We remind that the three most probable origins of Radon inside the NEMO-3 tracking chamber were the emanation from materials used to wrap the scintillator blocks inside the tracking chamber, the poor tightness against Radon of the seals closing the chamber, and the diffusion of Radon from PMT's emanation or from external Radon in the lab. Taking into account this knowledge, the strategies developped against Radon for SuperNEMO are the following

1. The tracker will be isolated from the rest of the detector using a thin foil, very tight to Radon and not degrading significantly the energy resolution performance of the calorimeter . With a 30μm thickness of EVOH foil, the Radon reduction rate measured by the UTEF-CTU laboratory is 31000. However pure EVOH foils are sensitive to humidity, which produces mechanical cracks. Selection of appropriate films is under tests. The use of composite materials including EVOH or nylon is under study.
2. All materials inside the tracker have to be very radiopure. The Radon emanation of these materials has also to be measured. Radon emanation measurements will also be performed after the assembly of the tracker, to be sure that no mechanical process during assemblying induces a significative Radon contamination. A Radon concentration line, similar to the one developped in Heidelberg and used for BOREXINO, has been constructed by the UCL group to measure this emanation with a sensitivity of 0.2 mBq/m^3. The idea is to concentrate Radon emanation into a Radon trap like active charcoal or organic zeolith and then to measure Radon from the trap.
3. Radon-free air will be flushed around the PMT glass, to avoid a too high Radon concentration close to the PMT. The emanation of the PMT glass has been measured by the UNIBA Bratislava laboratory at the level of $(5.7 \pm 2.1)10^{-7}$ Bq/s. With the

flushing of Radon-free air close to the PMT, the contribution of the PMT emanation to the Radon level in the tracking chamber of the demonstrator should be well below the required activity limit (contrary to the NEMO-3 detector, the calorimeter of the SuperNEMO demonstrator is installed outside the tracking chamber). Morever, like in NEMO-3, the detector (tracker and calorimeter) will be surrounded by a Radon-tight structure. Radon-free air will be flushed inside this tent in order to prevent external Radon to diffuse inside the tracking chamber.

4. The incoming gas used inside the tracking chamber (mixture of 95% of Helium, 4% of alcohol, 1% of Argon) needs also to be as low radiopure as possible in Radon. It should be purified and measured. The usual technique (Radon trap by active charcoal at -50 degrees) can be applied to purify Helium gas. However, alcohol and Argon can be trapped and can saturate the Radon trap, which will become inefficient. The CPPM group in cooperation with chemistry laboratories, is studying the best adapted charcoal or organic zeolith able to trap Radon and not Argon nor alcohol.
5. The possibility to increase the gas flux should be kept under study. A typical flux of 3 m^3/h for the demonstrator volume of 20 m^3 would provide a Radon reduction factor greater than 7, if Radon contamination inside the incoming gas stays negligible. But recycling of the gas, gas purification, and helium-alcohol separation could be necessary for the whole SuperNEMO detector and must be studied seriously.

2.2.4 Demonstrator module

A first SuperNEMO module, named SuperNEMO demonstrator, will be installed in Modane Underground Laboratory. The main goals of the demonstrator module are :

- Demonstration of the feasibility of a large scale detector production with the requested performances (calorimeter energy and time resolution, tracker efficiency and radiopurity).
- Measurement and validation of the Radon background contribution especially from internal materials outgasing.
- Measurement and validation of the background contribution from the detector components
- Finalization of the technical choices.

The size and the design of the demonstrator correspond to the final design of the SuperNEMO modules. The only difference is the thickness of the source foils which is 55 mg/cm^2 for the demonstrator (comparable to NEMO-3), instead of 40 mg/cm^2 for the baseline design, in order to accomodate 7 kg of source foil (instead of 5 kg for standard SuperNEMO modules) and to optimize the physical performances of the demonstrator. With 7 kg of ^{82}Se and 2.5 years of data taking, the sensitivity of the demonstrator will be

$$T^{0\nu}_{1/2}(^{82}\mathrm{Se}) > 6.6\ 10^{24}\ \mathrm{years(90\%C.L.)}$$

It is equivalent to the expected sensitivity of GERDA Phase 1 of 3 10^{25} years obtained with ^{76}Ge, assuming equal nuclear matrix elements and using the phase space ratio for these two isotopes. Thus the sensitivity of the SuperNEMO demonstrator to the effective Majorana neutrino mass will be similar to GERDA Phase 1.

The construction of the tracking detector and the γ veto ("calorimeter X-walls" and "calorimeter veto") has been funded by UK and is under progress (UCL, MSSL, Manchester

Univ.), for a delivery in LSM Modane in 2013 and a first underground commissioning. The calorimeter is under the French responsability and must be funded in the next year in order to be installed in 2014 in Modane. 5 kg of enriched ^{82}Se are available. Radiopurity measurement of the source foils is foreseen in 2013. First data of the SuperNEMO demonstrator could be taken in 2015.

Chapitre 3

Germanium detectors

Ultra radiopure Germanium semiconductor diodes have been used historicaly as one of the first detectors for the direct search of $\beta\beta$-decay using source as detector [44]. The ^{76}Ge $\beta\beta$ emitter has unfortunately a relatively low transition energy $Q_{\beta\beta} = 2039$ keV [45]. Therefore germanium experiments are very sensitive to 2.6 Mev γ-rays from ^{208}Tl, to standard cosmogenics [1] like ^{60}Co ($T_{1/2} = 5.272$ years) and ^{68}Ge ($T_{1/2} = 270$ days), and other possible contaminations like ^{42}K recently observed in GERDA. However Germanium detectors are today well established detectors, manufactured in large amount, and excellent energy resolution of few keV at 2 MeV is obtained when diodes are used at Liquid Nitrogen temperature. Also recent development of Broad-Energy Germanium detectors provides superior pulse shape discrimination performances for the reduction of multi-Compton background.

I will first briefly present the results obtained 10 years ago by Heidelberg-Moscou and IGEX experiments. I will then present the new experiment GERDA recently installed in LNGS and I will summarize its preliminary results and possible improvements.

3.1 Heidelberg-Moscou and IGEX experiments

The Heidelberg-Moscou experiment has been running during 13 years from 1990 until 2003 in Gran Sasso Underground Laboratory (LNGS, Italy). The experiment was carried out with 5 high purity germanium detectors with Ge enriched to 86% in ^{76}Ge corresponding to a total of ≈ 10 kg of ^{76}Ge and a total exposure of 71.7 kg year. The energy resolution integrated over 8 years and over the 5 detectors was 3.3 keV at $Q_{\beta\beta} = 2039$ keV.

Pulse shape analysis (PSA) has been developped to suppress the γ's background events which correspond mainly to multi-sites events (MSE) due to multiple Compton interactions. In contrast, $\beta\beta$ events are confined to a few mm region in the detector (corresponding to the track length of the emitted electrons), and consequently appear as single-site events (SSE). The PSA has been tested with an external ^{228}Th source. Standard γ lines are reduced by a factor ≈ 5 (20%) while the known SSE line at 1593 keV, corresponding to double escape peak of the 2615 keV [2], is only reduced by a factor ≈ 2 (62%). The same order of reduction

1. Cosmogenics are long-lived cosmic ray induced isotopes produced during the germanium enrichment process or during the detector fabrication above ground

2. The double escape peak correspond to the peak produced when incident gamma-rays of a certain energy interact with the detector by pair production and deposit all of their energy in the detector except

is found for the γ lines observed in a calibration measurement with a Ra source and in the full energy of the background spectrum.

Part of the collaboration has claimed a 3.3σ indication of $\beta\beta0\nu$ signal after analysing the full statistic and after applying the pusle shape analysis (often called *Klapdor's claim*) [47]. When applying a specific pulse shape analysis using reference signal shapes created by double beta decay, the confidence level becomes 4.2σ. Figure 3.1 shows the published energy spectrum measured with 4 detectors from 1995 until 2003, without PSA, after PSA SSE selection and after specific $\beta\beta$ PSA. We mention also that the four lines 2010, 2016, 2022 and 2053 observed near the $Q_{\beta\beta}$ region, are consistent in intensity with normal known γ-lines. Possible origin of the unknown line at 2030 keV is discussed in [47] and might be understood as originating from electron conversion of the γ-line at 2118 keV originating from ^{214}Bi.

This positive result has not been admitted by the rest of the collaboration. The result indeed depends on the background description and on the reliability of the pulse shape analysis.

One member of the collaboration has recently performed a complete analysis of the origins and descriptions of the background using measurements with sources and MC simulations. The model accounts for the ^{226}Ra, ^{232}Th and ^{60}Co contaminations, the muon induced neutrons and the $\beta\beta2\nu$ decay. The obtained value of the background using this model is (11.8 ± 0.5) counts/keV, corresponding to 0.17 counts/(keV.kg.y), which is higher than the background used in the publication (10.0 ± 0.3 counts/keV). Using this background and without PSA analysis, the peak significant at $Q_{\beta\beta}$ is only 1.3σ [48] and the 68% C.L. interval of $T_{1/2}^{\beta\beta0\nu}(^{76}Ge)$ is $[0.4 - 1.4]$ 10^{25} y with a central value of 2.2 10^{25} y.

At the same time, another germanium experiment, named IGEX [49], has been carried out with three enriched ^{76}Ge detectors of 2 kg each operating in the Canfranc Underground Laboratory (LSC, Spain) with pulse-shape analysis electronics, and three other smaller detectors in Baksan Low-Background Laboratory. A total exposure of 8.87 kg.y has been collected. The level of background was ≈ 0.2 cts/(keV.kg.y). No excess of signal has been observed (see Figure 3.2 correponding to a limit of $T_{1/2}^{\beta\beta0\nu}(^{76}Ge) > 1.57$ 10^{25} years (90% C.L.) [50].

3.2 The GERDA experiment

The GERDA experiment consists of using bare Germanium detectors directly immersed inside Liquid Argon which acts both as cryogenic liquid and shield against external γ's. Morever, the detection of the scintillation light emitted in Argon can be used as an active shield against external γ's.

The cryostat is a stainless steel tank (≈ 25 tons) with internal copper shield (≈ 20 tons) on the inner surface of the cylindrical part of the cryostat to suppress background contribution of the stainless steel. Its dimensions are an inner diameter of 4 m, and a total height of ≈ 4 m. It contains about 100 tons of liquid Argon. The cryostat is installed inside a larger water tank for extra γ and neutrons shield (diam=10m, height=8.5m) (the attenuation

1022 keV, the difference in energy being the result of the escape of both of the 511 keV photons that are produced when the positron from the electron-positron pair is annihilated.

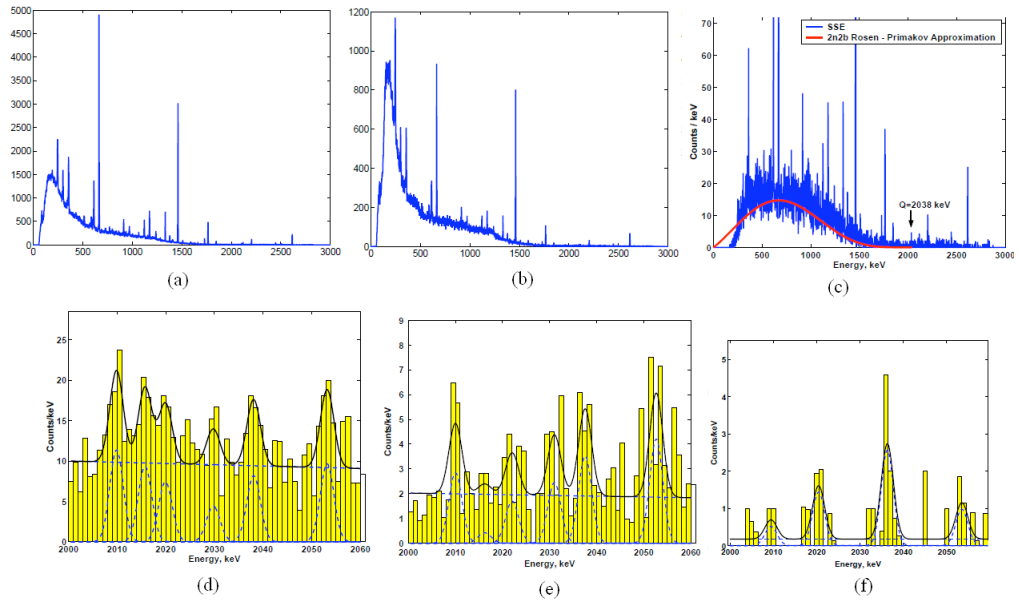

FIGURE 3.1: Energy spectrum measured with 4 detectors from 1995 until 2003 : (a) and (d) without pulse shape analysis (PSA) ; (b) and (e) with PSA Single Site events selection ; (c) and (f) after specific $\beta\beta$ PSA [47].

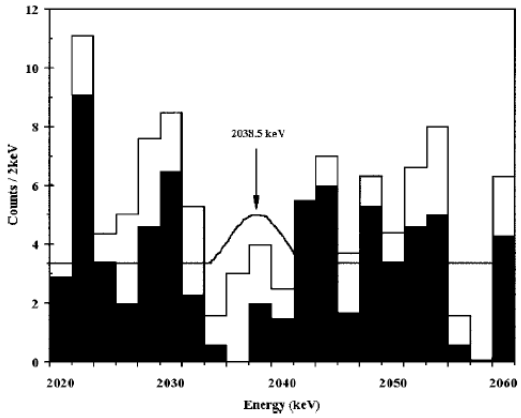

FIGURE 3.2: Energy spectrum measured by the IGEX experiment with 8.87 kg.y of ^{76}Ge exposure. The darkened spectrum results from the application of PSD to $\approx 45\%$ of the total data set. The Gaussian curve represents the 90% C.L. excluded $\beta\beta0\nu$ signal [50].

length of a 2.615 MeV γ in water is ≈ 0.04 cm^{-1}. The Ge detector array is made up of individual detector strings and is situated in the central part of the cryostat. This strings design allows to deploy crystals progressively inside the experiment (see Figures 3.3 and 3.4). Huge efforts and work have been done to ensure a ultra radiopure liquid Argon and selection of radiopure materials.

The background due to external γ's (from the lab or from the cryostat) at $Q_{\beta\beta} =$ 2039 keV has been calculated by a Monte-Carlo simulation and is expected to be at the

level of 10^{-4} cts/(keV.kg.y) [51].

The first phase of data taking (Phase 1) has started in November 2011. The 8 enriched germanium detectors used previously in Heidelberg-Moscow (5) and IGEX (3) experiments and one extra natural germanium crystal have been installed inside the cryostat. It corresponds to about 18 kg of enriched ^{76}Ge. The goal is to reach a level of background of 0.01 cts/(keV.kg.y). It would correspond to a sensitivity of $\approx 3.\ 10^{25}$ y in 1 year of measurement.

In the second phase (Phase 2), new broad-energy germanium (BEGe) detectors will be deployed. These detectors are good candidates to supress multi-site background events via a pulse shape analysis. The detection of the scintillation light from argon as external background veto will be also installed. The goal is to reach a level of background of 0.001 cts/(keV.kg.y). In total 35.5 kg of germanium enriched in the isotope ^{76}Ge at 88% will be used to produce BEGe detectors. Adding the 18 kg of Phase 1, GERDA could measure up to ≈ 50 kg of enriched ^{76}Ge. A level of background of 0.001 cts/(keV.kg.y) in Phase 2 will lead to a sensitivity of $\approx 2.\ 10^{26}$y in 2 years of measurement.

Depending of the achieved background, extra enriched germanium detectors could be produced and installed inside GERDA for a third phase. The goal is to reach a sensitivity of $\approx 10^{27}$y with 100 kg of enriched Ge and 10 years of measurement, with a background lower than 0.001 cts/(keV.kg.y).

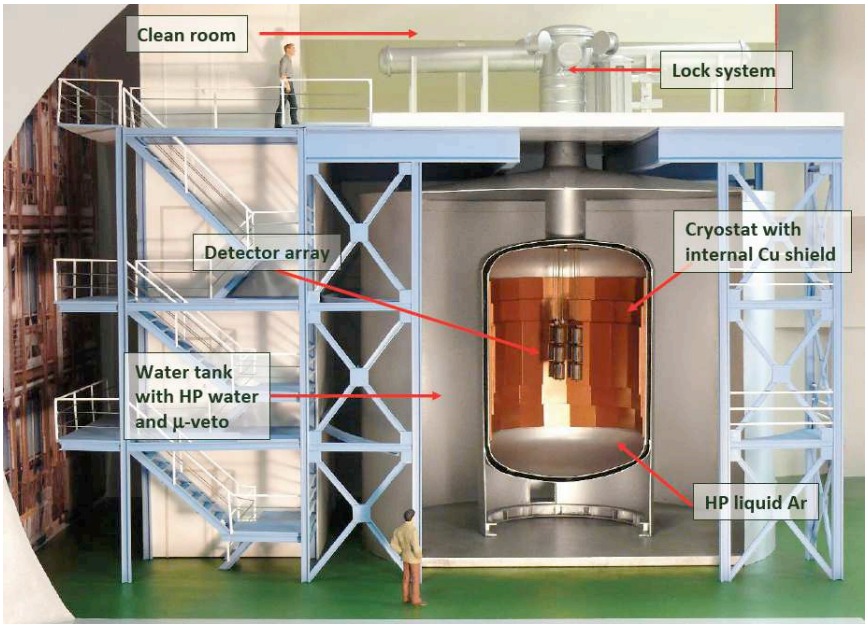

FIGURE 3.3: Schematic view of the GERDA experiment.

3.2.1 Phase 1

The liquid Argon cryostat is running since December 2009 and the operation of the cryostat is very stable from the begining.

A single string supporting three natural germanium detectors has been first installed inside the liquid Argon cryostat for background measurement. And in June 2011, 3 enriched

FIGURE 3.4: Some pictures of the GERDA assembly : the stainless steal cryostat ; the water tank and the clean room above ; inner view of the water tank ; deployment of the first array with three natural germanium detector ; deployment in November 2011 of the 3 arrays with 8 enriched germanium detectors (17.7 kg of ^{76}Ge, GERDA Phase 1).

germanium detectors have been deployed.

The energy resolutions measured with calibration runs are good. Preliminary values are FWHM $\approx$ 4 keV at 2615 keV for natural germanium detectors and 4 to 5 keV for enriched germanium detectors.

However one prominent and unexpected background has been observed : the contribution of ^{42}K, the progeny of ^{42}Ar, about 20 times higher than expected. ^{42}K is mostly a pure β emitter (81.9% with Q_β = 3525 keV and a half-life $T_{1/2}$ = 12.36 h, with a most intense γ-ray at 1524.7 keV (18.1%) (see Figure 3.5). If β and β/γ from the ^{42}K beta decay are emitted close to, or on the surface of the germanium crystals, they can produce events with energies above 1525 keV and ranging into the energy region of interest of $Q_{\beta\beta}$.

The measured counting rate in the line 1525 keV ($\approx$ 1 cts/(kg.day)) was more than one order of magnitude higher than when adopting the 90% upper limit of $^{42}\mathrm{Ar}/^{40}\mathrm{Ar} < 4.3\ 10^{-21}$ given by the DBA experiment assuming a homogeneous distribution in the liquid argon. The reason is that ^{42}K is positively charged after its production. It is then drifted by the moderate electrical fields produced by the germanium diodes bias towards the germanium detectors, which leads to a background enhancement. It has been verified with the LArGe facility that the counting rate of the ^{42}Ar (^{42}K) signal depends on the electric fields in the liquid argon in the vicinity of the germanium detectors. In order to avoid ^{42}K ions to drift towards the germanium crystals, two copper electrostatic shields have been installed inside the cryostat : a small closed cylinder surrounding the detectors array and a larger one, outside it, to protect against the convective liquid argon flow. The reduction of the

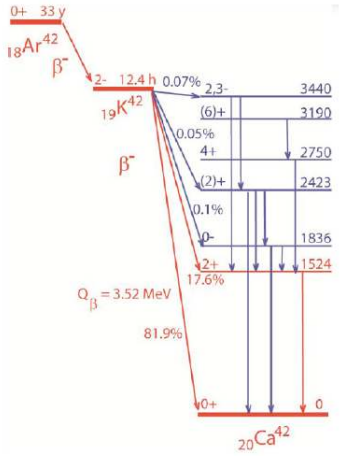

FIGURE 3.5: Deacy diagram of ^{42}Kr.

1525 keV γ line has been successfully observed with the shrouds.

In November 2011 (1.11.11 !), the 8 available enriched germanium detectors and 1 natural germanium have been deployed inside GERDA cryostat in the form of 3 arrays, each surrounded by a mini-shroud. It corresponds to the GERDA Phase 1 data taking. In the $\beta\beta0\nu$ energy region, the preliminary observed level of background is $\approx 1.7\ 10^{-2}$ counts/(keV.kg.y). It corresponds almost to the required level of background of the Phase 1. A single dominant contribution to the background at $Q_{\beta\beta}$ cannot be identified and its understanding is statisticaly limited and will require longer measurements. Possible origins of background are the 2615 keV γ line from ^{208}Tl, the ^{214}Bi γ lines, some residual contribution from ^{42}K, and degraded α's and long-lived cosmogenic isotopes.

3.2.2 Phase 2 : BEGe detectors and LAr scintillating veto

Broad Energy Germanium detectors

When the background events are produced by multiple Compton interaction of γ's, their topology is characterized by multiple interaction sites inside the crystal (MSE). Such events are produced either by external γ's emitted by ^{238}U and ^{232}Th external contamination or by internal γ's emitted by ^{60}Co and ^{68}Ge cosmogenics. Such events are different from $\beta\beta$ events for which the topology is a single site event (SSE). Pulse shape analysis allows to distinguish partially SSE and MSE events. Recently it was realized that commercially available Broad Energy Germanium detectors (BEGe) produced by Canberra Company exhibits superior pulse shape discrimination performances. The crystal is made of p-type HPGe (with point-contact) with the Li-drifted n+ contact (0.5 mm thickness) covering the whole outer surface, including most of the bottom part (see Figure 3.6).

The GERDA collaboration has carried out several tests and measurements of large BEGe detectors in vacuum and then in liquid argon cryostats [53] [54] [55]. Pulse shape analysis has been tested by using ^{228}Th, ^{226}Ra and ^{60}Co source measurements (Figure 3.7). Two types of samples have been used to define the PSA parameters : (i) double escape peak (DEP) at 1519 keV from the 2615 keV ^{208}Tl γ-ray has been used as a substitute for $\beta\beta$ events, since

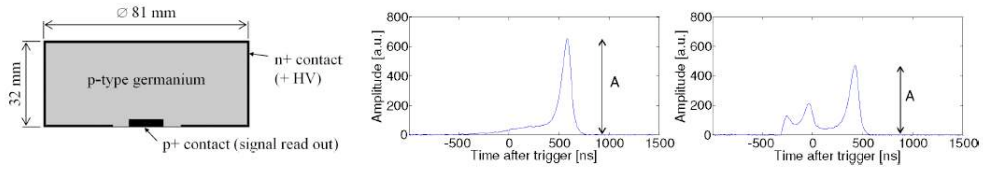

FIGURE 3.6: (Left) Schematic view of a point-contact Broad Energy Germanium (BEGe); (Center) Single Site Event ($\beta\beta0\nu$ topology); (Right) Multi Site Event (Multi Compton background topology)

it corresponds to pure e^+e^- pairs produced in a single site (SSE); (ii) single escape peak (SEP, where only one of the two 511 keV γ annihilation escapes, the second deposits its full energy) and full energy absorption (FEA, where the initial γ deposits all its energy) have been used as representative samples with dominant MSE events. After applying the PSA to the energy spectrum obtained with the source measurements, it has been demonstrated that the DEP events at 1592 keV are accepted in 89% of the case (Monte Carlo simulation confirmed the 90% efficiency to keep $\beta\beta0\nu$ events) while the Compton continuum events in the ^{76}Ge $Q_{\beta\beta}$ energy region are supressed by factors ≈ 100 for ^{60}Co, ≈ 5 for ^{226}Ra (^{214}Bi) and ≈ 2.5 for ^{228}Th (^{208}Tl).

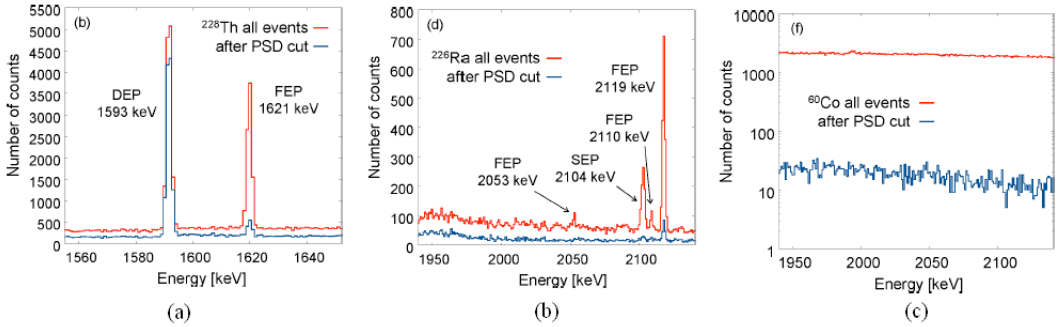

FIGURE 3.7: Result of the pulse shape discrimination with BEGe detectors, using ^{228}Th, ^{226}Ra and ^{60}Co sources. The double escape peak (DEP) events at 1592 keV are accepted in 89% of the case, while the Compton continuum events in the $Q_{\beta\beta}$ energy region are supressed by a factor 2.5 (^{228}Th) up to ≈ 100 (^{60}Co).

Morever, it has been also observed that BEGe detectors are very stable, with no charge collection losses, and an excellent energy resolution of ≈ 2 keV, achieved with two different large detectors (630 and 900 g). It is almost a factor of two better than germanium detectors used in previous experiments or in GERDA Phase 1.

BEGe detectors are thus excellent candidates for the second phase of GERDA. The collaboration has decided to use the 36.5 kg available enriched germanium (in form of ingots) to produce ≈ 20 BEGe detectors in Canberra (in Oak Ridge, TN, US) for a total mass of enriched Ge ≈ 20 kg. A second production campaign is planned with the 13 kg rest of germanium (to be reprocessed chemicaly)

Liquid argon scintillating veto

A liquid argon scintillating detector, called LArGe, has been developped by the GERDA collaboration and installed in LNGS, in order to study the efficiency of the liquid argon scintillation to tag an external γ's (active LAr shield). The scintillation light yield ≈ 40 photons/keV for ultra pure Argon. In LArGe, the number of collected photoelectrons is only 0.05 γe/keV. BEGe detector has been installed inside the LArGe cryostat and background suppression measurements have been carried out using external and internal ^{226}Ra (^{214}Bi) and ^{228}Th (^{208}Tl) sources.

Table 3.1 summarizes the supression factors of the continuum Compton background, observed in the $\beta\beta0\nu$ energy region (2004-2074 keV) using the LAr scintillating veto and the pulse shape discrimination. The LAr scintillation veto is very efficient for ^{208}Tl (^{228}Th) but relatively less for ^{214}Bi (^{226}Ra). This is because, the most intense γ-ray emitted by ^{214}Bi, above $Q_{\beta\beta}$, is the 2204 keV (4.86% branching ratio), corresponding to a maximum deposited energy in argon of 130 to 200 keV in order to be able to deposit 2004 to 2074 keV in the BEGe detector. With 0.05 γe/keV, it corresponds to an average of 6 to 10 photoelectrons only. However, in the case of ^{208}Tl, the excess energy deposited in liquid argon by the 2615 keV γ-ray is 610-680 keV, high enough to produced a significantly large number of photoelectrons well above the detection threshold.

Based on the successful background suppression achieved with LArGe and the current background counting rate in GERDA, the collaboration decided to prepare a design to instrument the LAr in Gerda. Different options are currently under development : scintillation readout using photomultiplier tubes (PMT's), scintillating and wave length shifting (WLS), fibers coupled to SiPMs, and large-area SiPMs or APDs.

3.2.3 Comments

I would like to emphasize that the pulse shape discrimination and the LAr scintillation veto are only efficient to reduce external γ background. However, background produced by β-decay or degraded α from potential surface contaminations of the detectors (like β from ^{42}K), or in the vicinity of the germanium crystals, cannot be tagged by the LAr veto and are not rejected by the pulse shape discrimination since they are single site events. The thick dead layers of Li (0.5 mm thickness) on the surface of the BEGe detectors contribute to protect from α's and β's provided that lithium layers are radiopure.

Source	Position	Rejection factor		
		LAr veto	PSD	Total
^{226}Ra	Internal	4.6	4.1	45
	External	3.2	4.4	18
^{228}Th	Internal	1175 ± 200	2.4	5000 ± 1500
	External	25	2.8	130 ± 15

TABLE 3.1: Background supression factors observed in the $\beta\beta0\nu$ energy region (2004-2074 keV) obtained using, either the LAr scintillating veto, the pulse shape discrimination and by combining both.

3.3 The MAJORANA experiment

Another germanium experiment, named MAJORANA experiment, is under development in the USA. The construction of the MAJORANA demonstrator has been funded by DOE and NSF. In contrast with GERDA, the germanium detectors are runned in vacuum Nitrogen cryostat with standard low-background passive lead and copper shield and an active muon veto (see Figure 3.8). 40 kg of germanium detectors will be measured with the demonstrator : 20 kg of 86% enriched Ge and 20 kg of natural germanium crystals. Two independent cryostats will be constructed using ultra-clean, electroformed copper (the electroforming will be performed underground). As GERDA, p-type and point-contact detectors (BEGe detectors) will be used in order to obtain a good pulse shape discrimination against multi-site events produced by external γ's. The detectors will be also deployed in strings. Each cryostat contains 35 detectors assembled in 7 strings (detectors are relatively smaller than GERDA).

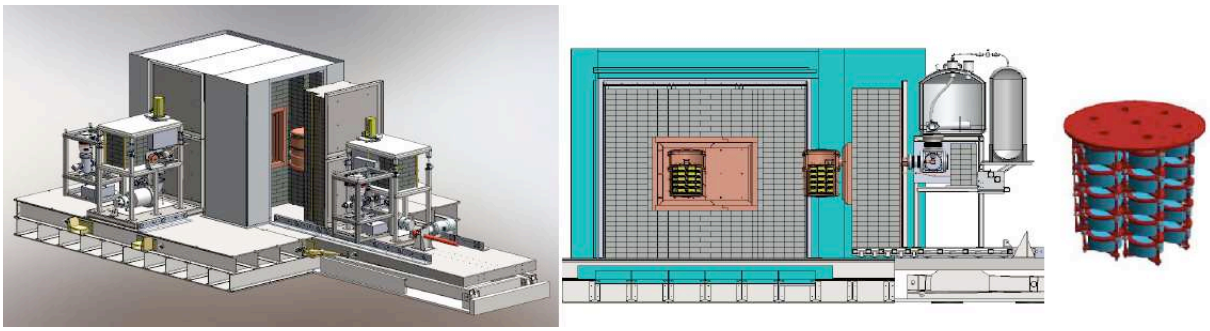

FIGURE 3.8: Schematic view of the LArGe Facility and some pictures.

The experiment will be located in the so-called Davis Campus in the Sanford Underground Laboratory (SUL, 4850 feet deep) in the Homestake mine (South Dakota, USA). The outfitting is underway and the lab will be ready in spring 2012. The 20 kg enriched Ge have been delivered and first batch of BEGe detectors with natural germanium are available.

The plan is first to test 2 or 3 strings (10-15 detectors) in a prototype cryostat (with some non-electroformed components) in summer 2012. Then it is planed to run the first electroformed cryostat (with 3 strings natural Ge and 4 strings of enriched Ge) in spring 2013 in SUL and the second cryostat (up to 7 strings ^{enr}Ge) in fall 2014.

Since there is no possible active shield (no LAr veto as GERDA), the main issue is to demonstrate the capability to develop an ultra radiopure cryostat and an ultra radiopure inner shield in order to reach the target background of $10^{-2} - 10^{-3}$ counts/(keV.kg.y).

3.4 Towards the ton scale : which limitations ?

B. Majorovits has done a very interesting study [56] of the possible limitations of the next generation of experiments measuring, not anymore $\approx 100\ kg$ but a ton of germanium, with a required background of $\approx 10^{-5}$ counts/(kg.y.keV) in the $\beta\beta0\nu$ energy region. Three limiting origins of background have been listed : the crystal metalization ("the good"), the Pb on surfaces ("the bad") and the Ge cosmogenic isotope ("the ugly").

1. The metalization of the surface of germanium detectors is in general done with aluminum. The contaminations introduced by this aluminium in cosmogenics ^{26}Al (β^+-decay, $Q_\beta = 4$ MeV, $T_{1/2} = 7.4\ 10^5$ years) and ^{22}Na ($Q_\beta = 2.84$ MeV, $T_{1/2} = 2.6$ years) or in natural radioactivity ^{226}Ra and ^{228}Th, are a possible source of background. Maximal radio-impurities of less than 3.3 mBq/kg, 0.6 mBq/kg, 0.2 mBq/kg and 0.2 mBq/kg are required in order not to exceed individual background contributions of larger than 10^{-6} counts/(kg.y.keV) from ^{26}Al, ^{22}Na, ^{226}Ra and ^{228}Th, respectively. Several sample of aluminium have been measured with ultra low background HPGe detectors with this required sensitivity and it has been verified that one sample was pure enough (< 0.15, < 0.26, < 0.28 and < 0.58 mBq/kg in ^{26}Al, ^{22}Na, ^{226}Ra and ^{228}Th, respectively) [57].
2. The usual contamination in ^{210}Pb, observed on the crystal surface produces a limiting background from degraded α's. To illustrate, 100 of ^{210}Pb nuclei per m^2 would produce $\approx 10^{-5}$ counts/(kg.y.keV) in the ^{76}Ge $\beta\beta0\nu$ energy region. Experimental tests of etching of germanium crystals have been recently performed with Canberra in order to measure the removal and deposition efficiencies of ^{210}Pb. Reduction factors of 1000 or higher have been obtained. But deposition by non pure solvent has been also observed. It means that ^{210}Pb screening methods and clean solvents ($< 10\mu$Bq/m^3) are needed.
3. The most dangereous background is the bulk contamination of the germanium crystals in ^{68}Ge cosmogenic isotope ($T_{1/2} = 3.84$ years) [58]. About 0.5 ^{68}Ge nucleus per kg would produce 10^{-5} counts/(kg.y.keV) in the ^{76}Ge $\beta\beta0\nu$ energy region. The depletion of ^{68}Ge in enriched ^{76}Ge is not known and measurements for ^{70}Ge depletion are inconsistents (from $2\ 10^{-2}$ to $7\ 10^{-5}$). It means that next gereneration experiments require R&D on deenrichment of ^{68}Ge with a deenrichment factor of at least $2\ 10^{-5}$ to get less than 0.5 ^{68}Ge nucleus per kg.

To conclude, I would like to add another possible limitation, which illustrates the difficulty and the danger to scale a double beta experiment to the ton scale. The Pb(n,γ's) reactions[3] can produce the 2041 keV γ-rays (only 2 keV above $Q_{\beta\beta} = 2039$ keV) and the 3062 keV γ-rays [59]. The former is also a dangerous background for ^{76}Ge experiments, because the double escape peak energy ($3062 - 2 \times 511 = 2040$ keV) coincides with the $Q_{\beta\beta}$ value. The measured rate of this transition is too small to explain the Klapdor's claim. This background is dangerous for the MAJORANA experiment, which uses traditional lead shield, but it might be significantly reduced using depth and/or an inner layer of Cu within the shield.

With this example, we see that very rare or even unknown γ-rays may appear at the $Q_{\beta\beta}$ value and dedicated extra neutrons capture measurements are probably needed.

3. neutron capture on Pb leading to the emission of γ-rays

Chapitre 4

Bolometer detectors

The use of bolometers for $\beta\beta0\nu$-decay searches was suggested by Fiorini and Niinikoski [62] and applied first by the Milano group in the MIBETA experiment [61] using natural $Te0_2$ crystals as bolometers.

The main advantage to use $Te0_2$ crystal is that the natural abundance of ^{130}Te (the $\beta\beta$ emitter) in tellerium is high, about 34 %. However its $Q_{\beta\beta} = 2530.3 \pm 2.0$ keV [63] is lower than the 2615 keV γ ray from ^{208}Tl. Experiments using TeO_2 crystals are therefore sensitive to Compton electron background due to ^{232}Th contamination.

In order to avoid to enrich $\beta\beta$ isotopes, the Milano group decided in the 90's to continue using natural $Te0_2$ crystals and to developp a larger detector, CUORICINO, which has been running from 2003 until 2008 in Gran Sasso, and measured about 10 kg of ^{130}Te. It is a pilot detector for a larger experiment, CUORE, currently in construction, which will measure up to 200 kg of ^{130}Te.

I will first detail the CUORICINO experiment and I will present its main results and limitations. Then I will present the current development of the large CUORE experiment. Finally, I will present the current developments and projects of scintillating bolometers. I will detail it because I think that it is one of the most promising technique for the $\beta\beta0\nu$ search.

4.1 The CUORICINO experiment

4.1.1 Description of the detector

CUORICINO is an array of 62 TeO_2 crystals, a total mass of crystals of 40.7 kg, corresponding to a total mass of 11.64 kg for enriched ^{130}Te isotope. As shown in Figure 4.1, the CUORICINO detector is a tower composed of 11 layers of 4 crystals, each one with a dimension $5 \times 5 \times 5$ cm^3 and a mass of 790 g, and two layers of 9 smaller crystals, $3 \times 3 \times 6$ cm^3 and 330 g. Two small crystals were enriched in ^{130}Te at 75 % and two other ones in ^{128}Te at 82.3 %. All crystals were grown with pre-tested low radioactivity material by the Shanghai Institute of Ceramics. They were lapped with specially selected low contamination polishing compound. The mechanical structure was made of oxygen-free high-conductivity copper and Teflon. A sketch of the tower assembly inside the low radioactive shield is shown in Figure 4.1. The CUORICINO cryostat operated at a temperature of about 8 mK. Thermal pulses were measured with NTD Ge thermistors. The average

FWHM energy resolutions at $Q_{\beta\beta} = 2530$ keV are 7 and 9 keV, for the $5 \times 5 \times 5$ cm^3 and $3 \times 3 \times 6$ cm^3 crystals, respectively. The spread in the FWHM is about 2 keV in both case.

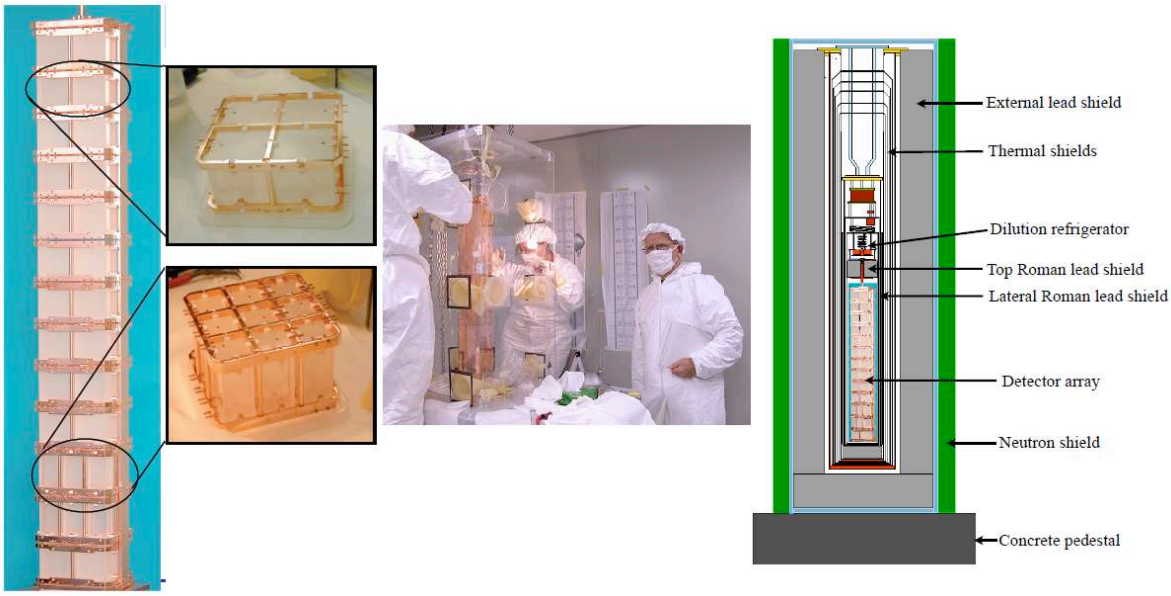

FIGURE 4.1: Pictures of the CUORICINO tower, and layout of its assembly inside the cryostat and shields.

The excellent energy resolution has a sense only if the energy calibration of the bolometers is stable and if any drift is well controlled. The gain of each bolometer is stabilized by means of a Si resistor, attached to each bolometer that acts as a heater. Heat pulses are periodically (every 300 s) supplied by a calibrated ultrastable pulser [64]. Any variation in the voltage amplitude recorded from the heater pulses indicates that the gain of that bolometer has changed. The heater pulses are used to measure (and later corrected offline) for the gain drifts.

4.1.2 $\beta\beta0\nu$ result and background study

The total exposure obtained with CUORICINO was 19.75 kg.y of ^{130}Te. The $\beta\beta0\nu$ detection efficiency is 0.83%. Figure 4.2 shows the energy spectrum around the $Q_{\beta\beta}$ value. No excess of events has been observed at $Q_{\beta\beta}$, resultingg to a lower limit on the $\beta\beta0\nu$-decay half-life of [65] :

$$T_{1/2}(\beta\beta0\nu) > 2.8\ 10^{24}\ \text{y (90\% C.L.)}$$

The observed peak at 2506 keV corresponds to the pile-up of the two external γ-rays (1173.2 and 1332.5 keV) emitted by external ^{60}Co. It gives a posteriori a good cross-check of the energy calibration and the energy resolution.

We also mention that the searches for both 0ν and 2ν double-beta decay to the first excited 0^+ state in ^{130}Xe were performed recently by studying different coincidence scenarios [66]. No evidence for a signal was found. The resul-

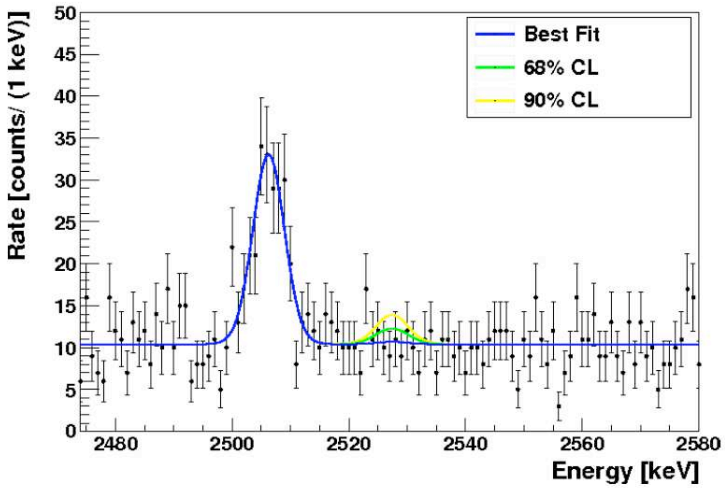

FIGURE 4.2: Energy spectrum in the $\beta\beta0\nu$ region [65]

ting lower limits on the half-lives are $T^{2\nu}_{1/2}(^{130}\text{Te} \rightarrow ^{130}\text{Xe}^*) > 1.3\ 10^{23}$ y (90% C.L.) and $T^{0\nu}_{1/2}(^{130}\text{Te} \rightarrow ^{130}\text{Xe}^*) > 9.4\ 10^{23}$ y (90% C.L.)

The level of background in the $Q_{\beta\beta}$ region is 0.16 counts/(keV.kg.yr). Taking into account the energy FWHM resolution of 7 keV at $Q_{\beta\beta}$, it corresponds to a level of background in the $\beta\beta0\nu$ region of interest of 1.12 counts/(FWHM.kg.yr).

The origin of the observed background has been studied carefully by the collaboration in order to define a strategy to reduce it for a larger detector like CUORE. Figure 4.3 shows the energy spectrum in the full energy range. The background is dominated by γ's below the 2615 keV γ ray line from ^{208}Tl, while α's are the main origin of background above 2615 keV. In the $\beta\beta0\nu$ energy region, both γ's and degraded α's contribute to the observed background. The α-particles are produced from surface contaminations in ^{238}U, ^{232}Th and ^{210}Pb (from Radon deposition during the construction) on the surfaces of the crystals or the surface of the copper holders facing the crystals. The α-particles can mimic a $\beta\beta0\nu$ event if they deposit a part of their energy elsewhere and about 2530 keV ($Q_{\beta\beta}$-value) in the crystal.

The measurement of the different origins of the background was done by analysing both the coincidence and anti-coincidence spectra. Final spectrum and fitted Monte-Carlo background spectrum in the $\beta\beta0\nu$ region is shown in Figure 4.3. The conclusion of this analysis was the identification of three main contributions of background in the $\beta\beta0\nu$ energy region :

- $30 \pm 10\%$ of the background is due to multi-Compton events due to the 2615 keV gamma ray from the decay chain of ^{232}Th from the contamination of the cryostat shields ;
- $10 \pm 5\%$ is due to surface contamination of the TeO_2 crystals with ^{238}U and ^{232}Th (primarily degraded alphas from these chains) ;
- $50 \pm 20\%$ is ascribed to similar surface contamination of inert materials surrounding the crystals, most likely copper.

The level of backrgound due to degraded α's particles from the crystal and copper surfaces is

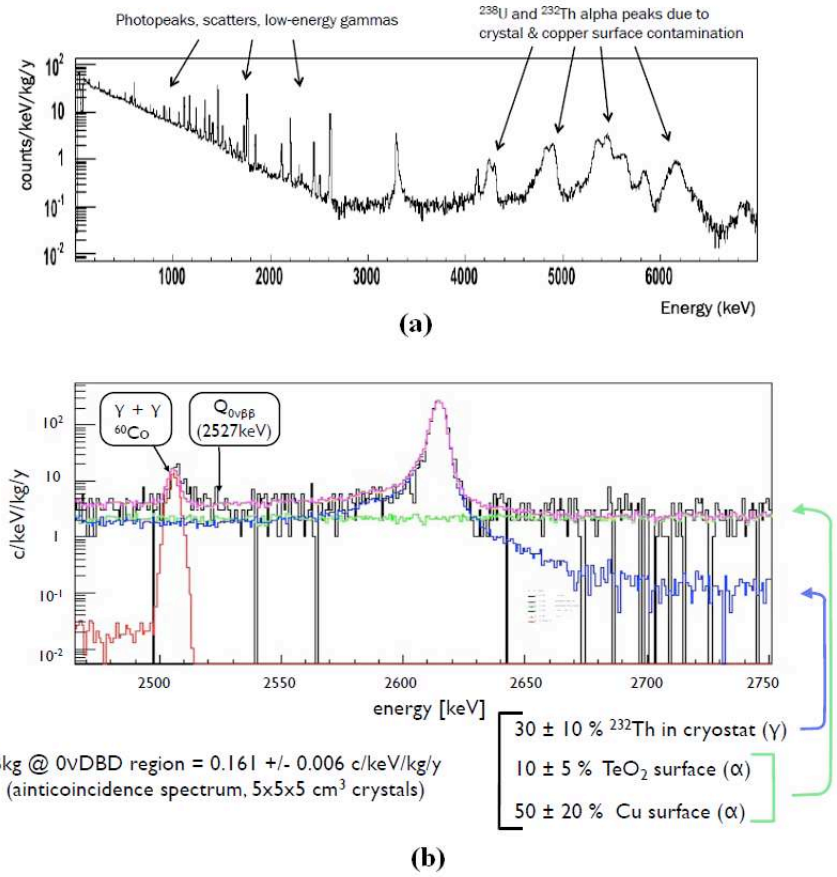

FIGURE 4.3: (a) Energy spectrum in the full energy range; (b) Energy spectrum in the $\beta\beta0\nu$ region and fitted Monte-Carlo background model.

measured in the 2.7 to 3.2 MeV energy window and is 0.104 ± 0.002 counts/(keV.kg.yr) [68]. The γ of 2615 keV from the ^{232}Th contamination of the cryostat increases the backrgound level in the $\beta\beta0\nu$ region to 0.16 counts/(keV.kg.yr).

The contribution of cosmic ray muons to the CUORICINO background has been recently measured [67]. From these measurements, an upper limit of 0.0021 counts/(keV.kg.yr) (95% C.L.) was obtained on the cosmic ray-induced background in the $\beta\beta0\nu$ energy region.

We mention that the response of a TeO_2 bolometer to α particles has been investigated using a TeO_2 crystal containing ^{147}Sm (α emitter) [69]. Signal pulse shape shows no difference between α and β/γ particles. Therefore no pulse shape analysis can be applied to recognize an *alpha* interaction.

4.2 The CUORE experiment

4.2.1 Description of the detector

CUORE will consist of an array of 988 TeO_2 cubic detectors, similar to the $5 \times 5 \times 5$ cm^3 Cuoricino crystals described above. The total mass of the crystals will be 741 kg,

corresponding to 206 kg of ^{130}Te. The detectors will be arranged in 19 individual towers and operated at 10 mK in the Gran Sasso underground laboratory in a new large cryostat with improved external shield (see Figure 4.4) The expected energy resolution FWHM of the CUORE detectors is 5 keV at the $Q_{\beta\beta}$ transition energy. This resolution represents an improvement over that seen in Cuoricino and has already been achieved in tests performed in the CUORE R&D facility at LNGS with first delivered crystals [72]. CUORE is expected to accumulate data for about 5 years of total live time. The experiment is currently being constructed and first data-taking is scheduled for 2014. The construction of the new large low radioactive cryostat is a delicate and long task and inner vessels should be produced in 2012.

The CUORE collaboration will first operate a single CUORE-like tower in the former Cuoricino cryostat. This configuration, named CUORE-0, will validate the assembly procedure and the readiness of the background reduction measures. The assembly of CUORE-0 is now completed (see Figure 4.5) and data collection will start in 2012 for two years of running.

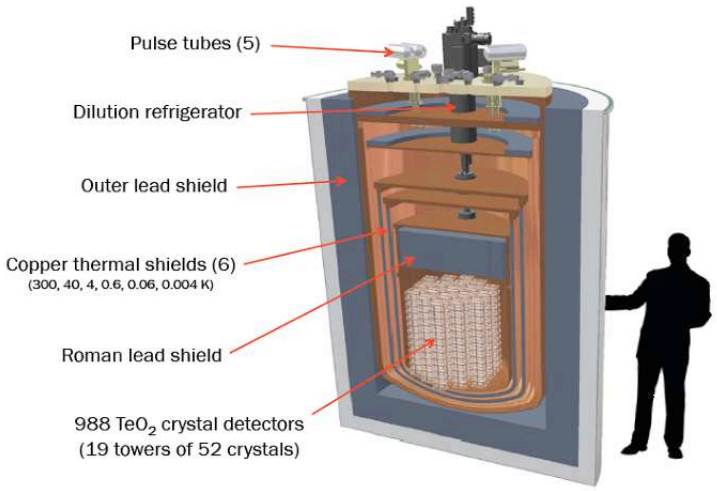

FIGURE 4.4: Schematic view of the CUORE experiment.

4.2.2 Background reduction

On the basis of the CUORICINO background analysis, the R&D for CUORE has pursued two major complementary issues : the reduction of surface contamination of crystals and copper in order to reduce the contribution of degraded α's particles, and the creation of an experimental setup in which potential background contributions are minimized by the selection of extremely radio-pure construction materials and the use of highly efficient shields, in order to reduce the contribution of external 2615 keV γ's.

CUORE crystals are produced following a controlled protocol [72]. Several surface-treatment techniques were developed to clean the surface of crystals and copper [71]. Since the required surface contamination levels are extremely low, of the order of 10 to 100 μBq/m^2, undetectable with any standard technique used in surface analysis, the surface radiopurity of the crystals have been measured in the CUORICINO cryostat by assembling

FIGURE 4.5: Pictures of the CUORE-0 tower during its assembly in LNGS.

them as an array of 3×4 crystals (Three Tower Test, TTT). Results show that the best results were obtained either with passive chemical cleaning and polyethylen barrier, or with plasma cleaning. The level of background measured in the anticoincidence spectrum in the 2.7 to 3.9 MeV energy window (contribution of degraded α's) is statisticaly limited and is about 0.05 counts/(keV.kg.yr) corresponding to a reduction factor of about 2 compared to CUORICINO. If we extrapolate CUORICINO background analysis result, half of this background is dominated by copper surface contamination.

The bulk contamination was measured (with Cryogenic validation runs CCVR) to be lower than 5.3 10^{-14} g/g for ^{238}U (0.67 μBq/kg) and 2.1 10^{-13} g/g for ^{232}Th (0.84 μBq/kg) (90% C.L.) [68]. These values are well below the concentration limits of 3 10^{-13} g/g in ^{238}U and ^{232}Th, requested for TeO_2 crystals to be used in CUORE experiment.

The final background budget expected in the $\beta\beta0\nu$ region is sumarized in Table 4.1, both for CUORE-0 and CUORE [73]. The background is dominated by degraded α's from surface contaminations of the copper facing the crystals, or by external γ's from cryostat or shield in the case of CUORE-0 (which will be installed inside the CUORICINO cryostat). A higher radiopurity cryostat facility and a higher shield efficiency is expected for CUORE. The CUORE collaboration expects to reach a level of background of 0.01 cts/(keV.kg.yr). Background suppression could be improved by installing suface sensitive bolometers (SSB, see next section). But only first data collection in 2014 will tell us the real level of background!

4.2.3 Expected sensitivity for CUORE-0 and CUORE

An optimistic scenario is to consider that the irreducible background for CUORE-0 comes from the 2615 keV ^{208}Tl line due to ^{232}Th contaminations in the cryostat, in the case that all other background sources (i.e., surface contaminations) have been rendered negligible. This would imply a lower limit of 0.05 cts/(keV.kg.yr) on the expected background in CUORE-0. The expected sensitivity is $T_{1/2}(\beta\beta0\nu) > 6\ 10^{24}$ yr (90% C.L.) after 2 years of measurement.

Similarly, an upper limit of 0.11 cts/(keV.kg.yr) follows from scaling the Cuoricino

Bkg source	CUORE-0	CUORE	Source of data
External (μ+n+γ)	$< 1.0\ 10^{-2}$	$< 2.0\ 10^{-3}$	measured flux + MC
γ from cryostat + shield	0.05	$< 1.0\ 10^{-3}$	material selection + cuoricino
Cu det. holder (bulk)	$< 2.0\ 10^{-3}$	$< 2.0\ 10^{-3}$	HPGe + NAA + MC
Cu det. holder (surface)	$\leq 4.0\ 10^{-2}$	$\leq 2.5\ 10^{-2}$	TTT + MC
TeO_2 (bulk)	$< 4.0\ 10^{-4}$	$< 1.1\ 10^{-4}$	CCVR
TeO_2 (surface)	$< 7.3\ 10^{-3}$	$< 5.5\ 10^{-3}$	CCVR + MC

TABLE 4.1: Background budget in counts/(keV kg yr) expected in the $\beta\beta0\nu$ region, both for CUORE-0 and CUORE.

background in the conservative case, described above, of a factor of 2 improvement in crystal and copper contaminations. The expected sensitivity becomes $T_{1/2}(\beta\beta0\nu) > 4\ 10^{24}$ yr (90% C.L.) after 2 years of measurement.

The significance level at which CUORE-0 can observe a signal corresponding to the ^{76}Ge claim, assuming the best expected background of 0.05 cts/(kev.kg.y), is shown in Figure 4.6.

For CUORE, with 19 complete towers, an energy resolution of 5 keV, and a level of backrgound of 0.01 cts/(keV.kg.yr), the expected sensitivity is $T_{1/2}(\beta\beta0\nu) > 10^{26}$ yr (90% C.L.) after 5 years of measurement.

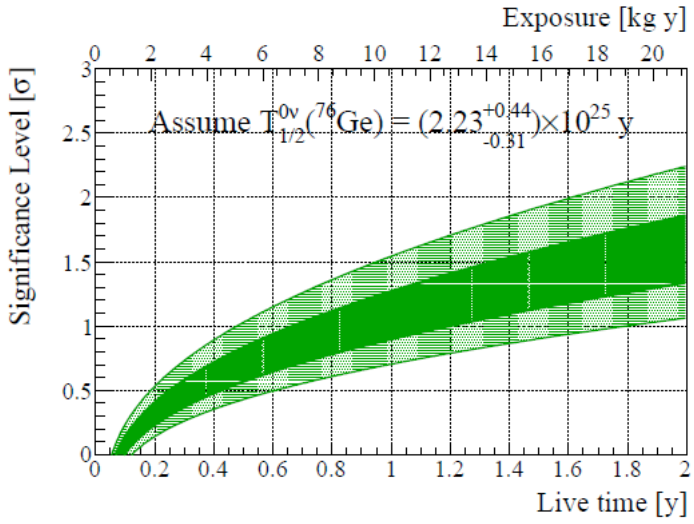

FIGURE 4.6: Significance level at which CUORE-0 can observe a signal corresponding to the ^{76}Ge claim, assuming the best expected background of 0.05 cts/(kev.kg.y). The inner band assumes the best-fit value of the ^{76}Ge claim, and its width arises from the 1σ range of QRPA-F NMEs calculated in [74]. The outer band accounts for the 1σ uncertainty on the ^{76}Ge claim in addition to the range of NMEs.

4.2.4 Surface-sensitive bolometers

In order to reduce the background due to degraded α's from the surface of the copper facing the crystals, it was proposed to develop a surface sensitive bolometer (SSB) [75]. The basic idea of the SSB is to surround the TeO_2 crystal (main absorber) with thin auxiliary absorbers which function as active shields and are operated as bolometers. The main absorber and the shields are thermally connected, and a near 4π coverage from external charged particles can be achieved. Charged particles from materials outside the SSB, such as α-particles, will be stopped and tagged by one of the active shields (surface events). They release part of their energy in the shield, but raise the temperature of all the detector elements as they are, in fact, all thermally connected. Because of the small heat capacity of the shield due to its small mass, the signal read by its thermistor will have a higher amplitude and faster rise time than the signal read by the thermistor attached to the main absorber. If, on the other hand, an energy deposition occurs inside the main absorber (bulk event), all of the thermistors will read pulses with comparable amplitudes and rise times. It is therefore possible to separate bulk and surface events by comparing amplitude and shape of pulses among the diferent thermistors. No degradation in energy resolution of the main absorber is expected since the device is still operating in the mode where phonon thermalization is nearly complete. Thus, the whole system does not act as an usual veto but acts as a pulse shaper.

Recently three prototype detectors have been tested [75]. The surface event rejection capability has been clearly demonstrated and preliminary results show that it is possible to detect energy depositions that occurred on the shields without separate readout channels for them. However, a real reduction of background without adding new contaminations from the SSB has still to be demonstrated with long background runs.

4.3 Scintillating bolometers

The two dominant sources of background in CUORE (using TeO_2 crystals) are external 2615 keV γ's from possible ^{232}Th (^{208}Tl) contamination inside the cryostat or the shield, and degraded α's from the surface of the copper facing the crystals :

- If the crystal is based on a double beta isotope with a $Q_{\beta\beta}$ transition value above 2615 keV, the external γ background is strongly suppressed.
- In the case of a scintillating bolometers, based on scintillating crystals, the simultaneous detection of heat and scintillation light allows the supresssion of the background due to degraded α particles, thanks to the different scintillation quenching factor between α and β/γ,

Thus scintillating bolometers appear to be a very promising technique to suppress the background. Its operating principle is illustrated in Figure 4.7.

The first light/heat measurement with a background discrimination for $\beta\beta0\nu$ DBD searches was performed by the Milano group in 1992 [76] but was not pursued due to the difficulties of running such a light detector at ultra low temperatures (10 mK). Scintillating bolometers were then developed [77] and optimized for Dark Matter searches [78][79]. Starting from that work, a long R&D program, coordinated by S. Pirro and mainly funded by ILIAS-IDEA (European FP7 program), investigated several scintillating bolometer candidates for a double beta experiment. The crystals are $CdWO_4$ (^{116}Cd, $Q_{\beta\beta}$ = 2809 keV),

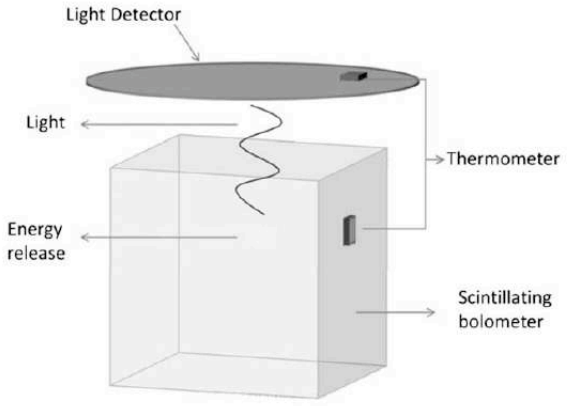

FIGURE 4.7: Operating principle of scintillating bolometers. The release of energy inside a scintillating crystal follows two channels : light production and thermal excitation. The heat is read out by a temperature sensor (NTD) glued on the primary crystal while the light is read by a second thin crystal (light detector) where it is completely converted into heat.

ZnSe (^{82}Se, $Q_{\beta\beta} = 2995$ keV), $ZnMoO_4$, $PbMoO_4$ or $MgMoO_4$ (^{100}Mo, $Q_{\beta\beta} = 3034$ keV) and $CaMoO_4$ (^{100}Mo and ^{48}Ca, $Q_{\beta\beta} = 4271$ keV).

Let's mention that a TeO_2 crystal cannot be operated as scintillating bolometer due to its extremely low light yield measured with pure and also doped samples [80].

The different experimental studies have demonstrated the feasibility of scintillating bolometers to discriminate α to β/γ events. Morever these studies have shown that a discrimination based only on the pulse shape analysis is achievable for some of the tested crystals. This feature would open the possibility of realizing a bolometric experiment that can discriminate among different particles, without the need of a light detector coupled to each bolometer.

I will summarize here the main results obtained with the different crystals and I will discuss the advantages and limitation of each one.

4.3.1 ^{116}Cd : $CdWO_4$ crystal

$CdWO_4$ is a well established scintillator crystal with a large light yield. It was the first crystal studied for $\beta\beta0\nu$ search. We mention that four enriched $^{116}CdWO_4$ crystals (total mass of 330 g of ^{116}Cd) were already used in the 90's, as standard scintillator at room temperature for the search of $\beta\beta0\nu$-decay in the Solotvina Underground Laboratory [81].

Several tests with various $CdWO_4$ crystals as scintillating bolometers were carried out in the last few years [82] [83]. We show in Figure 4.8 the result of the longest background measurement (1066 hours) performed with a large $3\times3\times6$ cm^3 426 g crystal. It was operated in a cryostat in Gran Sasso with a dedicated Roman lead and neutron shield in order to reduce as far as possible the environmental background. This plot shows how it is possible to separate very well the background due to α particles from the β/γ region. In particular it should be noticed that α continuum is completely removed thanks to the combined measurement of heat and scintillation. In the region above the 2615 keV line, β/γ events have not been observed, demonstrating the performance of this technique.

Since degraded α's are totaly suppressed, the residual possible background is either a ^{238}U and ^{232}Th bulk contamination inside the crystal or external γ's :

- ^{238}U and ^{232}Th bulk contamination : The only high energy $\beta+\gamma$ decays above 2.6 MeV present in the ^{238}U and ^{232}Th decay chain are shown in Figure 2.11. The $\beta+\gamma$ decays are always followed (or preceded) by an α emission. In the case of ^{238}U decay chain, the half life of the delay α-decay of ^{214}Po (164 μs) is shorter than the time response of the bolometer (of the order of the ms). Thus the $\beta+\gamma$ and α signals are piled-up and can be easily rejected (see Figure 4.8). In the case of ^{232}Th, rejection is more delicate. Indeed, the ^{208}Tl $\beta+\gamma$ decay is preceded by the α emission of ^{212}Bi with a half life of 3.05 mn. This pre-α can be used to reject the background event in the condition that internal contamination is not too large in order to avoid dead time.
- External γ background : The contribution of extremely rare high-energy γ-rays from ^{214}Bi in the $\beta\beta0\nu$ energy region for ^{116}Cd is negligible. The main source of γ background due to external contamination is induced by the ^{208}Tl decay. In fact, if contaminations are sufficiently close to the detectors, the probability of spurious counts between 2615 keV and 3198 keV, due to coincidences betwen 2615 keV and 583 keV gamma emitted in the ^{208}Tl decay, may not be negligible. Assuming the limit of contamination level measured in the copper structure surrounding the detector in CUORICINO, a GEANT4 simulation gives a limit of 10^{-4} counts/(keV.kg.yr) in the $\beta\beta0\nu$ energy region due to this main contribution.

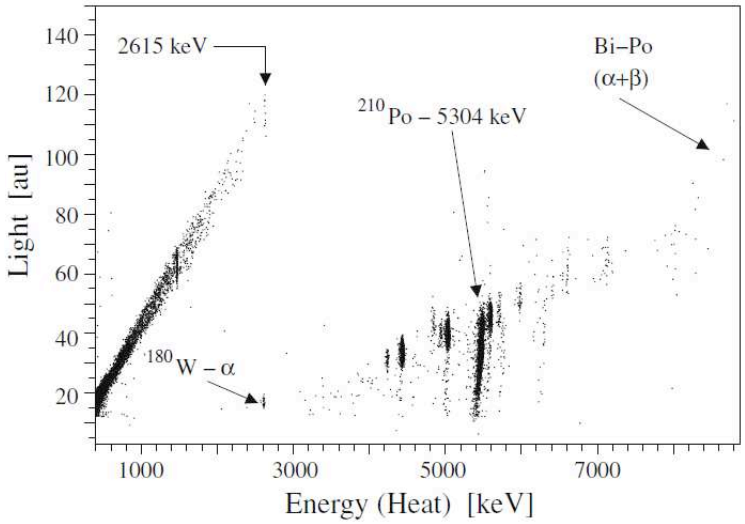

FIGURE 4.8: Result of a background measurement performed with a 3×3×6 cm^3 $CdWO_4$ crystal (426 g) during 1066 hours. No β/γ events have been observed above the 2615 keV ^{208}Tl line.

It has been also demonstrated [83] that the energy resolution is similar to standard TeO_2 bolomters, even with large $CdWO_4$ crystals. Figure 4.9 shows an example of Lights versus Heat scatter plot of β/γ events collected with a calibration run using an external ^{232}Th source. The observed γ lines appear as negative slope lines, due to energy anticorrelation between the heat and scintillation signals. This anticorrelation is a well known phenomena

and already observed for other scintillating bolometers. The important feature here is that the slopes of each γ line are the same. Therefore an energy anticorrelation correction can be applied offline in order to improve the energy resolution. Without correction, the energy resolution would be 16 keV at 2615 keV. After energy anticorrelation correction, the FWHM energy resolution becomes 6 keV at 2615 keV.

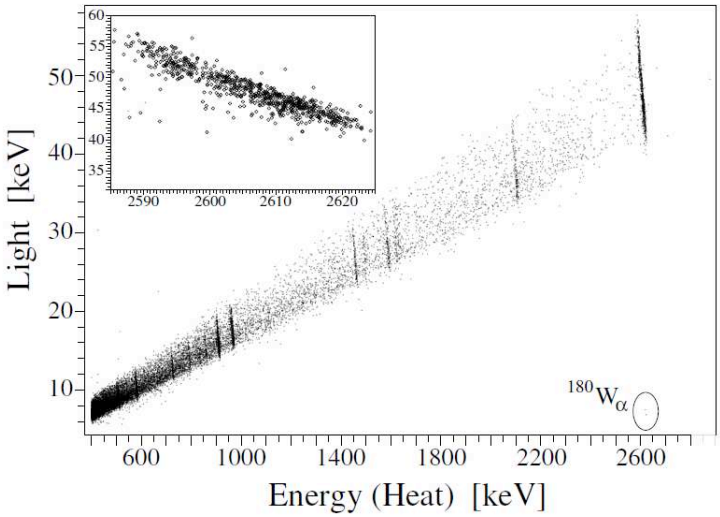

FIGURE 4.9: Scatter plot Light versus Heat obtained with a large $CdWO_4$ crystal (4 cm diameter and 5 cm height, 0.51 kg) in a 96 h calibration using an external ^{232}Th source. In the inset the highlight of the ^{208}Tl line..

Possible limitations

A possible limitation to use $CdWO_4$ crystals as scintillating bolometers is the presence of ^{113}Cd (12.2% in natural cadmium) which can produce high energy γ's up to 10 MeV in the case of neutron background, due to its large (n, γ) cross section (about 20.000 b). A future experiment using $CdWO_4$ would require an efficient neutron shield.

Production of scintillating crystals with enriched isotope might be a critical issue because it is necessary to avoid contaminations in transition metals, which would deteriorate optical and scintillation quality. Recently large enriched $^{116}CdWO_4$ crystals (82% of ^{116}Cd enrichment) have been produced [84]. A raw crystal with mass of 1868 g was grown from 2139 g of the initial $^{116}CdWO_4$ compounds. Then 3 near cylindrical shape $^{116}CdWO_4$ crystals (586 g, 589 g and 325 g) have been cut from the raw crystal. It has been also demonstrated that enriched ^{116}Cd can be recovered from $^{116}CdWO_4$ crystalline residue. Thanks to the careful purification of the initial components, the crystal has a high transmittance and a high light yield at room temprature. A background measurement over 1727 h in Gran Sasso, using sincillation light detection at room temperature allowed to measure radioactive contaminations : the activities of ^{226}Ra (^{214}Bi) and ^{228}Th (^{208}Tl) are $< 5\mu$Bq/kg and $\approx 60\mu$Bq/kg, respectively which is low enough for a cryogenic experiment. Isotopic composition of cadmium in the $^{116}CdWO_4$ crystals has been also measured. The isotope abundance for ^{113}Cd is 2.1%, about 6 times smaller than in natural cadmium (12.2%).

Finally, a limiting feature is the relative high cost for ^{116}Cd enrichement compared to ^{82}Se or ^{100}Mo. I note that the 600 g of enriched ^{116}Cd available from NEMO-3 could be used to developp extra $^{116}CdWO_4$ crystals.

4.3.2 ^{82}Se : ZnSe crystal

ZnSe scintillating bolometer is another good candidate for $\beta\beta0\nu$ search and ^{82}Se can be easily enriched by centrifugation. Experimental studies of several ZnSe crystals as scintillating bolometers have been performed in the last few years [85]. A relatively large light yield and good energy resolution have been obtained.

However an unexpected characteristic has been observed with ZnSe : the sintillation light yield for α is larger than for β/γ of the same energy, equivalent to a quenching factor larger than one (see Figure 4.10). No other scintillator with a quenching factor higher than 1 for α particles have ever been reported before in literature. Possible effects of scintillation light self-absorption or transparency of the light detector to the scintillation photons have been investigated but they cannot explain the anormal quenching factor.

The problem for $\beta\beta0\nu$ search is that the α band is spread to lower light signal and higher heat signal. Some α particles can then be misidentified as β/γ events and thus produce a background in the $\beta\beta0\nu$ region of interest. This problem appears to be connected to the quality of crystal surface or to the presence on the surfaces of residuals of the abrasive, non-scintillating, powder used for polishing.

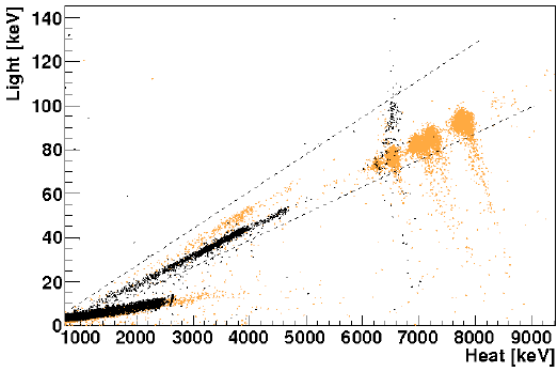

FIGURE 4.10: Scatter plot of Light vs. Heat recorded with a large ZnSe crystal in two different runs with alpha sources at different positions on the crystal. The dotted lines identify the opening of the alpha band on a wide angle, due to the variation of the Quenching Factor upon source position [85].

This effect might be a limitation for α background rejection and makes ZnSe a not as good candidate. However recently a high α rejection efficiency has been obtained by using a pulse shape analysis of the light signal instead of the standard amplitude. A dedicated run with a large ZnSe crystal was performed where the Light Detector was operated at a slightly higher temperature than usual, in order to have faster response and the signal sampling was increased to improve the resolution on the signal shape. A light pulse shape parameter (here named Test Value Right, TVR) has been developped. Figure 4.11 shows the distribution of TVR versus the heat energy obtained with this dedicated run with sources producing β/γ's

up to 2.6 MeV and α's up to 5 MeV. A high α rejection efficiency has been obtained near the $Q_{\beta\beta}$ energy region.

The most critical point for ZnSe crystal is the risk of a unreproductibility of its characteristics with different samples of crystal growing, due to contaminations in transition metals. An important work has been performed in order to define a protocole for ZnSe growing, avoiding any metals contamination. Recent preliminary cryogenic tests of new crystals grown with this protocole, are very promizing.

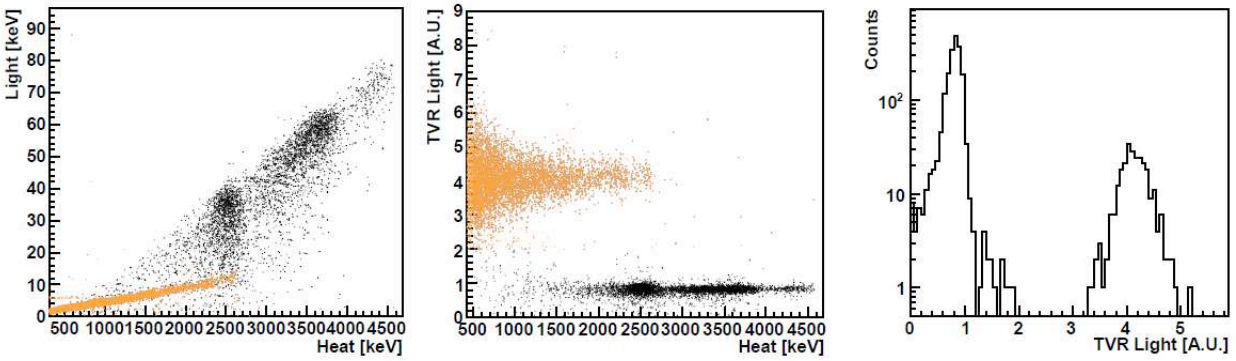

FIGURE 4.11: Large ZnSe crystal (41 mm diameter and 17 mm height) exposed to α and β/γ source : (Center) Distribution of the TVR pulse shape parameter on light pulses versus the amplitude of the heat pulses. Black points are α particles and colored points are β/γ's ; (Right) TVR distribution for light pulses between 2.4 and 2.6 MeV, the nearest energy window to the $Q_{\beta\beta}$ value (3 MeV) ; (Left) Scatter plot of Light versus Heat.

Two years ago, the LUCIFER project has been funded by the european grant ERC. The goal is to build a demonstrator with few tens of kg of enriched $Zn^{82}Se$ and to reach a level of background of 10^{-3} cts/(keV.kg.yr). The design of the LUCIFER experiment is similar to CUORICINO. It consists of a tower of 12 modules, each elementary module corresponds to an array of 4 ZnSe crystals (each crystal 5×5×5 cm^3, 660 g) read out by a single light detector. The setup could house up to ≈ 20 kg of ^{82}Se isotope corresponding to an expected sensitivity of ≈ 10^{26} yr (90% C.L.) after 5 years of running and a level of background of 10^{-3} cts/(keV.kg.yr). Today the R&D efforts in LUCIFER are the production of pure natural ZnSe crystals without metalic contaminations in order to obtain good heat and light performances and good reproductibility of the crystals growing. 10 kg of enriched Se has been already purchased (URENCO). Studies are in progress to purify Se, to define protocole to obtain good beads for crystal production (powder is not good for crystals production) and to obtain a good efficiency for the process of crystallization. The optical quality and radiopurity of the obtained enriched $Zn^{82}Se$ crystal will be also studied carefully.

4.3.3 ^{100}Mo : $ZnMoO_4$ and $CaMoO_4$ crystals

$ZnMoO_4$ and $CaMoO_4$ crystals are two promising candidates, which have been recently tested as scintillating bolometers [82][86][87][88].

The main advantage of these two crystals is that the pulse shape analysis of the heat signal alone, without any need of light readout, is sufficient to discriminate β/γ to α par-

ticles. It has been initialy observed [87] that the thermal signal induced by β/γ and α particles shows a slightly different time development. This feature seems to be explained by the relatively long scintillation decay time (hundreds of μs) observed in these crystals. This long decay, combined with a high percentage of non-radiative de-excitation of the scintillation channel, will transfer phonons (heat signal) to the crystal. This extra phonon signal is extremely small but is different in amplitude for β/γ and α particles, because of a different scintillation light yield.

Recently two different ZnMoO4 crystals, grown by the Nikoleav Institute of Inorganic Chemistry (NIIC, Novosibirsk, Russia), $\approx$ 30 g each, have been tested in LNGS [88] to validate this feature. A β/γ to α discrimination of 20 σ has been obtained at 2.6 MeV, using only a pulse shape analysis of the heat signal. The crystals are also very radiopure : the limits obtained after a long background measurement (407 hours) are $< 32\mu$Bq/kg for ^{228}Th and ^{226}Ra.

However if we take into account the slow response of the detector, the pile-up of two successive $\beta\beta2\nu$ decays becomes the limiting background ! With the $\beta\beta2\nu$ half-life of $T^{2\nu}_{1/2} = 7\ 10^{18}$ years for ^{100}Mo, and assuming a time window of 5 ms in which one cannot distinguish two different pulses, this background has been estimated by Monte-Carlo simulations at the level of $2\ 10^{-3}$ cts/(keV.kg.yr).

This background is still negligeable for an experiment with few tens of kilograms of crystal. For instance, assuming the CUORICINO cryostat equipped with ZnMoO4 crystals, equivalent to $\approx$ 30 kg of crystal and 13 kg of Mo, and a typical energy resolution of FWHM= 5 keV, the expected background is 0.3 counts/year in the FWHM energy window at $Q_{\beta\beta}$. It would correspond to a sensitivity of $T^{0\nu}_{1/2} > 0.7\ 10^{26}$ yrs in 5 years of running. However, for larger isoptope mass, developments of new NTD readout, delivering faster phonon signal, are required.

Recently a project of a $\beta\beta$ pilot experiment [89], has been proposed by french, ukrainian and russian collaboration. It is a step-by-step program and the pilot experiment consists of first assembling 4 $ZnMoO_4$ crystals with enriched ^{100}Mo. The mass of each crystal would be around 400 g, corresponding (with the four crystals) to a total mass of 675 g of ^{100}Mo and an expected sensitivity on the $\beta\beta0\nu$ half-life of 10^{24} y after 1 year of data collection and an expected zero background. A cryogenic test of a large $ZnMoO_4$ crystal of $\simeq$ 300 g is foreseen in the next months in CSNSM Orsay.

I note that the 7 kg of enriched ^{100}Mo available from NEMO-3 could be used to developp $Zn^{100}MoO_4$ crystals.

CaMoO4 is also a good candidate. Unfortunately, the $\beta\beta2\nu$-decay of ^{48}Ca, with $Q_{\beta\beta} = 4.27$ MeV, although only 0.18% of natural isotopic abundance, will result in an irreductible background in the $\beta\beta0\nu$ region of ^{100}Mo. This background can be easily evaluated as $\approx$ 0.01 counts/(keV.kg.yr). A new collaboration, named AMORE, propose to use $^{40}Ca^{100}MoO_4$ with depleted ^{40}Ca [90]. Indeed, about 30 kg of ^{40}Ca (^{48}Ca $< 0.001\%$) is available today (from the enrichment in the 80's in Russia of the $\approx$ 30 g of ^{48}Ca used in NEMO-3 and TGV experiments). Recently three large crystals of $^{40}Ca^{100}MoO_4$ with enriched ^{100}Mo and depleted ^{40}Ca have been produced and should be tested soon in the Yang Yang Underground Laboratory in South Corea (700 m depth).

Chapitre 5

Other experiments

5.1 Liquid scintillators experiments

Recently two large existing liquid scintillator detectors, Kamland and SNO, initialy developped for neutrino oscillation measurements, have been reused as $\beta\beta$ detectors by adding $\beta\beta$ isotope inside the liquide scintillator. It allows to reach relatively quickly a large amount of isotope $\approx$ 100 kg. I will review these two projects : Kamland-Zen and SNO+.

5.1.1 KAMLAND-Zen experiment

KAMLAND-Zen proposed to measure ^{136}Xe isotope. This is because ^{136}Xe is the simplest and least costly $\beta\beta$ isotope to enrich, its high $\beta\beta2\nu$ half-life ($\simeq$ 2 10^{21} y) reduces naturally the $\beta\beta2\nu$ background, and it is relatively easy to dissolve Xenon gas in liquid scintillator with a mass fraction of a few %. The original idea to dissolve Xenon gas in liquid scintillator installed in a very low background detector has been initially proposed by R.S. Raghavan in 1994 [91]. And KAMLAND-Zen collaboration did it !

KAMLAND [92] is an ultra low background detector, installed 1000 m deep in the Kamioka mine (Japan) and built in 1998-2001. It was initialy designed to confirm the solar neutrino oscillation by detecting the reactor anti-neutrino deficit with an oscillation length $\approx$ 175 km. KAMLAND consists of a sphere (13 m diameter) filled with ultra radiopure liquid scintillator (1200 m^3, $\approx$ 1 kton) contained in a second sphere filled of inert buffer oil (shield), surrounded by a water Cerenkov outer detector. The energy resolution of the liquid scintillator detector is FWHM $\approx 6.5\%/\sqrt{E(MeV)}$ with 34% of photo-coverage (1325 17" PMT's + 554 20" PMT's). A long R&D program has provided a purification of the liquid scintillator at a level of $0.2 - 2\ 10^{-18}$ g/g in ^{238}U and $1.9 - 4.8\ 10^{-17}$ g/g in ^{232}Th.

The major modification of KAMLAND-Zen [93] to the KamLAND experiment was the installation in summer 2011 of an inner, very radiopure (2 10^{-12} g/g in ^{238}U and 3 10^{-12} g/g in ^{232}Th), very thin (25μm) and very transparent balloon ($\approx$ 3.1 m diameter), suspended at the center of the KamLAND detector (see Figure 5.1). This ballon contains 13 tons of Xe-loaded liquid scintillator (Xe-LS). The external liquid scintillator acts as an active shield against external γ's.

In August and September 2011, 330 kg of xenon gas, 91% enriched in ^{136}Xe, has been dissolved in liquid scintillator and filled inside the balloon in KAMLAND. Data taking started in September 2011. The 2.5% (mass ratio) of Xenon dilution in the liquid scintillator

allows to maintain the KAMLAND energy resolution of FWHM $\approx 10\%$ at $Q_{\beta\beta}(^{136}Xe)$. It is also important to emphasize that the systematic variation of the energy reconstruction over the Xe-LS volume is less than 1% and the detector energy response is stable to within 1% also.

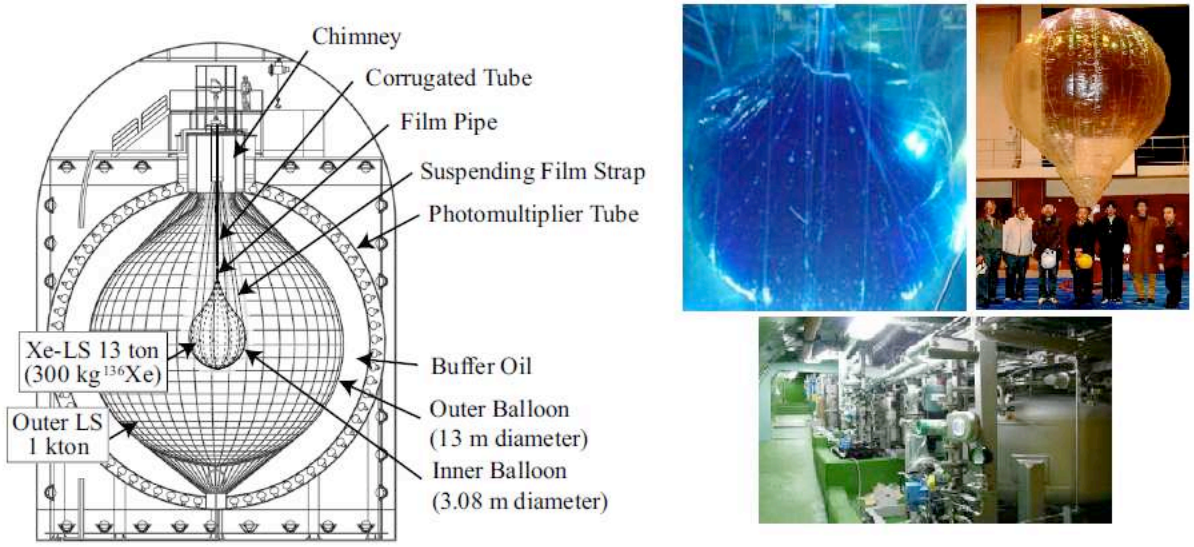

FIGURE 5.1: (Left) Schematic view of the Kamland-Zen detector ; (Right) Pictures of the mini ballon during tests in air and in water ; View of the Xenon distribution.

In order to reduce the background from the ballon material, the reconstructed vertex of events must be within 1.2 m of the ballon center, defining the fiducial volume with an effective mass of ^{136}Xe of 129 kg. The residual ^{238}U and ^{232}Th concentration internal to the Xe-LS are measured using sequential decays of ^{214}Bi$-^{214}$Po and ^{212}Bi$-^{212}$Po and estimated to be $\approx 3\ 10^{-16}$ g/g and $\approx 2.2\ 10^{-15}$ g/g, respectively. It corresponds to a negligeable background in the $\beta\beta0\nu$ energy region. One possible important background is the production of ^{10}C(β^+, $T_{1/2}$ = 29.4 mn, Q_β=3.65 MeV) by spallation of carbon ($^{12}C + \mu \rightarrow^{10} C + 2n + \mu$) inside the Xe-LS. The expected number of background events is expected to be few counts per year. A dedicated electronic has been developped in order to detect the light produced by the crossing muon followed by detection of the delayed 2.2 MeV γ-rays produced by the $n - p$ capture of the two neutrons ($T_{1/2} = 207\mu$s). This veto, not yet used in preliminary analysis, allows to reject 95% of the delayed ^{10}C decay.

Figure 5.2 shows the energy spectrum of selected $\beta\beta$ events, with the best fitted background, after the first 77 days of collected data with the effective mass of 129 kg ^{136}Xe [93]. A very nice signal of $\beta\beta2\nu$-decay (more than 35000 $\beta\beta2\nu$ events observed in only 77 days !) is well observed, providing an improved measurement of the ^{136}Xe $\beta\beta2\nu$-decay half-life :

$$T^{\beta\beta2\nu}_{1/2}(^{136}\mathrm{Xe}) = 2.38 \pm 0.02(\mathrm{stat}) \pm 0.14(\mathrm{syst})\ 10^{21}\ \mathrm{years}$$

value in agreement with the result obtained by EXO-200.

But unfortunately an unexpected background has been observed in the $\beta\beta0\nu$ energy region, with a strong peak significantly above the Q-value of the $\beta\beta$ decay. The collaboration has investigated all the possible contaminants with a peak structure in the 2.4-2.8 MeV

energy window. It comes that two dominant contaminations can fit well the observed peak : ^{110m}Ag (β-decay with associated γ's, $T_{1/2}$ = 360 days, Q_β = 3.01 MeV) and ^{208}Bi (EC-decay, $T_{1/2} = 5.31\ 10^5$ years, $Q_\beta = 2.88$ MeV, γ of 2614.5 keV in 100% of the case).

- The ^{110m}Ag isotope is a fission product, which has probably contaminated the detectors materials by fallout from the Fukushima reactors accident in March 2011. Measurements of soil or ocean samples around Fukushima but also of soil samples taken near the inner ballon production facility have confirmed the contamination in ^{110m}Ag. The contamination of the inner ballon by the Fukushima fallout is also consistent with the surface activity ratio of ^{134}Cs to ^{137}Cs (0.662 Mev γ) measured on the surface of the nylon ballon.
- The ^{208}Bi isotope is not a fission product. However it has been conservatively considered as a possible background although its origin is unknown. We mention that its measurement by γ spectroscopy is difficult since it decays to the excited ^{208}Pb state producing in 100% of the case the same γ of 2615 keV as in the ^{208}Tl decay.

Assuming these two contaminations, a limit to the half-life of the $\beta\beta0\nu$ decay has beed derived :

$$T_{1/2}^{\beta\beta0\nu}(^{136}\text{Xe}) > 5.7\ 10^{24} \text{ years (90\% C.L.)}$$

KAMLAND-Zen has to be shut down in the next year for security check, allowing some upgrade of the detector. New measurements could start in 2013.

I think that this preliminary result presented by Kamland-Zen collaboration illustrates an important feature : a pure calorimeter detector with a relatively modest energy resolution (FWHM of few percent at $Q_{\beta\beta}$) is a well detector to reach a high sensitivity in case of no background, but cannot distinguish a possible signal to a mimicking γ emitter backrgound in case of possible contamination. Indeed, looking at the energy spectrum obtained today (Figure 5.2), it is difficult to distinguish between a possible contamination in ^{208}Bi, whose origin is unknown and is not understood, or a possible presence of $\beta\beta0\nu$ signal. Who knows ?... I would like also to underline that a possible risk of contamination of the xenon itself has to be also considered for next measurements.

5.1.2 SNO+ experiment

SNO+ [94] [95] proposes to fill the Sudbury Neutrino Observatory (SNO) [96] with ultrapure Nd-loaded liquid scintillator (LAB), in order to investigate the isotope ^{150}Nd. ^{150}Nd has the largest phase space factor of all double beta decay isotopes and its $Q_{\beta\beta}$ value of 3.37 MeV places it just above the Q_β value of ^{214}Bi (3.27 MeV) and therefore above the Radon background)

The present plan is to dilute 0.1% in mass of natural neodynium salt in 1 ktons of liquid scintillator, providing a source of 56 kg of enriched ^{150}Nd (the natural abundance in the ^{150}Nd isotope is 5.6%). Actually, up to 1% of Nd can be loaded in liquid scintillator but the light yield becomes too small [97]. Optimization studies suggest 0.3% loading Nd might be a better compromise between light output and statistics. Given the liquid scintillator light yield and photocathode coverage of the experiment, an energy resolution performance of about 6.4% FWHM at $Q_{\beta\beta}$, is expected. External backgrounds can be rejected by the external water shielding, self-shielding of the scintillator and with a 50% fiducial volume selection.

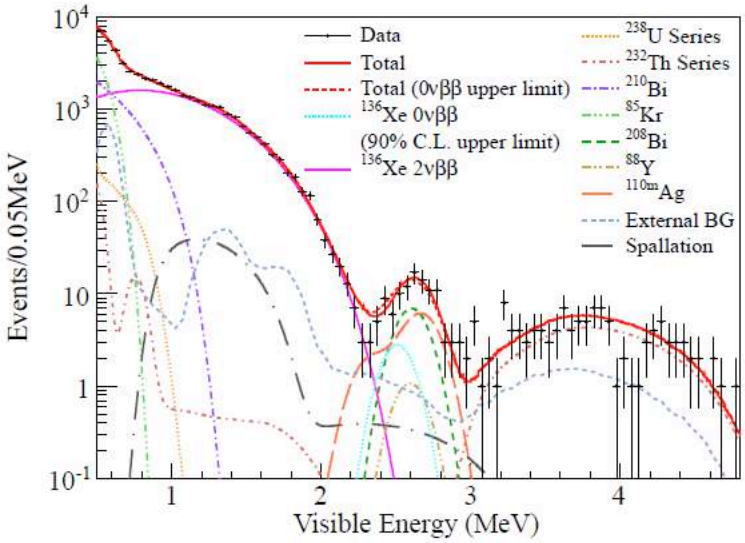

FIGURE 5.2: Result after 77 days of data collection : energy spectrum of selected $\beta\beta$-decay candidates together with the best-fit backgrounds and $\beta\beta 2\nu$-decays, and the 90% C.L. upper limit for $\beta\beta 0\nu$ process.

SNO+ requires to modify the support system of the inner acrylic vessel. Indeed, in SNO, the acrylic vessel, which was filled with heavy water, had to be held up. In SNO+, it is filled with LAB and it must be held down. Last data of SNO have shown that the inner surface of the acrylic vessel has been probably contaminated by leaks of mine dust. Therefore the inner surface of vessel must be cleaned. Also, since radiopurity requirements are more stringent for SNO+, the interface regions (like source deployment) must be very tight against leak of external mine air.

A crucial point is the radiopurity of the liquid scintillator. An extensive set of scintillator purification systems (distillation and in-situ recirculating purification) are under construction with the aim of reaching the purity levels (10^{-17} g/g of ^{238}U and ^{232}Th chain activities) achieved by the Borexino experiment [98][99]. The approach of Borexino is being followed for SNO+.

Another crucial point is the purification of the neodynium chloride salt. A newly developed "self-scavenging" technique has been developped and found to effectively remove thorium and similar containments from the neodymium chloride [100].

Figure 5.3 shows the expected background, which includes the $\beta\beta 2\nu$ from ^{150}Nd, ^{8}B solar neutrinos, ^{208}Tl and ^{214}Bi, for 3 years of data collection. The total expected background is $\approx$ 40 counts/(FWHM.year). SNO+ compensate this relatively large background (due to a modest low energy resolution) by a large statistic. The expected sensitivity on the $\beta\beta 0\nu$-decay half-life, after 3 years of data collection, is $T_{1/2} > 6\ 10^{24}$ years (90% C.L.). A fiducial volume of 50% of the acrylic vessel, 80% detector live time and backgrounds equivalent to those achieved in Borexino, were used in the sensitivity calculations.

The use of enriched ^{150}Nd would obviously improve the sensitivity of SNO+. There are today two possible techniques to enrich Nd : the Atomic Vapour Laser Isotope Separation (AVLIS) and the high-temperature centrifugation. Both techniques are studied in

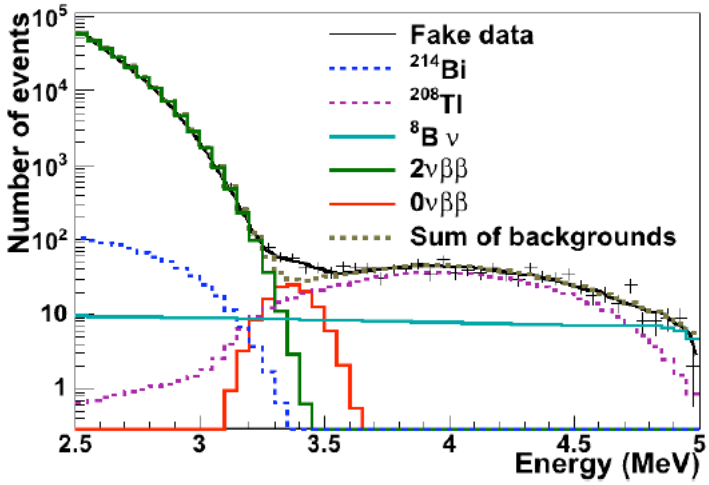

FIGURE 5.3: Simulated event energy spectrum showing the expected backgrounds and $\beta\beta0\nu$ signal (assuming $T^{0\nu}_{1/2} = 10^{24}$ yrs) for a 3 years run with 0.1% Nd-loading.

collaboration with SuperNEMO.

It is scheduled to start taking data with the acrylic vessel filled with pure water in fall 2012 and to built the scintillator process systems in parallel. Water will be replaced by purified liquid scintillator in 2013 and data will be collected during few months. First data with ^{nat}Nd-loaded scintillator are foreseen by the end of 2013 or in 2014.

5.2 Xe TPC experiments

5.2.1 Liquid Xenon TPC : the EXO-200 experiment

The EXO-200 detector, shown in Figure 5.4, is a time projection chamber (TPC) using 200 kg of liquid Xenon (enriched at 80% in ^{136}Xe), and located in the Wast Isolation Pilot Plant (WIPP, USA, 1600 m.w.e. depth). It started taking data in May 2011.

The main advantage of a liquid TPC is its compact geometry. The TPC is a cylinder of 40 cm diameter and 44 cm length with a cathod grid dividing the cylinder into two identical regions. Each end of the TPC contains two wire grids and an array of 250 large-area avalanche photodiodes, that allows for simultaneous readout of ionization and scintillation in liquid xenon. Wire grids provide a 2-dimensional transversal localization and energy information while the third longitudinal coordinate is obtrained from the scintillation light. The proved energy resolution is FWHM = 3.3% at $Q_{\beta\beta}$, using the anti-correlation between ionization and scintillation [102]

The ability of the TPC to reconstruct energy depositions in space is used to remove interactions at the detector edges where the background is higher. It reduces to a fiducial volume containing 63 kg of ^{136}Xe. It also provides a discrimination between single-cluster depositions, characteristic of $\beta\beta$ and single β decays in the bulk of the Xenon, from multi-cluster ones, generally due to γ-rays.

The first phase of data taking has been devoted for the measurement of the $\beta\beta2\nu$-decay and a relatively low electric field has been applied in order to provide more stable

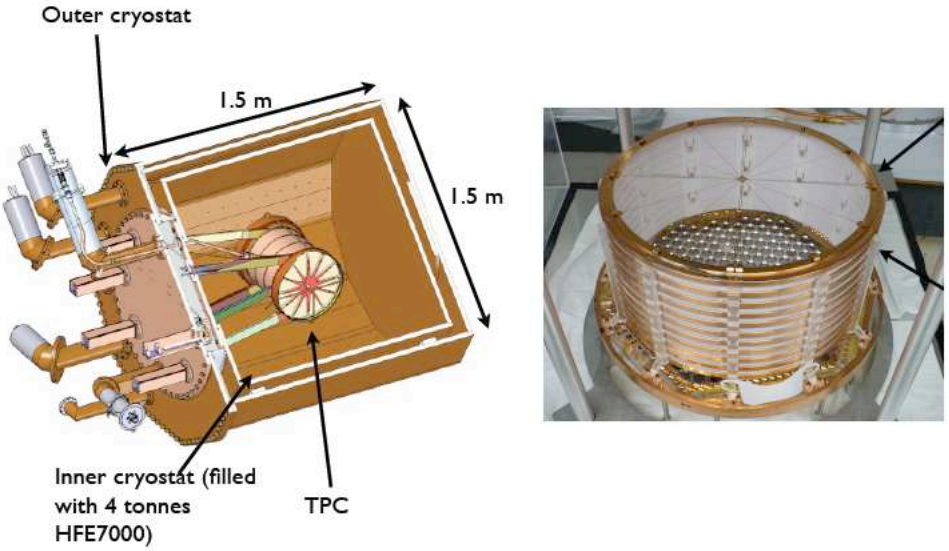

FIGURE 5.4: (Left) Schematic view of the EXO-200 TPC inside the cryostat ; (Right) Picture of the TPC during its assembly with APD holes.

operation at the expense of the ionization energy resolution. The collaboration has recently published the result obtained with first month of data, reporting the first observation of the $\beta\beta2\nu$-decay of ^{136}Xe (just few months before Kamland-Zen, which confirmed the result). The measured energy spectrum is presented in Figure 5.5 both in single and multi-cluster channels. The backgrounds involving γ-rays are readily identified by their clear multi-cluster signature, while the single-cluster spectrum is dominated by a large structure with a shape consistent with the $\beta\beta2\nu$-decay of ^{136}Xe with a half-life of :

$$\mathrm{T}^{2\nu}_{1/2} = 2.11 \pm 0.04(\mathrm{stat}) \pm 0.21(\mathrm{syst}) \times 10^{21} \text{ yrs}$$

The dominant background in the $\beta\beta0\nu$ is expected to come from the radon in the cryostat-lead air-gap and the ^{232}Th and ^{232}U in the TPC vessel. We mention that a very low level of Radon contamination has been measured inside the Liquid Xenon of 4.5 μBq/kg. Only limit has been set for Thoron with an acivity $< 0.04\mu$Bq/kg. Results of the $\beta\beta0\nu$ search should be published before summer 2012.

The EXO-200 target is to reach a level of background of $\sim 10^{-3}$ cts/(keV.kg.yr) in the $\beta\beta0\nu$ energy region. With 200 kg of liquid Xenon, an energy resolution of 3.3% FWHM at $Q_{\beta\beta}$ and a fiducial volume efficiency of 40%, it would correspond to a background of about 16 counts/(FWHM.yr). This background is compensated by a large amount of mass (80 kg of ^{136}Xe) and therefore large statistics. The expected sensitivity is $T^{0\nu}_{1/2} > 6\ 10^{25}$ yrs (90% C.L.) after 5 years of data collection.

It is clear that an additional background suppression or a higher energy resolution is needed for a ton scale experiment. To reduce the background, the ultimate goal of the EXO collaboration is to develop the so-called *barium tagging* [103]. It consists of tagging the Ba^{++} ion ($\beta\beta$ decay daughter of ^{136}Xe) with optical spectroscopy methods by laser fluorescence excitation. Research and development for Barium ion grabbing and tagging is ongoing in parallel with the EXO-200 experiment.

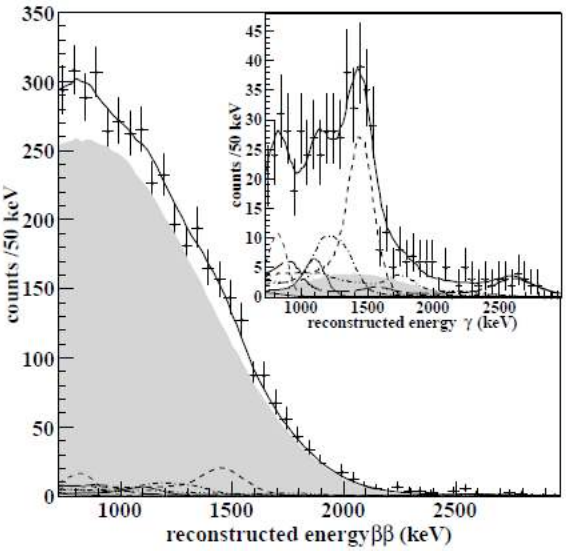

FIGURE 5.5: Energy distributions from 752.66 hrs of EXO-200 single-cluster events (main panel) and multi-cluster events (inset). The result of the fit (solid line) contains $\beta\beta 2\nu$-decay (shaded region) and prominent background components of the TPC vessel.

5.2.2 Gaseous Xenon TPC

The use a high pressure gaseous Xenon (HPXe) TPC provides an higher energy resolution and a recontruction of the tracks in order to identify the $\beta\beta$ event topology

It has been experimentaly demonstrated [104] that high energy resolution can be obtained in high pressure gaseous xenon chamber, as illustrated in Figure 5.6 A striking feature in Figure 5.6 is the apparent transition at density $\rho = 0.55$ g/cm ^{3} (equivalent to about 50 bars). Below this density, the energy resolution is approximately constant. Extrapolating this observed resolution as $\sqrt{E}$ to the ^{136}Xe $Q_{\beta\beta}$ value, one could get an energy resolution of FWHM$\approx$ 0.3%, close to the ultimate resolution obtained from the Fano factor of gaseous Xenon. And this energy resolution should be constant even at high pressure up to $\approx$ 50 bars.

The second possible advantage of gas relative to liquid is the ability to exploit the topological signal of a $\beta\beta 0\nu$ decay : an ionization track, of about 20 cm length at 15 bar, tortuous because of multiple scattering, and with larger depositions or blobs in both ends.

The Gothard TPC [105] in the 90's represented a pioneering gaseous xenon TPC. Despite a modest energy resolution, it however demonstrated the potential of a gaseous TPC to powerfully utilize the rich topological signature of $\beta\beta 0\nu$ events in the gas, with the characteristic of two blobs topology, to further reduce background. Last few years, new projects were proposed using new technologies : electroluminescence, ion TPC and Micromegas.

Electroluminescence and the NEXT-100 experiment

The NEXT-100 experiment, located in Canfranc Underground Laboratory (Spain), proposes to use the electroluminescence technique for the TPC readout. The principle of NEXT-100 is as follows (Figure 5.7) :

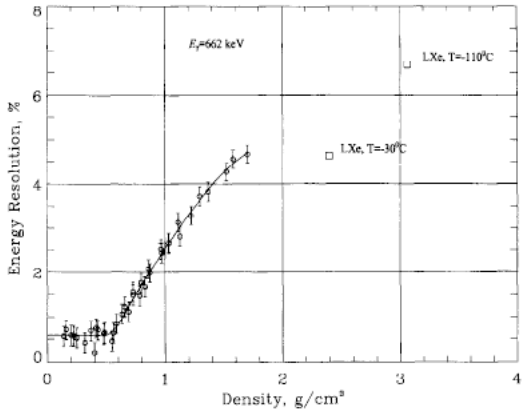

FIGURE 5.6: The energy resolution (FWHM) for ^{137}Cs 662 keV γ-rays, as a function of xenon density, for the ionization signal only [104].

- The prompt primary scintillation light emission (in VUV) is detected via photodetectors (60 PMT's) behind a transparent cathode. This faint signal determines the t_0 time used for event position along the longitudinal drift.
- Then ionisation electrons drift toward the opposite anode with a velocity ≈ 1 mm/μs in a 0.5 kV/cm electric drift. The diffusion is not negligeable at 10 bar : about 9 mm/$\sqrt{\text{m}}$ transverse, and about 4 mm/$\sqrt{\text{m}}$ longitudinal.
- An additional grid in front of the anode creates 0.5 mm thick region of more intense field ($E/p \approx 4$ kV/cm/bar). A secondary scintillation light, named *electroluminescence*, is created in between grids by atomic desexcitation, with very linear gain of order 10^3 and over a ≈ 2 μs interval. Finally, a segmented photodetector plane (7500 SiPM channels), located just behind the anode, performs the "tracking"
- The electroluminescence light, emitted isotropically, also reaches the cathode. The same array of PMT's used for t_0 measurement is also used for accurate calorimetry. A coating on the inner surface of the vessel improves the light collection.

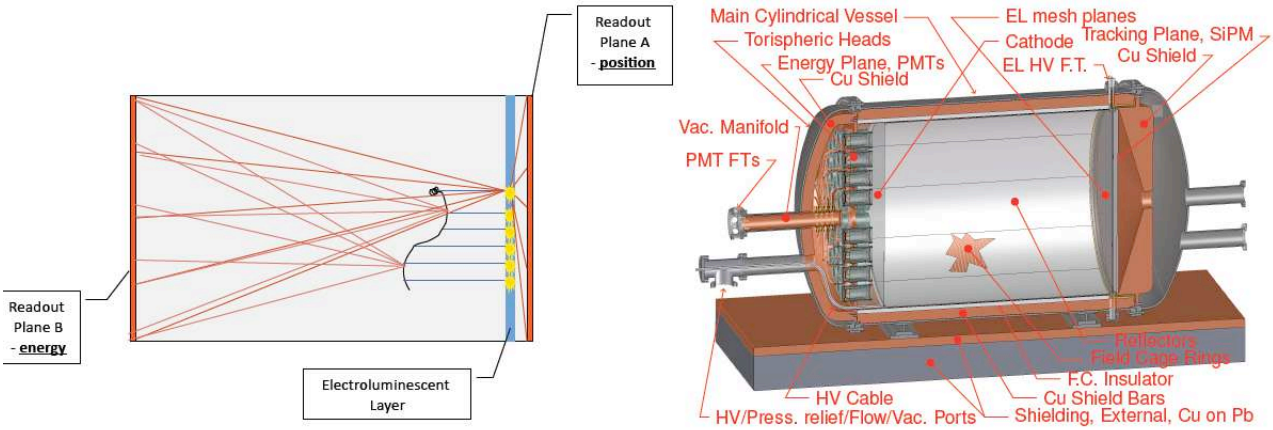

FIGURE 5.7: (Left) Principle of the electroluminescence TPC ; (Right) Design of the NEXT-100 TPC.

The baseline design of NEXT-100 (Figure 5.7) consists of a Stainless-steal vessel with a drift length of almost 2 m and a diameter of $\simeq$1.3 m (corresponding to a volume of $\simeq$2 m^3). The operation pressure ranges from 10 up to 15 bars, corresponding to $\simeq 100 - 150$ kg of Xenon.

Two prototypes have been developped :

- The NEXT-DBDM prototype (Berkeley) has been developped to demonstrate the capability to obtain a good energy resolution in HPXe using electroluminescence. Only 1 plane of PMT's located in the cathode has been used for calorimetry. An energy resolution of 1% FWHM at 662 keV (^{137}Cs γ source) has been obtained at 15 bars. However the prototype is smaller than the final NEXT-100 chamber, although the ratio drift length over diameter is similar. Also a radial dependence (solid angle) of the collected light has been observed and must be corrected carefully.
- The NEXT-DEMO demonstrator (IFIC Valencia) has been developped to demonstrate both the energy resolution and the capability for tracking topology with two planes of photodetectors (PMT and SiPM). The drift region is only 30 cm. First tracks reconstruction have been presented, showing visible blobs at the extremity of the tracks. However the complete analysis has not yet been presented, in order to quantify the background rejection and the $\beta\beta$ efficiency.

The NEXT-100 target is to reach an energy resolution better than 1% FWHM at $Q_{\beta\beta}$, a level of background of 2 10^{-4} cts/(keV.kg.yr) in the $\beta\beta0\nu$ energy region, with a $\beta\beta$ efficiency of 30% due to a $\beta\beta0\nu$ topological signature for background suppression. One of the most critical backgrounds comes from the rare 2447 keV γ-ray emitted by ^{214}Bi. When the γ is totaly contained, it produces a peak very close to the expected $\beta\beta0\nu$ signal at $Q_{\beta\beta} = 2462$ keV.

The NEXT-100 detector is foreseen to be installed in Canfranc end of 2013, although the construction of the detector is not yet totaly funded.

MICROMEGAS and the T-REX project

Micromegas is a very promising readout technique for a HPXe TPC. The Micromegas readouts [106] make use of a metallic micromesh suspended over a pixellised anode plane by means of insulator pillars, defining an amplification gap of the order of 25 to 150 μm. Electrons drifting towards the readout, go through the micromesh holes and trigger an avalanche inside the gap, inducing detectable signals both in the anode pixels and in the mesh.

It has been measured recently [107] that standard microbulk micromegas planes, manufactured out of kapton and copper foils, are very radiopure with activities < 30 μBq/cm^2 for ^{232}Th and ^{238}U chains. Also large surfaces are now available. It makes Micromegas as a very attractive technique for $\beta\beta0\nu$ researches.

A R&D program, named T-REX, funded by an european grant, has started few years ago in Zaragoza University and Canfranc (initialy within the NEXT collaboration) [108].

The work performed up to now has been focused in establishing the capability of microbulk readouts to work in high pressure Xe, and more specifically to measure their energy resolution in those conditions. For that task two prototypes have been built.

The first prototype (NEXT-0-MM) is a stainless steel vessel of 2 litres, with a diameter of 14 cm and a drift region of 6 cm, and it is devoted to measurements with small scale

readouts, to study gain, operation point, and energy resolution with low energy γ's or α's. A resolution of 2% FWHM have been achieved with 5.5 MeV α particles, for pressures up to 5 bar [109]. Depending on the ionization quenching of α with respect to electrons, it corresponds to an energy resolution of 1% to 3% FWHM at $Q_{\beta\beta}$. It is an important result because it shows that microbulk Micromegas work well in pure high pressure Xe without any quencher.

The second prototype (NEXT-1-MM), of much larger size (drift of 35 cm and a readout area of 30 cm diameter), is capable of fully confining a high energy electron track and will therefore probe the detection principle in realistic conditions.

We mention that another collaboration, EXO-gas, also develops a gas TPC to search for the double beta decay of ^{136}Xe, and considers Micromegas as an option for its readout [110].

5.3 Crystals at room temperature

5.3.1 CANDLES-III

CANDLES proposes to use natural CaF_2 crystals as scintillating detectors for the measurement of the isotope ^{48}Ca. The main advantage of ^{48}Ca is its high transition energy $Q_{\beta\beta} = 4274$ keV, well above the ^{208}Tl γ-ray (2.6 MeV), the ^{214}Bi β-decay (3.3 MeV end point), and α's from natural radioactivity (max. 2.5 MeV with scintillation quenching factor). Another advantage is its low atomic mass, providing a larger number of nuclei per mass unit. However, its natural abundance is very low, only 0.187% and it is today very difficult to enrich ^{48}Ca in large quantities. I mention that historicaly CaF_2 was one of the most sensitive technique used for the search of $\beta\beta0\nu$ [112].

CANDLES-III (Figure 5.8) is an array of 96 natural pure CaF_2 crystals ($10\times10\times10$ cm^3), for a total mass of ≈ 300 kg, corresponding to about 300 g of ^{48}Ca. Crystals are immersed in two liquid scintillators : an internal one (in the vicinity of the crystals) which acts as a wavelength shifter for the UV light emitted by the CaF_2 crystals (conversion phase), and an external one which acts as an active veto gainst external background. This setup is installed inside a pure water buffer (3 m diameter and 4 m height) for an additional passive shield. The scintillation light emitted by the CaF_2 crystals in the veto liquid scintillator is read out by 48 13" PMT's and 14 17" PMT's. The decay constants of the two involved scintillation processes are different (≈ 1 μs for CaF_2 and ≈ 10 ns for the liquid scintillator), which provides the capability of a pulse shape discrimination. The achieved energy resolution is $\approx 4.5\%$ FWHM at $Q_{\beta\beta}$. The detector has been installed in the Kamiokande Underground Laboratory (Japan) and its commissioning has started in June 2011.

There are two potential backgrounds, coming from ^{238}U and ^{232}Th contaminations inside the crystals or in the conversion phase liquid scintillator in the vicinity of the crystals :

- (β + delay α) pile-up events from ^{212}Bi-^{212}Po (β up to 2.2 MeV and quench $\alpha \approx$ 2.5 Mev) and ^{214}Bi-^{214}Po cascades,
- ($\beta + \gamma$) pile-up events from ^{208}Tl decay (β up to 2.6 MeV and γ 2.6 MeV).

The crystals and the liquid scintillator must be ultra radiopure : the average radiopurities of the crystals are ≈ 36 μBq/kg and ≈ 28 μBq/kg in ^{238}U and ^{232}Th chains, respectively. Residual BiPo β + delayα pile-up events are identified using pulse shape analysis with a rejection efficiency of $\approx 90\%$ [111]. $\beta+\gamma$ pile-up events are the dominant background. Despite a modest energy resolution, the $\beta\beta2\nu$ background is negligeable, about 0.01 counts per year.

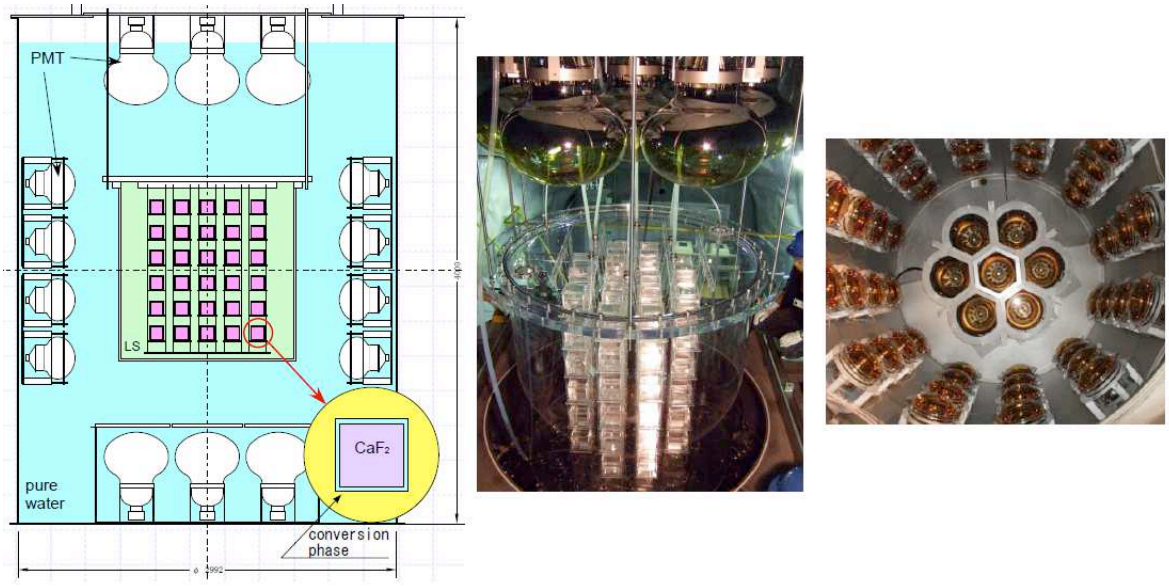

FIGURE 5.8: Schematic view of the CANDLE-III detector and some pictures.

The total expected level of background in the $\beta\beta0\nu$ energy region (estimated by Monte-Carlo) is about 10^{-3} cts/(FWHM.kg.yr), equivalent to about 0.3 counts per year [113]. It corresponds to an expected sensitivity of $T^{0\nu}_{1/2} > 3.7\ 10^{24}$ yrs (90% C.L.) with 5 years of collected data.

A R&D program for ^{48}Ca enrichment is in progress. Two methods are tested. The first one is a chemical process. When a calcium solution migrates through "crown" Ether (resin or liquid), Ca^{2+} ions are attracted by negative charged O^- of the CO dipole in Ether. Adsorption of ^{40}Ca (97% natural abundance) is slightly more efficient than ^{48}Ca, providing a chemical enrichment in ^{48}Ca. This method, first tested with resin crown ether, is now tested in liquid phase (Hiroshima Univ.), in which extraction is expected to be faster. However this method is not very efficient. The goal is to enrich ^{48}Ca at a level of $\approx 2\%$ (factor 10). The second methode of enrichment is the laser separation by radiation pressure. A bench test is in progress in Fukui Univeristy. I also remind that a R&D program of ^{48}Ca enrichment using AVLIS technique is in progress in South Corea, within the SuperNEMO collaboration [43]. The goal is to provide a significant amount of ^{48}Ca, about 1 kg within 3 years.

Two other improvements of the CANDLES experiment are investigated by the collaboration : the purification of CaF_2 crystals at the level of about 1 μBq/kg and the improvement of the energy resolution, by cooling the CaF_2 crystals.

A future detector, proposed by the CANDLES Collaboration, would contain 2 tons of CaF_2 crystal with 2% ^{48}Ca enrichment, equivalent to about 21 kg of ^{48}Ca. Assuming an improved energy resolution of 3% FWHM at $Q_{\beta\beta}$, and crystals radiopurities of 1 μBq/kg, the expected sensitivity would be $T^{0\nu}_{1/2} > 2.5\ 10^{26}$ yrs (90% C.L.) with 5 years of collected data. The $\beta\beta2\nu$ background is not anymore negligeable, with about 0.2 expected counts per year in the $\beta\beta0\nu$ region. We note that the current CANDLES-III detector could reach the same sensitivity if calcium was enriched to 13% using AVLIS method.

5.3.2 COBRA

COBRA [114] is a proposed array of ^{116}Cd-enriched CdZnTe semiconductor detectors at room temperature. The final aim of the project is to deploy 117 kg of ^{116}Cd with high granularity. Small scale prototypes have been realized at LNGS (Italy). The proved energy resolution is 1.9% FWHM. The project is in R&D phase. Recent results on pixellization shows that the COBRA approach may allow an excellent tracking capability, equivalent to a solid state TPC.

Chapitre 6

Summary

We are today in a period of intense activities with a large variety of $\beta\beta$ experiments, starting to take data or in the construction phase. These projects aim to demonstrate the capability to reduce the background by at least one order of magnitude with at least 100 kg of isotope.

We emphasize that the search of $\beta\beta0\nu$-decay requires several experimental techniques and more than one isotope. This is because there could be unknown background and gamma transitions, and a line observed at the end point in one isotope does not necessarily imply that $\beta\beta0\nu$ decay was discovered. Nuclear matrix elements are also not very well known.

We must also always keep in mind that every time one starts running a new $\beta\beta$ detector, a new unexpected background is discovered. The Radon background in the first phase of NEMO-3, the α's contamination on surface of the materials in TeO_2 bolometers, the ^{42}K contamination in the liquid argon in GERDA, and recently the contaminants from Fukushima fallout (and possibly from other origins) in KAMLAND-Zen are few examples. Actually, no $\beta\beta$ experiment has succeeded in obtaining a zero backgroundat the 10 kg scale. So it is very premature to project experiences at the ton scale. The first chalenge today is to run a modular pilot experiment with zero background, in the first phase at the 10 kg scale, which can be later enlarged to contain about 100 kg of isotope.

Germanium detectors

The new GERDA experiment (installed in LNGS, Italy) uses Ge detector array, directly immersed inside liquid Argon, which acts both as cryogenic liquid and shield against external γ-rays. The strings design allows to deploy crystals progressively inside the experiment. GERDA started taking data (Phase 1) with refurbished enriched ^{76}Ge crystals, which were used in the 90's in the previous Heidelberg-Moscow and IGEX experiments. It corresponds to about 20 kg of ^{76}Ge. First data have shown a prominent and unexpected background : the contribution of ^{42}K, the progeny of ^{42}Ar, about 20 times higher than expected. This is because of the drift of the ^{42}K ion towards the germanium crystals before decaying. A copper cylinder surrounding the array of crystals reduced this background to a level of 6 10^{-2} cts/(keV.kg.y) in the $\beta\beta0\nu$ energy region. It is 3 times lower than the level of background measured in Heidelberg-Moscow experiment but still a factor 6 higher than the Phase 1 target (10^-2 cts/(keV.kg.y)).

Two methods are under development in order to reduce the background, with the aim

to reach a level of 10^{-3} cts/(keV.kg.y). First, new commercially available Broad Energy Germanium (BEGe) detectors will be deployed. They provide a superior pulse shape discrimination performances against multi-compton events, produced by external γ-rays. The collaboration is also preparing a design for the detection of the scintillation light from argon, as an additional external background veto. We underline that the pulse shape discrimination and the LAr scintillation veto are only efficient to reduce external γ background. Potential background produced by β-decay or degraded α from surface contaminations of the detectors (like β from ^{42}K), or in the vicinity of the germanium crystals could be a limiting background.

In parallel, the MAJORANA experiment (WIPP, USA) is under construction in the USA. It will measure 20 kg of Ge with similar BEGe detectors, but in an ultra radiopure electroformed cryostat and with a standard lead shield.

For the next generation of germanium experiments, the most dangereous background is the potential bulk contamination of the germanium crystals in ^{68}Ge cosmogenic isotope. R&D on ^{68}Ge deenrichment will be required for ton-scale projects..

Bolometers

The assembly of CUORE-0 first tower is now completed and data collection will start in 2012 for two years of running, using CUORICINO cryostat (LNGS, Italy). The goal is to demonstrate a background lower than 0.05 cts/(keV.kg.yr). The expected sensitivity is $T_{1/2}(\beta\beta0\nu) > 6\ 10^{24}$ y (90% C.L.) after 2 years of measurement. The first data of CUORE in the new large cryostat is expected for 2014. The required background of less than 0.01 cts/(keV.kg.y) should be dominated by degraded α's from the copper surface surrounding the crystal and external γ's. With the complete detector (988 crystals, 206 kg of ^{130}Te), it will correspond to an expected sensitivity of 10^{26} y. If SSB detectors are able to reject α background and effectively achieve a background of 10^{-3} cts/(keV.kg.y), CUORE could improve its sensitivity up to $7\ 10^{26}$ y.

Recent results obtained with scintillating bolometers indicate that it is a very promising calorimetric technique for the search of $\beta\beta0\nu$ decay. First, it provides the possibility to study 4 different isotopes (^{116}Cd, ^{82}Se, ^{100}Mo and ^{48}Ca) with a high $\beta\beta0\nu$ detection efficiency (almost 100%) and a good energy resolution. The α discrimination allows to reject the dominant background due to degraded α particles and also to identify and reject possible residual bulk contaminations of the crystals in ^{232}Th and ^{238}U. Also, the $Q_{\beta\beta}$-values above the 2615 keV γ-rays from ^{208}Tl allow to suppress strongly the background due to external γ's. The potential residual backgrounds in the $\beta\beta0\nu$ energy region are rare high energy γ-rays from ^{214}Bi contamination inside the shield, or coincidences of the 2615 keV and 583 keV γ-rays emitted by ^{208}Tl, with the condition that ^{208}Tl contaminations are sufficiently close to the detectors. Assuming the radiocontamination level measured in CUORICINO cryostat and shield, the expected level of background would be in the range 10^{-3} (conservative) to 10^{-4} counts/(keV.kg.yr) in the $\beta\beta0\nu$ energy region.

The LUCIFER project, funded by the european grant ERC, did the choice to use ZnSe crystal because of its large light yield and its "natural" radiopurity. Despite an unfavourable quenching factor which should limit the β/γ to α discrimination, recent preliminar results using a pulse shape analysis of the light signal have shown the possibility to discriminate α particles with a high efficiency. Finaly a possible $\beta\beta0\nu$ signal discovery could be confirmed

or ruled out by the SuperNEMO experiment without any theoretical uncertainty of the nuclear matrix elements, since SuperNEMO will study the same ^{82}Se isotope.

$ZnMoO_4$ and $CaMoO_4$ crystals are also excellent candidates because the pulse shape analysis of the heat signal alone, without any need of light readout, is sufficient to discriminate β/γ to α and therefore to reject the α background. The 7 kg of enriched ^{100}Mo from NEMO-3 could be reused for this measurement. However development of $ZnMoO_4$ crystal is very recent and only small crystals have been produced so far. It appears also that the pile-up of two successive $\beta\beta2\nu$ decays becomes the limiting background, estimated at the level of $2\ 10^{-3}$ cts/(keV.kg.yr). It is due to the relatively "low" $\beta\beta2\nu$ half-life of the ^{100}Mo. This background is acceptable for a few tens of kg mass scale experiment. But for larger isotope mass, developments of new NTD, delivering faster phonon signal, are required in order to reduce this unexpected background. $ZnMoO_4$ could be also used in LUCIFER. Recently a project of a $\beta\beta$ pilot experiment has been proposed by french, ukrainian and russian collaboration. It is a step-by-step program and the pilot experiment consists of first assembling 4 $ZnMoO_4$ crystals with enriched ^{100}Mo. The mass of each crystal would be around 400 g, corresponding (with the four crystals) to a total mass of 675 g of ^{100}Mo and an expected sensitivity on the $\beta\beta0\nu$ half-life of 10^{24} y after 1 year of data collection and an expected zero background. A cryogenic test of a large $ZnMoO_4$ crystal of $\simeq$ 300 g is foreseen in the next months in CSNSM Orsay (see level).

For $CaMoO_4$, the $\beta\beta2\nu$-decay of ^{48}Ca, although only 0.18% of natural abundance, will result in a large background in the $\beta\beta0\nu$ region of ^{100}Mo. The AMORE experiment propose to use $^{40}Ca^{100}MoO_4$ using the 30 kg of depleted ^{40}Ca available today in Russia.

Production of scintillating crystals with enriched isotope is a critical issue because it is necessary to avoid possible contaminations in transition metals, which would deteriorate optical and scintillation quality, and contaminations in ^{238}U and ^{232}Th. Recently large enriched $^{116}CdWO_4$ crystals have been produced and scintillation performances and radiopurity have been validated. Also three crystals of $^{40}Ca^{100}MoO_4$ with enriched ^{100}Mo and depleted ^{40}Ca have been recently produced by AMORE and should be tested in the Yang Yang Underground Laboratory (South Corea). Production of very pure enriched $Zn^{82}Se$ crystal (with no metallic contamination) is in progress for LUCIFER project.

Ideally, a large cryostat, like CUORE or EUREKA, would be an ideal facility to accomodate all the four possible crystals, for a unique $\beta\beta$ cryogenic experiment.

NEMO-3 and SuperNEMO tracko-calo detectors

The combination of a tracking detector and a calorimeter provides a direct reconstruction of the tracks of the two emitted electrons from the source foil. It also allows to identify and measure each background component with a high rejection efficiency. However the price is a lower $\beta\beta0\nu$ efficiency and a lower energy resolution. In any case, I think that a direct confirmation by a tracko-calo detector is required if a $\beta\beta0\nu$ signal is observed by a calorimetric detector. It is thus a complementary approach. NEMO could also distinguish the underlying mechanisme (standard process versus V+A right-handed weak current) using the reconstructed angular distribution between the two emitted electrons.

The NEMO-3 detector (Modane, France) has demonstrated the performances of this technique with about 10 kg of isotopes and a sensitivity of 10^{24} y with ^{100}Mo. The residual backgrounds were the tail of $\beta\beta2\nu$-decay due to the modest energy resolution, the

contamination of the ^{100}Mo source foils in ^{208}Tl (≈ 100 μBq/kg), and radon contamination (≈ 5 mBq/m^3) inside the tracking chamber.

The future SuperNEMO detector is based on an extension and an improvement of the techniques used in NEMO-3. The goal is to accomodate about 100 kg of enriched $\beta\beta$ isotope in order to reach a sensitivity of 10^{26} y. The design is a planar and modular geometry, composed of 20 modules. The baseline is to measure ^{82}Se but ^{150}Nd and ^{48}Ca are also studied. The $\beta\beta2\nu$ background is reduced by the relatively high half-life of ^{82}Se (about 14 times higher than ^{100}Mo), and the improvement of the calorimeter energy resolution ($\approx 4.5\%$ FWHM at $Q_{\beta\beta}$). The radiopurities of the ^{82}Se foils and the Radon contamination must be improved by a factor ≈ 50. Developments of new Se purification techniques and foils production are in progress. A dedicated BiPo detector will be installed mid-2012 in Canfranc in order to measure and validate the radiopurities of the ^{82}Se foils. The design of the SuperNEMO detector is optimized to avoid external Radon diffusion inside the tracking chamber and inner materials are selected to avoid inner Radon emanation.

A first SuperNEMO module, named SuperNEMO demonstrator, will be installed in the Modane Underground Laboratory. It will accomodate 7 kg of ^{82}Se. The construction of the tracking detector and the γ veto has been funded by UK and is under progress, for a delivery in LSM Modane in 2013. First data could be taken in 2015. The sensitivity of the demonstrator will be $T^{0\nu}_{1/2} > 6.6\ 10^{24}$ years(90%C.L.), with 2.5 years of collected data.

Two other isotopes are also studied by the collaboration : ^{150}Nd and ^{48}Ca. A R&D program of ^{48}Ca enrichment using the Atomic Vapour Laser Isotope Separation (AVLIS) technique is in progress in South Corea. The goal is to provide a significant amount of ^{48}Ca, about 1 kg within 3 years. Enrichment of ^{150}Nd is also investigated with two possible techniques : the Atomic Vapour Laser Isotope Separation (AVLIS) and the high-temperature centrifugation.

Large liquid scintillator detectors

Recently two large existing ultra radiopure liquid scintillator detectors, Kamland and SNO, initialy developped for neutrino oscillation measurements, have been reused as $\beta\beta$ detectors by adding isotope inside the liquide scintillator. It allows to reach relatively quickly a large amount of isotope (≈ 100 kg) but with a limited energy resolution.

KAMLAND-Zen (Kamioka, Japan) proposed to measure ^{136}Xe isotope. This is because ^{136}Xe is the simplest and least costly $\beta\beta$ isotope to enrich, its high $\beta\beta2\nu$ half-life ($\approx 2\ 10^{21}$ y) reduces naturally the $\beta\beta2\nu$ background, and it is relatively easy to dissolve Xenon gas in liquid scintillator with a mass fraction of few %. KAMLAND-Zen started taking data in September 2011, with 300 kg of ^{136}Xe. An energy resolution of $\approx 10\%$ FWHM at $Q_{\beta\beta}$ has been obtained. A 40% fiducial volume has been applied in order to reduce external background. The $\beta\beta2\nu$-decay has been measured with a high signal over background ratio and high statistics. But, unfortunately, unexpected background has been observed in the $\beta\beta0\nu$ energy region. This background is explained by a contamination of some detector materials in ^{110m}Ag and ^{208}Bi. ^{110m}Ag is a known fission product coming from the Fukushima fall-out and its half-life is fortunately relatively small, about 1 year. However the origin of ^{208}Bi contamination (half-life $\approx 5\ 10^5$ years) is still not understood, and it has been conservatively considered as a possible background. A possible risk is a contamination of the xenon itself. This issue has to be considered seriously. New measurements could start in 2013 after a

1 year shut-down.

SNO+ (Sudbury, Canada) proposes to fill the SNO detector with ultrapure Nd-loaded liquid scintillator, in order to investigate the isotope ^{150}Nd. ^{150}Nd has the largest phase space factor of all double beta decay isotopes and its $Q_{\beta\beta}$ value of 3.37 MeV places it just above the Q_β value of ^{214}Bi (3.27 MeV) and therefore above the Radon background. However theoretical uncertainties on its nuclear matrix element are relatively large because it is a highly deformed nucleus. The present plan is to dilute 0.1% in mass of natural neodynium salt, providing a source of 56 kg of ^{150}Nd. A larger mass could be loaded in a second phase, up to 150 kg of ^{150}Nd. An efficient method has been developped to purify neodinium salt and purification systems of the liquid scintillator are under construction. However the expected background is relatively large, $\approx$ 40 counts per year in the $\beta\beta0\nu$ FWHM energy window, due to a modest energy resolution of 6.4% FWHM at $Q_{\beta\beta}$. First data with ^{nat}Nd-loaded scintillator are foreseen by the end of 2013 with an expected sensitivity of $T_{1/2} > 6\ 10^{24}$ years (90% C.L.) after 3 years of data collection. Enrichment of ^{150}Nd is investigated in collaboration with SuperNEMO.

Xenon TPC experiments

EXO collaboration decided to developp a liquid Xenon TPC with the main advantage to provide a large mass of Xenon with a relatively small TPC chamber. EXO-200 (WIPP, USA) is a small TPC ($\approx$ 0.05 m^3) containing 200 kg of liquid Xenon, enriched at 80% in ^{136}Xe. An energy resolution of 3.3% FWHM at $Q_{\beta\beta}$ has been obtained. The experiment started taking data in May 2011. Results obtained with first month of data have been recently published, reporting the first observation of the $\beta\beta2\nu$-decay of ^{136}Xe (only few months before Kamland-Zen). The EXO-200 target is to reach a level of background of $\sim 10^{-3}$ cts/(keV.kg.yr) in the $\beta\beta0\nu$ energy region. With the fiducial volume efficiency of 40%, the expected sensitivity is $T^{0\nu}_{1/2} > 6\ 10^{25}$ y (90% C.L.) after 5 years of data collection. In order to reduce the background for a ton scale experiment, the ultimate goal of the EXO collaboration is to develop the so-called barium tagging. It consists of tagging the Ba^{++} ion ($\beta\beta$ decay daughter of ^{136}Xe) with otpical spectroscopy methods by laser fluorescence excitation. Research and development for Barium ion grabbing and tagging is ongoing in parallel with the EXO-200 experiment.

The use a high pressure gaseous Xenon (HPXe) TPC provides an higher energy resolution and a partial recontruction of the tracks in order to identify the $\beta\beta$ event topology. The NEXT collaboration (Canfranc, Spain) proposed to use the electroluminescence technique for the TPC readout. An energy resolution of 1% FWHM at 662 keV (corresponding to 0.5% at $Q_{\beta\beta}$) has been measured with a prototype running at 15 bars. The NEXT-100 TPC chamber, with a volume of $\approx$ 2 m^3, is under construction, and will contain 100 kg of enriched Xenon gas at a pressure of 10 bars. It is foreseen to be installed in Canfranc end of 2013, although the construction of the detector is not yet totaly funded. The target is to reach an energy resolution better than 1% FWHM at $Q_{\beta\beta}$, with a level of background of $2\ 10^{-4}$ cts/(keV.kg.yr) in the $\beta\beta0\nu$ energy region, and a $\beta\beta$ efficiency of 30% taking into account the $\beta\beta0\nu$ topological signature for background suppression.

The T-REX R&D program (Zaragoza-Canfranc, Spain) is studing the MICROMEGAS technique for an alternative TPC readout. Standard microbulk micromegas planes, manufactured out of kapton and copper foils, are today available in large surface and are very

radiopure. A first prototype has demonstrated the capability of micromegas readouts to work in high pressure Xe. A second larger prototype is under development in order to measure the energy resolution and the topology signature capability in real conditions.

I emphasize that one of the most critical background for Xenon TPC comes from the rare 2447 keV γ-ray emitted by ^{214}Bi. When the γ is totaly contained, it produces a peak very close to the $Q_{\beta\beta}$-value of 2462 keV.

Crystals at room temperature

CANDLES proposes to use natural CaF_2 crystals as scintillating detectors for the measurement of the isotope ^{48}Ca. The main advantage of ^{48}Ca is its high transition energy $Q_{\beta\beta} = 4274$ keV. Unfortunately, its natural abundance is very low, only 0.187% and it is today technically very difficult to enrich it. CANDLES-III (Kamiokande, Japan) is an array of 96 natural CaF_2 crystals, for a total mass of ≈ 300 kg, corresponding to about 300 g of ^{48}Ca. Crystals are immersed in a two-phase liquid scintillator which acts as an active veto gainst external background. The achieved energy resolution is $\approx 4.5\%$ FWHM at $Q_{\beta\beta}$. The commissioning of the detector has started in June 2011.

Potential ^{238}U and ^{232}Th contaminations inside the crystals or in the liquid scintillator in the vicinity of the crystals can produce background by the pile-up of $(\beta+\gamma)$ from ^{208}Tl decay or by the pile-up of $(\beta + \text{delay } \alpha)$ from the $Bi - Po$ cascades. This second background can be identified using a pulse shape analysis with a rejection efficiency of $\approx 90\%$. Taking into account the radiopurity measurement of the crystals, ≈ 30 μBq/kg in ^{238}U and ^{232}Th chains, the expected level of background in the $\beta\beta0\nu$ energy region (estimated by Monte-Carlo) is about 10^{-3} cts/(FWHM.kg.yr), equivalent to about 0.3 counts per year. It corresponds to an expected sensitivity of $T^{0\nu}_{1/2} > 3.7\ 10^{24}$ yrs (90% C.L.) with 5 years of collected data.

A R&D program for ^{48}Ca enrichment is in progress, with two possible techniques : chemical process by migration of a calcium solution through "crown" Ether, and laser separation by radiation pressure. I remind that ^{48}Ca enrichment using AVLIS technique is also in progress in South Corea, with the aim to enrich 1 kg within 3 years. Two other improvements of the CANDLES experiment are also investigated : the purification of CaF_2 crystals at the level of about 1 μBq/kg and the improvement of the energy resolution, by cooling the CaF_2 crystals.

We also mention the COBRA project, in R&D phase. It consists of an array of ^{116}Cd-enriched CdZnTe semiconductor detectors at room temperature. Small scale prototypes have been realized at LNGS (Italy). The proved energy resolution is 1.9% FWHM. But level of background is still high. Recent results on pixellization shows that the COBRA approach may allow an excellent tracking capability, equivalent to a solid state TPC.

Summary of the expected sensitivities

I have tried to summarize in Table 6.1 and Figures 6.1 and 6.2 the expected sensitivities of the new $\beta\beta$ projects, on the limit half-life $T_{1/2}(\beta\beta0\nu)$ and on the corresponding effective Majorana neutrino mass $\langle m_{ee}\rangle$. The minimum and maximum $\langle m_{ee}\rangle$ values correspond to the uncertainty range of the nuclear matrix elements given in Tables 1.2 and 1.1.

Expected sensitivities have been calculated with 5 years of data collection, except GERDA Phase 1 (1 year), SuperNEMO demonstrator (2.5 years), CUORE-0 (2 years)

and SNO+ Phase 1 (3 years), and using the Feldman-Cousins statistical method [115].

For the scintillating bolometers, I have assumed a CUORICINO-like setup equipped with enriched scintillating bolometers, assembled in 13 layers of 4 crystals, each one with a dimension $5 \times 5 \times 5$ cm^3 (like in CUORICINO). It corresponds to a total volume of crystal of 6500 cm^3. The densities used for the calculation are : 7.9 g/cm^3 for $^{116}CdWO_4$, 4.3 g/cm^3 for $Zn^{100}MoO_4$, 4.7 g/cm^3 for $^{40}Ca^{100}MoO_4$ and 5.26 g/cm^3 for $Zn^{82}Se$. I have also assumed a level of background of 10^{-3} counts/(keV.kg.yr), corresponding to the conservative value estimated by Monte-Carlo.

I have assumed a fiducial volume of 50% for Kamland-Zen and 40% for EXO-200, and an efficiency of 30% for NEXT-100, due to topology signature. The efficiencies of the other calorimeter experiments are assumed to be 100%, although it might be slightly lower ($\approx$ 90%) due to additional background rejection.

I have intentionally not specified projects at the "ton scale", because I think that it does note make sense today. Each project is separated is different phases. Some are rather realistic, some are optimistic. I let the reader be judge. No... Actually, only real data will be judge !

Project	Phase	Isotope	Mass isotope	Energy resol. (FWHM at $Q_{\beta\beta}$)	Efficiency $\beta\beta0\nu$	Bkg at $Q_{\beta\beta}$ cts/(keV.kg.yr)	Bkg at $Q_{\beta\beta}$ cts/(FWHM.yr)	$T_{1/2}(\beta\beta0\nu)$ (90% C.L.)	$\langle m_{ee}\rangle$ (meV) m_{min}	m_{max}	start data
GERDA	Phase 1	^{76}Ge	20 kg	4 keV	~ 1	0.06*	5*	$2\ 10^{25}$ y	210	530	2011
					~ 1	10^{-2}	0.8	$3\ 10^{25}$ y	167	421	
	Phase 2	^{76}Ge	50 kg	3 keV	~ 1	10^{-3}	0.15	$2\ 10^{26}$ y	41	103	2013
	Phase 3	^{76}Ge	200 kg	3 keV	~ 1	10^{-3}	0.3	10^{27} y	29	73	
SuperNEMO	1 module	^{82}Se	7 kg	≈ 200 keV	~ 0.2	$\approx 5\ 10^{-5}$	0.07	$6.6\ 10^{24}$ y	190	460	End 2014
	20 modules	^{82}Se	100 kg	≈ 200 keV	~ 0.2	$\approx 5\ 10^{-5}$	1	10^{26} y	48	118	...
	20 modules	^{150}Nd(50%)	50 kg	≈ 200 keV	~ 0.2	$\approx 5\ 10^{-5}$	1	$0.3\ 10^{26}$ y	55	210	...
	20 modules	^{48}Ca(50%)	50 kg	≈ 200 keV	~ 0.2	$\approx 5\ 10^{-5}$	1	$0.75\ 10^{26}$ y	100	275	...
CUORE	CUORE-0	^{130}Te	11 kg	5 keV	~ 1	0.05	10	$6\ 10^{24}$ y	184	390	2012
	19 towers	^{130}Te	200 kg	5 keV	~ 1	0.01	37	10^{26} y	45	95	2014
	19 tow. + ssb	^{130}Te	200 kg	5 keV	~ 1	0.001	3.7	$6\ 10^{26}$ y	18	39	...
ZnSe	1 tower	^{82}Se	19.1 kg	5 keV	~ 1	10^{-3}	0.17	10^{26} y	48	118	...
ZnMoO4	1 tower	^{100}Mo	12.3 kg	5 keV	~ 1	10^{-3}	0.14	$0.7\ 10^{26}$ y	37	94	...
CaMoO4	1 tower	^{100}Mo	15.3 kg	5 keV	~ 1	10^{-3}	0.15	$0.8\ 10^{26}$ y	35	88	...
CdWO4	1 tower	^{116}Cd	16.4 kg	5 keV	~ 1	10^{-3}	0.25	$0.7\ 10^{26}$ y	60	113	...
K-Zen	Phase 1	^{136}Xe	300 kg	100 keV	~ 0.5	...	≈ 150*	$5.7\ 10^{24}$ y*	250	600	2011
	Phase 2	^{136}Xe	800 kg	80 keV	~ 0.5	...	$1-2$	$\approx 10^{26}$ y	60	140	2013
SNO+	^{nat}Nd	^{150}Nd	56 kg	210 keV	~ 1	...	40	$6\ 10^{24}$ y	130	470	2014
	^{enr}Nd (50%)	^{150}Nd	500 kg	210 keV	~ 1	...	40	$6\ 10^{25}$ y	40	150	...
EXO	EXO-200	^{136}Xe	160 kg	80 keV	~ 0.4	10^{-3}	16	$6\ 10^{25}$ y	77	185	2012
NEXT	NEXT-100	^{136}Xe	90 kg	25 keV	~ 0.3	$2\ 10^{-4}$	0.5	10^{26} y	60	143	2014
CANDLES	Candles-III	^{48}Ca	0.3 kg	210 keV	~ 1	10^{-3}	0.3	$4\ 10^{24}$ y	430	1200	2011
	13% enr.	^{48}Ca	20 kg	135 keV	~ 1	10^{-3}	0.3	$2.5\ 10^{26}$ y	54	150	2011

TABLE 6.1: Summary of the characteristics and expected sensitivities of current and possible future experiments. * refers to already obtained values. Otherwise, it corresponds to expected values. Limits on the $\beta\beta0\nu$ half-life $T_{1/2}(\beta\beta0\nu)$ have been calculated with 5 years of collected data, except GERDA Phase 1 (1 year), SuperNEMO demonstrator (2.5 years) and CUORE-0 (2 years), and using the Feldman-Cousins method [115]. The corresponding limits on the effective Majorana neutrino mass $\langle m_{ee}\rangle$ have been calculated using the nuclear matrix elements given in Tables 1.2 and 1.1.

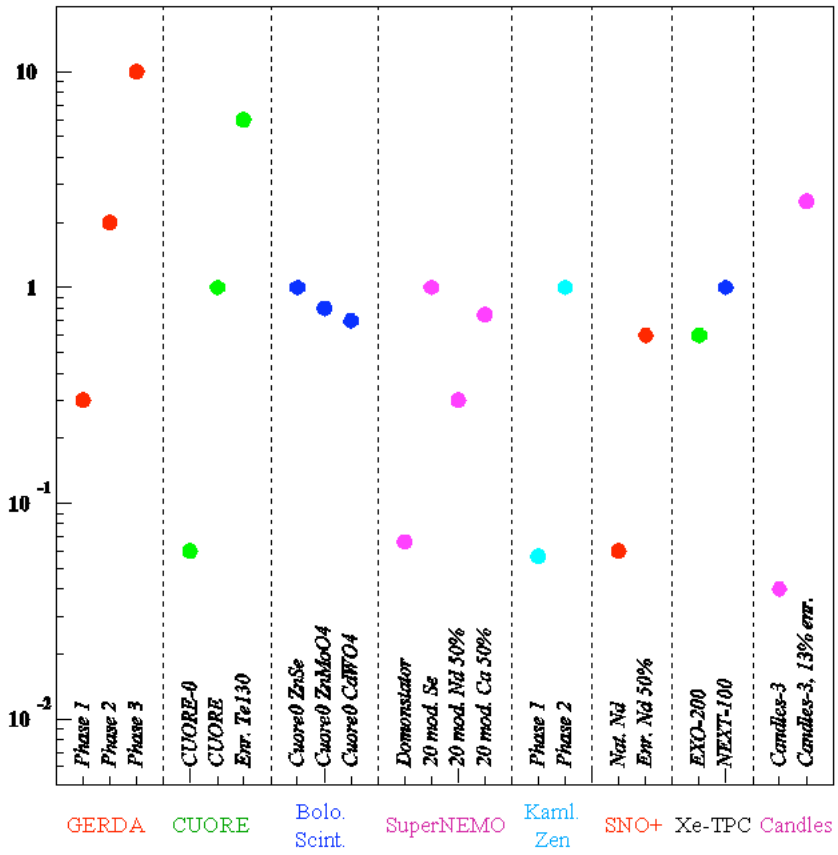

FIGURE 6.1: Expected sensitivity on $T^{0\nu}_{1/2}$ (90% C.L.) in 10^{26} years, for current or possible future experiments. See text for discussion.

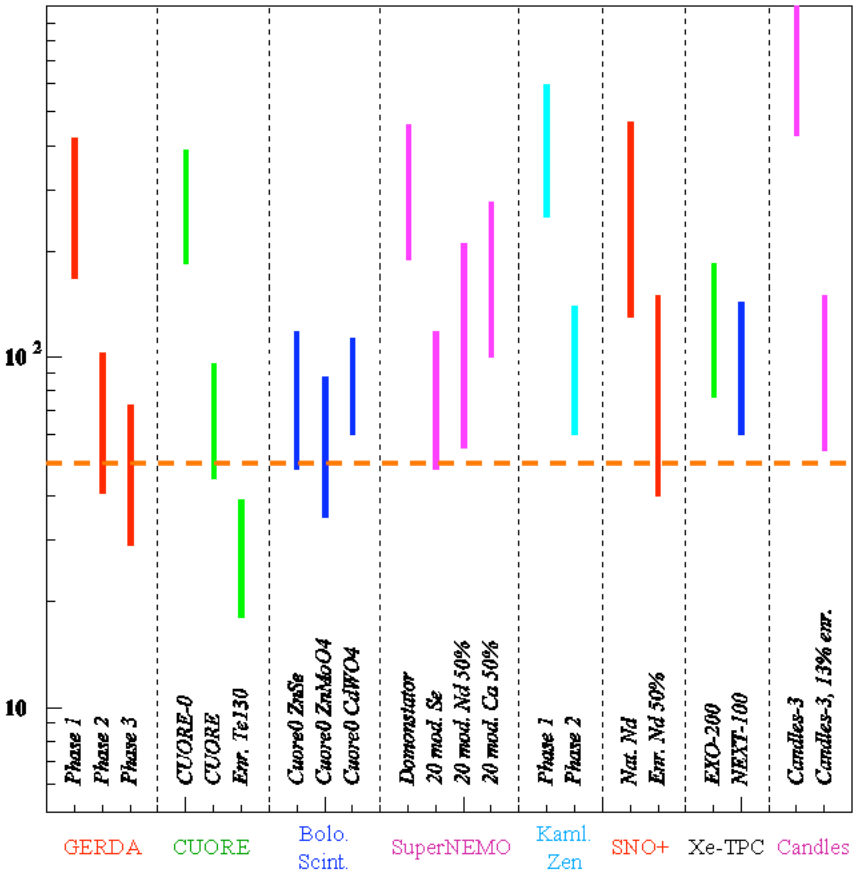

FIGURE 6.2: Expected sensitivity on the effective Majorana neutrino mass $\langle m_{ee} \rangle$ (in meV), for current or future possible experiments (see text for discussion). The horizontal dashed line corresponds to the upper limit of the inverted hierarchy region.

Deuxième partie

The BiPo detector

Chapitre 7

General description of the BiPo detector

7.1 Introduction

One of the troublesome sources of background for SuperNEMO is a possible contamination inside the source foils of ^{208}Tl ($Q_\beta = 4.99$ MeV) and ^{214}Bi ($Q_\beta = 3.27$ MeV) produced from the decay chains of ^{232}Th and ^{238}U respectively. The required radiopurities of the SuperNEMO double beta decay foils are $\mathcal{A}(^{208}\text{Tl}) < 2$ μBq/kg and $\mathcal{A}(^{214}\text{Bi}) < 10$ μBq/kg in order to achieve the desired SuperNEMO sensitivity. A first radiopurity measurement of purified selenium samples can be performed by γ spectrometry with ultra low background HPGe (High Purity Germanium) detectors. However the best detection limit that can be reached with this technique for ^{208}Tl is around 50 μBq/kg, which is one order of magnitude less sensitive that the required value. In order to achieve the required sensitivity for SuperNEMO, the collaboration has decided to develop a BiPo detector dedicated to the measurement of ultra-low levels of contamination in ^{208}Tl and ^{214}Bi in the foils. Moreover, it must be able to qualify the radiopurity of the foils in their final form, before installation into the SuperNEMO detector, and the measurement must not exceed a few months.

In 2007, a 3 years R&D program, funded by ANR, has been carried out in order to validate the BiPo measurement technique and to measure the different components of the background. Three different prototypes have been developed in order to explore different techniques for the final BiPo detector.

- The BiPo-1 prototype uses face-to-face thin scintillators coupled directly to low radioactive PMT's by an optical guide
- The BiPo-phoswich prototype is similar to BiPo-1 but it uses the phoswich technique
- The BiPo-2 prototype uses a single large scintillator plate coupled on its extremities to multiple PMT's in order to get a more compact geometry.

Results of the BiPo-1 prototype have shown that the background is at the required level and that a sensitivity of few μBq/kg in ^{208}Tl is reachable.

Thus end of 2009, the collaboration has decided to build a medium-size BiPo detector named BiPo-3, with a total surface area of 3.6 m^2 using the BiPo-1 technique and geometry. The size of the detector is a compromise to fulfil the requirements of a relatively small detector and a good enough sensitivity in order to quantify the radiopurity of the first

selenium $\beta\beta$ foil sources used for the SuperNEMO demonstrator. The construction of the detector is almost complete and its installation will start in Canfranc mid-2012.

In this report, I will first present the experimental principle of the BiPo detector, the possible components of observable backgrounds and the detection efficiency calculated by simulation. I will then present the results obtained with the BiPo-1 prototype. A summary of the results obtained with the two other BiPo-2 and phoswich prototypes will be presented and the choice for the BiPo-1 technique will be discussed. Finally I will present the final BiPo-3 detector and I will give a status report of its construction and commissioning.

7.2 Measurement principle of the BiPo detector

In order to measure ^{208}Tl and ^{214}Bi contaminations, the underlying concept of the BiPo detector is to detect with organic plastic scintillators the so-called BiPo process, which corresponds to the detection of an electron followed by a delayed α particle. The ^{214}Bi isotope is a (β,γ) emitter (Q_β = 3.27 MeV) decaying to ^{214}Po, which is an α emitter (7.7 MeV) with a half-life of 164 μs. The ^{208}Tl isotope is measured by detecting its parent, ^{212}Bi. Here ^{212}Bi decays with a branching ratio of 64% via a β emission (Q_β = 2.25 MeV) towards the daughter nucleus ^{212}Po which is a pure α emitter (8.78 MeV) with a short half-life of 300 ns (Figure 7.1).

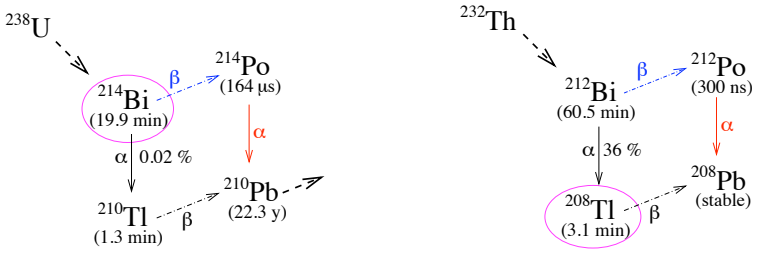

FIGURE 7.1: BiPo processes for ^{214}Bi and ^{208}Tl measurement.

The BiPo experimental intent is to install the double beta decay source foil of interest between two thin ultra-radiopure organic plastic scintillators. The ^{212}Bi (^{208}Tl) and ^{214}Bi contaminations inside the foil are then measured by detecting the β decay as an energy deposition in one scintillator without a coincidence from the opposite side, and the delayed α as a delayed signal in the second opposite scintillator without a coincidence in the first one. Such a BiPo event is identified as a *back-to-back* event since the β and α enter different scintillators on opposite sides of the foil. The timing of the delayed α depends on the isotope to be measured (Figure 7.2). The energy of the delayed α provides information on whether the contamination is on the surface or in the bulk of the foil.

A second topology of BiPo events can in principle be used. This involves the *same-side* BiPo events for which the prompt β signal and the delayed α signal are detected in the same scintillator without a coincidence signal in the scintillator on of the opposite side. The detection of the *same-side* events would increase by about 50% the BiPo efficiency. However, it will be shown in section 8.7 that the level of background measured in BiPo-1 using the *same-side* topology is much larger than the one measured in the *back-to-back* topology. For this reason, only *back-to-back* topology will be used for the rest of the BiPo-1 analysis.

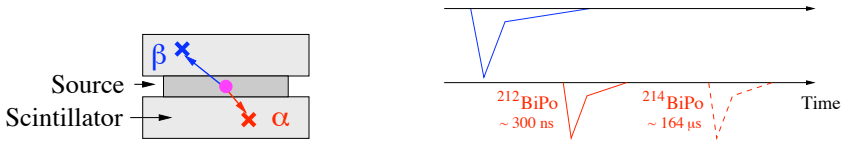

FIGURE 7.2: The BiPo detection principle with plastic scintillators and the time signals seen with PMT's for a *back-to-back* BiPo event. On the left image, the dot represents the contamination, the blue and red crosses represent energy depositions in the scintillators by the prompt beta and the delayed α respectively.

7.3 The different components of the background

7.3.1 Random coincidences

The first limitation of the BiPo detector is the rate of random coincidences between the two scintillators giving a signal within the delay time window (Figure 7.3a). A delay time window equal to about three times the half-life of the α decay is choosen (1 μs for ^{212}Bi and 500 μs for ^{214}Bi) in order to contain a large part of the signal and to minimize the random coincidence. The single counting rate is dominated by Compton electrons due to external γ. BiPo must be built with thin scintillators, with low radioactivity materials and installed inside a low radioactivity shield in an underground laboratory in order to reduce the γ event rate. Additionally pulse shape analysis of the delayed signal is performed in order to discriminate between electrons and α events, thus rejecting random Compton electron coincidences due to external γ.

7.3.2 Radiopurity of the scintillators

The second source of background that mimics a BiPo event comes from ^{212}Bi or ^{214}Bi contamination on the surface of the scintillator that is in contact with the foil. This surface contamination of the scintillators produces a signal indistinguishable from the true BiPo signal coming from the source foil, as shown in Figure 7.3b.

In principle, ^{212}Bi or ^{214}Bi contamination in the scintillator volume (bulk contamination) is not a source of background, because the emitted electron should trigger one scintillator block before escaping and entering the second one, as shown in Figure 7.3c. The two fired scintillator blocks are in coincidence and this background event is rejected. However, if the contamination is not deep enough inside the scintillator but quite near the surface, the electron from the ^{212}Bi-β decay will escape the first scintillator and will fire the second one without depositing enough energy to trigger the first one. It will appear exactly like a BiPo event emitted from the foil.

7.3.3 Radon and thoron

Other possible sources of background are via thoron (^{220}Rn) or radon (^{222}Rn) contamination of the gas between the foil and the scintillators. Thoron and radon decay to ^{212}Bi and ^{214}Bi respectively and a bismuth contamination on the surface of the scintillators is thus observed. In order to suppress this source of background, radiopure gas and materials without thoron and radon emanation around the scintillators are required.

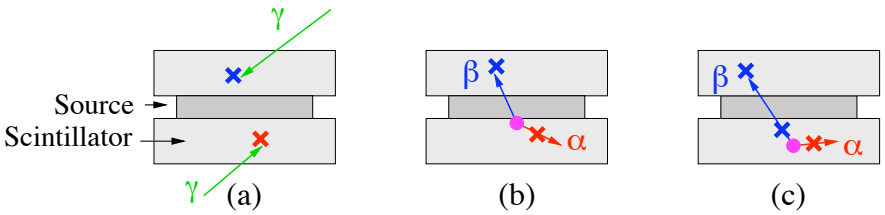

FIGURE 7.3: Illustration of the possible sources of background : (a) random coincidences due to the γ flux, (b) ^{212}Bi or ^{214}Bi contamination on the surface of the scintillators and (c) ^{212}Bi or ^{214}Bi contamination in the volume of the scintillator. The dots correspond to the contamination, the blue and red crosses represent the prompt and delayed signals respectively.

7.4 Detection efficiency

7.4.1 Energy quenching of α particles

The efficiency of the BiPo detector is limited by the capacity of an α to escape from the source foil being measured, and then deposit an amount of scintillation light above the detection threshold. Due to the very large stopping power for α particles and subsequent large excitation-to-scintillation energy partition, the amount of light produced by an α is smaller than that produced by an electron of the same energy. As it will be described in the next section, the uncertainty in the quenching factor, defined as the ratio of the amount of light produced by an electron to the one produced by an α of the same energy, is one of the main systematic error of the BiPo efficiency, which is estimated to be 20%.

A dedicated measurement of the quenching factor has been performed with the polystyrene-based plastic scintillators used in BiPo [122] for different α energies. The α particles of 5.5 MeV emitted by an ^{241}Am source were used. Their energies have been reduced either by adding successively 6 μm Mylar foils, or by adding a precise distance of air (minimum 0.9 mm) between the source and the scintillator. A dedicated setup (Figure 7.4) has been developed which allows to control the distance of air. A mylar diaphragm has been added on the entrance surface of the scintillator in order to reduce the deposited energy spread of the alphas. In order to have a constant collection efficiency of the scintillation light on the PMT, a 6 μm aluminized mylar has been added on the entrance surface of the scintillator.

A GEANT4 simulation of α particles emitted by ^{241}Am, either crossing several foils of Mylar, or a variable distance of air has been done in order to determine the expected energy spectrum deposited in the scintillator (see Figure 7.5). Then the quenching factor is calculated by comparing the observed energy (see Figure 7.6) with the energy obtained with 1 MeV electrons from a ^{207}Bi source.

Results of the measured quenching factors are presented in Figure 7.7. The value of the quenching factor for α's with an energy of 8.78 MeV has been obtained separately using NEMO-3 data by analysing the BiPo decays on the surface of the NEMO-3 scintillators. A new setup using an aluminized scintillator is under development in order to remove the aluminized mylar and consequently to improve the accuracy of the measurement. As it will be discussed in next sections, the energy threshold used in BiPo for delayed signal is

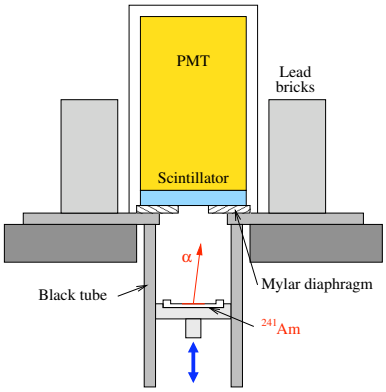

FIGURE 7.4: Setup developed to measure the quenching factors of α's in the organic plastic scintillator using an air absorber.

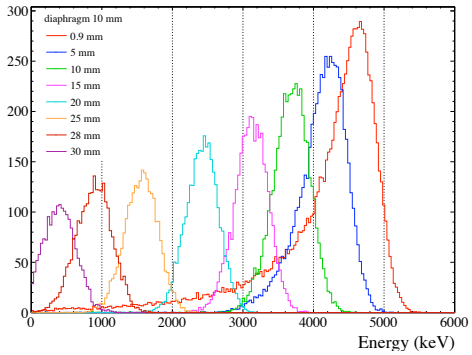

FIGURE 7.5: Expected charge spectrum deposited in the polystyren scintillator by α particles emitted by ^{241}Am, and crossing different distances of air, calculated by GEANT4 simulation.

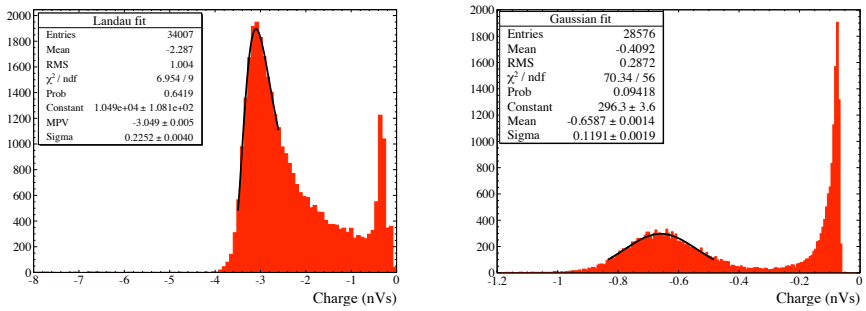

FIGURE 7.6: Example of two measured charge spectra for alphas emitted by an ^{241}Am with two different distances of air : (left) 0.9 mm of air ; (right) 25 mm of air.

150 keV, which corresponds for an α particle to an energy of about 2.5 MeV. Thus the quenching factor for alphas at lower energy is not an issue here.

Recently a semi-empirical method of calculating the quenching factors for scintillators has been proposed and is described in [123]. It is based on Birk's formula with the

total stopping power for electrons and ions which are calculated with the ESTAR and SRIM codes. The method has only one free parameter, the Birk's factor k_B [124]. Our measurements are in relative good agreement with the calculation with a Birk's factor, $k_B = 9.0 \times 10^{-3}$ g MeV^{-1} cm^{-2}. An effective model of the quenching factor, which fits the measured values has been used for the BiPo simulations and is presented in Figure 7.7.

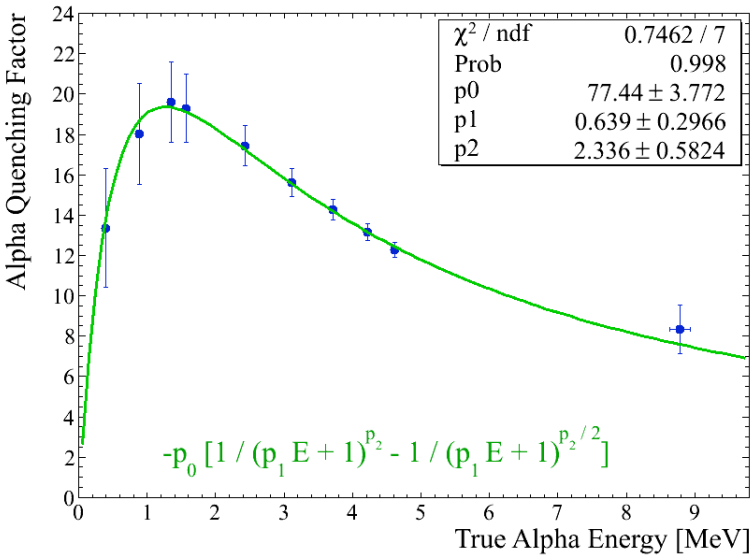

FIGURE 7.7: Quenching factors of α's in the organic plastic scintillator as a function of the energy deposited by the α on the scintillator : the blue dots correspond to the measured values using air absorber and the green curve to the effective values used in the BiPo simulations.

7.4.2 Efficiencies

The efficiency of the BiPo detector has been calculated with a GEANT4 Monte Carlo simulation. The ^{212}BiPo events have been simulated assuming a uniform ^{212}Bi contamination in the volume of a ^{82}Se foil 40 mg/cm^2 (80 μm) thick. Only *back-to-back* BiPo events have been selected. The *back-to-back* BiPo event is recognized as a prompt signal above 100 keV without any coincident signal above 10 keV in a second PMT of the opposite side. This signal is then followed by a delayed signal above 150 keV in the second PMT (delayed α particle) without a coincident signal above 10 keV in the first PMT. The BiPo events are rejected in the case of a back-scattering of the β in one scintillator, with a deposited energy above the 10 keV threshold, before entering the second scintillator. Such events with two scintillators in prompt coincidence are rejected as candidates of ^{212}Bi contamination in the scintillators (see section 7.3). The energy thresholds have been determined at posteriori from the results obtained with the BiPo-1 prototype.

The total efficiency to detect a BiPo cascade is 5.5% [1].

1. If both the *back-to-back* and the *same-side* events are selected, the total efficiency becomes equal to

The systematic error on the efficiency is dominated by the uncertainty on the energy threshold for α's. The value of the energy threshold is correlated to three parameters : the exact values of the quenching factor of the α's, the BiPo-1 energy calibration, and the effective corrections of the non-uniformity of the light collection along the surface of the scintillators. Taking into account the possible systematic errors on these three parameters, one estimates that the error on the energy threshold for α's is within a factor of 2. The variation of the BiPo efficiency as a function of the energy threshold is shown in Figure 7.8. The efficiency depends very slightly on the energy threshold of the prompt β signal. However, the efficiency varies by $\pm 20\%$ if the energy threshold of the delayed α signal varies from 75 keV to 300 keV. Thus the systematic error of the BiPo efficiency is estimated to be 20%.

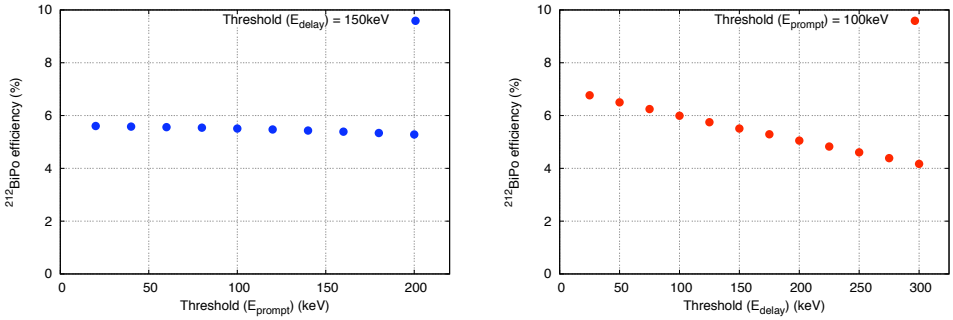

FIGURE 7.8: BiPo detection efficiency for ^{212}Bi calculated by Monte Carlo simulations : (left) as a function of the energy threshold to detect the prompt signal assuming an energy threshold of the delayed signal of 150 keV ; and (right) as a function of the energy threshold to detect the delayed signal assuming an energy threshold of 100 keV for the prompt signal.

The BiPo efficiency depends on the localization of the ^{212}Bi and ^{214}Bi contamination in the foil. If the contamination is only on the surface of the foil, the BiPo efficiency is larger and has been calculated to be 10%. The BiPo efficiency depends also on the composition of the foil. For instance with an aluminium foil 40 mg/cm^2 (150μm) thick which has been used to calibrate BiPo-1 (see section 8.5), the BiPo efficiency calulated by simulation is only 3.4%. The difference in efficiency between aluminium and selenium foils is explained by their different Z/A ratios. This ratio is larger for aluminium (Z/A=13/27=0.48) than for ^{82}Se (Z/A=34/82=0.41). Therefore the ionization by an α particle is larger in an aluminium foil, consequently, its probability to escape from it is smaller than from a selenium foil. A summary of the calculated BiPo efficiencies with different cases is given in Table 7.1.

8.3%

Type of foil	Type of contamination	Efficiency
^{82}Se 40 mg/cm^2	Bulk	5.5%
^{82}Se 40 mg/cm^2	Surface	10%
Aluminium 40 mg/cm^2	Bulk	3.4%
No foil	Scintillators surface	27%

TABLE 7.1: BiPo efficiencies calculated by Monte-Carlo simulations for different types of measurements.

Chapitre 8

The BiPo-1 prototype

8.1 Description of the BiPo-1 prototype

The BiPo-1 detector is composed of 20 similar modules. Each module consists of a gas and light tight box, containing two thin polystyrene-based scintillator plates of dimension $200\times200\times3$ mm^3 which are placed face-to-face. Each scintillator plate is coupled to a low radioactivity 5" photomultiplier (PMT R6594-MOD from Hamamatsu) by a UV Polymethyl Methacrylate (PMMA) light guide (Figure 8.1). Each module has a sensitive surface area of 0.04 m^2. The scintillators have been prepared with a mono-diamond tool from scintillator blocks produced by JINR Dubna (Russia) for NEMO-3. The surface of the scintillators facing the source foil has been covered with 200 nm of evaporated ultra-pure aluminum in order to optically isolate each scintillator and to improve the light collection efficiency. The entrance surface of the scintillators has been carefully cleaned before and after aluminium deposition using the following cleaning sequence : acetic acid, ultra pure water bath, isopropanol and finally a second ultra pure water bath. The sides of the scintillators and light guides are covered with a 0.2 mm thick Teflon layer for light diffusion. Materials of the detector have been selected by HPGe measurements to confirm their high radiopurity. Table 8.1 gives the total radioactivity for the components of a BiPo-1 module.

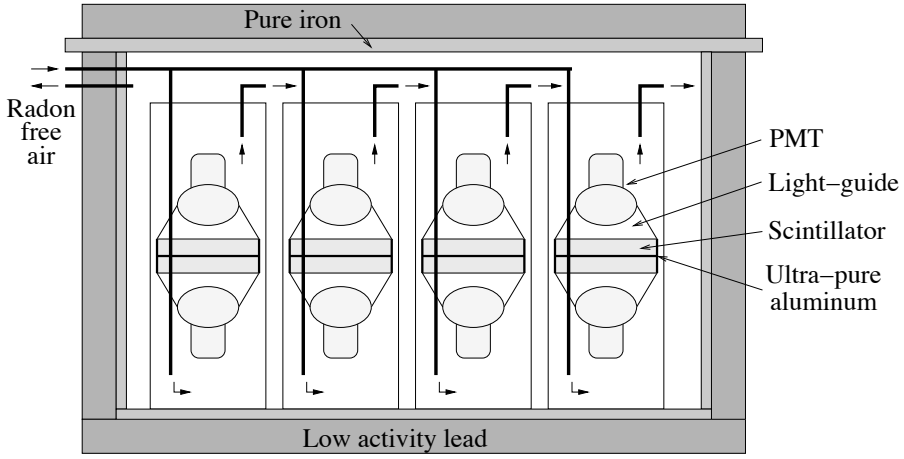

FIGURE 8.1: Schematic view of the BiPo-1 prototype inside its shield.

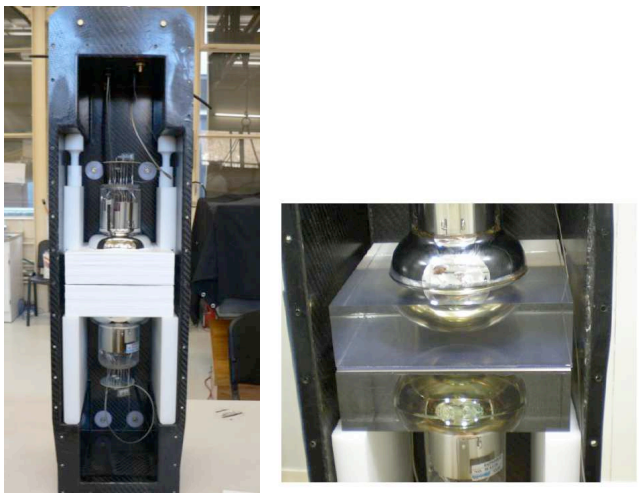

FIGURE 8.2: Photos of the BiPo-1 prototype.

Type of materials	^{232}Th	^{238}U	^{40}K	^{210}Pb
Photomultipliers	0.028	0.48	1.0	
PMMA (light guide)	<0.01	< 0.015	<0.15	
Module containers (carbon fiber)	0.09	0.06	0.7	
Black polyethylene	<0.003	0.01	0.2	
Screws	<0.01	<0.01	<0.03	1.1
Glue	<0.002	<0.004	<0.01	
Cables and gas tubes	<0.002	<0.004	<0.01	

TABLE 8.1: Radioactivity HPGe measurements for the BiPo-1 materials. Activities are given in Bq per BiPo-1 module.

The modules are shielded by 15 cm of low activity lead which addresses the external γ flux. The upper part of the shield which supports the lead is a pure iron plate 3 cm thick. Radon-free air ($\mathcal{A}$(radon) of few mBq/m^3) flushes the volume of each module and also the inner volume of the shield.

The first three modules of BiPo-1 were initially installed in the new Canfranc Underground Laboratory in Spain. Due to the temporary closure of this Laboratory, BiPo-1 was completed in the Modane Underground Laboratory where it has been running since May 2008.

8.2 Electronic readout, trigger and acquisition

Photomultiplier signals are sampled with MATACQ VME digitizer boards [120] developed by LAL Orsay and IRFU Saclay (see Figure 8.5). The features of the MATACQ board are the following : 4 channels, 2.5ms time window, 1 GS/s high sampling rate, 12-bit amplitude resolution and 1 Volt amplitude dynamic range. The level of the electronic noise is about 250 μV (r.m.s.).

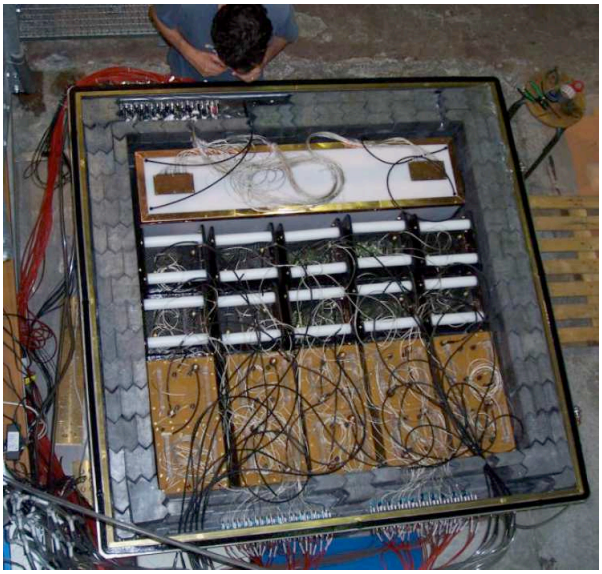

FIGURE 8.3: Photos of the BiPo-1 prototype.

The gain of the PMT is adjusted in order to have a signal amplitude of about 500 mV for 1 MeV electron. The single photoelectron level is about 1 mV corresponding to about 2 keV. The acquisition is triggered each time a PMT pulse reaches 50mV, corresponding to an energy threshold of 100 keV.

The trigger logic is illustrated in Figure 8.4. The signals of the trigger PMT and its face-to-face neighbourg PMT are sampled during 1.5 ms. After a 10 μs dead time, a watchdog of 1 ms is started, waiting for a possible second delayed pulse above 10 mV (20 keV) in these two PMT's. If the second delayed trigger is validated, pulses of the two PMT's are sampled during 1 ms. Finally, the prompt and delayed samplings are stored on computer. If no second delayed trigger is validated, only the first prompt sampling is stored. The first prompt trigger allows tagging the ^{212}Bi$\rightarrow^{212}$Po cascade and the second delayed trigger allows tagging the ^{214}Bi$\rightarrow^{214}$Po cascade.

A dedicated trigger board (see Figure 8.5) has been developed in LAL Orsay in order to trigger both the ^{212}Bi$\rightarrow^{212}$Po and the ^{214}Bi$\rightarrow^{214}$Po cascades with this double sampling technique. We use one trigger board to control 5 MATACQ digitizer boards (20 channels or PMT's). Thus two trigger boards and 10 MATACQ boards have been used for the BiPo-1 prototype. Details of the trigger board and its connection to the MATACQ boards are shown in Figure 8.6.

The trigger board has been available only in mid-2009, while BiPo-1 prototype was already running with MATACQ board alone in auto trigger mode. Thus the first phase of data collection with BiPo-1 ran until June 2009 and was dedicated to the background measurement of ^{212}Bi (^{208}Tl). In a second phase, the new trigger board was installed in July 2009 in order to measure simultaneously the ^{212}Bi and ^{214}Bi background.

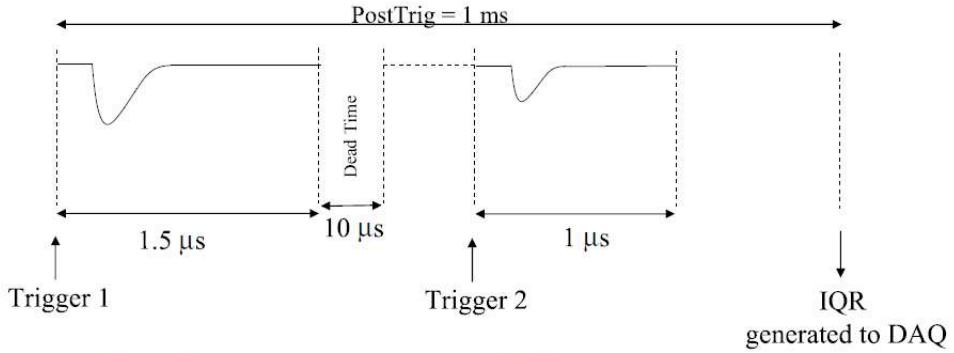

- MATACQ Sampling of the PMT signal during 1.5 µs
- Dead time during ~ 10 µs in order to avoid any trigger on PMT delay noise (refiring, bounce)
- MATACQ Sampling of the PMT signal during 1 µs in case of a second delay hit
- IQR generated after 1 ms

FIGURE 8.4: Trigger logic

FIGURE 8.5: (Left) Picture of the MATACQ digitizer board; (Right) Picture of the BiPo double sampling trigger board.

8.3 Energy and time calibration

The linearity and the gain stability of all PMT's were initially measured on a PMT test bench originally developed for the LHCb experiment [121]. During the assembly, each BiPo-1 module was also tested and calibrated in energy. An ^{241}Am source emitting 5.5 MeV α particles and a ^{207}Bi source emitting 1 MeV conversion electrons have been used. The test bench was successfully used to measure the response of the BiPo-1 modules over the entire surface of the scintillators. A decrease of 30% in the light collection was observed when the electron or α source was moved from the center of the scintillator to the edges. This non-uniformity is due to the fact that the PMT has been positioned very close to the scintillator (6 mm) in order to maximize the amount of detected light and to achieve an

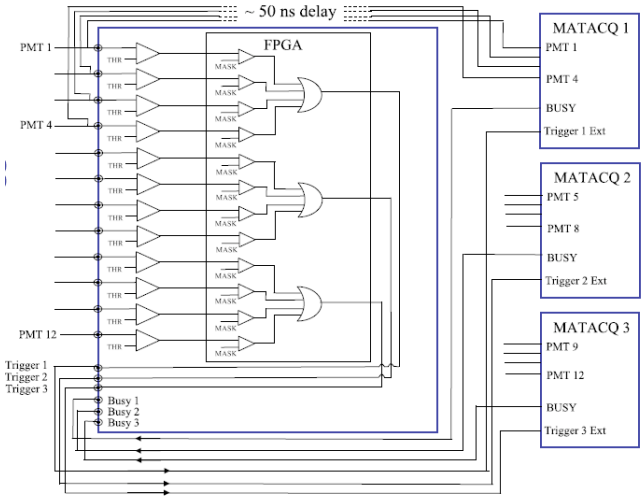

FIGURE 8.6: Trigger logic and connection to the MATACQ boards

energy threshold as low as possible. This non-uniformity of the light collection produces an uncertainty of about 30% on the value of the energy threshold. This uncertainty is negligible for the BiPo detection efficiency as it is shown in Figure 7.8. Moreover the energy measurement is not the critical issue for BiPo-1 since a BiPo event is recognized by its delay time and topology.

The energy and time calibrations of the 20-module BiPo-1 detector with its low radioactivity shield, were performed using a ^{54}Mn source (γ of 835 keV). The energy calibration was performed by measuring the Compton edge at 639 keV for electrons fully contained in one scintillator (Figure 8.7). The time calibration is performed by using a Compton electron produced in one scintillator which crossed over into the second scintillator (Figure 8.8). The average time difference between the two PMT's is measured and corrected in the BiPo analysis software.

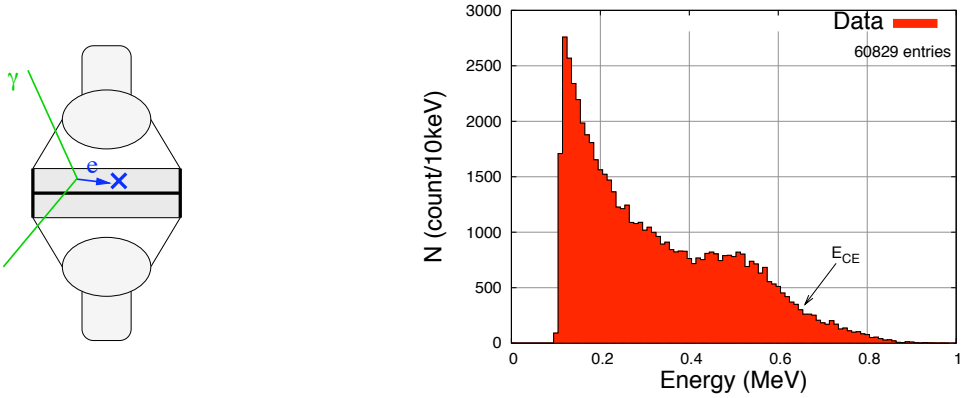

FIGURE 8.7: Energy calibration with a ^{54}Mn source : (left) showing the principle of the method and (right) an example of the energy spectrum obtained with a scintillator.

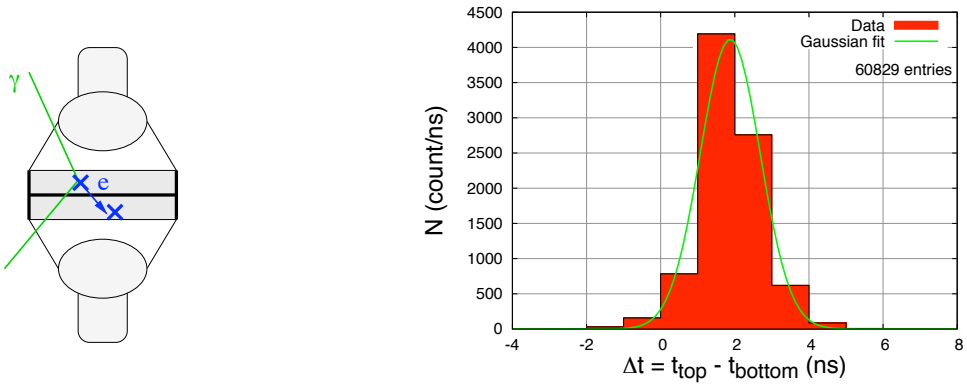

FIGURE 8.8: Time calibration with a ^{54}Mn source : (left) showing the principle of the method and (right) an example of the time distribution obtained with one module.

8.4 Selection of the BiPo events

The search for a BiPo cascade is performed in off line analysis by a study of the two sampled and recorded PMT signals from a given BiPo module. The *back-to-back* BiPo event is recognized as a prompt signal above 100 keV without any coincident signal above 10 keV in a second PMT of the opposite side. This signal is then followed by a delayed signal above 150 keV in the second PMT (delayed α particle) without a coincident signal above 10 keV in the first PMT. A minimum delay time of 20 ns is required in order to reject possible correlated signals due to an external particle shower produced by a cosmic ray or a high energy γ. The maximum delay time of 2.35 μs, given by the sampling board, corresponds to an efficiency of 99.6% to tag the delayed α from ^{212}Po. A true BiPo event observed with BiPo-1 is shown in Figure 8.9.

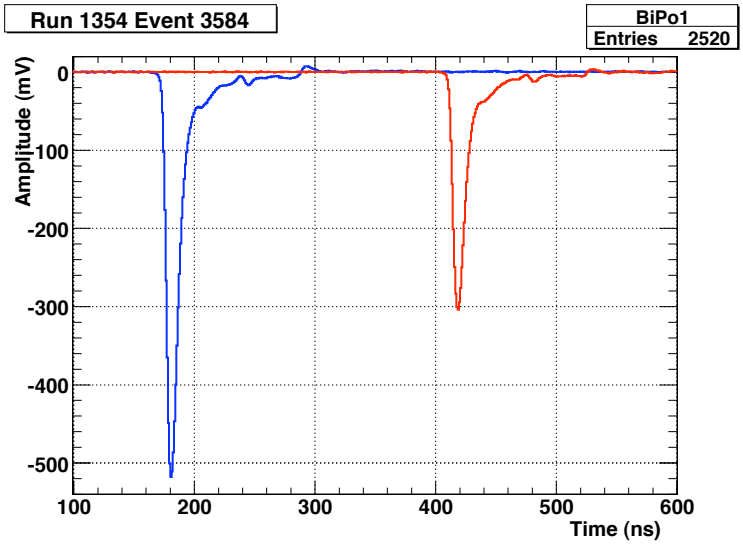

FIGURE 8.9: Example of a BiPo event observed in BiPo-1 : the blue curve is the prompt signal, the red curve is the delayed signal.

8.5 Validation of the BiPo-1 technique with a calibrated foil

The first BiPo-1 module was dedicated to test the detection of bulk ^{212}Bi contamination in a calibrated foil. A 150 μm thick aluminium foil (40 mg/cm^2) with an activity $\mathcal{A}(^{212}\text{Bi}\rightarrow^{212}\text{Po}) = 0.19 \pm 0.04$ Bq/kg was first measured with low background HPGe detectors, and then installed between the two scintillators of the BiPo-1 module.

After 160 days of data collection, a total of 1309 *back-to-back* BiPo events were detected. Taking into account the 3.4% efficiency calculated by GEANT4 simulations with a 20% systematic error (see section 7.4.2), this corresponds to an activity of $\mathcal{A}(^{212}\text{Bi}\rightarrow^{212}\text{Po}) = 0.16 \pm 0.005(stat) \pm 0.03(syst)$ Bq/kg, in agreement with the HPGe measurement. The distribution of the delay time between the two signals is presented in Figure 8.10. The half-life obtained from the fit is $\text{T}_{1/2} = 276 \pm 12(stat)$ ns. This measured half-life is in agreement with the experimental weighted average value of 299 ns for ^{212}Po [125]. These results confirm the measurement principle and the calculated efficiency.

The energy spectra of the prompt β and the delayed α are presented in Figure 8.10. There is good agreement with the expected spectra calculated by simulations. The energy spectrum of the first signal corresponds to a typical β spectrum with $Q_\beta = 2.25$ MeV. The energy spectrum of the delayed signal goes up to 1 MeV as expected for the α of 8.78 MeV from ^{212}Po and a quenching factor of $\text{Q}_f \sim 9$ at 8.78 MeV (see Figure 7.7). No evidence of a peak at the 1 MeV endpoint in the energy spectrum of the delayed α indicates that the radioactive contamination is inside the volume and not on the surface of the aluminium foil.

8.6 Discrimination of β and α particles

The excitation of the scintillator depends on many factors including the energy loss density and a larger dE/dx for alphas enhances the slow component of the decay curve. This behaviour has been already observed in organic liquid scintillators [126]. We show here that this difference is also observed in polystyrene-based plastic scintillator and can be used to discriminate alphas from electrons.

The average PMT signal obtained with a BiPo-1 module for electrons (^{207}Bi source) or α (^{241}Am source) is presented in Figure 8.11. A small but significantly larger component in the tail of the signal is well observed for α particles compared to electrons. A pulse shape discrimination was developed using this set of data. The discrimination factor χ is defined as the ratio of the charge q in the slow component to the total charge Q of the signal. The charge q is integrated from 15 ns after the signal peak to 900 ns. This integration window was optimized in order to maximize the discrimination.

This electron and α pulse shape discrimination has been applied to the set of the BiPo events detected with the calibrated aluminium foil inside a first BiPo-1 module in order to calculate its global efficiency. As shown in Figure 8.12, a good separation is observed for β and α signals although the discrimination becomes less efficient at low energy. By selecting a discrimination factor of $\chi > 0.2$ as applied to the delayed signal allows one to keep 90% of the true BiPo events and reject 85% of the random coincidences as is shown in Figure 8.13.

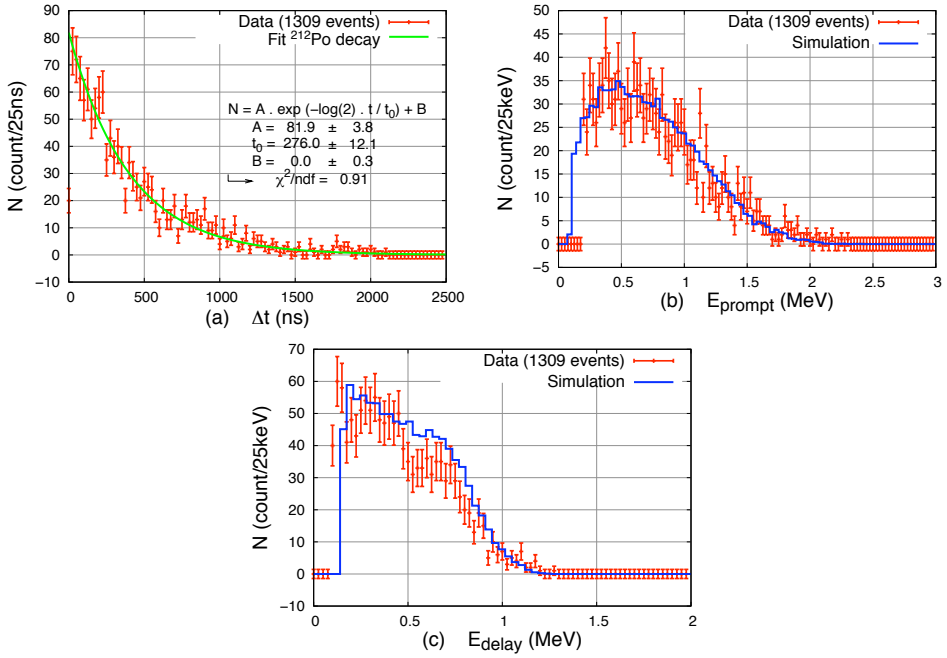

FIGURE 8.10: (a) The delay time distribution between the β and α decays, (b) energy distribution of the prompt β and (c) energy distribution of the delayed α, for the 1309 BiPo events detected with the calibrated aluminium foil. The red crosses are the data and the blue histograms are the distributions calculated by simulations. The green curve in the delay time distribution is the results of the exponential decay fit.

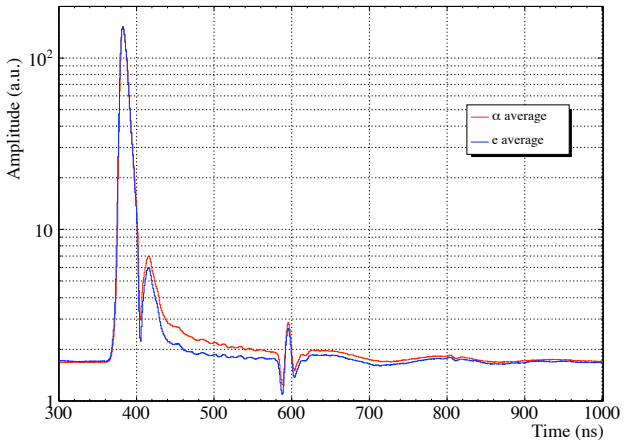

FIGURE 8.11: Average PMT signals obtained with a BiPo-1 module, in blue line for 1 MeV electrons (^{207}Bi source), and in red line for 5.5 MeV α (^{241}Am). The amplitudes have been normalized to the first peak. The secondary peaks are due to electronic bounces in the PMT HV divider due to an imperfect impedance matching.

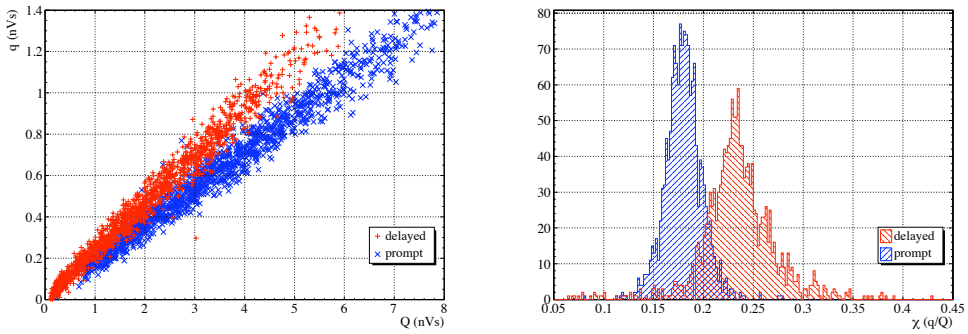

FIGURE 8.12: Discrimination of the prompt β and delayed α signals using the BiPo events measured with the calibrated aluminium foil : (Left) Distribution of the charge q in the slow component of the signal as a function of the total charge Q of the signal; (Right) Distribution of the discrimination factor $\chi = q/Q$.

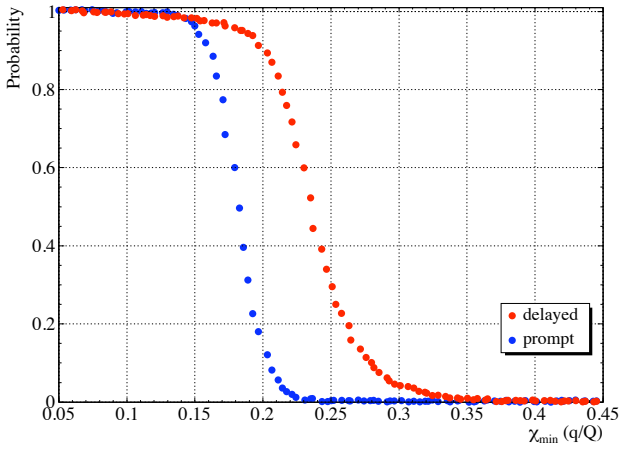

FIGURE 8.13: Probability of selecting an electron (blue dot) or an α (red dot) as a function of the lower limit χ_{min} set by the discrimination factor χ. The criterion $\chi > 0.2$ allows one to keep 90% of the α particles and to reject 85% of the electrons.

8.6.1 Random coincidences

The single counting rate τ_0 of a BiPo-1 scintillator without any coincidence in the opposite scintillator of the same module, measured in the Modane Underground Laboratory with an energy threshold of 150 keV, is $\tau_0 \approx 20$ mHz. This counting rate which is dominated by Compton electrons produced by external γ's is stable and independent of the modules. It corresponds to an expected number of coincidences for the ^{212}Bi measurement of $N_{coinc}(^{212}\text{BiPo}) = 2.10^{-3}$ events/(BiPo-1 module)/month, a negligible background.

This result can be extrapolated to a larger BiPo detector with a sensitive surface of 12 m^2. The number of random coincidences, N_{coinc}, is given by

$$N_{coinc} = 2 \,.\, N_{modules} \,.\, \tau_0^2 \,.\, \Delta T_{coinc} \,.\, T_{obs}$$

where $N_{modules}$ is the number of modules, ΔT_{coinc} is the delay time window and T_{obs} is the duration of the measurement. Given a detector composed of larger but thinner $300 \times 300 \times 1.5$ mm^3 scintillator plates, corresponding to a total of 130 modules, one can expect to have the same single counting rate τ_0 since the volume of the scintillator plates is the same as the one in the BiPo-1. The delay time window ΔT_{coinc} is chosen equal to three times the half-life of the delayed α decay of the polonium in order to contain 87.5% of the BiPo events. The expected number of coincidences for the ^{212}Bi measurement is $N_{coinc}(^{212}\text{BiPo}) = 0.25$ events/month, low enough to reach a sensitivity of 2 μBq/kg in ^{208}Tl as required by SuperNEMO.

However, for the ^{214}Bi measurement, the number of random coincidences $N_{coinc}(^{214}\text{BiPo})$ becomes too large because of the longer half-life of ^{214}Po and $N_{coinc}(^{214}\text{BiPo}) = 135$ events/month. This background can be reduced by applying the electrons-α discrimination defined earlier to the delayed signal in order to select only delayed α particles and reject the Compton electron coincidences. The number of random coincidences after electrons-α discrimination becomes $N_{coinc}(^{214}\text{BiPo}) = 20$ events/month. Given no other background component, this would correspond to a sensitivity of about 10 μBq in ^{214}Bi as required by the SuperNEMO experiment.

8.6.2 Measurement of the scintillator bulk radiopurity in ^{208}Tl

A BiPo-1 module has been dedicated to measure the bulk radiopurity of the organic polystyrene-based plastic scintillators produced by JINR Dubna and used in BiPo-1. This module is similar to a standard BiPo-1 module except that it is equipped with two thicker scintillator blocks $20 \times 20 \times 10$ cm^3 each, that are wrapped with aluminized Mylar. One of these blocks is from the NEMO-3 batch production used in BiPo-1. The second one is from a newer manufacturing process at JINR in 2007.

The ^{212}Bi contamination inside the scintillator blocks is recognized as a prompt signal from one PMT and a delayed signal of up to 1 μs from the same PMT. Since the delayed α is fully contained in the scintillator, its deposited energy in scintillation is expected to be around 1 MeV, due to the quenching factor. Thus, it is required that the energy of the delayed signal be greater than 700 keV (5 sigma less than 1 MeV). After 141 days of data collection, 10 events have been detected in the scintillator block from the NEMO-3 batch production and 24 events in the block from the new production. These numbers are in agreement with the expected number of BiPo events emitted from the aluminized Mylar surrounding the scintillator. However, if it is assumed that all the detected BiPo events come from a bulk contamination of the scintillators, a conservative upper limit on the contamination from ^{208}Tl in the scintillators would be :

- NEMO-3 batch production used in BiPo-1 : $\mathcal{A}(^{208}\text{Tl}) \leq 0.13$ μBq/kg
- New JINR Dubna production : $\mathcal{A}(^{208}\text{Tl}) \leq 0.3$ μBq/kg

Given a bulk contamination in the scintillator of $\mathcal{A}(^{208}\text{Tl}) = 0.13$ μBq/kg, the expected background level for BiPo-1, calculated by Monte Carlo simulations, is equal to 0.003 *back-to-back* BiPo events/month/module. For a larger BiPo detector with a sensitive surface of 12 m^2, this background corresponds to 0.9 BiPo-like events/month, which is low enough to reach the radiopurity performance required by SuperNEMO.

8.7 Measurement of the scintillators surface radiopurity

Surface radiopurity in ^{208}Tl

Thirteen BiPo-1 modules have been used for background measurements of the scintillator surfaces. The scintillators were placed face-to-face without a foil between them. After 488 days of data collection, a total of 42 *back-to-back* BiPo events have been observed. One module appeared to be more polluted with 12 events detected. The other events were uniformly distributed in the other 12 modules and in arrival time. The contaminated module has been removed from the analysis. For the 12 remaining modules, corresponding to an integrated scintillator surface of 468 m^2.days, only 30 *back-to-back* BiPo events have been observed. For the same period of 488 days of data collection, the expected number of random coincidences is about 0.2 (see section 8.6.1) and the expected background due to a bulk contamination in the scintillators has a maximum of 0.6 BiPo events (see section 8.6.2). Thus, the background observed in BiPo-1 corresponds to a ^{212}Bi bismuth contamination on the surface of the scintillators. Taking into account the 27% efficiency, calculated by simulations, to detect the BiPo cascade from a ^{212}Bi pollution on the surface of the scintillators (see Table 7.1) with a 20% systematic error, this corresponds to a surface background of the BiPo-1 prototype of $\mathcal{A}(^{208}\text{Tl}) = 1.5 \pm 0.3(stat) \pm 0.3(syst)$ μBq/m^2 in ^{208}Tl.

The distribution of the delay time between the two signals is presented in Figure 8.14. Despite the low statistics, it is compatible with an exponential decay distribution with a half-life of $T_{1/2} = 305 \pm 104(stat)$ ns. The energy spectra of the prompt β and delayed α signals, also presented in Figure 8.14, are in good agreement with the expected spectra calculated by the simulations. The energy distribution of the delayed signal is centered around 1 MeV as expected for the 8.78 MeV α emitted from ^{212}Po on the surface of the scintillators with a quenching factor of 9. The origin of the few events at lower energies is still unknown.

There are several possible origins of the surface background observed with BiPo-1. It might be due to contaminations either during the surface machining of the scintillator plates, during the cleaning procedure of the scintillators or during the evaporation of the aluminium on the entrance face of the scintillators [1]. A possible contamination of the deposited aluminium is unlikely to be the origin of the background. The radiopurity of this aluminium has been measured with low background HPGe and $\mathcal{A}(^{208}\text{Tl}) < 0.2$ mBq/kg. This radiopurity corresponds to less than 2 BiPo events, which is much less than the 30 background events observed in BiPo-1. Another possible origin of the observed background is a thoron contamination between the two scintillators. Considering a typical gap of air of 200 μm, the 30 observed background events would correspond to a thoron activity of the air of $\mathcal{A}(\text{thoron}) \sim 30$ mBq/m^3. However, this level of contamination seems too large compared to an estimation of thoron emanation from the PMT's.

The result of the background measured in BiPo-1 can be extrapolated to a larger BiPo detector. Figure 11.23 shows the expected sensitivity of the final BiPo-3 detector in ^{208}Tl as a function of the duration of the measurement. The calculation is done with a 3.6 m^2 selenium foil (40 mg/cm^2 thick) assuming that the surface background of this detector is the same as that measured in BiPo-1 ($\mathcal{A}(^{208}\text{Tl}) = 1.5$ μBq/m^2). The expected number of background events is equal to 5.1 counts/month. The required SuperNEMO sensitivity of

1. The evaporation was done with a sputtering setup which was carefully cleaned.

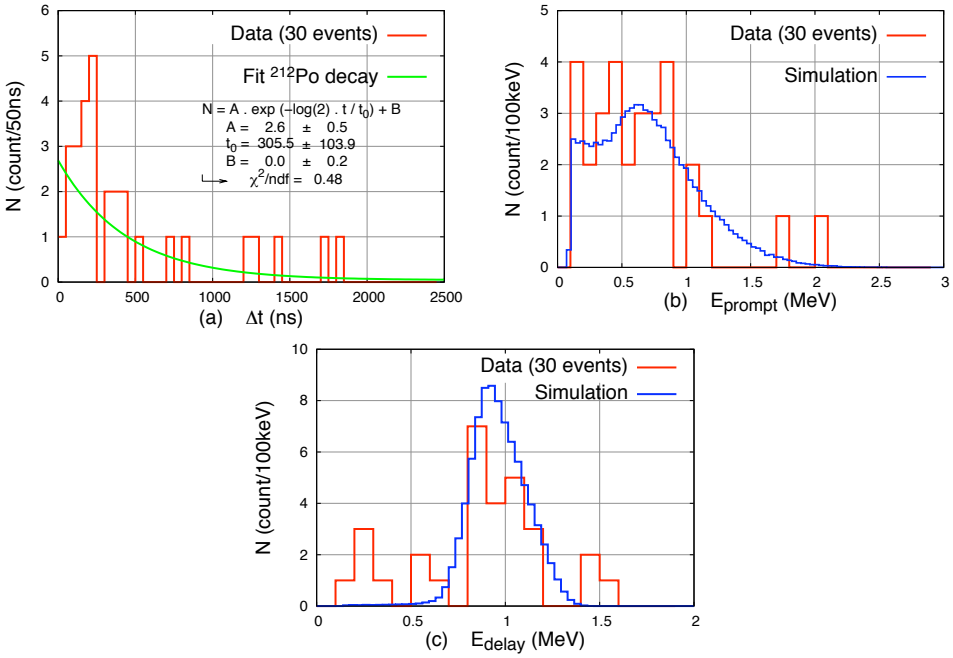

FIGURE 8.14: Distributions (a) of the delay time, (b) of the energy of the prompt signal and (c) the energy of the delayed signal, shown in red for the 30 BiPo background events observed during 423 days of data collected with 12 BiPo-1 modules, and in blue for the Monte-Carlo simulations. The green curve in the delay time distribution is the results of the exponential decay fit.

2 μBq/kg (90% C.L.) in ^{208}Tl could be obtained in one year of measurement. If the level of background is three times smaller, the required sensitivity of 2 μBq/kg can be reached after six months.

An analysis has also been performed by selecting the *same-side* BiPo events with prompt and delayed signals in the same scintillators in order to measure the background in this topology. A total of 223 *same-side* BiPo background events have been observed in Phase 1. It corresponds to a background about 7 times greater than the one measured in the *back-to-back* topology. The energy spectrum of the delayed signals is flat up to 1 MeV which rejects the hypothesis of contamination in the scintillator. The most probable origin of this background is a ^{212}Bi (^{208}Tl) contamination in the epoxy (Araldite 2020) which has been used to attach the scintillators to the optical guide. Taking into account the uncertainty of the thickness of the epoxy, this would correspond to an activity in ^{208}Tl of the Araldite 2020 of $\mathcal{A}(^{208}\text{Tl}) = 0.5 \pm 0.3$ mBq/kg.

Surface radiopurity in ^{214}Bi

A high number of ^{214}Bi-^{214}Po events have been observed during the background measurement. This level of background, about 10 to 100 times higher than the surface background

requirements, was due to radon background. This background indeed was correlated to the radon-free air flux. Large increase was also observed when the radon-trap facility was off. One of the main reason is that the PMT's, which is the main source of radon emanation, were not enclosed inside the separate tightness box.

In conclusion, special attention has been carried out for the design of the BiPo-3 detector in order to suppress the radon background, as discussed in Sections 11.1.3.

8.8 Summary of the BiPo-1 results

The BiPo-1 prototype with 0.8 m^2 of sensitive surface has been fully operational since May 2008 in the Modane Underground Laboratory. The detection efficiency has been experimentaly verified by measuring a calibrated aluminium foil. The random coincidences have been measured and are negligeable for ^{208}Tl. For ^{214}Bi, it has been verified that random coincidences can be reduced by applying an electrons-α discrimination with a high enough efficiency in order to reach the SuperNEMO required sensitivity in ^{208}Tl and ^{214}Bi. A first phase of data collection with BiPo-1 ran until June 2009 and was dedicated to the background measurement of ^{212}Bi (^{208}Tl). The most challenging background is a contamination on the surface of the scintillators in contact with the foils. After more than one year of data collection, a surface activity of $\mathcal{A}(^{208}\mathrm{Tl}) = 1.5 \pm 0.3(stat) \pm 0.3(syst)$ μBq/m^2 has been measured. Given this level of background, a larger BiPo-3 detector having few m^2 of active surface area, is able to qualify the radiopurity of the SuperNEMO selenium double beta decay foils with the required sensitivity of $\mathcal{A}(^{208}\mathrm{Tl}) < 2$ μBq/kg (90% C.L.) with a few months measurement. However, improvement of radon supression must be developed for future detectors in order to reduce the too high level of radon (^{214}Bi) background observed in BiPo-1.

Chapitre 9

The BiPo-1 phoswich prototype

9.1 Principle of the BiPo phoswich detector

The phoswich technique is used in nuclear detectors to discriminate electrons, α and γ particles. It consists of using two successive layers of scintillators with different scintillation time constant. We have proposed to use this technique for BiPo. The basic idea is to deposit a thin (few 100 μm) and fast (few ns) scintillator plate on the surface of a thicker and slower scintillator. As illustrated in Figure 9.1, the prompt electron (from the Bismuth beta decay) deposits its energy in the two scintillators, producing a scintillation signal with both a fast and a slow component, while the delayed α (from the Polonium decay) deposits all its energy in the first thin scintillator, giving a fast scintillation signal without slow component. Finally, an external γ has very low probability to interact with the thin scintillator producing in general a signal with only a slow component.

Therefore, the phoswich technique should allow to improve the discrimination between the different type of particles and consequently it could reduce the random coincidence background. It could also reduce the background in the topology of same-side BiPo events. If it is the case, the phoswich technique could allow to measure the surface radiopurity of thick materials using BiPo same-side event topology.

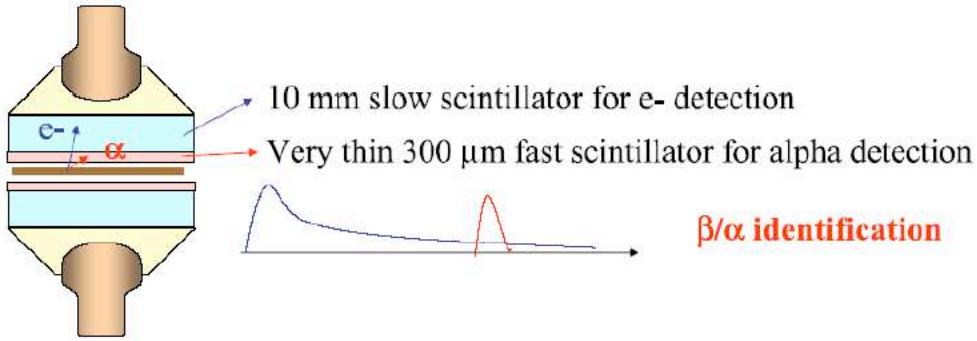

FIGURE 9.1: Principle of the phoswich e^-/α rejection.

Phoswich prototypes have been developed by IFIC laboratory (Valencia, Spain) in 2008

and 2009. BC-400 and BC-444 scintillators (both developed by Bicron) have been selected for the fast and slow scintillators, respectively. Their decay constant are 2.4 ns and 285 ns, respectivelly. The required thickness of the thin scintillator has been studied by Monte-Carlo simulations. A phoswich BiPo event is recognized as a prompt signal (electron) with a slow and fast component followed by a delayed signal (α) with only a fast signal.

We are then faced with a contradiction. On the one hand, the thin (fast) scintillator must be thick enough so that the fast scintillation signal produced by electrons is sufficiently large to be measured. On the other hand, the thin scintillator must be thin enough in order to minimize the energy lost by the crossing electron and therefore maximize the deposited energy in the second slow scintillator for tagging. The optimal thickness has been evaluated by Monte Carlo simulation and is about 300 μm. A first prototype has been built in 2008. It is similar to the standard BiPo-1 prototype with two phoswich modules face-to-face. A Phoswich scintillator consists of a fast BC-400 scintillator plate 200×200 mm^2 and 300 μm thick glued with Araldite 2020 to a thicker BC-444 scintillator plate 200×200 mm^2 and 10 mm thick.

9.2 Detection efficiency of the phoswich detector

The phoswich prototype has been first tested and calibrated on the test bench in Orsay with (e^-, γ) (^{207}Bi source) and α (^{241}Am source). Then it was mounted inside a BiPo-1 gas-tight container and installed inside the BiPo low radioactive shield in Modane. A calibrated aluminium foil (150 μm thick), similar to the one used for BiPo-1 validation (same size and same activity in ^{208}Tl), has been installed between the two phoswich scintillators in order to compare the features of the phoswich BiPo-1 prototype with the standard BiPo-1 prototype. The phoswich prototype has been running from June 2008 to March 2009 using the same acquisition and threshold energy than standard BiPo-1 prototype. Selection of *back-to-back* and *same-side* BiPo events is identical to the one applied for BiPo-1 standard prototype.

After 271 days of data collections, 985 *back-to-back* BiPo events and 1255 *same-side* BiPo events have been detected. Figure 9.2 shows the delay time distribution between the prompt and delayed signals both for *back-to-back* and *same-side* events. Both distributions are in agreement with an exponential decay with the ^{212}Po half-life of $T_{1/2} = 300$ ns. The corresponding detection efficiency is

$1.6 \pm 0.1\%$ for *back-to-back* events

$1.9 \pm 0.1\%$ for *same-side* events

The phoswich detection efficiency is about twice smaller than the efficiency of standard BiPo detector. Indeed, with phoswich scintillators, the amplitude of the prompt electron signal is lower than for standard BiPo scintillator since electron deposits only part of its energy in the fast scintillator. Most of the electron signal is produced inside the slow scintillator and consequently with a smaller amplitude. The detection efficiency is therefore smaller since a trigger defined with an amplitude threshold is applied. A trigger using a charge threshold could be developed in order to possibly increase the phoswich BiPo efficiency.

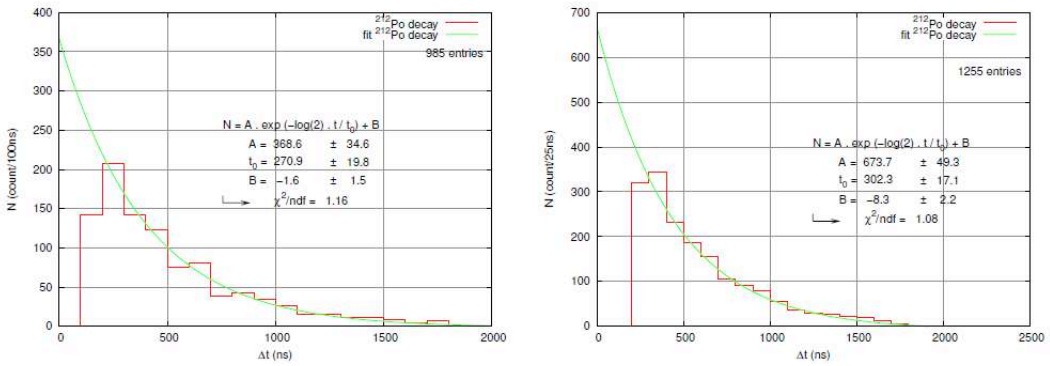

FIGURE 9.2: Delay time distribution between the prompt and delayed signal both for *back-to-back* (left) and *same-side* (right) events detected after 271 days of data collections with the aluminium foil installed inside the phoswich prototype.

9.3 e^-/α discrimination

To study the efficiency for electrons and α discrimination with the phoswich scintillator, we follow the same analysis developed with the BiPo-1 prototype. We use the set of the BiPo events (*back-to-back* and *same-side* events) detected with the calibrated aluminium foil inside the phoswich module. Prompt and delayed signals correspond to electron and α type events respectively. Figure 9.3 shows the average signals for electrons and α. The amplitudes have been normalized to the maximum peak. A larger component in the tail of the signal is well observed for electrons compared to α particles. A pulse shape discrimination was developed using this set of data. The discrimination factor χ is defined as the ratio of the charge q in the fast component to the total charge Q of the signal. Figure 9.4 shows the discrimination factor χ for both electrons and α and the difference as a function of the integration window of the fast component. The discrimination is maximal for an integration window of 65 ns (between 20 ns before the peak and 45 ns after the peak). Figure 9.5 shows the probability to identify either an electron or a α particle as a function of the criteria value applied to the discrimination factor. For instance, the condition $\chi > 0.9$ allows to recognized correctly 93 % of α particles but 20 % of electrons will be identified as α particles. The efficiency to tag α drops sharply if we want to increase the efficiency to identify properly the electrons. This misidentification corresponds to electrons, which deposit all their energy inside the thin fast scintillator without reaching the slow scintillator, either because they are emitted almost tangent to the scintillator or because they are backscattered inside the thin scintillator. It is illustrated in the Figure 9.6, which shows the discrimination factor versus the total charge (or energy) for both prompt electrons and delayed α particles. At low energy (below $\approx$ 0.5 MeV), most of the electrons are contained inside the thin fast scintillator and are identified as α particles.

9.4 Thermal assembly

A second prototype has been developed by IFIC, in which the thin fast scintillator has been thermaly welded to the thick scintillator using a heating and pressure process

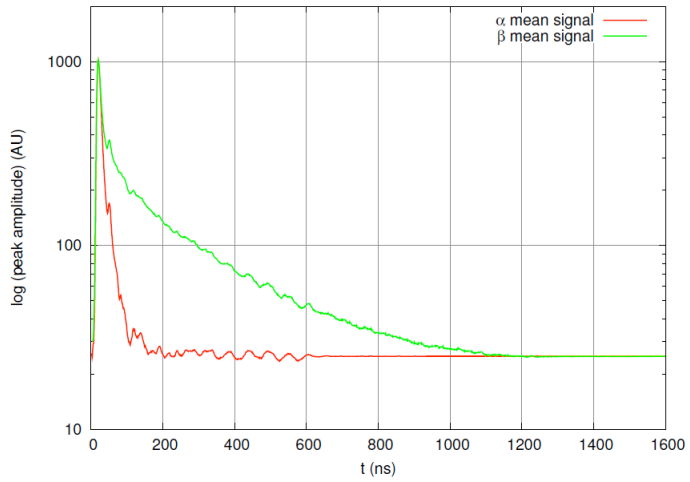

FIGURE 9.3: Average signals for prompt electrons (green curve) and delayed α (red curve). The amplitudes have been normalized in arbitrary unit to the maximum peak.

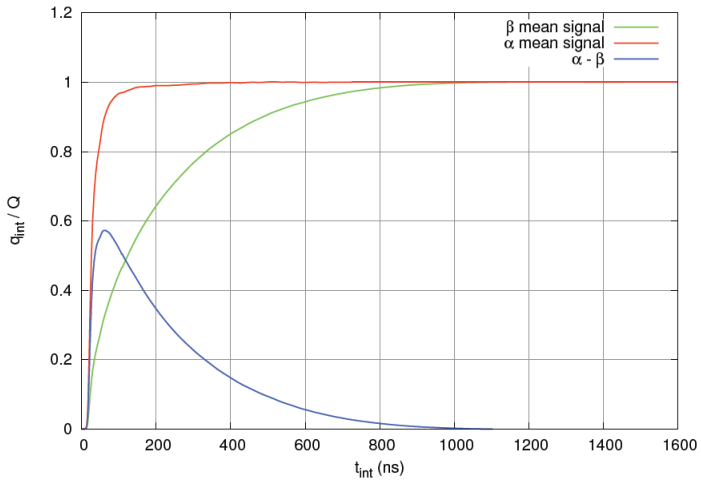

FIGURE 9.4: (left) Distribution of the discrimination factor $\chi = q/Q$ as a function of the integration time window t_{int} of the fast signal for prompt electron signals (red curve) and delayed α signals (green curve) : the difference (blue curve) is maximum for $t_{int} = 65$ ns.

under vacuum. The aim was to avoid the glue between the thin and fast scintillators, which might be a source of background. Figure 9.7 shows the experimental setup for thermal assembly. The thick scintillator is set on a copper plate heater contained in a teflon box. This thermal setup is then installed inside a press system made of two thick stainless steel plates enclosing the thermal set-up. Perfect flatness of all surfaces of the press and thermal setup components (teflon box, copper plate heater..) have been obtained by an additional machining. The thermal setup is tightly packed in the press system with the bolts fastened with a digital torque wrench to set the torque at a desired value. The tightness of the bolts is crucial. The force applied on each bolt has been calculated using the expansion

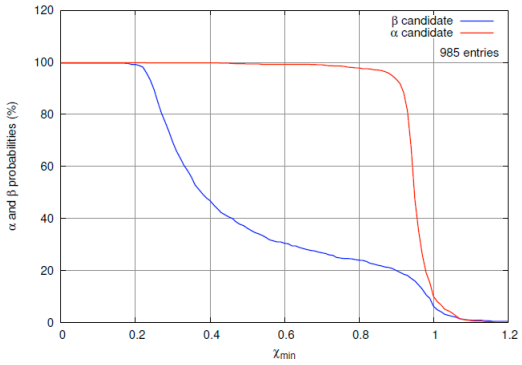

FIGURE 9.5: Probability distribution to identify correctly an electron (blue curve) and an α particle (red curve) as a function of the minimum value required to the discrimination factor : with the condition $\chi = q/Q > 0.9$ applied to delayed signals, 90 % of random coincidence signals (Compton electron produced by external γ-rays) are rejected while 93 % of delayed α from BiPo decay are identified correctly.

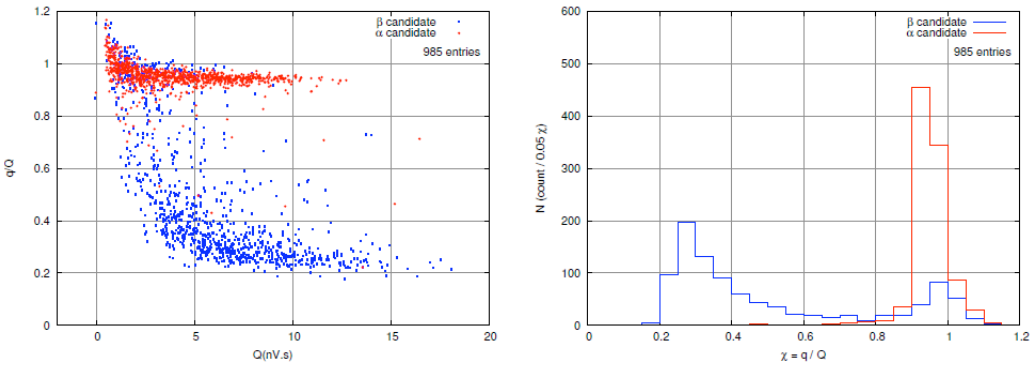

FIGURE 9.6: (left) Distribution of the discrimination factor $\chi = q/Q$ as a function of the total charge Q of the signal in blue for prompt electron signals and in red for delayed α signals ; (right) Distribution of the discrimination factor $\chi = q/Q$.

coefficients of the thermal setup materials. Then the thermal setup is introduced in the vacuum chamber. Vacuum pressure, temperature profiles and operational parameters have been optimized. Scintillator is set to the softening (so-called Vicat) temperature of 70 °C which requires 78 °C in the copper plate heater according to the heat conduction equation. The key parameter for preserving the quality of the surfaces is the vacuum : the heat conduction process which allows to control the temperature (heat conduction equation) is valid only if the vacuum pressure is maintained during all of the heating and cooling time processes. The other key parameter for welding is the pressure uniformity which is easy for small samples, but more difficult for larger samples. A prototype of 20×20 cm^2 has been successfully produced and tested. The scintillation light yield is comparable to the light yield produced in the phoswich prototype assembled with epoxy glue. However the BiPo detection efficiency and e^-/α discrimination was also comparable to the former prototype.

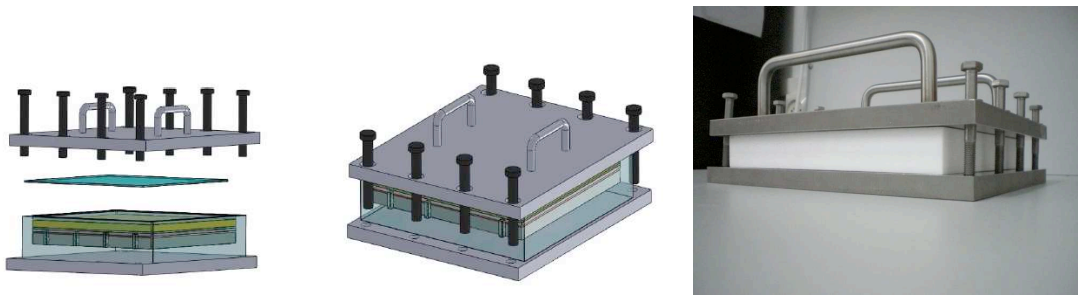

FIGURE 9.7: Schematic view and picture of the phoswich press for thermal assembly of the two scintillators.

9.5 Conclusion

In conclusion, the phoswich technique allows an excellent e^-/α discrimination for electrons with an energy larger than about 0.5 MeV. However, electrons with smaller energies are identified as α particles which limits strongly the capability of e^-/α discrimination in the case of the ^{212}Bi$-^{212}$Po cascade. Morever, the BiPo efficiency using *back-to-back* events is about twice smaller with phoswich scintillators. This efficiency can be increased by a factor of two if we use *same-side* events. Due to a limited e^-/α discrimination, a limited BiPo efficiency, and more expensive technique, it was decided to use standard BiPo-1 technique to build a larger BiPo-3 detector.

Chapitre 10

The BiPo-2 prototype

The BiPo-2 prototype (Figures 10.1 and 10.2) consists in two scintillators plates (Bicron BC-408) of $75 \times 75 \times 1$ cm^3 (0.56 m^2). These plates are produced by molding. It gives a polished surface without any treatment. It minimizes the risk of surface radioactive contamination, if mold is radiopure or if there is no transfer on the surface of the scintillator plate during the molding process. The scintillation light is collected by total internal reflectivity. The read out is done on the two lateral sides of each plate with five 3" radiopure PMT's coupled by PMMA optical guide. It corresponds to a total of 20 PMT's.

We wanted to test this design because we listed three advantages, compared to BiPo-1 :

- There is no treatment of the entrance surface of the scintillators compared to BiPo-1 (no machining, no aluminium deposition)
- The detector is more compact. Several modules of two scintillators plates can be piled up, as shown in Figure 10.3, in order to have a compact BiPo detector.
- If a good spatial resolution (few cm) can be achieved, the random coincidence background would be reduced and it would give the capability to detect hot spot contaminations on the double beta foils.

The BiPo-2 prototype has been built in 2007, tested first in LAL Orsay clean room, and then tested inside the low radioactive BiPo shield in Modane in 2008.

The Trigger is performed using the same external trigger board as BiPo-1. One requires at least 2 PMT's in coincidence, with a threshold of 10 mV (few photoelectrons). If the trigger is validated, all the 20 PMT's signals are digitized by 5 MATACQ boards. Figure 10.4 shows an example of a BiPo-2 α event observed in a scintillator plate with the 10 digitized PMT signals.

10.1 Light collection efficiency and energy threshold

The light collection efficiency, directly correlated to the energy threshold is an important issue. Thus first measurements have been performed by moving either a ^{241}Am source (α 5.5 MeV) or a ^{207}Bi source (γ and e^- conversion of 1 MeV) along the surface of the scintillator plates. Figure 10.5 shows the energy spectra obtained with the sources in the middle of the scintillator plates. A relatively good light collection is observed. The energy threshold has been estimated to be 100 keV for the first plate and 150 keV for the second one. The energy response is quite uniforme along the plate with a relative variation of about

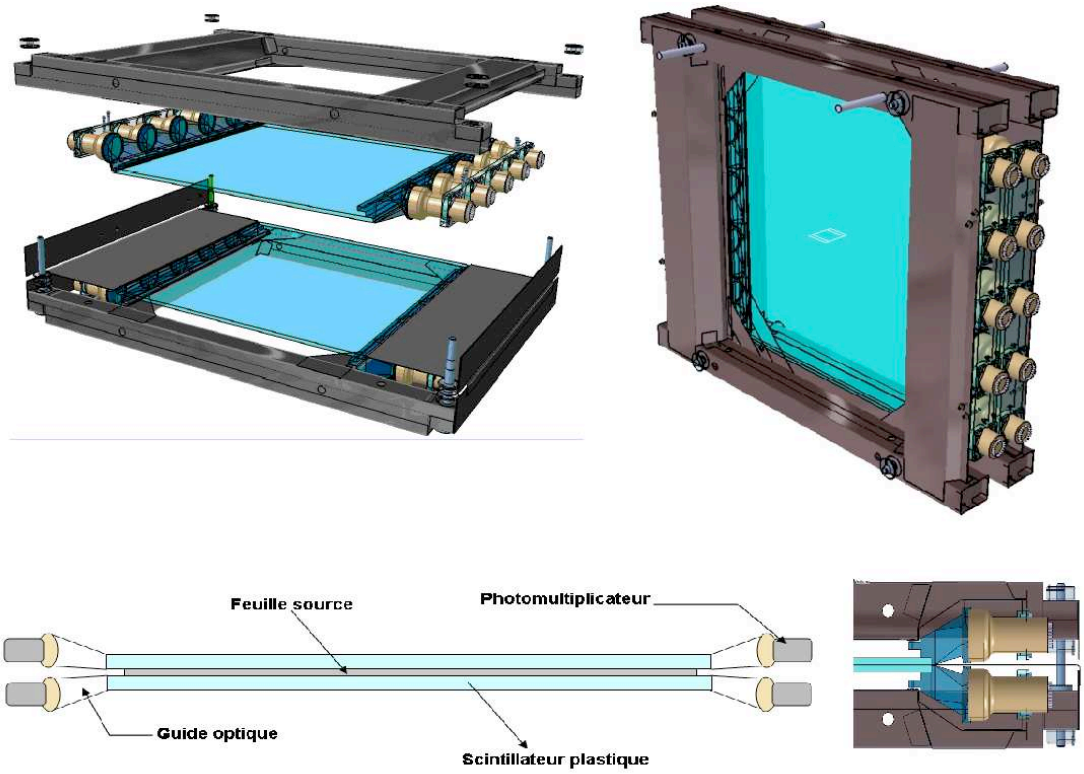

FIGURE 10.1: Schematic view of the BiPo-2 prototype

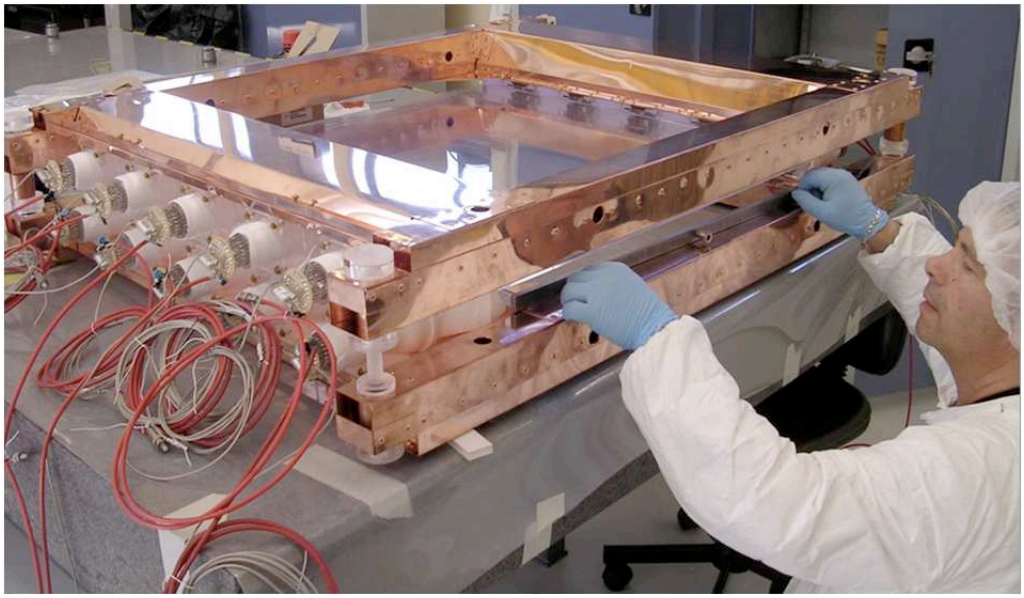

FIGURE 10.2: Pictures of the BiPo-2 prototype

20%, which can be corrected using the reconstructed position of the event (see next section).

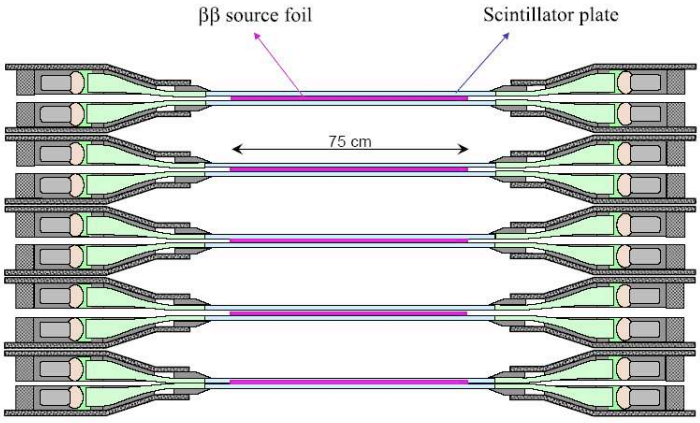

FIGURE 10.3: Schematic view of a possible BiPo detector with large detection surface, using the BiPo-2 design

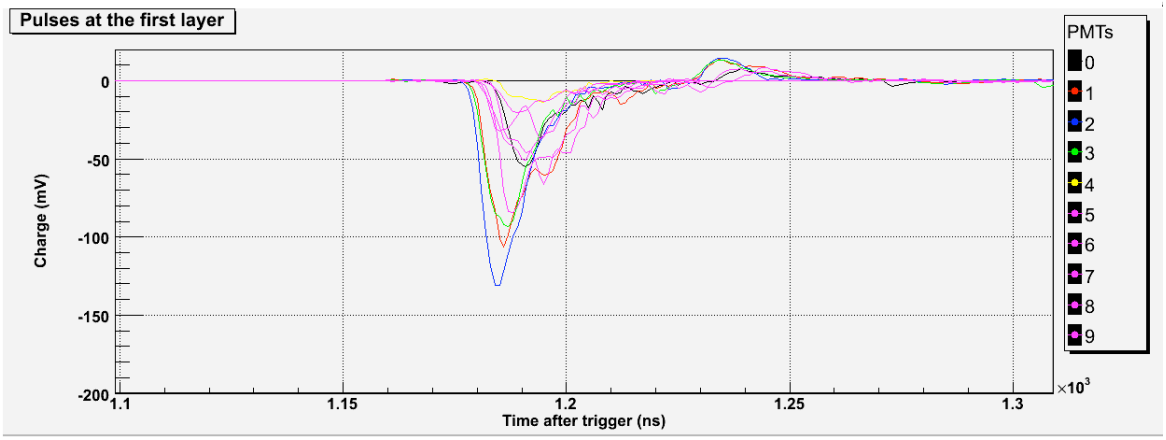

FIGURE 10.4: Display of a BiPo-2 event with the 10 digitized PMT pulses.

However a non negligeable optical cross-talk has been observed. This is an important limitation since coincidences are used to reject ^{238}U or ^{232}Th bulk contaminations inside the scintillators.

This is the first reason why the BiPo-2 design was not selected for the construction of the large BiPo-3 detector.

10.2 Position reconstruction and spatial resolution

The position reconstruction has been calibrated using a mapping of the ^{241}Am α source on the surface of the scintillator. The (x, y) position is reconstructed using the barycenter of the number of photoelectrons collected on each PMT. It has been demonstrated that $\approx 80\%$ of events are reconstructed at the source position $\pm$ 10cm, as shown in Figure 10.6.

Then a calibration run has been performed with a thorium source (a 2×2 mm^2 thin

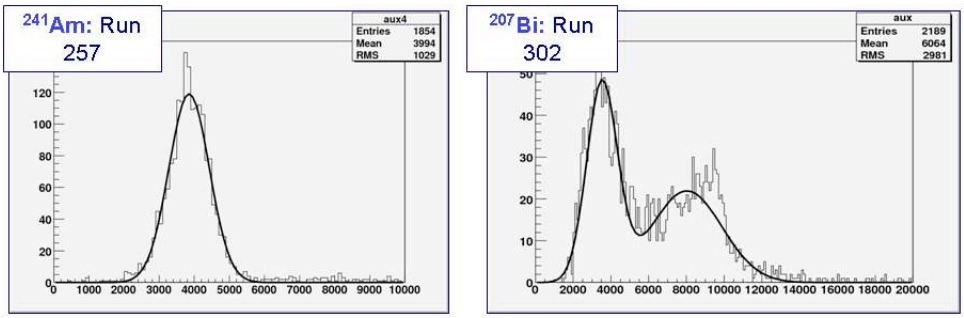

FIGURE 10.5: Energy spectrum measured by BiPo-2 prototype with an ^{241}Am (α) source and a ^{207}Bi (EC, γ) source.

foil) at different positions on the scintillator plate (full maping). ^{212}Bi-^{212}Po events have been reconstructed. The distributions of the reconstructed positions of the prompt β and delayed α events are presented in Figure 10.6. The distribution of the distance between the reconstructed positions of the delayed hit and the prompt hit of a same ^{212}Bi-^{212}Po decay is also presented in Figure 10.6. We see that $\approx$ 90% of the delayed α signals are reconstructed with a position of less than 15 cm from the reconstructed position of the prompt β event. It means that any delayed signal with a reconstructed position farther than 15 cm from the prompt signal will be recognized and rejected as a random coincidence background. Thus the equivalent surface of possible random coincidence background is $\pi 15^2 \approx 700$ cm^2. This is only 20% less than the surface of a BiPo-3 scintillator. Morever the BiPo-2 scintillator plates (10 mm thick) are 5 times thicker than BiPo-3 scintillators (2 mm). Since the coincidence rate is dominated by external γ-ray interactions, it is proportional to the thickness of the scintillator (see section 11.3.3). Therefore, with no e^-/α discrimination, the random coincidence background in BiPo-2 is expected to be $5 \times 0.8 \approx 4$ times larger than in BiPo-3. Finally, the e^-/α discrimination, which reduced by a factor ≈ 10 the coincidence background in BiPo-3, is not possible in BiPo-2 (see next section 10.4). In conclusion, one expects a coincidence background in BiPo-2 40 times larger than with BiPo-3 design. And ^{214}Bi radiopurity cannot be measured in BiPo-2 with the required sensitivity.

This is the second reason why the BiPo-2 design was not selected for the construction of the large BiPo-3 detector.

10.3 Validation of the BiPo-2 efficiency with a calibrated aluminium foil

The experimental validation of the BiPo-2 prototype has been carried out with the same method than BiPo-1, by testing the detection of bulk ^{212}Bi contamination inside a calibrated aluminium foil. A 150 μm thick aluminium foil 60 $\times$ 75 cm^2, with an activity $\mathcal{A}(^{212}\text{Bi}\rightarrow^{212}\text{Po}) = 0.19 \pm 0.04$ Bq/kg initialy measured with low background HPGe detectors) has been installed between the two scintillators of the BiPo-2 prototype. The prototype was installed inside the BiPo low radioactive shield in Modane. After 157 days of data collection, 10914 *same-side* events were detected on the scintillator plate #1, 7157 *same-side* events were detected on the scintillator plate #2, 5491 *back-to-back* events were detected

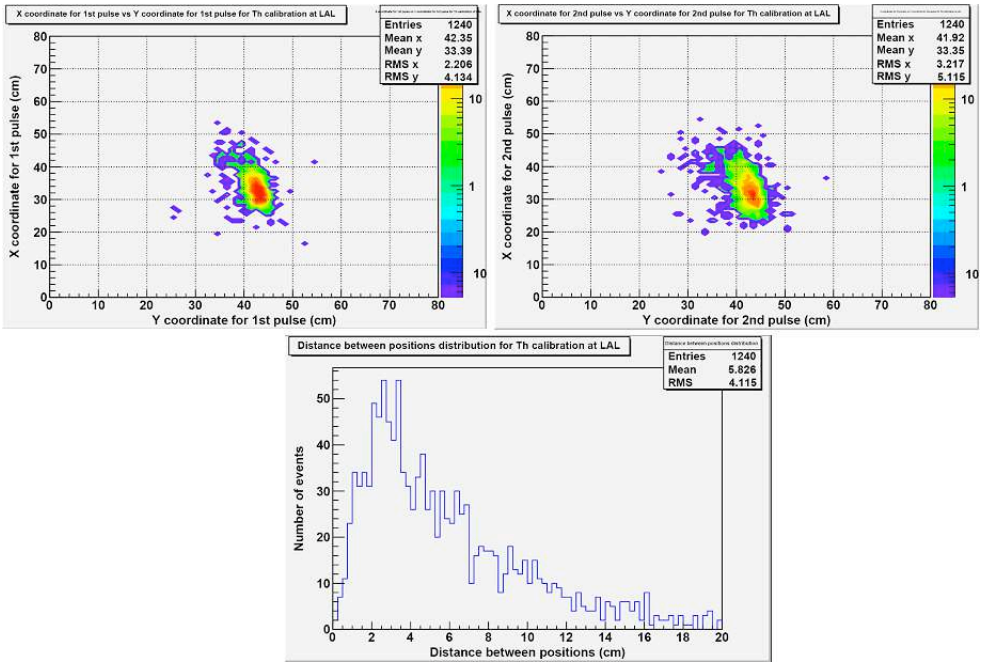

FIGURE 10.6: Position recontruction of BiPo events produced by a Thorium point-like source : (Upper Left) position of the prompt signal ; (Upper Right) position of the delayed signal ; (Lower) distance between the prompt and delayed events.

on plates #1-2 and 2844 *back-to-back* events were detected on plates #2-1. As shown in Figure 10.7, the delay time distribution between the prompt and the delayed signals is well fitted by an exponential decay with an half-life of $T_{1/2} = 303.4 \pm 2.9$ ns, in agreement with the ^{214}Po α-decay half-life. Taking into account the activity of the aluminium foil, it corresponds to an BiPo efficiency ε of

- $\varepsilon = 3.0\%$ for *same-side* events on plate #1
- $\varepsilon = 2.0\%$ for *same-side* events on plate #2
- $\varepsilon = 1.5\%$ for *back-to-back* events on plates #1-2
- $\varepsilon = 0.75\%$ for *back-to-back* events on plate #2-1

The lower efficiencies observed for *same-side* events on plate #2 (compared to plate #1) and for *back-to-back* events on plates #2-1 (compared to plates #1-2) are due to a lower light collection and therefore a higher energy threshold for plate #2, in which 3 PMT's (among 10 PMT's) were missing. It explains also the smaller efficiencies observed in the *back-to-back* channel compared to *same-side* channel (the efficiency should be roughly the same for *same-side* and *back-to-back* channels).

If one renormalizes to the plate #1, we obtain an efficiency of 6% for *same-side* events and 5% for *back-to-back* events.

In conclusion, the BiPo-2 efficiency for *back-to-back* events is the same than BiPo-1. However, if one can combine *back-to-back* and *same-side* events without adding background, the BiPo-2 efficiency becomes twice higher than in BiPo-1 (in which *same-side* events cannot be used due to a too high background in this channel)

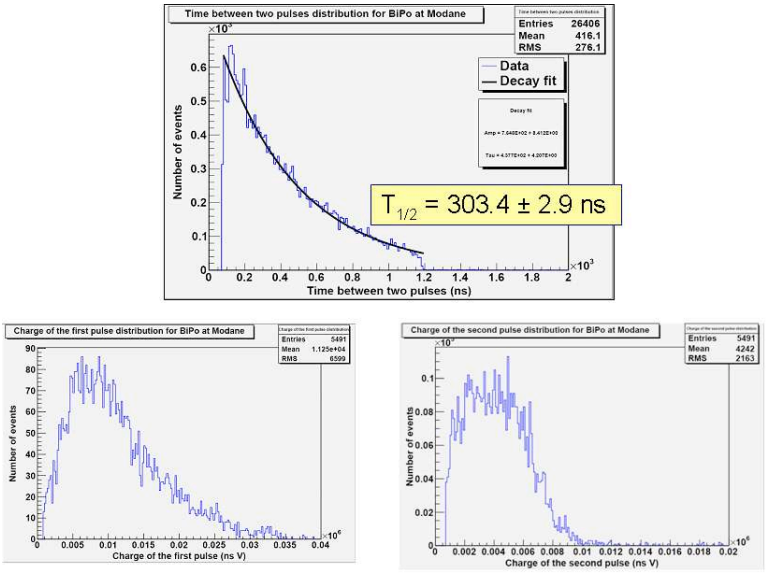

FIGURE 10.7: Delay time distribution between the prompt and the delayed signals measured with an calibrated aluminium foil ; Energy spectrum of the prompt (left) and delayed (right) signals.

10.4 e^-/α discrimination

The e^-/α discrimination has been studied using the same method than in BiPo-1 (see Section 8.6). The e^-/α pulse shape discrimination has been first determined with calibration runs performed with ^{241}Am α source and ^{241}Bi source (γ and e^- conversion of 1 MeV). Then the sample of pure prompt β delayed α signals collected with the aluminium foil has been used to measure the e^-/α discrimination.

A discrimination method similar to the one implemented in BiPo-1 has been developed using a discrimination factor $\chi = q/Q$, which is defined as the ratio of the charge q contained in the slow component (the tail) after a given time of the begining of the pulse to the total charge Q of the pulse. A systematic study of the optimal slow component window (optimal area of the charge q) has been performed. No e^-/α discrimination has been found. To illustrate this result, Figure 10.8 shows the average signal for e^- and for α particles with the e^-/α sample collected with the aluminium foil.

10.5 Conclusions

The light collection and the efficiency obtained with the BiPo-2 meet the requirements. However three important limitations have been observed with this prototype :

- The optical cross-talk is too large to be able to reject coincidence background mostly from the external γ-rays and from possible bulk scintillator contaminations
- The e^-/α discrimination is not possible
- The random coincidence is expected to be about 40 times larger than with BiPo-1 design, and consequently too large to be able to reach the required sensitivity in ^{214}Bi.

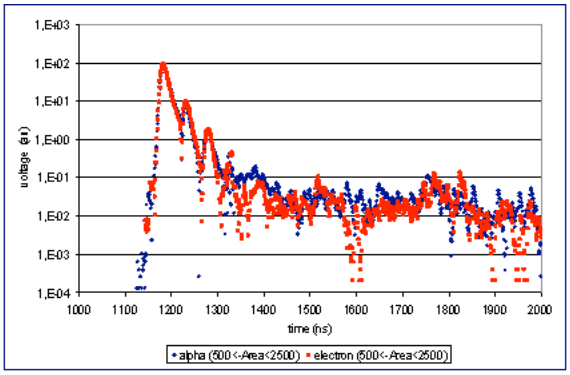

FIGURE 10.8: Average signal of the prompt $e-$ (red) and delayed α (blue) events, measured with the aluminium foil

In conclusion, the BiPo-2 design has not been selected for the construction of the large BiPo-3 detector.

Chapitre 11

The BiPo-3 detector

Results of the BiPo-1 prototype have shown that the background is at the required level and that a sensitivity of few μBq/kg in ^{208}Tl is reachable.

Thus end of 2009, the SuperNEMO Collaboration has decided to build a medium-size BiPo detector named BiPo-3, with a total surface area of 3.6 m^2 using the BiPo-1 technique and geometry. This detector will be installed in the Canfranc Underground Laboratory (Spain) mid 2012.

The size of the detector is a compromise to fulfil the requirements of a relatively small detector (and thus a relatively small number of readout channels) and a good enough sensitivity to measure the radiopurity of the first selenium $\beta\beta$ foil sources used for the SuperNEMO demonstrator.

The improvements for the BiPo-3 detector, compared to BiPo-1 prototype, are the following.

- The surface of the scintillator plates has been increased by a factor 2.25, from 200×200 mm^2 (BiPo-1) to 300×300 mm^2, in order to reduce the number of channels.
- The thickness of the scintillator plates has been reduced from 3 mm (BiPo-1) to 2 mm in order to reduce the single counting rate due to external γ-rays and thus to reduce the random coincidence background.
- The shape of the light guides has been optimized in order to obtain a response of the scintillator as uniform as possible along the surface, while losing as little as possible scintillating light collection on the PMT.
- A new dedicated setup for the aluminization of the scintillators and a cleaner process for the scintillators machining have been developed in order to improve the radiopurity of the scintillator surface.
- The radon suppression has been improved.

We give first a description of the detector. Then we describe the different improvements obtained for BiPo-3. We then give the results obtained with the BiPo-3 prototype. Finally, we give a status report of the construction of the detector.

11.1 Description of the detector

The BiPo-3 detector is composed of two modules. Each module (see Figure 11.1) consists of two rows of 40 optical sub-modules arranged face-to-face like in BiPo-1. Each optical sub-module consists of a polystyrene-based scintillator plate coupled with a PMMA optical guide to a 5 inches low radioactive PMT. The size of each scintillator is $300\times300\times2$ mm^3. The BiPo-3 detector corresponds to a total number of 80 optical sub-modules and a total detector surface of 3.6 m^2.

The scintillators are prepared, as in BiPo-1, with a monodiamond tool from raw and radiopure polystyrene scintillator blocks produced by JINR Dubna. The surface of the scintillators facing the source foil are covered with 200 nm of evaporated ultrapure aluminum (same aluminium sample as the one used for BiPo-1) in order to optically isolate each scintillator and to improve the light collection efficiency. The entrance surface of the scintillators are carefully cleaned before and after aluminium deposition using the same cleaning sequence as the one used in BiPo-1 : acetic acid, ultra pure water rinse, isopropanol and finally a second ultra pure water rinse. The light guide is wrapped first with a Tyvek layer in order to diffuse and collect the light to the PMT, and then covered with a black polyethylene film to avoid any optical crosstalk between optical sub-modules.

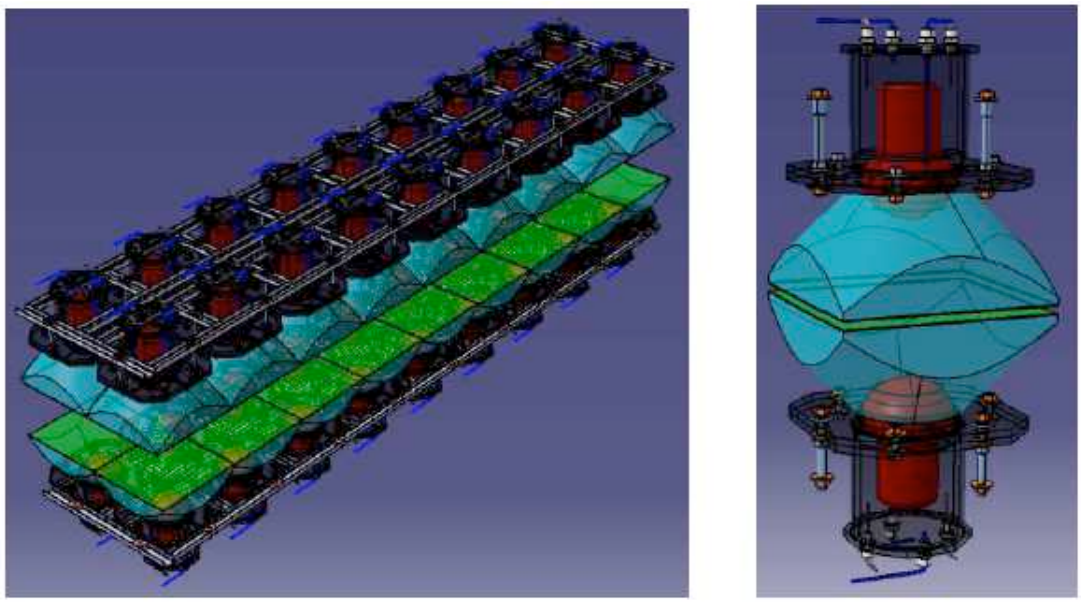

FIGURE 11.1: Details of the assembly of the 40 optical sub-modules inside a BiPo-3 module. On the right, a zoom of one optical sub-module with the two thin scintillators (in green) face-to- face, coupled with a PMMA optical guide (blue) to a low radioactive 5 inches PMT (red)

11.1.1 Mechanical Structure

The mechanical structure supporting the optical sub-module (see Figure 11.2) is a welded pure iron structure closed with pure iron plates (2 mm thick). The upper part of the module

can be moved up manually using hydrolic jack in a clean room in order to install the $\beta\beta$ source foils inside the detector. The tightness of the BiPo-3 modules is performed using silicon seals. All the materials of the detector have been selected by HPGe measurements to confirm their high radiopurity. The total mass of one BiPo-3 module is approximately 700 kg.

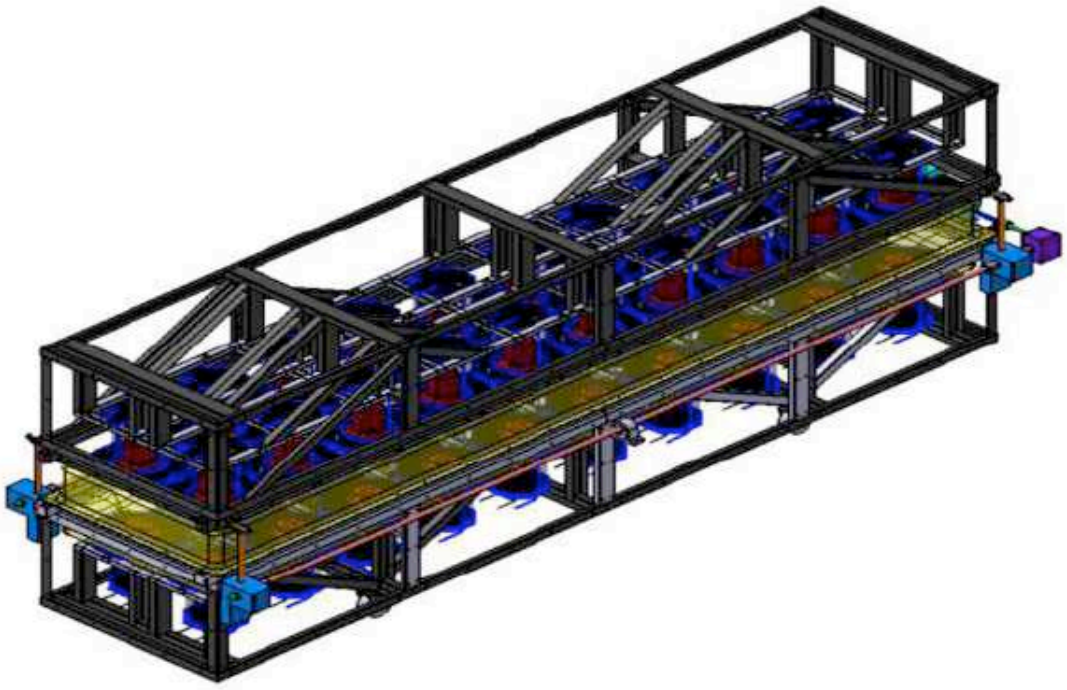

FIGURE 11.2: View of the welded mechanical structure of one BiPo-3 module, supporting the 40 optical sub-modules

11.1.2 External γ shield

The two BiPo-3 modules are installed inside a low radioactive shield (see Figure 11.3). The shield corresponds to a tight stainless steel tank. A wall of low activity lead (in form of $20 \times 10 \times 5$ cm^3 bricks) is assembled inside the tank. The upper part of the tank, which supports the lead, is a pure iron plate (2 cm thick). The thickness of lead is 15 cm for the bottom and the top sides and 10 cm for the lateral sides. The external part of the tank is covered on its lateral sides by standard cubitainers (50 cm large), filled with pure water.

11.1.3 Radon suppression

Special attention is required for the radon suppression. Radon was one of our main critical issue since we had observed radon background in the BiPo-1 prototype, due to a radon diffusion between the two scintillator faces. In order to suppress potential radon background, we have defined three separate volumes, in which pure Nitrogen will be flushed :

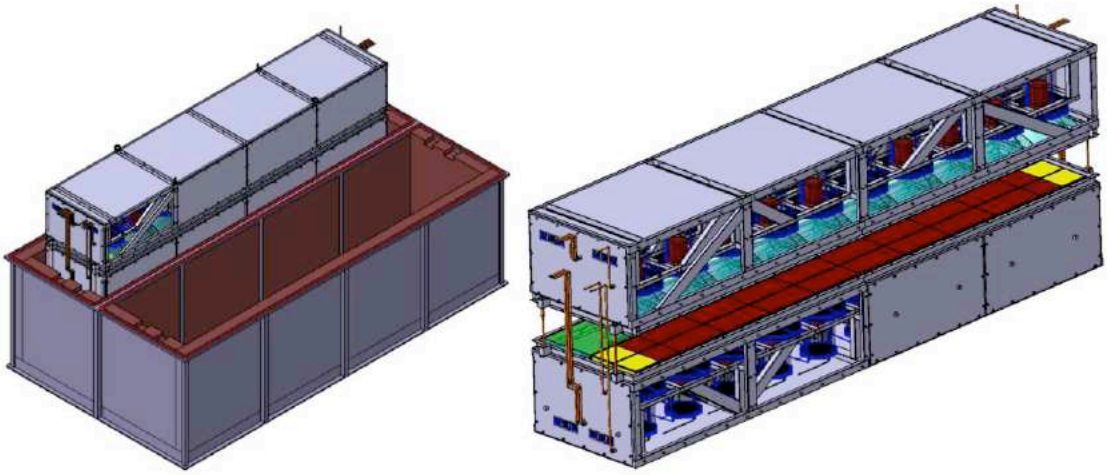

FIGURE 11.3: (left) View of one of the two BiPo-3 modules inside the shield; (right) view of the BiPo-3 module with its upper part open vertically for source installation (some pure iron plates have been removed for illustration)

- The most critical volume corresponds to the volume surrounding the scintillators and the optical guides. It is isolated by a radon tight film (made of EVOH and High Density Polyethylene) placed as a large sheet between each optical guide. The tightness is performed on the top of the optical guide.
- The PMT's, which are the main source of radon emanation, are enclosed in a gas tight black box (black polyethylene).
- Finally the mechanical structure of the two BiPo-3 modules and the shield tank are gas tight structures in order to avoid any external radon diffusion inside the detector.

The total volume of the BiPo-3 detector to be flushed is about 2 m^3.

The seals are performed using silicon RTV 615 mixed with pure Selenium powder in order to obtain a black seal against light leaks. RTV 615 is relatively permeable to radon. An external layer of PVA glue will be added to improve the radon tightness, as illustrated in Figure 11.4.

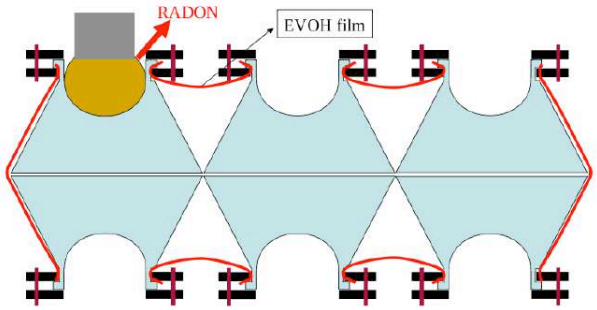

FIGURE 11.4: Schematic view of the radon barrier with an EVOH film.

11.1.4 Electronic readout, trigger and acquisition

We reuse the same electronic and acquisition system developed for BiPo-1. Each one of the two BiPo-3 modules has its own independent acquisition allowing to manipulate one module without perturbing the measurement of the second one. Four trigger boards and 20 MATACQ boards are required for the complete acquisition of the two modules.

11.1.5 Operation procedure

The procedure to install a foil source for measurement inside the BiPo-3 detector is the following :

- The upper part of the shield is opened with the LSC crane.
- The HV cables, signal cables and optical fibres are disconnected
- The BiPo-3 module is removed with the crane and deposited on a trolley. Then it is moved to the LSC clean room.
- The upper part of the detector is opened in a clean atmosphere with a manual hydraulic jack. An opening of about 20 cm is enough to install source foils inside the detector.

11.2 Study and development of the optical submodules

Before starting the construction of the BiPo-3 detector, we first studied and sought to improve the features of the optical submodules, particularely the aluminization process, the gluing process of the scintillators, the shape of the light guide and the optical crosstalk.

11.2.1 Aluminization

The residual contamination in ^{232}Th and ^{238}U, observed on the surface of the BiPo-1 scintillators, might be an accidental deposition during the aluminization process. Indeed an old evaporation facility available in IPN Orsay had been used for BiPo-1 and its vacuum chamber was probably already polluted, even if we used a new radiopure copper crucible.

In order to improve the radiopurity, a new evaporation facility was mounted in IPN Orsay (Département de cibles fixes). The vacuum chamber is large enough to aluminize the larger BiPo-3 scintillators (300×300mm^2). A picture of the setup is shown in Figure 11.5

11.2.2 Optical guides

Material selection

In BiPo-1 and BiPo-2 prototypes, we used raw blocks of UV-enhanced PMMA available from NEMO-3. These blocks were too small for BiPo-3.

The selection and purchase of new PMMA has been a long adventure with the manufacturer companies ! First batch of selected PMMA became strongly yellow with poor transmission after the annealing procedure. The second batch appeared to be not enough transparent in UV and large background was detected at relatively low energy due to scintillation light produced in the PMMA close to the PMT.

FIGURE 11.5: Picture of the aluminization facility in IPN Orsay used to evaporate a layer of 200 nm of ultra radiopure aluminium on the entrance face of the BiPo-3 scintillators

Finally a UV-enhanced PMMA could be selected. Its transmission spectra is shown in Figure 11.7. Its transmission in the UV region allows to detect the UV part of the scintillation light (see Figure 11.6). This PMMA was also slightly yellow after the annealing procedure but it became transparent after few days of exposure in natural light. It was probably due to an uncomplete polymerization of the PMMA during its production.

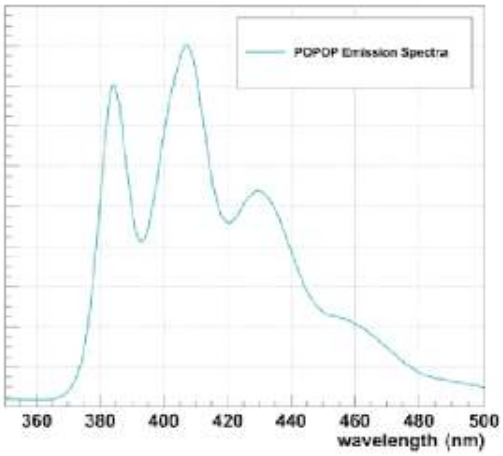

FIGURE 11.6: Emission spectra of the Popop molecule used in the polystyren based scintillators.

Gluing the scintillator plate with the light guide

The gluing of a large 300×300 cm^2 scintillator plate on the optical guide is a delicate procedure. It is indeed difficult to obtain a good optical contact without any bubbles and defects. Several glues have been tested : the Stycast epoxy glue, the Araldite 2020 epoxy glue, the Bicron optical glue and the UV-Dymax glue. Their radiopurities have been measured by HPGe spectroscopy, and activities are lower than $\approx 100\mu$Bq/kg in Th and U chains. After

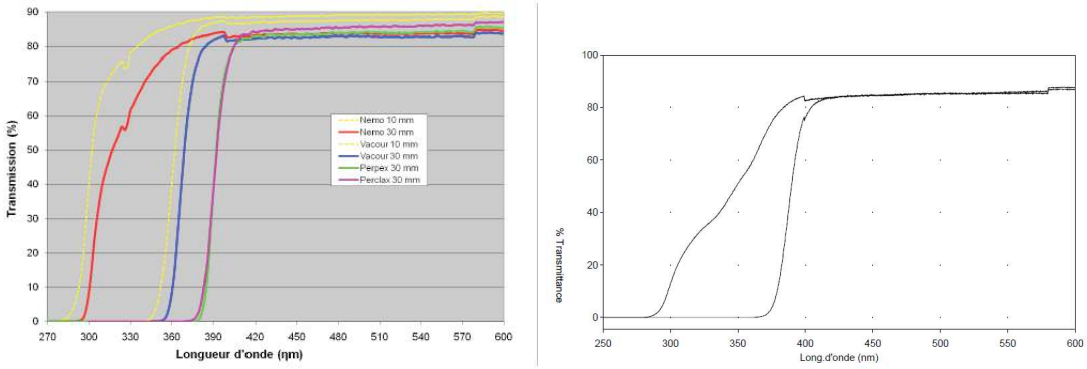

FIGURE 11.7: (Left) Transmission spectra of various PMMA (including NEMO-3 PMMA) ; (Right) Transmission spectra of the UV PMMA selected for BiPo-3, compared to standard PMMA from the same company.

several tests, excellent gluing quality without any buble and with good reproductibility has been obtained with the Stycast glue and 300×300 cm^2 scintillator plates with a 2 mm thickness. However the gluing has proven to be more difficult with thicker 3 mm scintillators plates which are less flexible, resulting in little bubles. Araldite was slightly more difficult to use. Bicron is an expensive glue without obvious advantage. The quality and reproductibility of the optical contact using the UV Dymax glue was excellent due to the simplicity of using this glue with a UV lamp. However an ageing of the scintillator yield has been observed when using this Dymax glue. It is probably due to the fact that we must flash the glue, and consequently the scintillator with a UV lamp in order to polymerize the UV glue. This flash might deteriorate the scintillator properties. In conclusion, the Stycast has been selected for BiPo-3.

Optimization of the shape

We have faced a contradiction to design the optical light guide. Indeed, in one hand the PMT must be as close as possible to the scintillator plate in order to collect the highest amount of scintillation light on the PMT, on the other hand the PMT must be located as far as possible from the scintillator in order to obtain the most uniform response of the scintillator along its surface. Numerical optical simulations have been performed in order to optimize the shape. We have used the optical simulations developed in SuperNEMO [127]. The inputs of the simulation are the following :

- The emission spectra of the scintillating light is shown in Figure 11.6, and it corresponds to the expected emission spectra of the wavelength shifter (Popop) used in the Dubna scintillators.
- The transmission spectra of the PMMA plexyglass for the light guide corresponds to the measured spectra of the UV-enhanced PMMA used in BiPo-3 and is shown in Figure 11.7.
- The reflectivity factor of the aluminized face of the scintillator is attenuated by 20% to take into account the relative lower quality of the mirror obtained by aluminium sputtering.

The mechanical design and a picture of the optical guide is shown in Figure 11.8. Simulations have been performed with different distances LG separating the PMT to the scintillators, from 25 to 150 mm. Results are shown in Figure 11.9. The optimal distance is about 100 mm, allowing an almost uniform response of the scintillator (about 5% of reduction on the sides) while the total amount of collected light is reduced by about 20% only. Several prototypes have been machined with different distances LG in order to validate the numerical calculations. Results of the relative response of the optical module measured with α particles (^{241}Am source) as a function of the distance of the source to the center of the scintillator are presented in Figure 11.10 for two differents sizes $LG = 50$ mm and $LG = 100$ mm. These measurements have validated the choice of $LG = 100$ mm.

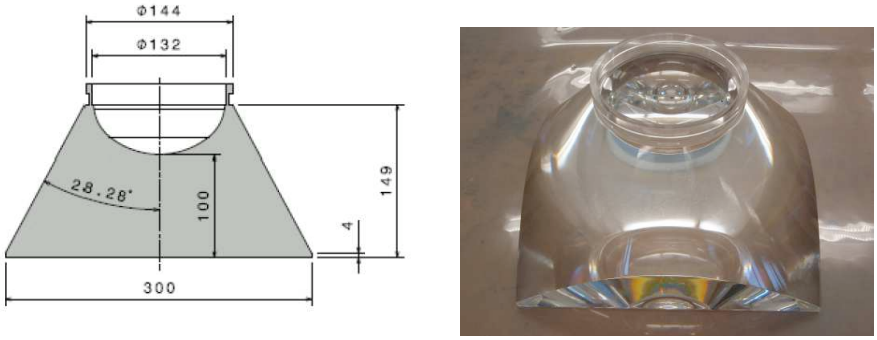

FIGURE 11.8: Mechanical design and picture of the BiPo-3 light guide with the nominal distance between the scintillator and the PMT of $LG = 100$ mm.

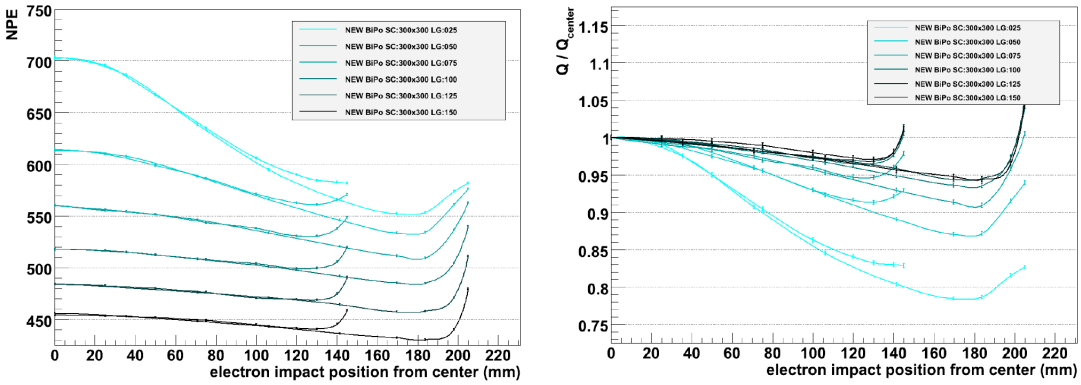

FIGURE 11.9: Simulation of the scan

11.2.3 Optical crosstalk

As it was discussed in former sections, BiPo events are selected by requiring no signal in coincidence in the opposite PMT in order to reject either bulk contaminations inside the scintillator near the surface, or random coincidences with Compton electron crossing the two scintillators. In consequence, any optical crosstalk between the two face-to-face scintillators must be avoided. The crosstalk is supressed thanks to the aluminization on the entrance

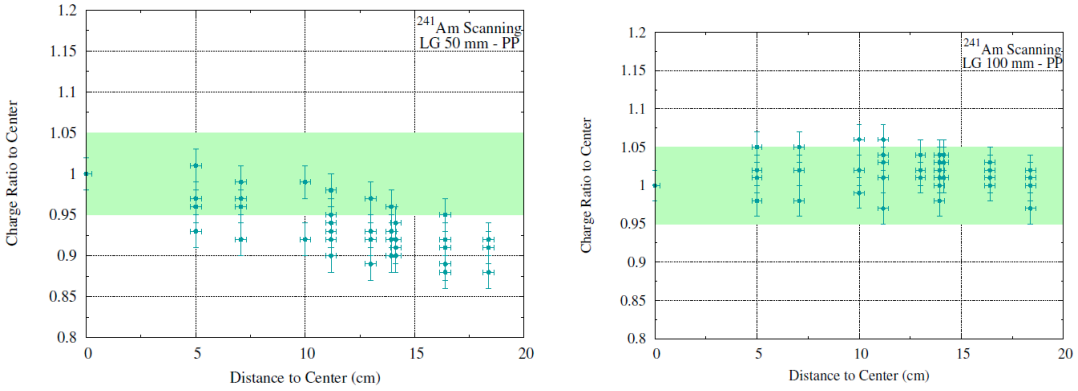

FIGURE 11.10: Measurements with 50 mm (left) and 100 mm (right)

surface of the scintillators. But residual crosstalk is possible if the thickness of deposited aluminium is too small, or if leaks exist on the edge of the scintillators.

A test bench has been developed in order to measure the level of optical crosstalk. The schematic view is shown in Figure 11.11. A 410 nm LED pulse is sent to the optical light guide near the upper PMT for triggering. The intensity of the LED corresponds to a signal of about 350 mV, equivalent to about 1 MeV. The signal of both PMT's are sampled simultaneously by the BiPo MATACQ board. The rate of optical crosstalk signal detected in coincidence in the second PMT as a function of its amplitude is presented in Figure 11.12. Only 0.1% of the LED pulses generates an optical crosstalk signal with an amplitude larger than 5 mv, which corresponds to the 10 keV energy threshold applied in BiPo to reject background coincidence. In other words, the BiPo detection efficiency is reduced by only 0.1% when the background coincidence rejection is applied.

A similar test has been carried out using Am α source on one scintillator with the second scintillator beside it (see Figure 11.11) in order to measure latteral crosstalk. No latteral optical crosstalk has been observed.

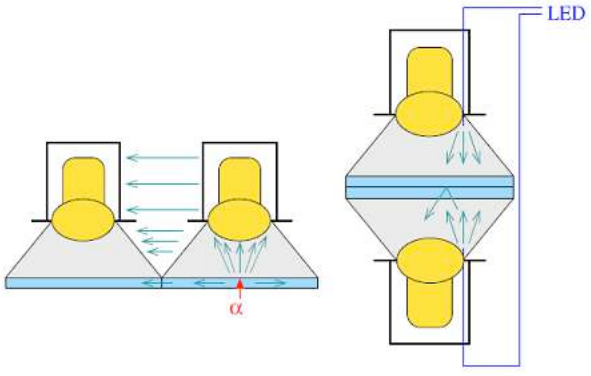

FIGURE 11.11: Schematic view of the test bench used to measure the optical crosstalk (Right) between two face-to-face scintillators using a LED pulse, and (Left) between two neighbour scintillators.

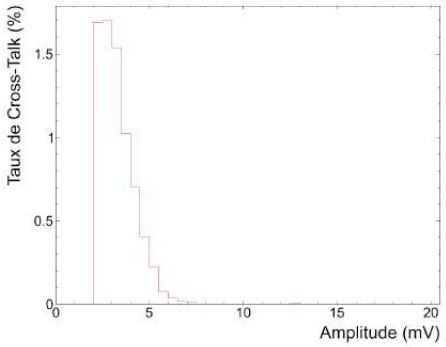

FIGURE 11.12: Rate of optical crosstalk signal detected in coincidence in the opposite PMT of the LED as a function of its amplitude.

11.3 Results of the BiPo-3 prototype

A BiPo-3 prototype has been built and installed in Canfranc in March 2011. A schematic view of the prototype is shown in Figure 11.13. It consists of two optical submodule face-to-face, installed inside a black polyethylene container. The thickness of one scintillator is 2 mm while the second one is 3 mm. The prototype is placed inside a low radioactive black polyethylene container separated into three volumes : the inner volume near the scintillator V2 isolated by the EVOH radon tight foil (in yellow), PMT volumes V5 and V6, and the upper and lower V3 and V4, as presented in Figure 11.13. Tightness is ensured via silicon seal. The container has been also enclosed in a plastic bag (volume V4). The volumes are flushed separately with pure Nitrogen in order to measure possible radon contamination as a function of different flushing scenarii.

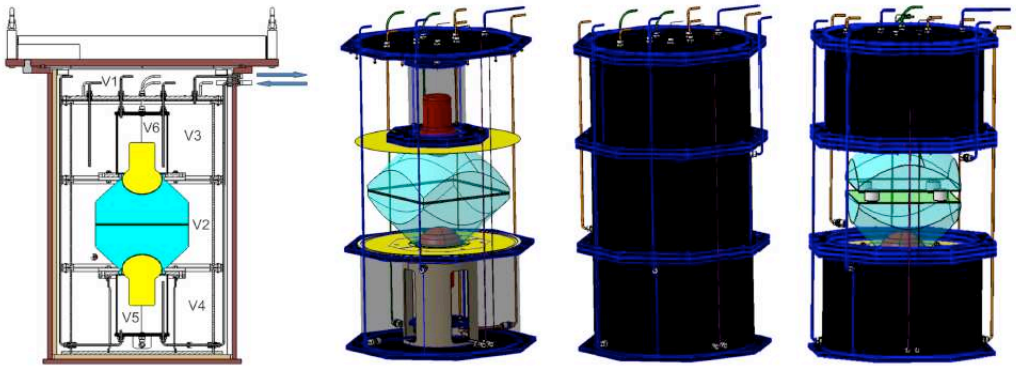

FIGURE 11.13: Schematic view of the BiPo-3 prototype.

The objectives and related issues of the BiPo-3 prototype are the following :

- Measure the random coincidence background, first by studying the single counting rate of the scintillators for different configurations of the shield, and then by comparing the effect of the scintillator thickness.
- Measure the surface background of the BiPo-3 scintillators in ^{208}Tl and ^{214}Bi.

– Measure the radon background and test the radon suppression with separated flushed volumes

11.3.1 Energy calibration

The energy calibration of the BiPo-3 prototype is performed using successively a ^{54}Mn source (γ of 835 keV) and a ^{22}Na source, located on the lateral side of the scintillators. The energy spectra of the Compton edges at 639 keV for ^{54}Mn, and 1062 keV for ^{22}Na, are measured using fully contained electrons in one scintillator, and without any coincidence in the opposite one. They are then fitted separately using the Monte-Carlo simulation, in which both the energy calibration (keV per unit of charge) and the energy resolution (FWHM at 1 MeV) are two free parameters. The non uniformity of the scintillator response (as a function of the position from the center of the scintillator), which has been previously measured on the test bench in LAL, is included in the Monte Carlo. A Kolgomorov test is then used to defined the best values for the energy calibration and the energy resolution. Figure 11.14 shows the results of the fit and the most probable values for the energy calibration and resolutions, both with ^{54}Mn and ^{22}Na. The values of the energy calibration obtained separately with the two calibration sources are in perfect agreement. The systematic error on the energy calibration is of the order of 1% only.

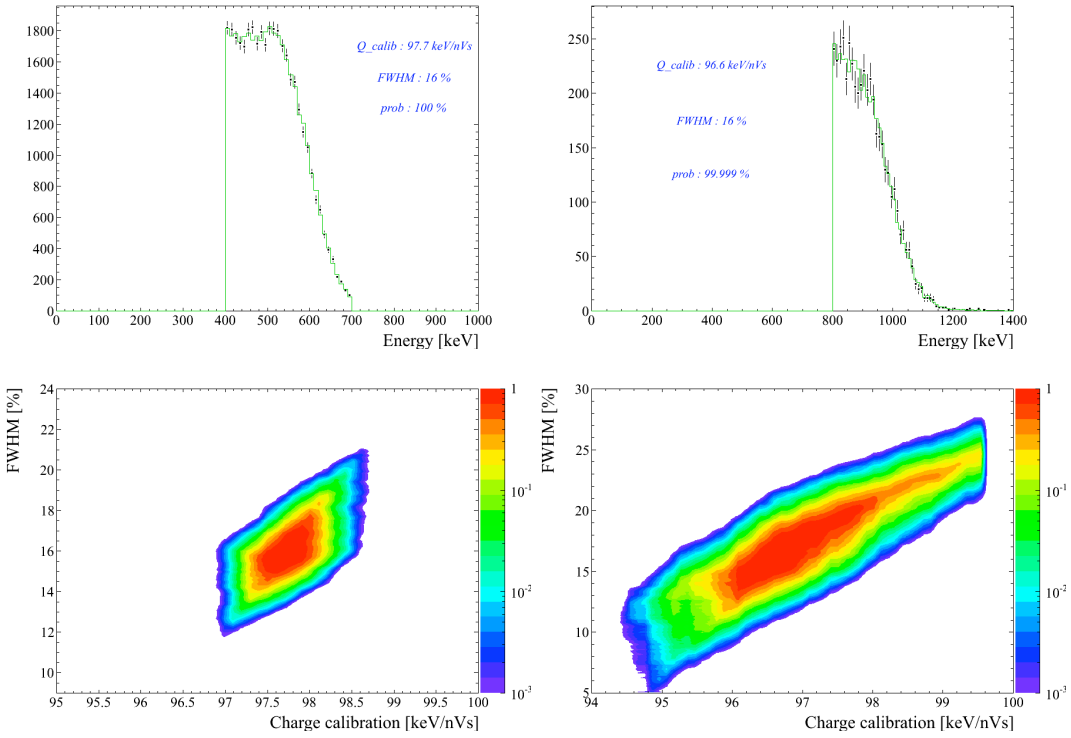

FIGURE 11.14: Energy spectrum of the compton edge measured with ^{54}Mn (upper left) and ^{22}Na (upper right) and result of the Monte-Carlo fit ; (Lower plots) Allowed region for the most probable values of the energy calibration and energy resolutions obtained with ^{54}Mn (left) and ^{22}Na (right).

11.3.2 Scintillation noise

Figure 11.15 shows the distribution of amplitude A versus charge Q and the ratio Q/A for detected PMT signals. Clearly two types of events appear. The first one with higher ratio $Q/A \approx 0.02$nVs/mv corresponds to scintillation signals produced inside the scintillator and in agreement with the values measured on test bench in Orsay with ^{207}Bi source. The second type of event is mostly present at low energy. It is not due to PMT noise. We think that this background corresponds to scintillation light produced in the PMMA. The narrower shape of its signal may be due to a faster scintillating process of PMMA compared to polystyren scintillator. This background is rejected with the pulse shape analysis, requiring $Q/A > 0.02$.

Similar background had been observed with a previous prototype whose optical guide was produced with standard PMMA with lower transmission in UV. This lower transmission required to increase the PMT gain by a factor of 2 (2.10^6) in order to have same signal amplitude (500 mV for 1 MeV electron). The scintillation background was then 100 times larger.

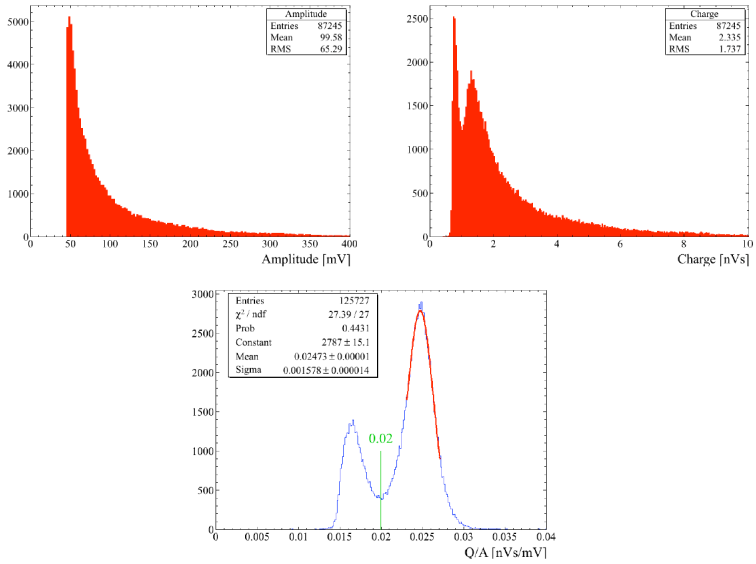

FIGURE 11.15: Noise observed in the BiPo-3 prototype running in Canfranc with the final selected UV-enhanced PMMA.

11.3.3 Random coincidence background

The level of random coincidence background is correlated to the single counting rate of the scintillators. Figure 11.16 shows the expected number of random coincidence events and the related expected sensitivity in ^{214}Bi of the BiPo-3 detector assuming 4 months of measurement and 90% efficiency for e^-/α discrimination (as obtained in BiPo-1 prototype). A single counting rate of 15 mHz is required in order to be able to reach the target sensitivity for SuperNEMO of 10 μBq/kg in ^{214}Bi with 4 months of measurements. It corresponds to about 2 random coincidence events per month.

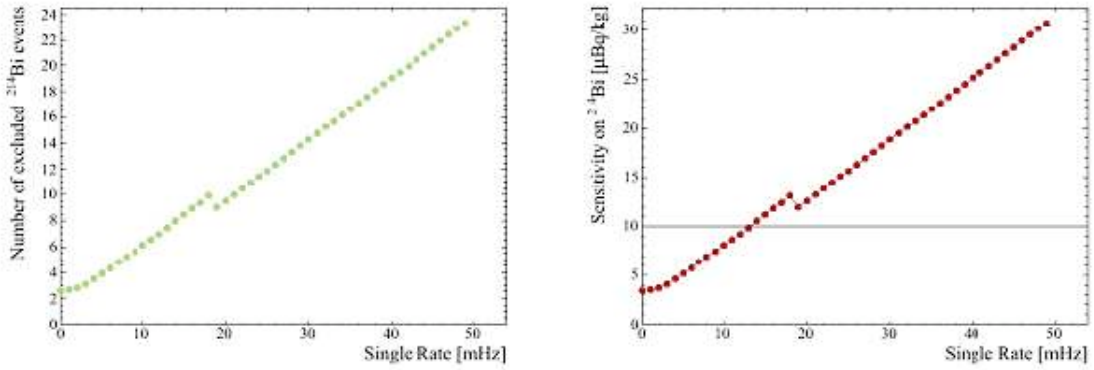

FIGURE 11.16: (left) Number of expected random coincidence events as a function of the single counting rate of the scintillator after 4 months of measurement with the BiPo-3 detector ; (right) Expected sensitivity in ^{214}Bi of the BiPo-3 detector as a function of the single counting rate, assuming 4 months of measurement and 90% efficiency for e^-/α discrimination.

The single counting rate of the BiPo-3 prototype has been measured with several configurations and thickness of the shield in order to optimize the design of the shield for a single counting rate of 15 mHz.

The counting rate is defined as the rate of scintillating signal above 150 keV (the nominal energy threshold of BiPo-3) requiring no coincident signal in the second scintillator (with an anticoincidence threshold of 10 keV corresponding to the anticoincidence threshold for BiPo event selection).

The following shield configurations have been tested :

- Only 1.5 cm of pure iron
- 1.5 cm pure iron + 5 cm of lead
- 1.5 cm pure iron + 10 cm of lead
- 1.5 cm pure iron + 5 cm of lead + 38 cm of water
- 1.5 cm pure iron + 10 cm of lead + 38 cm of water

The water containers have been installed outside of the lead and only on the lateral sides of the prototype. There is no water container on the top and the bottom of the detector. Figure 11.17 shows pictures of two configurations of shield.

The counting rates, measured for the 3 mm and 2 mm scintillators, are presented in Figure 11.18, as a function of the water equivalent thickness of the corresponding shield configuration. The rates have been fitted by a linear attenuation factor plus an internal constant contribution and are compared to the expected rate calculated by Monte-Carlo using the external γ flux measured in Canfranc.

Figure 11.19 shows the counting rate over time in the final shield configuration with 10 cm of lead and 38 cm of water. The rate was too high during the first week due to a radon contamination inside the detector, associated to a defect in the Nitrogen flushing system. As soon as the flushing system became efficient, the rate decreased and reached the nominal value of about 15 mHz for the 2 mm scintillator and about 20 mHz for the 3 mm scintillator. The ratio of the two rates is of the same order than the ratio of the two

FIGURE 11.17: Pictures of two configurations of shield tested with the BiPo-3 prototype in Canfranc.

scintillator thicknesses, demonstrating that the counting rate is still dominated by external γ, and especially by γ emitted from the ground. We believe that this rate can be still reduced by adding a layer of shield (lead or pure iron) under the detector.

In conclusion, we have demonstrated that a shield of 10 cm of lead and 38 cm of water is good enough to reach the required sensitivity of BiPo-3. We have also demonstrated that a scintillator thickness of 2 mm is optimal to reduce the counting rate and to contain the energy of the electrons.

11.3.4 Surface background measurement in ^{208}Tl and ^{214}Bi

A long run of background measurement has been performed in order to measure the surface background of the new BiPo-3 scintillators in ^{208}Tl and in ^{214}Bi. The two differences in the treatement of the scintillator surfaces, compared to BiPo-1 prototype, are the following :

- we use a new aluminium evaporation facility (never used before),
- the scintillator are machined under Nitrogen flush.

After 59.4 days of measurement, no ^{212}Bi$\rightarrow^{212}$Po event has been observed. It corresponds to an upper limit on the surface activity in ^{208}Tl of

$$\mathcal{A}(^{208}Tl) \leq 5.4 \mu Bq.m^{-2}$$

It has to be compared to the positive value measured in BiPo-1 prototype of $\mathcal{A}(^{208}\text{Tl}) = 1.5 \pm 0.4$ μBq/m^2.

After the same period of measurement, 6 ^{214}Bi$\rightarrow^{214}$Po events have been observed. It corresponds to a surface activity in ^{214}Bi of

$$0.6 \leq \mathcal{A}(^{214}\text{Bi}) \leq 23.0 \mu\text{Bq.m}^{-2} \quad (90\% \text{ C.L.})$$

However, the e^-/α discrimination has not yet been applied to this analysis. In consequence, about 4 random coincidence events are expected. Actually we can directly identify

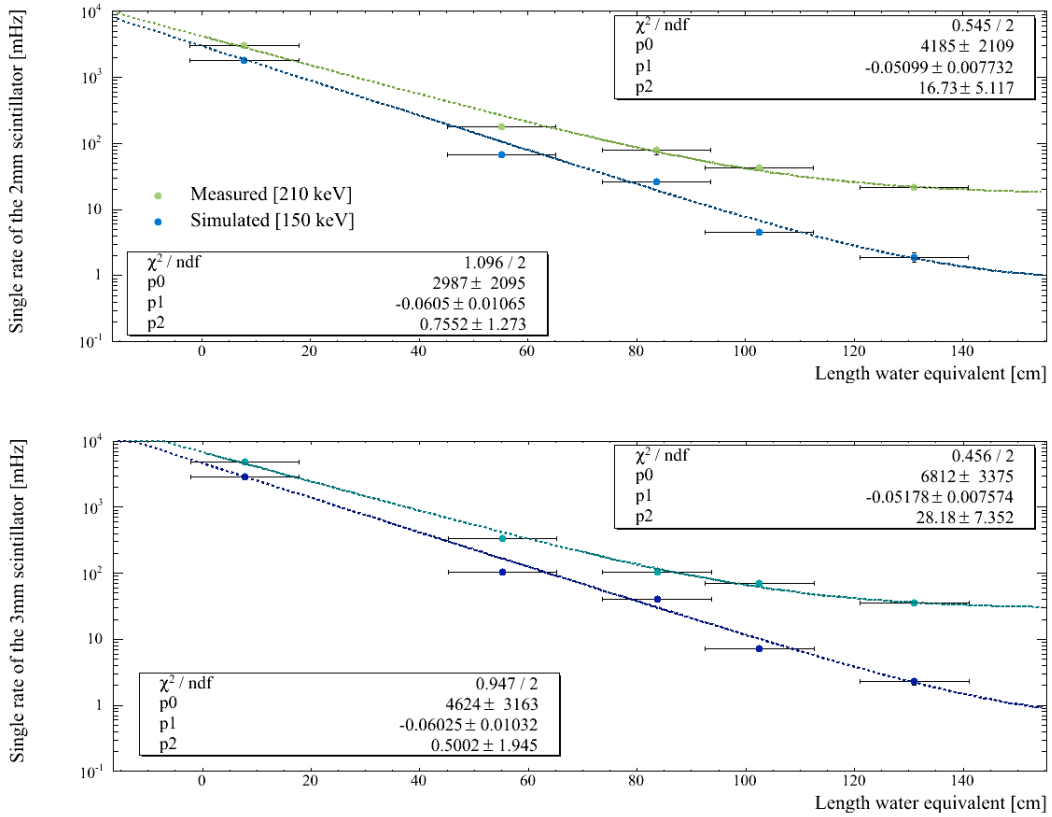

FIGURE 11.18: Single counting rate measured with the 3 mm (top) and 2 mm (bottom) thick scintillators of the BiPo-3 prototype in Canfranc as a function of the water equivalent thickness of the different configuration of shield. The nominal shield of 10 cm of lead and 35 cm of water corresponds to about 130 cm of water length.

and reject the coincidence events using the energy and delay time distributions of the delayed hits. Indeed, in the case of a ^{214}Bi$\rightarrow^{214}$Po decay from a ^{214}Bi contamination on the surface of the scintillator, the delayed α deposits all its available energy (7.7 MeV), corresponding to a scintillation energy of about 1 MeV due to the quenching factor. But in the case of random coincidence event, the energy distribution of the delayed hit is expected to be roughly decreasing and the delay time distribution roughly flat. Among the 6 detected ^{214}Bi$\rightarrow^{214}$Po events, 5 events have an energy lower than 500 keV and a flat delay time distribution, corresponding to random coincidence events. Only 1 event has an energy around 1 MeV as expected for ^{214}Bi$\rightarrow^{214}$Po event. It corresponds to an upper limit on the surface activity in ^{214}Bi of

$$\mathcal{A}(^{214}\text{Bi}) \leq 13.6 \mu\text{Bq.m}^{-2} \quad (90\% \text{ C.L.})$$

11.3.5 Radon study

The very low surface background observed in ^{214}Bi means that the radon background is very low, and much lower than previously with the BiPo-1 prototype in Modane. It validates

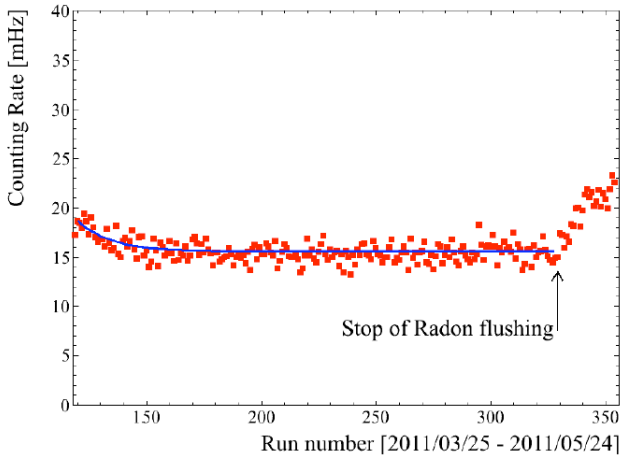

FIGURE 11.19: Single counting rate of the 2 mm scintillator of the BiPo-3 detector as a function of time (a run is equivalent to about 6 hours). The increase at the end of the long term measurement is due to a stop of the Nitrogen flushing.

the technical choices made to avoid radon contamination.

A second phase of radon background measurement has been performed by adding low radioactive delrin spacers between the two scintillators in order to increase the volume between the scintillators and consequentely to increase the efficiency and sensitivity to detect possible radon contamination (see Figure 11.13).

We first observed that the container of the prototype, which was directly in contact with the air of the lab, was not tight enough to suppress external radon diffusion (the radon activity of the LSC air is high, around 100 Bq/m^3). Several runs were carried out by increasing the Nitrogen flux inside the external V4 volume or by flushing only pure Nitrogen inside the volume V2 between the two scintillator (see Figure 11.13 for volumes definition). It has been demonstrated that radon background can be suppressed, just by flushing pure Nitrogen inside V2 with a relatively low flux of around 1 volume per hour (20 l/h).

11.4 Status of the construction

Today all the optical sub-modules have been produced, assembled and about 50 have been already successfully tested. The construction procedure was the following :

- The polysthyren-base scintillators have been produced in JINR Dubna in the form of large 1×1×2 m^3 cubes, and then machined roughly in the form of 305×305×6 mm^3 plates.
- Then the plates were machined in a french company to its final dimensions 300×300×2 mm^3. Special procedure conditions have been applied to avoid any radio-contamination on the surface of the scintillator : use of a diamond tool (radiopure), oil or water have been forbiden, Nitrogen has been flushed on the surface during the machning, and finally the last 100 μm of the scintillator surface has been machined at the last moment and finished scintillator plates have been immediatly protected

inside a tight plastic bag.
- The optical guides have been machined in the same company, then they have been annealed in an oven in clean room in LAL.
- The scintillators have been carefully cleaned using the following cleaning sequence : acetic acid, ultra pure water rinse, isopropanol and finally a second ultra pure water rinse.
- The scintillator have been glued on the optical guide under laminar flux in the clean room.
- Then the scintillator have been aluminized in IPN Orsay. The scintillators were always kept in clean condition in plastic boxes, wrapped with plastic film.
- Back to LAL clean room, PMT's were then glued to the optical guides. Gain, noise and linearity of all the PMT's have been early measured in LAL Orsay using a test bench developed for LHCb. The HV dividers have been also early installed on each PMT.
- The optical sub-modules have been wrapped with the Tyvek mask and then tested and calibrated on the test bench, in the clean room.

The acquisition used for the calibration on test bench is identical to the BiPo-3 acquisition. The calibration procedure is the following. The HV of the PMT is set to the value corresponding to a gain of 10^6 (nominal BiPo-3 running gain). It corresponds to a signal amplitude of about 500 mV for 1 MeV electron. The energy spectra is first measured with the ^{207}Bi source on the center of the scintillator. The peak corresponding to the 1 MeV conversion electron gives the absolute calibration. Then a mapping of the response of the optical sub-module is carried out with an ^{241}Am α source, by measuring the energy spectra at 25 successive positions (symmetrical and evenly spaced positions). Finally a second energy spectra with the ^{207}Bi source on the center of the scintillator is measured in order to control the stability of the PMT gain during the mapping. Figure 11.20 shows a typical energy spectrum obtained with the ^{241}Am α source and the ^{207}Bi source.

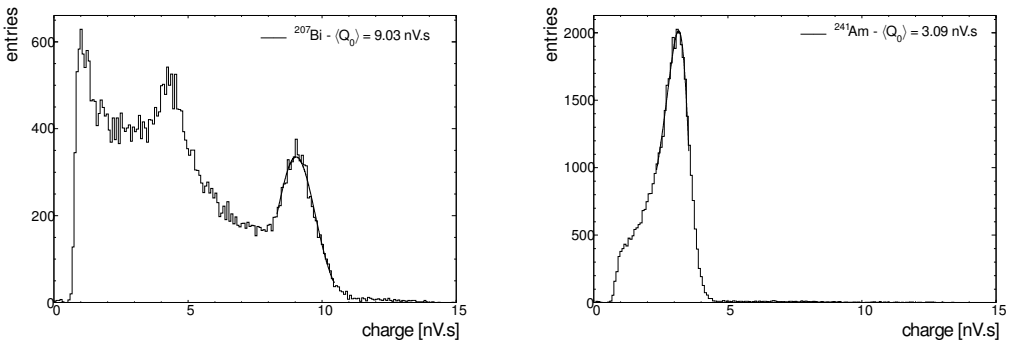

FIGURE 11.20: Energy spectrum measured on test bench with the ^{207}Bi source (left) and ^{241}Am α source (right).

Figure 11.21 shows a summary of the absolute calibration at 1 MeV for the first 50 optical submodules already tested : the charge corresponding to the 1 MeV e^- conversion emitted by the ^{207}Bi source is in the average about 8.5 nV.s, corresponding to about 250 photoelectrons (or about 1 photoelectron per 4 keV deposited), and it is stable at $\pm$ 10% (rms) from one

module to another one.

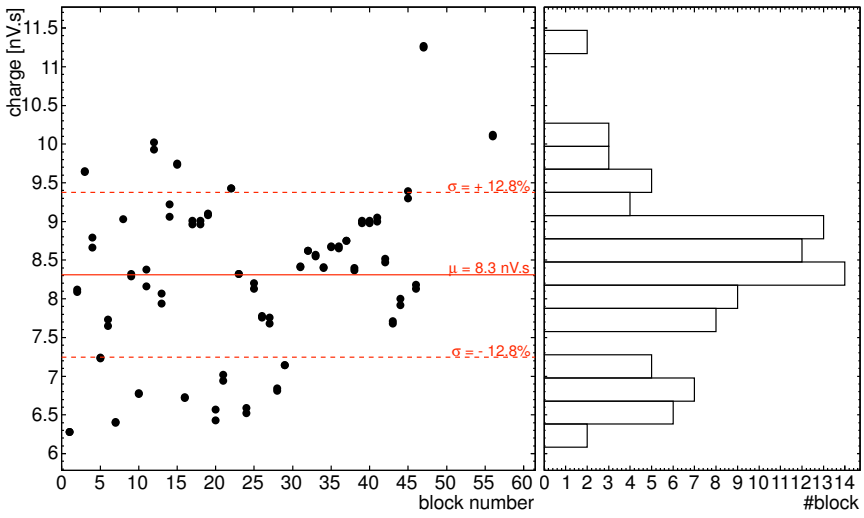

FIGURE 11.21: Charge measured for 1 MeV electron on the center of the scintillator plate versus the block number for PMT's with a gain of 10^6. The average charge is about 8.5 nV.s, corresponding to about 250 photoelectrons/MeV.

Figure 11.22 shows the relative charge measured with the ^{241}Am α source as a function of the distance of the source to the center of the scintillator. It is in relatively good agreement with the expected function calculated with numerical simulations. The fitted function is used in Monte Carlo in order to correct the energy response of the scintillator as a function of the position of the energy deposition on the scintillator.

The mechanical structures supporting the optical sub-module have been assembled in LAL Orsay. The installation of the BiPo-3 modules in Canfranc Underground Laboratory is foreseen in summer 2012. A background measurement of the first module will be carried out during few months. Measurements of first samples of SuperNEMO $\beta\beta$ source foils will start end of 2012.

11.5 Expected sensitivity of the BiPo-3 detector

The expected sensitivities in ^{208}Tl and ^{214}Bi, for the measurement of a ^{82}Se foil of 40 mg/cm^2 (SuperNEMO double beta foil) are presented in Figure 11.23. We have assumed only ^{232}Th and ^{238}U contamination on the surface of the scintillators, since it has been demonstrated using BiPo-1 and BiPo-3 prototype that random coincidences and thoron backgrounds are negligible. The black solid line corresponds to the conservative scenario assuming a level of surface background of $\mathcal{A}(^{208}\text{Tl}) = 1.5$ μBq/m^2 as measured in the BiPo-1 prototype. The yellow area corresponds to the uncertainty range (90% C.L.) of the surface activity measured with the BiPo-3 prototype in Canfranc. The larger uncertainty with the BiPo-3 prototype compared to BiPo-1 is due to a lower statistic. A sensitivity of $\mathcal{A}(^{208}\text{Tl}) < 10$ μBq/m^2 can be reached after 1 month of measurement and the required

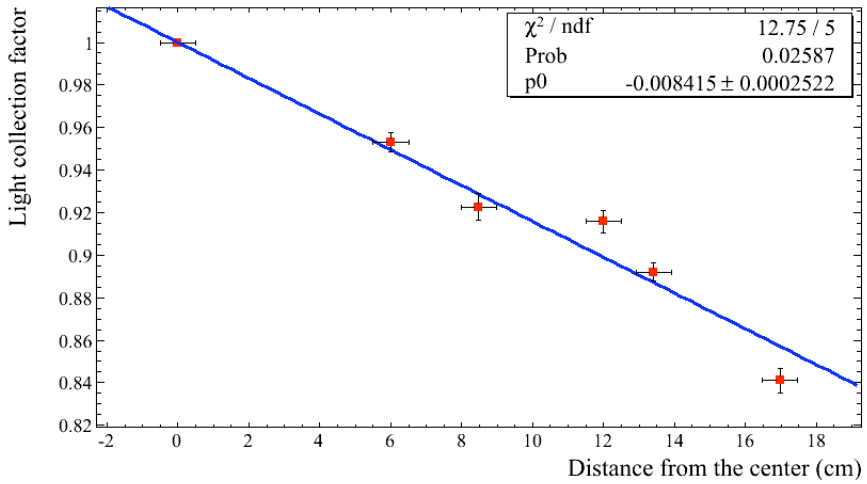

FIGURE 11.22: Relative charge measured with the ^{241}Am α source as a function of the distance of the source to the center of the scintillator. The charge is normalized to the charge measured at the center.

sensitivity of 2 μBq/m^2 could be reach in about 6 months.

The expected sensitivity in ^{214}Bi is presented in Figure 11.23. It assumes also only ^{238}U contamination on the surface of the scintillators since it has been demonstrated using the BiPo-3 prototype that random coincidences should be negligible with the proposed shield and the α/e^- discrimination. The yellow area corresponds to the uncertainty range (90% C.L.) of the surface activity measured with the BiPo-3 prototype in Canfranc while the black solid line corresponds to the most probable value. The required sensitivity of $\mathcal{A}(^{214}\text{Bi}) = 10$ μBq/m^2 could be reach in few months.

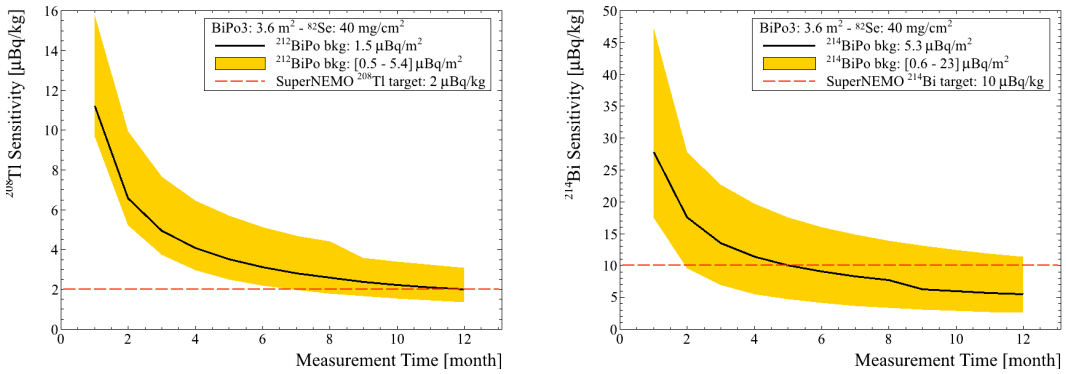

FIGURE 11.23: Expected sensitivity of the BiPo-3 detector for the measurement of a ^{82}Se foil of 40 mg/cm^2 (SuperNEMO double beta foil) : (left) Sensitivity in ^{208}Tl; (right) Sensitivity in ^{214}Bi. See the text for the legends.

Bibliographie

[1] K. Nakamura et al., Particle Data Group (http ://pdg.lbl.gov), JP G 37, 075021 (2010)

[2] E. Majorana, Nuovo Cim. 14, 171-184 (1937)

[3] C. Giunti and C.W. Kim, *Fondamentals of neutrino physics and astrophysics*, Oxford Univ. Press (2007)

[4] B. Kayser, *The physics of massive neutrino*, World Scientific Lecture Notes in Physics Vol. 25

[5] R.N. Mohapatra and G. Senjanovic, Phys. Rev. Lett. 44, 912-915 (1980) ;
R.N. Mohapatra and G. Senjanovic, Phys. Rev. D 23, 165 (1981) ;
W. Rodejohann, PRAMANA (Journal of Phys., Indian Academy of Sciences) Vol. 72, No. 1, 217-227 (2009)

[6] W.H. Furry, Phys. Rev. 56, 1184-1193 (1939)

[7] J. Schechter and J.W.F. Valle, Phys. Rev. D 25, 2951 (1982)

[8] W. Rodejohann, Int. Journal of Modern Physics E 20, 1833 (2011)

[9] M. Duerr, M. Lindner, A. Merle, JHEP 1106, 091 (2011)

[10] S. Eliseev et al. Phys. Rev. Lett. 106, 052504 (2011)

[11] S. Pascoli, S.T. Petcov, Phys. Rev. D 77, 113003 (2008)

[12] A. Dueck, W. Rodejohann and K. Zuber, Phys. Rev. D 83, 113010 (2011)

[13] F. Simkovic et al., Phys. Rev. C 79, 055501 (2009) ;
D. L. Fang et al., Phys. Rev. C 82, 051301 (2010)

[14] M. Kortelainen, O. Civitarese, J. Suhonen and J. Toivanen, Phys. Lett. B 647, 128 (2007) ;
M. Kortelainen and J. Suhonen, Phys. Rev. C 75, 051303 (2007) ;
M. Kortelainen and J. Suhonen, Phys. Rev. C 76, 024315 (2007)

[15] J. Menendez et al., Nucl. Phys. A818, 139-151 (2009)

[16] J. Barea, F. Iachello, Phys. Rev. C79, 044301 (2009)

[17] T. R. Rodriguez and G. Martinez-Pinedo, Phys. Rev. Lett. 105, 252503 (2010)

[18] P. K. Rath et al., Phys. Rev. C 82 (2010) 064310

[19] S.R. Elliot, arXiv :1110.6159

[20] F. Simkovic et al., Phys.Rev. C77, 045503 (2008)

[21] B.P. Kay et al., Phys. Rev. C 79, 021301 (2009)

[22] S.J. Freeman et al., Phys. Rev. C 75, 051301 (2007)

[23] J. Menendez et al., Phys. Rev. C 80 048501 (2009)

[24] J. Suhonen and O. Civitarese, Phys. Lett. B 668, 277 (2008)

[25] M. Kortelainen and J. Suhonen, Europhys. Lett. 58, 666 (2002)

[26] V.I. Tretyak, AIP Conf. Proc. 1417, 129-133 (2011) ; arXiv :1112.4183

[27] R. Arnold et al., Nucl. Instr. and Meth. A 536 (2005) 79-122.

[28] C. Augier, HDR, LAL-05-35 (2005)

[29] L. Simard, HDR, LAL-Note (2009)

[30] R. Arnold et al., Nucl. Instr. and Meth. A 606, 449-465 (2009)

[31] R. Arnold and Vera Kovalenko, NEMO-3 internal note, NemoDocDB-doc-671-v1

[32] R. Arnold, NEMO-3 internal note, NemoDocDB-doc-500-v1

[33] M. Bongrand, PhD Thesis, University of Paris-11, (2008)

[34] R. Arnold et al., Phys. Rev. Lett. 95, 182302 (2005)

[35] Nucl. Phys. A847, 168 (2010)

[36] Phys. Rev. Lett. 107, 062504 (2011)

[37] J. Argyriades et al., Phys. Rev. C 80, 032501 (2009)

[38] R. Arnold et al., Nucl. Phys. A 781 (2007) 209-226.

[39] R. Arnold et al., NEMO collaboration, Nucl. Instrum. Meth. A 474, 93 (2001).

[40] L. Simard, NEMO-3 Collaboration, presentation given at the 12th Int. Conf. on Topics in Astroparticle and Underground Physics (TAUP 2011), Sept. 2011, Mnchen, Germany

[41] R. Arnold et al., Nucl. Phys. A 765 (2006) 483-494.

[42] SuperNEMO TDR "Proposal for the participation of France in the construction of a preproduction prototype (demonstrator module) of the SuperNEMO double beta decay detector"

[43] C. J. Kim et al, Proceedings of the 10th International Workshop on Separation Phenomena in Liquids and Gases, pp. 86-90, Angra dos Reis, Brazil (2008)

[44] E. Fiorini et al. Phys. Lett. B 25, 602 (1967)

[45] G. Douysset et al. Phys. Rev. Lett. 86, 4259 (2001)

[46] H.V. Klapdor-Kleingrothaus et al., Eur. Phys. J. A 12, 147 (2001)

[47] H.V. Klapdor-Kleingrothaus et al., NIM A 522, 371-406 (2004)

[48] arXiv :0812.1206v1, PhD Thesis, University of Heidelberg, 110p (2008)

[49] C. E. Aalseth et al., Phys. Rev. C 57, 2108 (1999)

[50] C. E. Aalseth et al., Phys. Rev. D 65, 092007 (2002)

[51] I. Barabanov et al., NIM A 606, 790-794 (2009)

[52] D. Budjas, Dissertation, University of Heidelberg (2009)

[53] D. Budjas et al., Journal of Inst., 4 P10007 (2009)

[54] M. Barnabé Heider et al., Journal of Inst., 5 P10007 (2010)

[55] M. Agostini et al., Journal of Inst., 6 P04005 (2011)

[56] B. Majorovits, Int. Workshop on Double Beta Decay and Neutrinos, Osaka, Japan, 14-17 November 2011.

[57] B. Majorovits et al., N.I.M. A 647, 39-45 (2011)

[58] S. Elliot et al., Phys. Rev. C 82, 054610 (2010)

[59] D.M. Mei et al., Phys. Rev. C 77, 054614 (2008)

[60] G. Devlin et al., Phys. Rev. C 79, 054604 (2009)

[61] C. Arnaboldi et al., Phys. Lett. B557, 167 (2003)

[62] E. Fiorini and T. Niinikoski, NIM 224, 83 (1984)

[63] A.H. Wapstra, G. Audi, and C. Thibault, Nucl. Phys. A729, 337 (2003)

[64] C. Arnaboldi et al., IEEE Trans. Nucl. Sci., 50, 979 (2003)

[65] E. Andreotti et al., Astropart. Phys. 34 (2011) 822-831

[66] E. Andreotti et al., arXiv :1108.4313

[67] E. Andreotti et al., Astroparticle Physics 34, 18-24 (2010)

[68] F. Alessandria et al., arXiv :1108.4757, submitted to Astroparticle Physics

[69] F. Bellini et al., Journal of Inst., 5 P12005 (2010)

[70] F. Bellini, et al., Astropart. Phys. 33, 169-174 (2010)

[71] M. Pavan et al., Eur. Phys. J. A36, 159-166 (2008)

[72] C. Arnaboldi et al., J. Cryst. Growth 312, 2999-3008 (2010)

[73] P. Gorla, presentation given at the 12th Int. Conf. on Topics in Astroparticle and Underground Physics (TAUP 2011), Sept. 2011, Mnchen, Germany

[74] A. Faessler et al., Phys. Rev. D79, 053001 (2009)

[75] L. Foggetta et al., Astopar. Phys. 34, 809-821 (2011)

[76] A. Alessandrello et al., Nucl. Phys. B 28A, 233 (1992)

[77] C. Bobin et al., N.I.M. A 386 453 (1994)

[78] G. Angloher et al. Astropart. Phys. 23, 325 (2005)

[79] S. Cebrian et al. Phys. Lett. B 563, 48 (2003)

[80] N. Coron et al., N.I.M. A 520, 159 (2004))

[81] F.A. Danevich et al., Phys. Rev. C 68, 035501 (2003)

[82] S. Pirro et al., Phys. Atom. Nucl. 69, 2109 (2006)

[83] C. Arnaboldi et al., arXiv :1005.1239, submitted to Astroparticle Physics

[84] A. S. Barabash et al., Journal of Inst. 6 P08011 (2011)

[85] C. Arnaboldi et al., Astroparticle Physics 34, 344-353 (2011)

[86] L. Gironi et al, JINST 5 P11007 (2010)

[87] C. Arnaboldi et al., Astroparticle Physics 34, 797-804 (2011)

[88] J.W. Beeman et al., arXiv :1202.0238, published in Astropart. Phys. online version : http ://dx.doi.org/10.1016/j.astropartphys.2012.02.013

[89] J.W. Beeman et al., Phys. Lett. B 710 (2012) 318-323

[90] V.N. Kornoukhov, AMORE Collaboration, presentation given at the 12th Int. Conf. on Topics in Astroparticle and Underground Physics (TAUP 2011), Sept. 2011, Mnchen, Germany

[91] R.S. Raghavan, Phys. Rev. Lett 72, 1411-1414 (1994)

[92] S. Abe et al., Phys. Rev. C 81, 025807 (2010)

[93] A. Gando et al., arXiv :1201.4664

[94] M.C. Chen, Nucl. Phys. Proc. Suppl. 145, 65 (2005)

[95] J Hartnell for the SNO+ collaboration, arXiv :1201.6169

[96] J. Boger et al., Nucl. Inst. Meth. A 449, 172 (2000)

[97] M. Yeh et al., Nucl. Instrum. Meth. A 578, 329 (2007)

[98] G. Alimonti et al., Nucl. Inst. Meth. A 609, 58 (2009)

[99] R. Ford et al., AIP Conf. Proc. 1338, 183 (2011)

[100] S. Hans et al. AIP Conf. Proc. 1338, 17 (2011)

[101] N. Ackerman et al. (EXO Collaboration), Phys. Rev. Lett. 107, 212501 (2011)

[102] E. Conti et al., Phys. Rev. B68, 054201 (2003)

[103] W. Neuhauser et al., Phys. Rev. A 22, 1137 (1980) ;
M.K. Moe, Phys. Rev. C44, R931 (1991) ;
M. Danilov et al., Phys. Lett. B480, 12 (2000)

[104] A. Bolotnikov and B. Ramsey, Nucl. Inst. Meth. A396, 360-370 (1997)

[105] R. Luscher et al., Phys. Lett. B434, 407 (1998)

[106] Y. Giomataris et al., Nucl. Inst. Meth. A376, 29 (1996)
Giomataris et al., Nucl. Inst. Meth. A560, 405 (2006)

[107] S. Cebrian et al, Astropart. Phys. 34, 354-359 (2011)

[108] I.G. Irastorza et al., arXiv :1109-4021

[109] S. Cebrian et al., JCAP10 (2010) 010

[110] D. Franco et al., J. Phys. Conf. Ser. 309, 012004 (2011)

[111] S. Umehara et al., Phys. Rev. C 78, 058501 (2008)

[112] E. der Mateosian, M. Goldhaber, Phys. Rev. 146, 810 (1966) ;
R.K. Bardin et al., Phys. Lett. B 26, 112-116 (1967)

[113] S. Umehara, presentation given at the International Workshop on Double Beta Decay and Neutrinos, Osaka, Japan (2011)

[114] T. Bloxham et al., Phys. Rev. C 76, 025501 (2007) ;
K. Zuber, Phys. Lett. B 519, 1-7 (2001)

[115] G.J. Feldman and R.D. Cousins, Phys. Rev. D 57, 3873-3889 (1998)

[116] Y.A. Akovali, Nucl. Data Sheets 76, 127 (1995)

[117] L. Wissink et al., Nucl. Inst. Meth. A 397 (1997) 472-474.

[118] R. de la Fuente et al., J. Env. Rad. 99 (2008) 1553.

[119] R.V. Vasilyev (on behalf of the SuperNEMO collaboration), Physics of Particles and Nuclei Letters Vol. 6 No. 3 (2009) 241.

[120] D. Breton et al., IEEE Trans. Nucl. Sci. 52 (2005) 2853.

[121] R. Cizeron et al., LHCb Calorimeter Technical Note LHCB 2000-52.

[122] M. Bongrand (on behalf of the SuperNEMO collaboration), AIP Conf. Proc. 897 (2007) 14.

[123] V.I. Tretyak, Astropart. Phys. 33 (2010) 40.

[124] J.B. Birks, Proc. Phys. Soc. A 64 (1951) 874 ; J.B. Birks, The Theory and Practice of Scintillation Counting, Pergamon Press, Oxford 1964.

[125] Nuclear Data Sheets for A=212 104 (2005) 427.

[126] G. Alimonti et al., Astropart. Phys. 8 (1998) 141-157.

[127] J. Argyriades et al., Nucl. Inst. Meth. A625, 20-28 (2011)